COLLECTED PAPERS on Coherent Opto-Electronics

Vol. 0

April 1974 – June 1982

Motoichi OHTSU

Tokyo Institute of Technology

LIST OF PAPERS

[(pp. XX-XX); pages in this issue of the COLLECTED PAPERS**]**

[I] ORIGINAL PAPERS

[8] I. Siio, M. Ohtsu, and T. Tako, “Frequency Stabilization of a He-Xe Laser Using a Stark Spectrum in H_2CO,” Jpn. J. Appl. Phys., Vol.20, No.7, July 1981, pp.L508-L510.

(pp. 41-43)

[9] H. Tsuchida, M. Ohtsu, and T. Tako, “Frequency Stabilization of AlGaAs DH Lasers,” Jpn. J. Appl. Phys., Vol.20, No.6, June 1981, pp.L403-L406.

(pp.45-48)

[10] M. Ohtsu, S. Katsuragi, and T. Tako, “Performances of a Frequency Offset Locked He-Xe Laser System at 3.51 μ m,” IEEE J. Quantum Electron., Vol.QE-17, No.6, June 1981, pp.1100-1106.

(pp. 49-55)

[11] M. Ohtsu and T. Tako, “Mode Competition in the 3.51 μ m He-Xe Laser in an Axial Magnetic Field,” Jpn. J. Appl. Phys., Vol.17, No.1, January 1978, pp.177-182.

(pp.57-62)

[12] I. Siio, M. Ohtsu, and T. Tako, “Real-Time Processing System of the Measurement of Laser Frequency Stability,” Trans. IECE, Vol.J64-C, No.3, March 1981, pp.204-208.

【椎尾一郎、大津元一、田幸敏治、「レーザ周波数安定度の実時間測定装置の試作」、電子情報通信学会論文誌、第 J64-C 巻、第 3 号、1981 年 3 月、pp. 204-208】

(pp.63-67)

[13] H. Tsuchida, S. Sanpei, M. Ohtsu, and T. Tako, “Frequency Stability Measurement of Feedback Stabilized AlGaAs DH Laser,” Jpn. J. Appl. Phys., Vol.19, No.12 December 1980, pp.L721-724.

(pp. 69-72)

[14] M. Ohtsu and T. Tako,”Frequency-Offset-Locked He-Xe Laser at 3.51 μ m, Rev. Laser Eng., Vol.8, No.5, September 1980, pp.769-776.

【大津元一、田幸敏治、「3.51 μ m周波数オフセットロック He-Xe レーザ」、レーザー研究、第 8 巻、第 5 号、1980 年 9 月、pp. 769-776】

(pp. 73-80)

[15] T. Tako, M. Ohtsu, S. Katsuragi, M. Ohi, and Y. Akimoto, “Wavelength

Measurement of an H_2CO-Stabilized He-Xe Laser at 3.51 μm," Jpn. J. Appl. Phys., Vol.19, No.9, September 1980, pp.1683-1688.

(pp. 81-86)

[16] A. Kusnowo, M. Ohtsu, N. Kobayashi, and T. Tako, "Measurement of the saturated absorption signal of CH_4 at 3.39 μm using a He-Ne laser and a multipath cell", Appl. Opt., Vol.19, No.8, April 1980, pp.1227-1229.

(pp. 87-89)

[17] M. Ohtsu, I. Mitamura, and T. Tako, "Oscillating c haracteristics of He-Xe lasers at 3.51 μm ---- A Fabry-Perot Resonator-type and Waveguide-Type----," Rev. Spectroscopy, Vol.28, No.6, June 1979, pp.327-336.
【大津元一、三田村一郎、田幸敏治、「3.51 μ mHe-Xe レーザーの発振特性--ファブリ・ペロー共振器型および導波路型--」、分光研究、第 28 巻、第 6 号、1979 年 6 月、pp. 327-336】

(pp. 91-100)

[18] M. Ohtsu, S. Katsuragi, and T. Tako, "Theoretical Study of Mode Competition in the 3.51 μm He-Xe Laser in an Axial Magnetic Field," Bull. P.M.E. (T.I.T.), No.44, 1979, pp.1-18.

(pp. 101-118)

[19] M. Ohtsu, R. Koyama, and T. Tako, "Improvements in the Long-Term Frequency Stability of the He-Xe laser at 3.51 μm," Jpn. J. Appl. Phys., Vol.18, No.8, August 1979, pp.1621-1622.

(pp. 119-120)

[20] M. Ohtsu, R. Koyama, A. Kusnowo, and T. Tako, "Development of a Frequency-Offset-Locked He-Xe Laser at 3.51 μm," Jpn. J. Appl. Phys., Vol.18, No.8, August 1979, pp.1619-1620.

(pp. 121-122)

[21] M. Ohtsu and T. Tako, "Measurement of the width of the inverted Lamb dip in H_2CO at 3.51 μm," J. Appl. Phys., Vol.50, No.2, February 1979, pp.599-601.

(pp. 123-125)

[22] M. Ohtsu and T. Tako, "Frequency Stability of an H_2CO-Stabilized He-Xe Laser in an Axial Magnetic Field," Jpn. J. Appl. Phys., Vol.17, No.12, December 1978, pp.2169-2170.

(pp.127-128)

[23] M. Ohtsu, T. Akahane, and T. Tako, “Birefringence of n-Type Nematic Liquid Crystals Due to Electrically Induced Deformations of Vertical Alignment,” Jpn. J. Appl. Phys., Vol.13, No.4, April 1974, pp.621-629.
(pp. 129-137)

[II] PRESENTATIONS IN INTERNATIONAL CONFERENCES

[1] M. Ohtsu, "Noises and coherence in semiconductor lasers," Abstract of the Regional Symposium on Optoelectronics, Optical Fiber Communication and Solar Cell, November 19-20, 1984, Bangkok, Thailand, Sponsored by JSPS, pp.2-29 – 2-40.

[Invited Presentation]

(pp. 139-150)

[2] T. Tako, M. Ohtsu, and H. Tsuchida, "Limit of Frequency stability in semiconductor lasers," Abstracts of the United States-Japan Seminar on Coherence, Incoherence, and Chaos in Quantum Electronics, August 30, 1984, Nara, Japan, pp.60-62.

(pp. 151-153)

[3] Y. Teramachi and M. Ohtsu, "Specific instabilities in semiconductor lasers induced by reflected light," Abstracts of the United States-Japan Seminar on Coherence, Incoherence, and Chaos in Quantum Electronics, August 30, 1984, Nara, Japan, pp.63-66.

(pp. 155-158)

[4] T. Tako, M. Ohtsu, and H. Tsuchida, "Frequency Stabilization of AlGaAs lasers Based on the H_2O and Rb-D_2 Lines," Proceedings of the Third Symposium on Frequency Standards and Metrology, October 12-15, 1981, Aussois, France, (Journal de Physicuq, Colloque C8, supplement au no 12, Tome 42, December 1981, pp.C8-83 – C8-88.)

(pp. 159-164)

[5] T. Tako and M. Ohtsu, "H_2CO stabilized He-Xe laser, and its application to H_2CO molecular beam spectroscopy," Abstracts of the United States-Japan Seminar on Nonlinear Laser Spectroscopy, September 7-9, 1980, Hawai, USA, paper number Monday-#4.

(p. 165)

[III] REVIEW PAPERS

[1] T. Tako and M. Ohtsu, “Atomic and Molecular beam laser spectroscopy2, Oyo Butsuri, Vol.47, No.8, August 1978, pp.771-779.
【田幸敏治、大津元一、「原子分子ビーム・レーザー分光」、応用物理、第 47 巻、第 8 号、1978 年 8 月、pp. 771−779】

(pp. 167-175)

[IV] PUBLISHED BOOKS

N.A.

[Ⅴ] AWARDS

[1] M. Ohtsu, “Design of an ultrahigh resolution molecular beam spectrometer using an infrared laser,” Research Promotion Award, the Teshima Foundation, 25 February 1980.

JAPANESE JOURNAL OF APPLIED PHYSICS
VOL. 17, NO. 1, JANUARY, 1978 pp. 177–182

Mode Competition in the 3.51 μm He–Xe Laser in an Axial Magnetic Field

Motoichi OHTSU and Toshiharu TAKO

Research Laboratory of Precision Machinery and Electronics,
Tokyo Institute of Technology,
Nagatsuta-cho, Midori-ku, Yokohama 227

(Received November 9, 1976; revised manuscript received July 28, 1977)

Oscillating properties of a 3.51 μm He–Xe laser in an axial magnetic field and the competition phenomenon between two oppositely circularly polarized Zeeman components (the σ_+ and σ_- modes) are investigated. Under a magnetic field less than 133G, the shapes of the detuning curves of both modes were measured. In the total gas pressure range of 3 to 10 Torr, it was clearly observed that one of the σ_+ and σ_- modes was suppressed by the other within a certain frequency range. Both modes oscillated independently, however, when the total gas pressure was lower than 3 Torr. Furthermore, it was shown that even if the competition phenomenon occurred, the oscillating frequency range of the σ_+ or σ_- mode could be predicted when the total intensity detuning curve in a zero magnetic field was measured beforehand.

§1. Introduction

A large number of laser/molecular-absorber overlaps are known in saturated absorption spectroscopy. For example, inverted Lamb dips in the 3.39 μm methane line and in the 0.633 μm iodine line have been observed with He–Ne laser lines.[1,2] These dips have been applied to stabilize the wavelength of laser oscillations.[1,3] As another example, the inverted Lamb dip in the 3.51 μm formaldehyde (H_2CO) line has been observed with a He–Xe laser line ($3d_4$–$2p_9$).[4] In this case, since the absoption line frequency of H_2CO is about 200 MHz higher than the center of the gain curve of a He–Xe laser, Zeeman-tuning is employed to compensate for this frequency gap by applying an axial d.c.magnetic field to the laser tube. When an axial magnetic field is applied to a laser tube with non-Brewster windows, two oppositely circularly polarized Zeeman components (the σ_+ and σ_- modes) oscillate. The σ_+ mode is shifted toward the higher frequency and the σ_- mode toward the lower by the Zeeman effect. Transitions of the Xe ($3d_4$–$2p_9$) in an axial magnetic field are shown in Fig. 1. Since the common upper or lower levels of the Zeeman sublevels take part in the σ_+ and σ_- transitions, a competition phenomenon can be found between the σ_+ and σ_- modes. For the He–Ne laser, a competition phenomenon of the same kind,

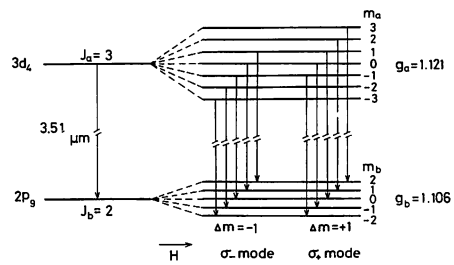

Fig. 1. Transitions of the 3.51 μm Xe line ($3d_4-2p_9$) in an axial magnetic field. Angular momenta of the upper and the lower levels are $J_a=3$, and $J_b=2$, respectively. Landé g-factors are $g_a=1.121$ and $g_b=1.106$, respectively. Two circularly polarized waves oscillate when an axial magnetic field is applied. Right-handed and left-handed components are called the σ_+ mode and the σ_- mode, respectively. The former is shifted toward the higher frequency and the latter toward the lower by the Zeeman effect.

and related oscillation properties in a weak axial magnetic field, have been measured by Tomlinson and Fork,[5] and these results have been compared with the Zeeman laser theory.[6] As for the He–Xe laser, the 2.65 μm transition is the only case for which a competition phenomenon has been reported.[7]

In this paper, the competition phenomenon of the 3.51 μm He–Xe laser in an axial magnetic field is investigated. The axial magnetic field is scanned up to 133G. The experiments are carried out for 0.5 Torr $< P_T <$ 10 Torr, where P_T is the total gas pressure in the laser

tube. Experimental results for $P_T<3$ Torr and $P_T\geqq 3$ Torr are compared. These results will be used to measure the absorption spectrum of H_2CO and to stabilize the wavelength of the He–Xe laser oscillation.

§2. Experimental Apparatus

The experimental apparatus is shown in Fig. 2. A capillary tube with a 3 mm inner diameter and a length of 200 mm was used. A solenoidal return-path of 2.5 mm diameter and 310 mm in length was used to avoid the separation between the He and Xe gases when these gases were excited by a d.c. discharge. Natural He and Xe gases were used in the present experiment.

Inadequate values of the total gas pressure P_T, the pressure ratio P_{He}/P_{Xe} of He and Xe, and the discharge current I_{dis} caused the separation between the He and Xe gases, or plasma instability. For the stable oscillation it was empirically found that the following conditions were necessary:

(1) $P_T<10$ Torr,

(2) $80<P_{He}/P_{Xe}<300$,

(3) $I_{dis}<15$ mA.

When $P_T=8$ Torr, $P_{He}/P_{Xe}=90$ and $I_{dis}=4$ mA, the maximum output power was obtained, and this was about 0.1 mW. Two dielectric multilayer-coated mirrors with reflectances of 99% and 90%, respectively, were used to form a plane-parallel optical resonator.

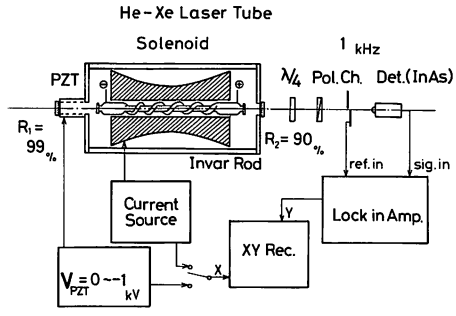

Fig. 2. Experimental apparatus: With a quarter-wave plate made of mica and a polarizer, intensities of the σ_+ and σ_- modes are separately detected with an InAs photodiode. A lock-in amplifier and a 1 kHz-chopper are used for phase sensitive detection. Laser windows are made of fused silica of 2 mm thickness, which are slightly tilted from the optical axis. One of the mirrors is mounted on a piezoelectric transducer (PZT), and four Invar rods are used to fix two mirror-holders.

A solenoid of 32 mm inner diameter and 310 mm in length was placed around the laser tube for applying the magnetic field. The ends of the solenoid were overwound to produce better uniformity of the field. The field uniformity was better than 0.3% over the complete length of the discharge. The solenoid produced a magnetic field strength of 66.6G/A.

The frequency shift of the center of the Xe line was 1.56 MHz/G in the approximation of the first-order Zeeman effect. Therefore, the axial magnetic field strength H required to tune the frequency of a He–Xe laser on the absorption line of H_2CO is about 133G. In order to use the He–Xe laser as a light source of the absorption spectroscopy of H_2CO, the competition phenomenon is investigated for $0\leqq H\leqq 133$G in the present experiment. When the magnetic field strength (H_a) is 87.5G, the Zeeman split is 273 MHz, which is equal to the axial-mode frequency interval. When $H>H_a$, the σ_+ and σ_- modes oscillate on adjacent axial-modes.

The two circularly polarized components (the σ_+ and σ_- modes) were detected separately with an InAs photodiode, by using a mica quarter-wave plate and a polarizer. The detuning curve for several values of field and mode intensities versus axial magnetic fields, with the cavity detuning held constant, were traced on an X-Y recorder.

§3. Experimental Results

In the preliminary experiment, the detuning curves of the σ_+ and σ_- modes were measured. For $P_T<3$ Torr, the shapes of both curves in an axial magnetic field were similar to those in a zero magnetic field. But for $P_T\geqq 3$ Torr, the shapes of both cases were considerably different from each other. To investigate the effect of the axial magnetic field, a number of measurement were carried out for 0.5 Torr$<P_T<10$ Torr. The experimental results for $P_T<3$ Torr and $P_T\geqq 3$ Torr are discussed separately below.

3.1 *At low pressure ($P_T<3$ Torr)*

The detuning curves of the σ_+ and σ_- modes for several values of magnetic field are shown in Fig. 3. In Fig. 4, the intensities

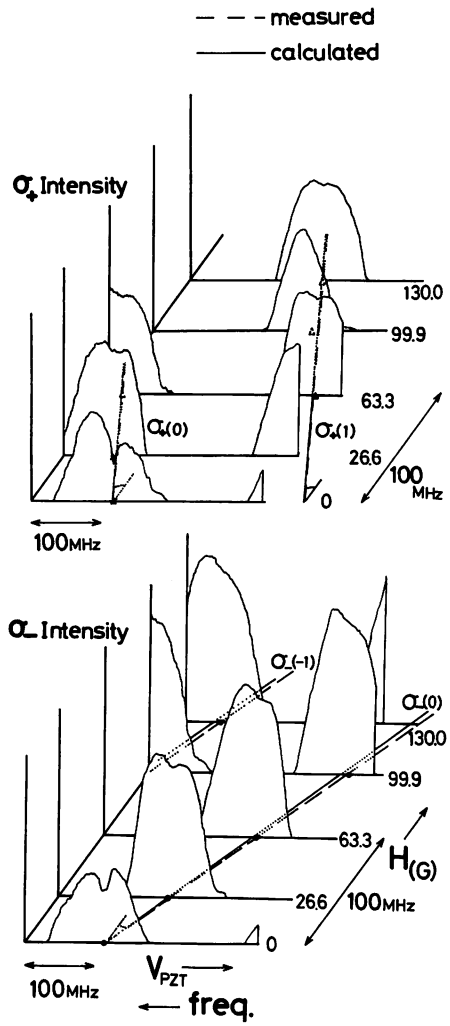

Fig. 3. Detuning curves of the σ_+ and σ_- modes for several values of magnetic field when $P_T=0.77$ Torr, $P_{He}/P_{Xe}=285$ and $I_{dis}=14.4$ mA. The axial-mode frequency interval is 273 MHz. The first axis represents the axial-mode frequency which is shifted by a d.c. voltage applied on a PZT. The higher frequency side is shown with an arrow. The second axis represents the magnetic field strength and the third axes represents intensities of the σ_+ and σ_- modes. In this figure, each axial-mode is labelled with an integer N, in order of decreasing frequency, and is shown as $\sigma_+(N)$ or $\sigma_-(N)$. Broken lines represent experimental results of frequency shifts of both modes and solid lines represent calculated values.

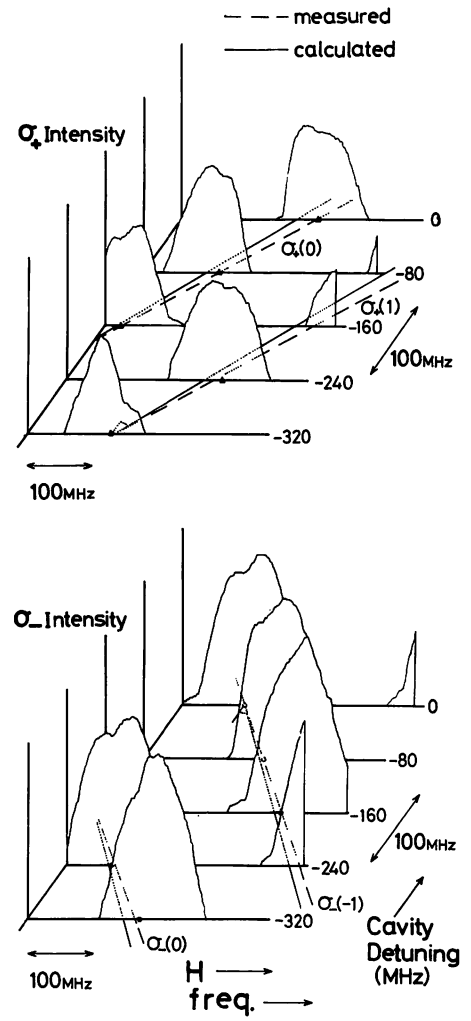

Fig. 4. Mode intensities as functions of the magnetic field with the cavity detuning held constant when P_T is low. Experimental constants are the same as in Fig. 3. The first axis represents the magnetic field strength, the second axis represents the axial-mode frequency and the third axes represent intensities of both modes. Broken and solid lines are also the same as in Fig. 3.

of both modes are also shown as functions of the magnetic field, with the cavity detuning held constant.

In Figs. 3 and 4, both the σ_+ and σ_- modes oscillate independently, and a competition phenomenon is not found. It is easy to see that the effect of the magnetic field in this case is only to split the detuning curve into two curves which move apart as a function of the magnetic field.

The positions of the center frequencies of the Lamb dips in Figs. 3 and 4 are connected by broken lines. These Lamb dips are asymmetrical and distorted. This is mainly caused by many kinds of isotopes which are contained in natural Xe gas. Though the Landé g-factors of the upper and the lower levels are $g_a=1.121$ and $g_b=1.106$, respectively,

the average value of these factors, 1.114, was used as an approximation, and the Zeeman split was calculated. Because the error due to this approximation remains less than 1% at $H \leqq 133$G, the following discussions are not biased by this approximation. These calculated values are shown by the solid lines in Figs. 3 and 4. In Fig. 3, the solid lines and the broken lines agree within an error of 2%, while in Fig. 4 this error is within 4%. Since it is difficult to hold the cavity detuning at a constant and reproducible value because of thermal expansion of the Invar rods, the errors in Fig. 4 are larger than those in Fig. 3.

3.2 *At high pressure ($P_T \geqq 3$ Torr)*

The results at $P_T = 8.17$ Torr are shown in Figs. 5 and 6, which correspond to Figs. 3 and 4, respectively. The upper part in each block is the experimental result. The lower part of the block of $H=0$ in Fig. 5 is the detuning curve of the total intensity, which was measured without a quarter-wave plate and a polarizer. This curve is similar to the upper curves of the same block. After shifting this detuning curve along the abscissa by an amount calculated from Figs. 3 and 4, the resultant curves are shown in the lower parts of the other blocks. These curves are imaginary ones which may be measured in the absence of mode competition.

The σ_+ and σ_- modes oscillate even at the wings of their imaginary detuning curves in the lower parts of each block. This means that these modes oscillate on two axial-modes at the wings because the gain curves of these modes are broader than the axial-mode frequency interval. On the other hand, the σ_+ or σ_- mode is suppressed in a certain frequency range in the upper part of the corresponding block. The suppressed mode is the one whose intensity, in the lower part of the block, is lower than that of the other. Furthermore, both modes in the upper part simultaneously oscillate in the other frequency range. In this range, the two curves in the lower part cross each other and both intensities are nearly equal. Therefore, the oscillating frequency range of the σ_+ or σ_- mode can be known when the intensities of both modes in the lower part are compared with each other. It was clearly observed that the widths of the

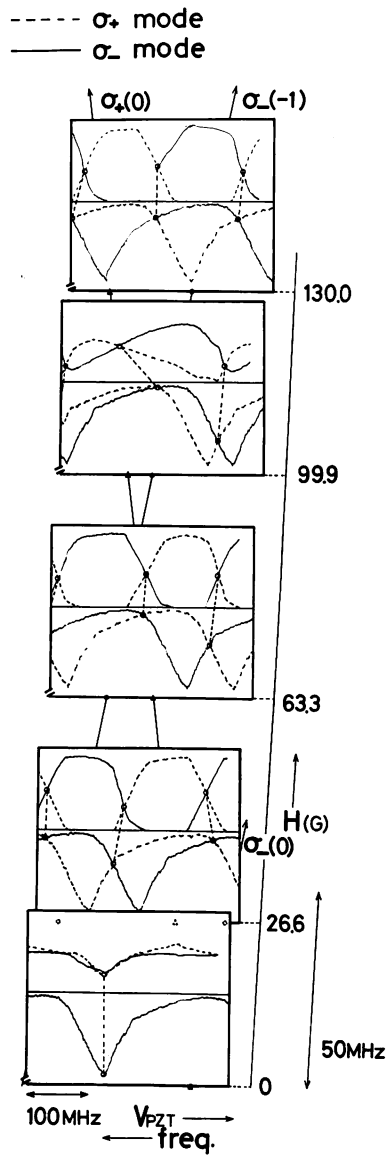

Fig. 5. Detuning curves of the σ_+ and σ_- modes for several values of magnetic field when $P_T = 8.17$ Torr, $I_{dis} = 5.2$ mA. Other constants and the three axes are the same as in Fig. 3. The broken curve represents the σ_+ mode, and the solid curve the σ_- mode. In each block, the upper part is an experimental result. The lower part at $H=0$ is an experimental result of the total intensity. After shifting this detuning curve by an amount calculated from Fig. 3, the resultant curves are shown in the lower part of each of the other blocks. The solid lines with arrows, which appear behind the blocks, represent frequency shifts calculated from Fig. 3.

detuning curves in the upper part were narrower than those in the lower part for $P_T \geqq 3$ Torr. By the above discussion, it is apparent that

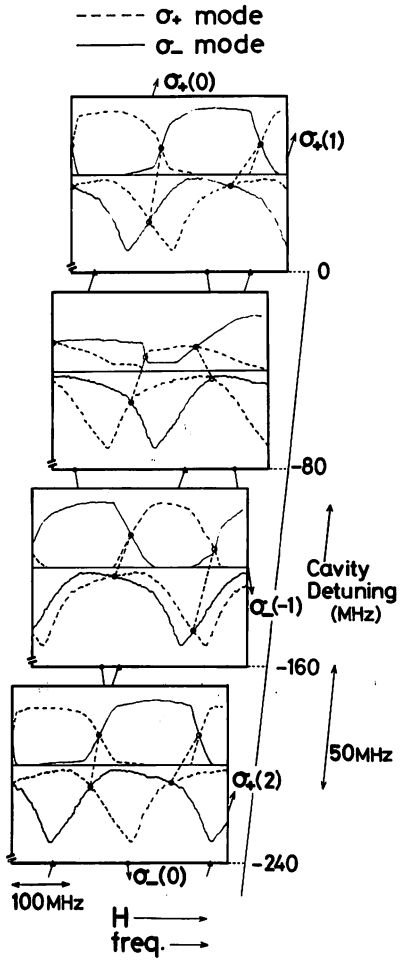

Fig. 6. Mode intensities as functions of the magnetic field with the cavity detuning held constant when P_T is high. The three axes are the same as in Fig. 4. The correspondence between the upper and the lower parts in each block and the experimental constants are the same as in Fig. 5. The broken curve represents the σ_+ mode and the solid curve the σ_- mode.

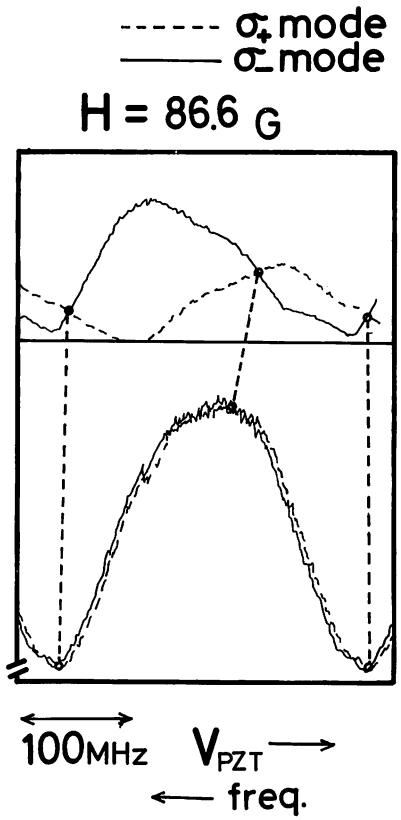

Fig. 7. Detuning curves of both modes at $H=86.6$ G when $P_T=3.79$ Torr, $P_{He}/P_{Xe}=88.5$ and $I_{dis}=9.8$ mA. The axial-mode frequency interval is 273 MHz. The correspondence between the upper and the lower parts is the same as in Fig. 5.

the effect of the magnetic field is not only to split the detuning curve into two curves but to cause mode competition between the σ_+ and σ_- modes for $P_T \geqq 3$ Torr.

Because both modes oscillate near the crossing point of the two detuning curves, it is expected that the σ_+ and σ_- modes oscillate simultaneously for a wide frequency range at $H=H_a$. This fact is shown in Fig. 7. The correspondence between the upper and the lower parts of Fig. 7 is the same as in Fig. 5. In Fig. 7, because $H \cong H_a=87.5$G, the two detuning curves in the lower part overlap with each other and, in fact, the σ_+ and σ_- modes in the upper part simultaneously oscillate for a wide frequency range. When $H>H_a$, the σ_+ and σ_- modes oscillate on adjacent axial-modes, but, as shown in Figs. 5 and 6, the competition phenomenon was still found in such high magnetic fields. This is a fact which has not been previously reported in the He–Ne laser.[5)]

§4. Discussion

The cavity mirrors were rotated around the optical axis of the laser, and the position of the mirrors where the laser beam was reflected was changed, but the shapes of the detuning curves in Figs. 5 and 6 were not influenced by these operations. This shows that the cavity anisotropy has little influence on mode competition in the present experiments. That is, g_{+-}, $g_{-+} \cong 0$, where g_{+-} and g_{-+} are two off-diagonal elements of the

anisotropy G-matrix represented by a circularly-polarized basis.[6] To know precisely the cavity anisotropy effect, it is necessary to measure the beat frequency between the σ_+ and σ_- modes and its locking phenomenon. If the cavity anisotropy is not negligible and frequency locking occurs, bumps should appear in the detuning curve.[5] In Figs. 5 and 6, this bump does not appear for $H \leqq 133$G, and therefore it can again be concluded that g_{+-}, $g_{-+} \cong 0$. Since two diagonal elements of the anisotropy G-matrix are not generally equal to each other ($g_+ \neq g_-$), the net gains of both modes must be different from each other. But since the intensity difference between the σ_+ and σ_- modes is negligible in Figs. 5 and 6, it can be concluded that $g_+ \cong g_-$.

It is still unknown why the competition phenomenon appears clearly for $P_T \geqq 3$ Torr, and further experimental and theoretical work is necessary to clarify this point.

As shown in §3.2, when the total intensity detuning curve in a zero magnetic field is measured beforehand, it is possible to predict the oscillating frequency range of the σ_+ and σ_- modes for any magnetic field strength. That is, after drawing imaginary detuning curves of the σ_+ and σ_- modes, as in Figs. 5 and 6, one needs only to compare the intensities of these curves with each other.

In order to measure the absorption spectrum of H_2CO, the necessary value of the magnetic field strength should be decided by using this prediction.

§5. Conclusion

In the present paper, the oscillating properties of the 3.51 μm He–Xe laser in an axial magnetic field, and the competition phenomenon between two circularly polarized Zeeman components (the σ_+ and σ_- modes) were investigated. Under a magnetic field less than 133G, a competition phenomenon was observed for 3 Torr $\leqq P_T <$ 10 Torr; that is, there existed a frequency range in which one of the σ_+ and σ_- modes was suppressed by the other. This competition phenomenon was not observed for $P_T <$ 3 Torr. It was shown that even if the competition phenomenon occurred, the oscillating frequency range of the σ_+ or σ_- mode could be predicted when the total intensity detuning curve in a zero magnetic field was measured beforehand. In the absorprion spectroscopy of H_2CO, the necessary value of the magnetic field strength can be obtained by using this prediction.

Acknowledgements

The authors wish to express their gratitude to Dr. M. Takami of the Institute of Physical and Chemical Research for his helpful advice in the design of He–Xe laser tubes and to Dr. T. Akahane of their laboratory for his valuable comments.

References

1) R. L. Barger and J. L. Hall: Phys. Rev. Letters **22** (1969) 4.
2) G. R. Hanes and C. E. Dahlstrom: Appl. Phys. Letters **14** (1969) 362.
3) G. R. Hanes and K. M. Baird: Metrologia **5** (1969) 32.
4) M. Takami and K. Shimoda: Japan. J. appl. Phys. **11** (1972) 1648.
5) W. J. Tomlinson and R. L. Fork: Phys. Rev. **164** (1967) 466.
6) M. Sargent III, W. E. Lamb, Jr. and R. L. Fork: Phys. Rev. **164** (1967) 436, 450.
7) W. Culshaw and J. Kannelaud: Phys. Rev. **156** (1967) 308.

UDC 621.375.826:621.317.361.087.9:519.233.4-37

レーザ周波数安定度の実時間測定装置の試作

非会員 椎尾 一郎† 正員 大津 元一† 正員 田幸 敏治†

Real-Time Processing System of the Measurement of Laser Frequency Stability

Itiro SIIO†, *Nonmember*, Motoichi ŌHTSU† *and*
Toshiharu TAKO†, *Regular Members*

あらまし レーザの周波数安定度を実時間で測定する目的で，マイクロプロセッサを用いたアラン分散実時間測定装置を製作した．アラン分散は周波数安定度を表す一つの指標である．この装置はマイクロプロセッサにより測定の空き時間のない周波数カウンタとアラン分散処理系を構成し，実時間でアラン分散を計算する．この装置の特徴は，① 実時間である，② 測定の空き時間がないので正しいアラン分散の値を知ることができる，③ 2系統の信号源のアラン分散を同時に測定できる，などである．試作した装置は，周波数変調された正弦波発振器からの信号を用いた試験の結果，正常な動作が確認された．更に従来の測定系と並列に使用したところ，結果が一致したので，レーザ周波数安定度測定に用いることができた．

1. まえがき

各種の気体レーザの周波数安定化が行われ[1),(2)]，その安定度も向上して分光実験などにも用いられるようになった[(3)]．その周波数安定度測定には従来オフラインのミニコンピュータや，実時間のコンピューティングカウンタHP 5390Aがよく用いられていた．しかしこれらは測定系が複雑であり高価であった．

一方筆者らは，高分解能レーザ分光用の周波数安定化レーザ，すなわち3.51 μm H_2CO 安定化He-Xe レーザの開発を行ってきた[(4),(5)]．このレーザを分光用光源として用いる場合，分光測定中に周波数安定度を実時間で測定する必要がある．特に周波数が安定で且つ可変の，周波数オフセットロック He-Xe レーザシステム[(5)]を光源として用いる場合，複数のHe-Xe レーザの周波数安定度を同時に実時間で測定する必要がある．

そこで筆者らは，安価で，実時間，2チャネル同時測定可能なレーザ周波数安定度測定装置を開発したので報告する．

†東京工業大学精密工学研究所，横浜市
Research Laboratory of Precision Machinery and Electronics, Tokyo Institute of Technology, Yokohama -shi, 227 Japan

論文番号：昭 56-137[C-30]

2. 周波数安定度の評価方法

周波数安定度を表すパラメータとしてはアラン分散 σ^2 の平方根が用いられる[(6)〜(8)]．これは次のように定義される．

図1に示すように，まず信号源の周波数を積分時間 τ で平均し，平均値 $\bar{f}_k$ を得る．連続する2個の平均周波数値 f_1 と f_2 についての標本標準偏差の2乗は，

$$\frac{1}{2-1}\sum_{i=1}^{2}\left(\frac{\bar{f}_1+\bar{f}_2}{2}-\bar{f}_i\right)^2=\frac{(\bar{f}_1-\bar{f}_2)^2}{2} \tag{1}$$

となるが，アラン分散はこれを n 個の平均値 $\bar{f}_k$ に対して計算し，それを平均したもので，

$$\sigma^2(\tau)=\frac{1}{n-1}\sum_{k=1}^{n-1}\frac{(\bar{f}_{k+1}-\bar{f}_k)^2}{2}\Big/\bar{f}^2 \tag{2}$$

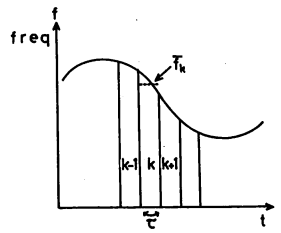

図1 信号源の周波数変化
Fig. 1 – Frequency change of the source signal.

で表される．但し，$\bar{f}$は信号源の公称周波数である．一般に周波数安定度は式(2)の平方根が用いられる．アラン分散は式(2)に示すように，平均された周波数データ数nと積分時間τの二つの変数の関数である．更に定義として測定の空き時間，すなわち図1で$\bar{f}_k$と$\bar{f}_{k+1}$の積分領域の境界部分の時間がゼロであることが要求されている．

3. レーザ周波数安定度の測定

図2は2台のレーザを用いてレーザの周波数安定度を測定する実験系を示している[5]．

2台のレーザの間のビート周波数が光検出器を用いて得られる．このビート周波数の揺らぎがレーザの相対的な安定度になるので，これを周波数カウンタで計数し，何らかの方法でアラン分散を計算すれば安定度が分かる．筆者らは従来，積分時間τの長いアラン分散には市販の周波数カウンタを用い，τが1s未満のものに対しては周波数－電圧変換器を用いていた．というのは，市販の周波数カウンタは表示とリセットに時間がかかり†，ゲート時間1s未満では測定の空き時間が大きくなり真のアラン分散が得られないおそれがあるためである．しかしながら，周波数－電圧変換器は精度の点でτの長い領域が測定できなくて††，結局，$0.1\,s<\tau<1s$の範囲では信頼できるアラン分積が得られなかった．このようにして得た周波数データは従来紙テープ又はアナログデータレコーダに記録され，オフラインのミニコンピュータ（PDP-11）によりアラン分散処理されていた．このため測定系が複雑であり，実時間でないので不便であった．

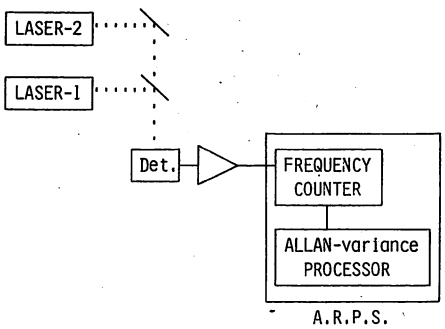

図2　周波数安定度の測定系
Fig.2 – The measurement system of the laser frequency stability.

† エレクトロニックカウンタVP4551Aの場合50ms以上．
†† 筆者らの3.51μm He–Xeレーザの場合，$\tau=10^{-1}$sで$\sigma\sim10^{-11}$になる．

そこで積分時間τの広い範囲にわたって実時間でアラン分散を測定するために，マイクロプロセッサを用いて図2の周波数カウンタとアラン分散処理系を一つにまとめたアラン分散実時間測定装置（Allan-variance Realtime Processing Systemの頭文字をとって以下ARPS と呼ぶ）を製作した．

4. ARPSのハードウェア

図3にARPSのハードウェア構成[9]を示す．

MPU（Micro processing unit）には6802 を用いた．浮動小数点演算を含む全プログラムは，PROM（Programmable read only memory）に固定した．3K ByteのRWM（Read write memory）は大半が周波数データを蓄えるために使用されている．プリンタは20けた感熱式である．キーボードはテンキーと五つの命令キーから成り，プリンタ出力とキーボードにより対話式でパラメータを設定でき，結果はこのプリンタに印字される．プリンタ，キーボードそして周波数カウンタのデータの入出力を行うためにMPUの周辺LSIの一つであるPIA(Peripheral interface adapter) を使用している．PIAは8 bit 入出力ポートを2系統と，割込やハンドシェークの管理のための入出力を4本備えている．ここではキーボードのスキャンなどのデータの入出力，プリンタとのオートマチックハンドシェーク，周波数カウンタからの割込管理を行わせている．なお，周波数カウンタのカウント値のデータは，ラッチからアドレスバスによって選択されるマルチプレクサを通して直接データバスに取り込んでいる．

周波数カウンタは2系統の2進カウンタとラッチで

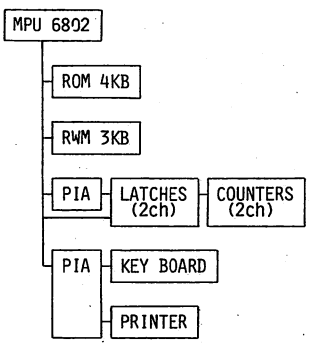

図3　ARPSのブロック図
Fig.3–The block diagram of the ARPS.

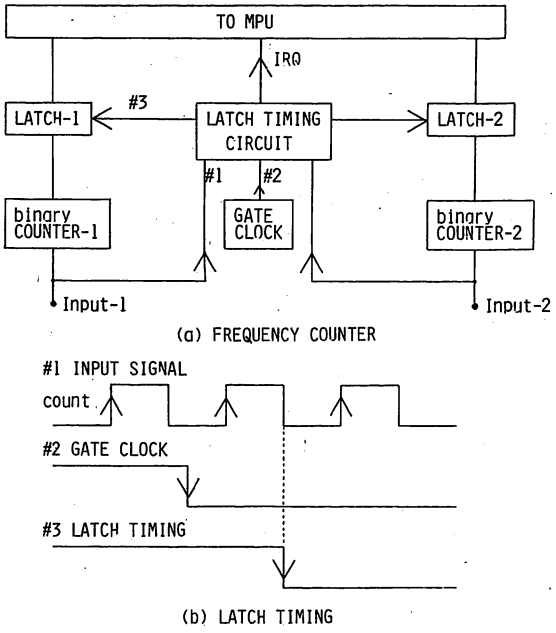

図4　周波数カウンタ部
Fig.4 – The frequency counter.

構成されている．それを図4(a)に示す．この2進カウンタはリセットを行わないので，常にオーバフローしつづけている．設定されたゲート時間が経過するとそのときのカウント値がラッチに送られる．カウント値は入力信号の立上りによって更新されるが，このときカウンタが正しい値に安定するまで数十ns 必要である．そこで不定の状態のカウント値をラッチに送らないために，D－フリップフロップを利用してゲートクロックを入力信号の立下りまで遅らせてラッチをかけている．この様子を図4(b)に示す．

カウント値がラッチされると同時にPIAの割込入力を通してMPUのIRQ (Interrupt request) 入力が立下りMPUに計数の終ったことが伝えられる．このときPIA に割込要求の入った入力ポートが記憶されているので，割込処理プログラム中でそれを調べれば2系統のカウンタのいずれがラッチされたのか知ることができる．周波数値は一つ前のゲート時間で計数された値との差と，ゲート時間からソフトウェアにより計算される．カウンタは2進24けたなので10進に換算すると約7けたの精度がある．

以上のようにカウンタがリセットされることなく累積されるので，空き時間を生ずることなく周波数を測定できる．

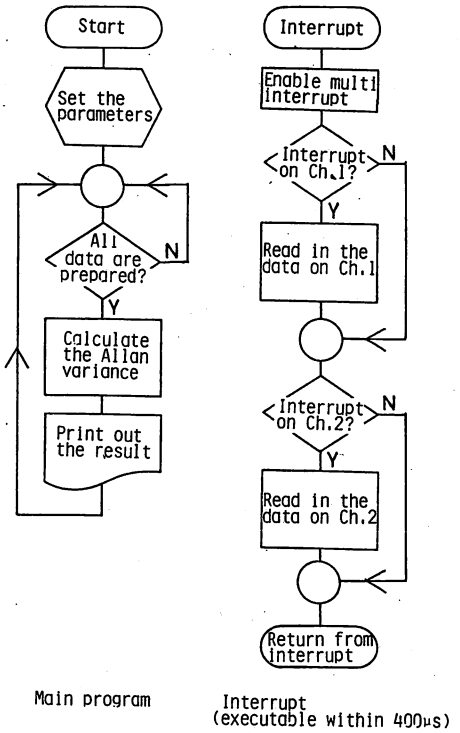

図5　アラン分散の計算プログラムのフローチャート
Fig.5 – The flowchart of the program.

5. ARPSのソフトウェア

図5にプログラムのフローチャートを示す．主プログラムでは最初に対話式にパラメータを設定する．このパラメータは周波数カウンタ2系統の各々のデータ数n，積分時間τ，規格化の定数である．この後，主プログラムは指定のデータ数のデータが採取されるまでループの中に入っている．そしていずれかの周波数カウンタからのデータがそろうと，そのカウンタからのデータ採取を中止してアラン分散の計算を行い結果を印字する．アラン分散の計算にはデータ数100個の場合約0.7sかかる．

一方，周波数カウンタのゲート時間ごとに割込が発生し，プロセッサは主プログラムでのレジスタを退避して割込処理プログラムを行う．ここでは2系統の周波数カウンタのいずれの割込であるかを判断してデータを取り込む．割込処理プログラムを実行中にもう一方の系統の周波数カウンタから割込要求が入る場合がある．この場合に対処できるように2重割込が可能になっている．割込処理プログラム実行中に2重に割込要

求が入ると，プロセッサはレジスタを退避して再び割込処理プログラムを実行するのである．

割込処理プログラムでは，周波数カウンタのラッチからデータを採取し前回の割込時の値との差を計算し，設定されているτに達しない間はデータを累計し主プログラムに帰る．このとき演算は4 Byte の整数形で行われ，浮動小数点演算を使用していないので高速である．そしてτ時間のデータが累積された場合には結果を浮動小数点表示に変換してメモリに格納する．このように割込処理プログラムではτ時間ごとの累積値をメモリに格納する仕事だけを行う．このためサンプル数だけのデータを蓄えるメモリが必要になるが，割込処理プログラムを速く終了することができる．この割込処理プログラムは，2系統のカウンタが同時に割込要求し最大の処理時間を要する場合でも約400μs以下で終了する．割込要求は周波数カウンタの最小ゲート時間の1 ms のときに最もひん繁に出されるが，この場合でもプロセッサは残りの600μs以上の時間を使って主プログラムを実行することができる．このような主プログラムと割込処理プログラムの2層の構造により，ARPS は2系統のアラン分散を同時に処理できる．

主プログラムでのアラン分散の計算では浮動小数点演算が使用されている．浮動小数点表示は実数 x を

$$x=\left(\frac{a_1}{N}+\frac{a_2}{N^2}+\cdots+\frac{a_m}{N^m}\right)\times N^{\alpha} \qquad (3)$$

の形で表現するもので，a_1，a_2，… が仮数，αが指数と呼ばれる．Nが大きいと表現できる数の範囲は大きくなるが，けた落ちが起きやすくなる[10]．ここでは $N=2$ とした．ARPSで採用した浮動小数点表示のデータ形式を図6に示す[11]．

仮数部3 Byteとその符号が1 bit，指数部7 bit の合計4 Byte を用いて一つの数値を表している．仮数は絶対値表示として1 Byte 目のMSB に符号ビットがある．指数は2進の1000000 を加えた7 bit で表現した．この表示で表現できる数 x の範囲は約 $10^{-19}<|x|<10^{+19}$ で，精度は10進表示で約7けたである．

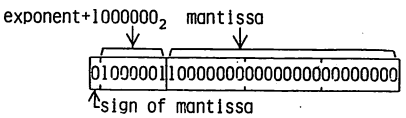

図6　浮動小数点表示のデータ形式（+1. の例）
Fig.6 – The data type of floating-point data （the case of +1. ）.

アラン分散計算に用いる浮動小数点演算は4則演算，2進10進相互変換，平方根などであるが，実時間処理に用いるため，プログラム自体は冗長でも実行速度の速いことを目標として作った．その結果実行速度は乗算が2.6ms 以下，加算が350μs 程度，平方根が16.6 ms 以下となった．このため100個のデータ数のアラン分散の計算を1 s 未満で処理するので，実時間処理を行うことができた．

6. 動作試験

ARPS は以下の方法で動作試験を行った．図7は500kHz で発振している電圧制御発振器に8.6 Hz の正弦波の制御信号を加え，±46 kHz の周波数変調のかかった信号を作り，この周波数変動のアラン分散の平方根の値を測定したものである．

一方，この場合のアラン分散の平方根の値は式(2)に従って簡単な計算により

$$\sigma(\tau)=\frac{92}{500}\times\frac{\sin^2(\omega\tau/2)}{\omega\tau} \qquad (4)$$

となる．但し，この場合 $\omega=2\pi\times8.6$ rad/s である．又，この試験信号では $\omega\tau=m\pi$ ($m=1, 2, 3,\cdots$) の場合アラン分散が測定開始時刻だけの関数になり，サンプル数 n を増しても収束しない．式(4)はこの場合，何回かのアラン分散測定の平均値を与える．このため試験では $\omega\tau=m\pi$ にならないようにτを設定した．図7によると，ARPS によって測定した結果と，式(4)の計算結果は良く一致しているので，ARPS は正常に動作していることが確認された．

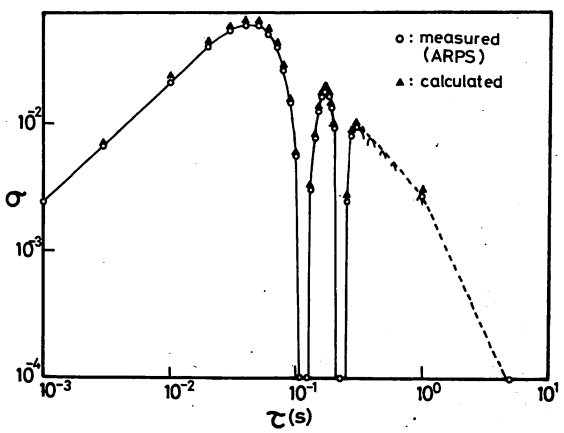

図7　ARPSの動作試験の結果
Fig.7 – The result of the operation test of the ARPS.

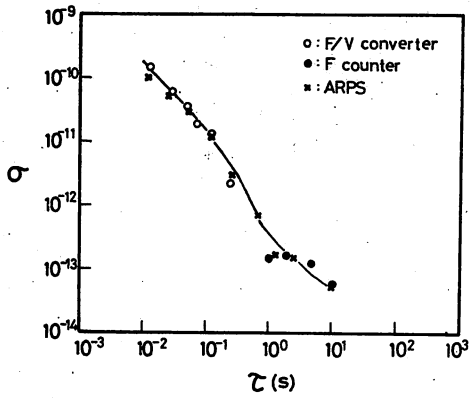

図8　3.51μm He-Xe レーザの周波数安定度の測定結果
Fig.8 – The results of the frequency stability of He-Xe lasers at 3.51μm.

図8はARPS を今までの測定系と同時に並列に用いて実際に 3.51 He-Xe レーザの周波数変動のアラン分散の平方根を測定し，両者の結果を比較したものである．

実験系は図2に示した配置になっていて，2台のレーザはビート周波数が2 MHz になるようにオフセットロックがなされている 3.51μm He-Xe レーザである[5]．このビート信号をTTL レベルに変換し，10分の1に分周してそのアラン分散を測定した．測定は従来の測定系，すなわち周波数－電圧変換器と市販の周波数カウンタを用いてミニコンピュータで処理し，並行してARPS によって処理を行った．そしてこれらを比較した．従来の方法は前述のように $0.1\,s<\tau<1s$ の領域の測定値が得られなかった．これに対してARPS は τ の広い範囲，すなわち $1ms\leqq\tau<2^{32}\times f^{-1}$ (s)の範囲で測定可能である．ここで f は入力信号の周波数 (Hz) である．τ の上限は周波数値を積分するときに4 Byte の整数形で計算されることによる．図8の結果，従来の系と測定値が一致したので，ARPS がレーザ周波数安定度の実時間測定に使用可能であることが確認された．

7. むすび

本研究で試作したARPSの特徴は，

(i)　実時間測定ができる．

(ii)　2系統のアラン分散を同時に処理する．

(iii)　$1ms\leqq\tau<2^{32}\times f^{-1}$(s)の広い範囲の τ について測定できる．

(iv)　従来の周波数カウンタと異なり，測定の空き時間がないので，アラン分散の定義に反さない．

(v)　周波数カウンタを用いているため，周波数－電圧変換器に比べて高精度である．周波数カウンタは2進24けたであり，τ 時間累積するためのメモリは2進32けたである．

(vi)　単機能の専用機としたため操作性が良く安価である．アラン分散を測定する市販の測定器にHP 5390Aがあるが，これが多機能であるため高価なのに対しARPSは安価であり，(ii)及び(iv)の項目の特長がある．

謝辞　本研究の一部は文部省科学研究費特定研究の補助によりまかなわれた．ARPS の製作に当って協力して頂いた波多腰栄一技官に深く感謝する．

文　献

(1) Barger, R.L. and Hall, J.L.: "Pressure shift and broadening of methan line at 3.39μ studied by laser saturated molecular absorption", Phys. Rev. Lett., 22, pp.4-8(1969).

(2) Hanes, G.R. and Baird, K.M.: "Preliminary wavelength, I_2 controlled He-Ne laser at 633 nm", Metrologia, 5, pp.32-33(1969).

(3) Ohtsu, M. and Tako, T.: "Frequency stability of an H_2CO-stabilized He-Xe laser in an axial magnetic field", Jpn. J. Appl. Phys., 17, pp.2169-2170(1978).

(4) Ohtsu, M., Koyama, R. and Tako, T.: "Improvements in the long-term frequency stability of the He-Xe laser at 3.51μm", Jpn. J. Appl. Phys., 18, pp.1621-1622(1979).

(5) Ohtsu, M., Koyama, R., Kusunowo, A. and Tako, T.: "Development of a frequency-offset-locked He-Xe laser at 3.51μm", Jpn. J. Appl. Phys., 18, pp.1619-1620(1979).

(6) Allan, D.W.: "Statistics of atomic frequency standards", Proc. IEEE, 54, pp.221-230(1966).

(7) Barnes, J.A., Chi, A.R., Cutler, L.S., Healey, D.J., Leeson, D.B., McGunigal, T.E., Mullen, Jr., J.A., Smith, W.L., Sydnor, R.L., Vessot, R.F.C. and Winkler, G.M.R.: "Characterization of Frequency Stability", NBS Tech. Note, No.394(1970).

(8) 周波数精密測定回路専門委員会："周波数安定度とその測定"，電気学会技術報告（II部），41, p.8（昭51）．

(9) 日立製作所："日立マイクロコンピュータシステムデバイスデータブック"（昭53）．

(10) 六田嘉明："浮動小数点プログラムの作り方"，インターフェース，25, pp.33-64(昭54)．

(11) 井波俊夫："8080A用浮動小数点演算プログラム"，インターフェース，25, pp.65-101(昭54)．

（昭和55年8月11日受付，10月31日再受付）

JAPANESE JOURNAL OF APPLIED PHYSICS
VOL. 19, NO. 12, DECEMBER, 1980 pp. L721–L724

Frequency Stability Measurement of Feedback Stabilized AlGaAs DH Laser

Hidemi TSUCHIDA, Seiichi SANPEI, Motoichi OHTSU and Toshiharu TAKO

Research Laboratory of Precision Machinery and Electronics, Tokyo Institute of Technology, 4259 Nagatsuta-cho, Midori-ku, Yokohama, Kanagawa 227

(Received September 8, 1980)

The frequency of a single longitudinal mode AlGaAs DH laser was stabilized at the resonant frequency of an external Fabry-Perot interferometer by controlling the temperature. The frequency stability was evaluated by using the square root of the Allan variance σ^2 and the power spectral density. The following value was obtained: $2.1\times10^{-9}\leqq\sigma\leqq9.6\times10^{-9}$ for 10 ms$<\tau<$500 s, where τ represents the integration time. The long-term frequency stability was improved for $\tau>10$ s.

§1. Introduction

Recently, spectral properties of semiconductor lasers have been improved. A stable single longitudinal mode oscillation has been obtained reproducibly for AlGaAs double heterostructure (DH) lasers and the spectral width of these lasers has been estimated to be less than 1 MHz by interferometric measurements.[1,2] However, because the band gap energy and the refractive index depend on temperature, the frequency of semiconductor lasers fluctuates when the temperature of the active region changes. The frequency of semiconductor lasers should be stabilized for a number of applications, such as heterodyne-type optical communication, high resolution spectroscopy, and metrology.

Several results for the frequency stabilization of semiconductor lasers using an external Fabry-Perot interferometer as a frequency reference have been reported.[3-5] In this method, the resulting frequency stability depends on the stability of the interferometer and on the traceability of the laser frequency to the interferometer. However, few authors have carefully considered about the stability of the interferometer and quantitatively estimated the frequency stability.

In this letter, the authors report the measurements of frequency fluctuations of AlGaAs DH lasers at free-running operation and the frequency stabilization of a DH laser by using an external Fabry-Perot interferometer. The frequency stability was evaluated by using the Allan variance[6] and the power spectral density, which are measures of frequency stability commonly used. For this measurements, the stability of a resonant frequency of the interferometer was also evaluated.

§2. Experimental Procedure

Figure 1 shows the block diagram of the apparatus used to stabilize the laser frequency. The experiments were carried out in an underground tunnel for the long-distance interferometry. The temperature in the tunnel was constant within 0.1°C/day.

Several single longitudinal mode AlGaAs DH lasers[7,8] ($\lambda=820\sim830$ nm) were driven by a dc current source. Temperature coefficient of the current source was 3 μA/°C. Each DH laser was mounted on a 5 mm thick copper plate. The temperature of the DH laser was

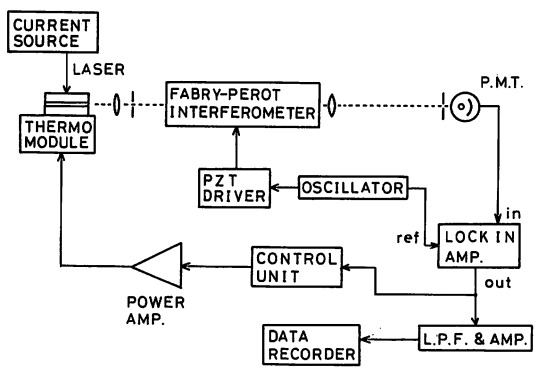

Fig. 1. Block diagram of the experimental apparatus.

controlled by a thermoelectrical cooler to which the copper plate was attached. The following operating conditions for DH lasers were employed: $I/I_{th}=1.10\sim1.25, T=15\sim25°C$, where I, I_{th} and T represent the injection current, the threshold current and the temperature of the copper plate, respectively. Under these conditions, DH lasers were operated in a single longitudinal mode.

An external Fabry-Perot interferometer was used as a frequency discriminator which was carefully constructed to maintain high stability. Two Al-coated flat mirrors with the reflectivity of 85% were used. The distance between these mirrors were kept 12.3 cm by using an Invar tube and piezoelectric transducer (PZT) as a spacer. This interferometer was installed in the alminium case and a plastic box to reduce the temperature change and air flow.

The frequency stability of the interferometer was measured by using a Lamb dip stabilized He–Ne laser at 633 nm (Spectra-Physics, SP-119). The frequency stability of the He–Ne laser itself was measured by using the error signals from the lock-in amplifier used for the frequency stabilization.

The laser beam was collimated by an objective lens and focused on a photomultiplier after passing through the interferometer. The optical axis was carefully adjusted so that the reflected beam from the interferometer did not disturb the laser oscillation. The interferometer length was piezoelectrically modulated at a frequency of 600 Hz. The first derivative signal of the transmission spectrum of the interferometer was obtained by synchronously detecting the output signal of the photomultiplier with a lock-in amplifier and was used as a frequency discriminator. The laser frequency was locked at the zero-crossing point of the first derivative signal. The output signal from the lock-in amplifier was fed to a propotional amplifier and then to the thermoelectrical cooler to control the temperature of the DH laser.

Error signals from the lock-in amplifier were proportional to the fluctuations of the laser frequency and were recorded by a data recorder. The Allan variance and the power spectral density were calculated from these signals, after analog-to-digital conversion.

§3. Experimental Results

Figure 2 shows frequency fluctuations of a DH laser. The upper trace corresponds to the free-running laser. The laser frequency varied about 60 MHz during a period of 10 min due to the changes in temperature. The lower trace corresponds to the stabilized laser. It can be seen that thermal drifts are reduced and that the laser frequency is stabilized with residual fluctuations of 5 MHz over a period of 40 min. It can be thought that the residual fluctuations with the period of about 25 s on this trace were caused by the response characteristics of the feedback loop.

Figure 3 shows the square root of the Allan variance σ^2, where τ and N represents the integration time and the number of data, respectively. The curve A represents the frequency stability of the Lamb dip stabilized He–Ne laser. The curve B represents the stability of the resonant frequency of the interferometer. The minimum value on this curve is

$$\sigma=2.1\times10^{-10} \quad \text{at } \tau=0.18\text{ s}. \tag{1}$$

For $\tau>0.18$ s, σ increases with increasing τ because of thermal drifts of the cavity length and is approximately expressed as

$$\sigma=5.7\times10^{-10}\cdot\tau^{1/2} \quad \text{for } 0.18\text{ s}\leqq\tau\leqq500\text{ s}. \tag{2}$$

For $\tau<0.1$ s, the frequency stability of the

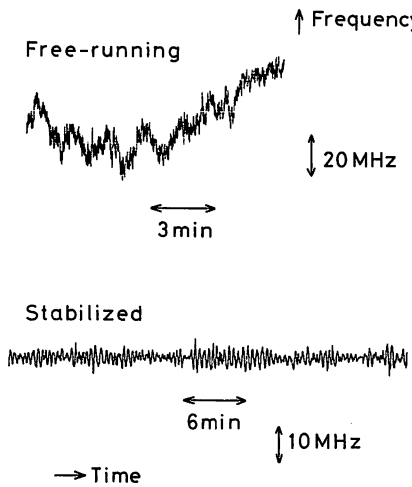

Fig. 2. Fluctuations of the laser frequency; upper and lower traces correspond to the free-running and the stabilized laser, respectively.

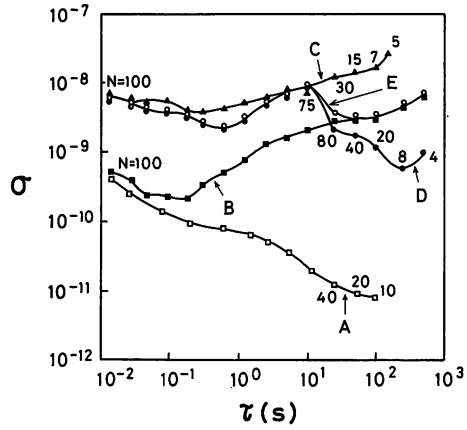

Fig. 3. The square root of the Allan variance σ^2, where τ and N represent the integration time and the number of data, respectively. A(□): The frequency stability of the Lamb dip stabilized He–Ne laser at 633 nm. B(■): The frequency stability of the external Fabry-Perot interferometer. C(▲): The frequency traceability of the free-running DH laser to the interferometer. D(●): The frequency traceability of the stabilized DH laser to the interferometer. E(○): The frequency stability of the stabilized DH laser estimated from the curves B and D.

Fabry-Perot interferometer was not able to be estimated because that of the He–Ne laser was not high enough.

Curves C and D in Fig. 3 represent the typical results for the DH laser and can be interpreted as representing the traceability of the laser frequency to the resonant frequency of the interferometer. The curve C represents the results for the free-running laser. These values can be considered as the frequency stability of the free-running laser because these are about ten times larger than those on the curve B at each value of τ in this figure. The minimum value on the curve C is

$$\sigma = 3.8 \times 10^{-9} \quad \text{at } \tau = 0.3 \text{ s}. \tag{3}$$

Due to thermal drifts, σ increases with increasing τ for $\tau > 0.3$ s, however, the stability is better than 1.0×10^{-8} for $10 \text{ ms} < \tau < 20$ s. The frequency stability of the free-running laser was almost independent of operating conditions such as injection current and temperature employed in this experiment. The curve D represents the result for the stabilized laser. The minimum value on this curve is

$$\sigma = 5.6 \times 10^{-10} \quad \text{at } \tau = 250 \text{ s}. \tag{4}$$

The frequency stability σ_s of the stabilized DH laser can be estimated by using the curves B, D and the following relation:[6]

$$\sigma_s \cong (\sigma_I^2 + \sigma_T^2)^{1/2}, \tag{5}$$

where σ_I and σ_T represent the values on the curves B and D, respectively. The curve E in this figure represents the estimated frequency stability σ_s. The value of σ_s is almost equal to σ_T for $\tau < 10$ s and is equal to σ_I for $\tau > 50$ s. A bump around $\tau = 25$ s corresponds to the periodic fluctuations on the lower trace of Fig. 2. It can be seen that the value of σ_s on the curve E is about ten times smaller than that on the curve C for $\tau > 20$ s. Though the relation between σ_s and τ is rather complicated on this curve, the minimum value of σ_s is

$$\sigma_s = 2.1 \times 10^{-9} \quad \text{at } \tau = 0.6 \text{ s}, \tag{6}$$

and stability is better than 9.6×10^{-9} for 10 ms $< \tau <$ 500 s.

Figure 4 shows the power spectral density S of the frequency fluctuations, where broken and solid curves represent the results for the free-running and the stabilized laser (curves C and D in Fig. 3), respectively. When the laser was stabilized, fluctuations for $f < 0.1$ Hz were reduced considerably and this fact indicates the improvement of the long-term frequency stability. The observed peak at $f = 0.04$ Hz on

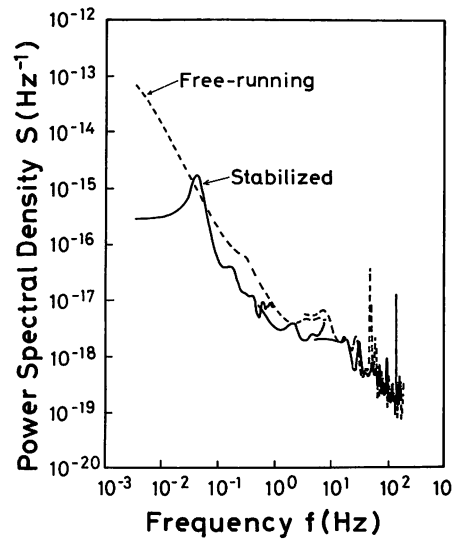

Fig. 4. Power spectral density of the frequency fluctuations; solid and broken curves correspond to the stabilized and the free-running laser, respectively.

the solid curve corresponds to the periodic fluctuations on the lower trace of Fig. 2. These fluctuations are considered to be the inherent characteristics in the feedback system used in this experiment. Comparing the two curves in this figure, it can be said that the band width of the feedback system was about 0.1 Hz, which was limited mainly by the response time of the thermoelectrical cooler and the copper plate. Higher stability can be expected by improving the feedback system including the control of the injection current, which will be reported later.

§4. Conclusion

In the present experiments, the frequency of an AlGaAs DH laser was stabilized by controlling the temperature at the resonant frequency of an external Fabry-Perot interferometer. The frequency stability was evaluated by using the Allan variance and the power spectral density. The following values were obtained:

(i) Free-running laser

$$3.8\times10^{-9}\leqq\sigma\leqq1.0\times10^{-8} \quad \text{for } 10\,\text{ms}<\tau<20\,\text{s}. \tag{7}$$

(ii) Stabilized laser

$$2.1\times10^{-9}\leqq\sigma\leqq9.6\times10^{-9} \quad \text{for } 10\,\text{ms}<\tau<500\,\text{s}. \tag{8}$$

It can be concluded that the long-term stability for the stabilized laser was improved compared to that of the free-running laser for $\tau>10$ s.

Acknowledgement

The authors would like to express their thanks to Drs. M. Nakamura, K. Aiki (Hitachi, Ltd.), F. Saito and R. Lang (Nippon Electric Co., Ltd.) for their supports to the experiments and helpful discussions. They also appreciate valuable discussions with Associate Prof. K. Iga and Mr. T. Takakura (now at Hitachi, Ltd.) of Tokyo Institute of Technology.

References

1) T. Takakura, T. Tako and K. Iga: Pap. Tech. Group on Optics & Quantum Electronics of IECE of Jpn. **OQE78-159** (1979).
2) T. Tako, T. Takakura and K. Iga: J. Opt. Soc. Am. **69** (1979) 1482.
3) Yu. A. Bykovkii, V. L. Velichanskii, I. G. Goncharov and V. A. Maslov: Sov. Phys.-Semicond. **4** (1970) 580.
4) J. L. Picque and S. Roizen: Appl. Phys. Lett. **27** (1975) 340.
5) T. Okoshi and K. Kikuchi: Electron. Lett. **16** (1980) 179.
6) D. W. Allan: Proc. IEEE **54** (1966) 221.
7) K. Aiki, M. Nakanura, T. Kuroda, J. Umeda, R. Ito, N. Chinone and M. Maeda: IEEE J. Quantum Electron. **QE-14** (1978) 89.
8) T. Furuse, I. Sakuma, Y. Ide and K. Nishida: Pap. Tech. Group on Optics & Quantum Electronics of IECE of Jpn. **OQE79-2** (1979).

レーザーオリジナル

3.51 μm周波数オフセットロックHe-Xeレーザー

大津元一*・田幸敏治*

(1980年7月23日　受理)

Frequency-Offset-Locked He-Xe Laser at 3.51 μm

Motoichi OHTSU* and Toshiharu TAKO*

(Received July 23, 1980)

A highly stabilized frequency-offset-locked He-Xe laser system is constructed for the high resolution laser spectroscopy of H_2CO ($5_{1,2}(\nu=0)) \rightarrow 6_{0,6}(\nu_5=1)$) at 3.51 μm. It is composed of two He-Xe lasers. The first laser is the H_2CO-stabilized He-Xe laser which is used as a frequency reference. The second laser is frequency-offset-locked to the first laser by using the beat frequency between these lasers. The frequency stability of the frist laser is 1.0×10^{-14} at $\tau=100$ s, where τ represents the integration time. The frequency traceability of the second laser to the first laser is expressed as $8.0\times10^{-13}\cdot\tau^{-1}$ for 10 ms$<\tau<$100 s. It is found that this value of the traceability was independent of the frequency modulation of the first and second lasers. The variable range of the frequency of the second laser is 18 MHz. In this range, the frequency traceability of the second laser to the first laser is independent of the beat frequency.

1. まえがき

近年，各種の高分解能レーザー分光が発達してきた。レーザー分光の高分解能化のためにはレーザー周波数を安定化することが必要である。従来，各種分子の飽和吸収線を用いた安定化レーザー（3.39 μm CH_4安定化 He-Ne レーザー[1]，633 nm I_2 安定化 He-Ne レーザー[2]，10.6 μm CO_2安定化 CO_2レーザー[3]など）では周波数安定度は10^{-10}～10^{-13}に達しているが，周波数を可変にすることはできない。これらを用いて分光測定を行なう場合にはStark効果などにより測定対象の原子・分子スペクトルの周波数掃引を行行なう必要がある。この場合，原子・分子に加える外場により測定対象スペクトルの状態が乱されることなどの理由により10^{-10}以上の高分解能が必要な場合には必ずしも有利ではない。そこで周波数が高度に安定化され周波数が可変のレーザーの開発が望まれる。さらに微弱信号測定の際にはレーザー周波数を変調でき測定の高感度化が計れることが必要であり周波数変調・無変調の両方を実現できるようなレーザーでなくてはならない。

以上のような背景のもとに筆者らはH_2CO（$5_{1,5}(\nu=0) \leftarrow 6_{0,6}(\nu_5=1)$）の飽和吸収分光，分子ビーム分光を高分解能・高感度で行なうための，周波数が安定化されかつ可変の3.51 μm He-Xe レーザー，すなわち 3.51 μm 周波数オ

* 東京工業大学精密工学研究所（〒227 横浜市緑区長津田4259）
* Research Laboratory of Precision Machinery and Electronics, Tokyo Institute of Technology 4259 (Nagatsuta, Midori-ku Yokohama 227)

フセットロック He-Xe レーザーを開発した。本論文ではこのレーザーの性能について報告する。なお，ここで用いる周波数オフセットロックの方法は単に分光用光源としてではなく各種計測用レーザー，通信用レーザーなどへも広く応用される可能性を有するものである。

2．実験装置

装置の開発にあたり次の性能が得られることを目標とした。

(1) 分光測定の際の分解能10^{-10}程度を得るためにレーザーの周波数安定度$\sigma \leqq 1 \times 10^{-12}$（$\tau = 1$ s で）であること。ここでσは周波数安定度を表わすパラメータ，Allan 分散σ^2の平方根であり，τはその測定の積分時間である。[4] 積分制御された周波数安定化レーザーでは$\sigma \propto \tau^{-1/2} \sim \tau^{-1}$であるため分光測定の際には測定時間を長くする（すなわちτを大きくする）方が有利であるが，ここでは測定対象である飽和吸収セル，分子ビーム装置を含め全実験系の安定度のバランスを考え，一回の測定が約1時間以内で終ること，すなわちレーザー周波数掃引の1ステップ当りの送り時間を1 s ～5 s とすることを目標としたため$\tau = 1$ s における上記σの値を便宜上の目標達成の目安とした。

(2) スペクトル幅1 MHz 程度のスペクトル測定のために周波数可変範囲は10 MHz 以上であること。

(3) 周波数変調および無変調が可能であること。

以上を同時に満たすようなレーザーを得るために Fig. 1 に示す装置を用いて実験を行なった。図中第1レーザーは H_2CO（$5_{1,5}(\nu=0) \rightarrow 6_{0,6}(\nu_5=1)$）の飽和吸収線の中心周波数に周波数安定化した 3.51 μm He-Xe レーザーであり，これは周波数基準発振器として用いられる。第2レーザーが 3.51 μm 周波数オフセットロックレーザーである。すなわち，第1レーザーとの間でビート信号を検出し，そのビート周波数が高安定周波数シンセサイザーからの出力周波数値に一致するように第2レーザー周波数を制御する。これにより第2レーザーの周波数は第1レーザー，すなわち周波数安定化レーザーの周波数に追随して安定化される。ここで周波数シンセサイザーの出力周波数を掃引すれば，2台のレーザー間のビート周波数が掃引され，従って第2レーザーの周波数も掃引される。このようにして第2レーザーは第1レーザーの周波数と同程度の安定度を保ち，かつ周波数可変のレーザーになりうる。図中，第1レーザーについては他で報告してあるので詳細は略する。[5,6] 両レーザー間のビート信号は InAs 検出器で検出し，広帯域増幅器Aで増幅し，ディスクリミネータにより TTL レベルに変換する。その周波数を分周器により1/10，または1/20に分周する。この出力信号の位相と周波数シンセサイザーの出力信号の位相とを位相比較器 ϕ/V によって比較し，その位相差に比例する電圧値を得る。この出力電圧を PZT 用電源(PZT driver)に入れてこれにより第2レーザーの共振器用鏡の1枚をマウントしている PZT を駆動し，第2レーザー周波数を制御する。

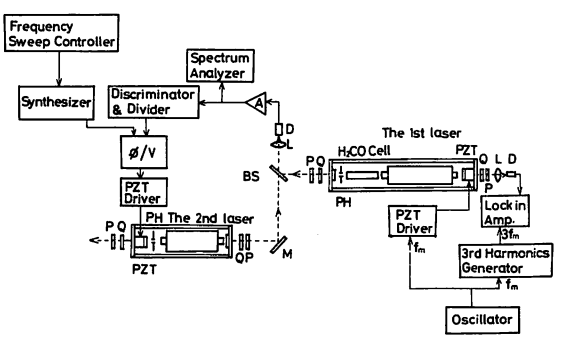

Fig. 1. Experimental apparatus. ϕ/V: A phase comparator. A: A wide band amplifier. BS: Beam splitter. D: InAs detector. L: Lens. M: Mirror. P: Polarizer. PH: Pinhole Q: Quater-wave plate.

以上が周波数オフセットロックレーザーの制御系であるがこのうち重要な役割を果たすものが位相比較器と PZT 用電源である。まず位相比較器のブロック図を Fig. 2 に示す。周波数オフセットロックの方法を用いるときに問題となる点は2台のレーザー間のビート周波数の変動が大きい場合ビート信号と周波数シンセサイザ

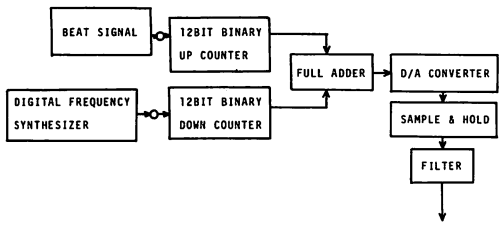

Fig. 2. The block diagram of the phase comparator.

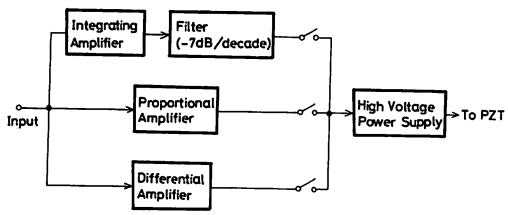

Fig. 3. The block diagram of the PZT driver.

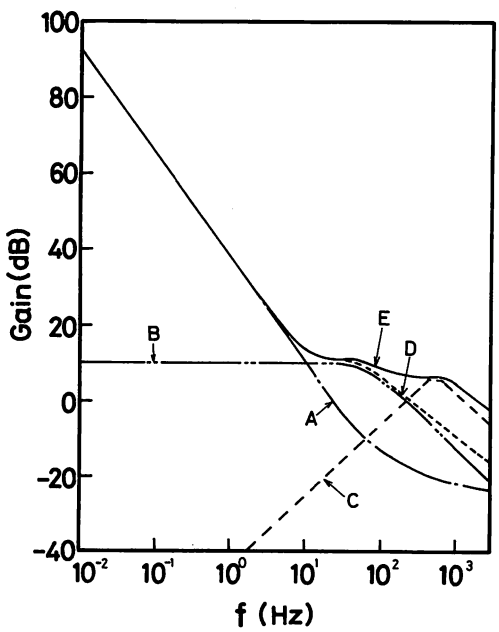

Fig. 4. The frequency dependence of the voltage gain of each amplifier in the PZT driver.
A: The integrating amplifier and the filter (− 7 dB/decade).
B: The proportional amplifier.
C: The differential amplifier.
D: The sum of the values on the curves A and B.
E: The sum of the values on the curves A, B, and C.

ーの出力信号との位相差が大きくなり位相比較器のカウンターがオーバーフローすることである。ここで試作した位相比較器は12ビット2進カウンターを用い全加算器により周波数シンセサイザー出力信号とビート信号とのカウント数の差を作りアナグロ信号に変換する方法をとっているため$\pm 2\pi\times 10^{11}$radの位相余裕度を有し，このようなオーバーフローを避けることができる。このように広いダイナミックレンジを有することにより周波数オフセットロックを安定に行なうことが可能である。次にPZT用電源のブロック図をFig. 3に示す。ここでは長期安定度を向上させるために制御用増幅器として積分増幅器を用いている。これにフィルター（−7 dB/decade)を直列接続することによりさらに長期（低周波数）での制御利得を向上させている。さらに短期安定度も向上させるために比例増幅器，微分増幅器を並列に接続する。これらの増幅器の利得の周波数特性をFig. 4に示す。積分増幅器とフィルターとともに比例，微分増幅器を併用すると周波数帯域が約1 kHzまで拡大していることがわかる。レーザー共振器に組込まれた状態でのPZT(Burleigh PZ-80）の応答周波数帯域は約1 kHzであることが確認されているのでこのPZT用電源によりPZTの応答周波数帯域全体にわたり制御することができる。次にFig. 1に示した装置によって第2レー

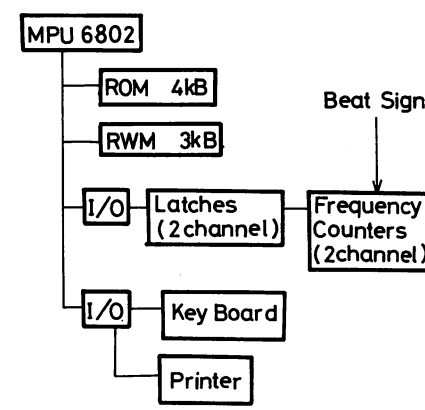

Fig. 5. The block diagram of the Allan variance real-time processing system(the ARPS).

ザーの周波数を安定化したときにその安定度 σ を測定する必要があるがこのレーザーを分光実験に用いるとき σ を実時間で測定しモニターできれば都合がよい。このような要望からAllan分散実時間測定装置(The Allan variance real-time processing systen, 略してARPSと呼ぶ) を開発した。[7]そのブロック図をFig. 5 に示す。マイクロプロセッサーには6802を用いている。ビート周波数は2進カウンターとラッチで構成された周波数カウンターで計数される。この2進カウンターはリセットを行なわずに常にオーバーフローしつづける方式をとっている。これによりカウントの際のゲートの閉じている時間，すなわち測定の空き時間を0にすることができる。Allan分散測定の際にはこの測定の空き時間は0でなければ測定誤差を生ずるので,[4] ARPSでは上記の方法によりこの誤差を生じないよう工夫されている。従来Allan分散を計算する際市販の周波数カウンターを用いていたがゲートの閉じている時間が長く $\tau \geqq 1$ s では誤差差が大きく測定不可能であった。[8]これにくらべARPSではこの誤差を消去でき 1 ms$\leqq\tau\leqq 10^3$ s まで測定可能となった。測定はキーボードと感熱プリンタを介し実時間で行なうことができる。

3．実験結果と考察

まず周波数基準となる第1レーザーの周波数安定度の測定結果をFig. 6 に示す。この H_2CO 安定化 He-Xe レーザーの周波数安定化の方法に関してはすでに報告してあるので,[5,6]ここでは要点を記すに留める。測定はFig. 5 のARPSにより実時間で行なった。制御に使用したPZT用電源はFig. 3 に示す周波数オフセットロック用のものと同型のものを用いた。曲線Aは積分増幅器とフィルターおよび比例増幅器を用いた場合，曲線Bはさらに微分増幅器をも併用した場合である。Fig. 4 に示したように微分増幅器を併用し周波数帯域を広大したので曲線Bの短期安定度は曲線Aよりも向上している。さらに同時に長期安定度も向上しておりFig. 6 の測定では τ の全範囲 (10 ms$\leqq\tau\leqq$500 s) にわたり曲線Bの安定度の方がすぐれていることがわかる。Fig. 6 の各曲線での σ の最小値は

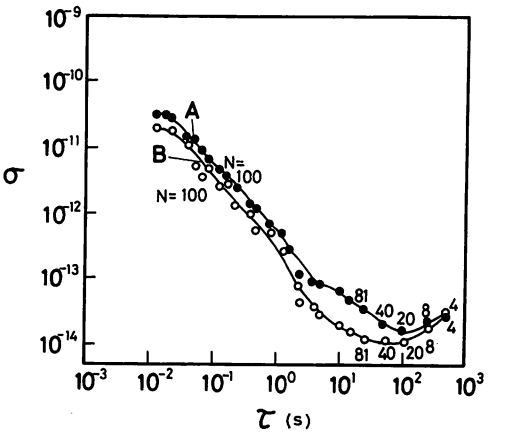

Fig. 6. The square root of the Allan variance σ^2 of the frequency fluctuations of the first laser. τ and N represent the integration time and the number of data, respectively. A: The result obtained by using the proportional amplifier with the integrating amplifier and the filter in the PZT driver. B: The result obtained by using the differential amplifier with the proportional amplifier, the integrating amplifier and the filter.

$$\left.\begin{array}{l}\text{曲線A：}\sigma = 1.6\times10^{-14}(\tau = 100\text{ s で})\\ \text{曲線B：}\sigma = 1.0\times10^{-14}(\tau = 100\text{ s で})\end{array}\right\}\quad(1)$$

である。以下の実験では第1レーザーの周波数安定化の方式としてはFig. 6 の曲線Bの場合のものを用いることにする。

次に第2レーザーを第1レーザーに対し周波数オフセットロックを施したときの結果について記す。Fig. 7 は両レーザー周波数 f_1, f_2 の間のビート周波数 f_1-f_2 の安定度を表わすAllan分散の平方根 σ をARPSを用いて測定した結果である。ここで $f_1-f_2=4$ MHz に設定した。ビート周波数の変動量は 3.51 μm He-Xe レーザー周波数 (85.5 THz) で規格化したものを用いて表わしている。Fig. 6 と同様曲線AはFig. 3 に示すPZT用電源中で積分増幅器とフィルター，および比例増幅器を用いた結果であり，

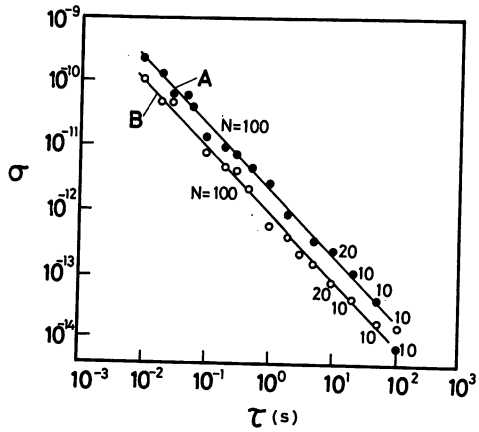

Fig. 7. The square root of the Allan variance σ^2 of the frequency fluctuations of the beat signal between the first and second lasers when the second laser was frequency-offset-locked to the first laser. The value of σ is normalized to the He-Xe laser frequency at 3.51 μm. A: The result obtained by using the proportional amplifier with the integrating amplifier and the fillter in the PZT driver. B: The result obtained by using the differential amplifier with the proportional amplifier, the integrating amplifier and the filter.

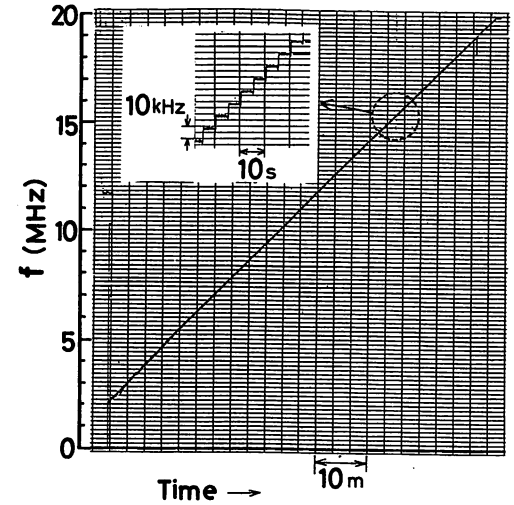

Fig. 8. The experimental result in which the beat frequency f_1-f_2 between the first and second lasers was automatically swept at 10k Hz interval when the second laser was frequency-offset-locked to the first laser. Therefore, the frequency of the second laser was swept at 10k-Hz interval in this figure.

曲線Bはさらに微分増幅器も併用した結果を示す。この場合でも曲線Bの方が曲線Aよりも安定度がすぐれていることがわかる。両曲線ともσは10ms$\leqq\tau\leqq$100 sの範囲でτ^{-1}にほぼ比例しており次のように表わすことができる。

$$\left.\begin{aligned}&\text{曲線A}：\sigma=2.0\times10^{-12}\cdot\tau^{-1}\\&\text{曲線B}：\sigma=8.0\times10^{-13}\cdot\tau^{-1}\end{aligned}\right\}\qquad(2)$$

Fig. 7 はビート周波数f_1-f_2の安定度，すなわち第1レーザー周波数f_1への第2レーザー周波数f_2の追随度を表わしている。そこで第2レーザー周波数f_2そのものの安定度を推定するにはFig. 7 とともにFig. 6 も用いる必要がある。Figs. 6, 7 のAllan分散の値をσ_1^2, σ_b^2, 求めようとする第2レーザー周波数のそれをσ_2^2と書くとAllan分散の定義により[4] 近似的に

$$\sigma_2^2\cong\sigma_1^2+\sigma_b^2\qquad(3)$$

と書くことができる。Fig. 6 の曲線BとFig. 7 の曲線B，および(3)式を用いると$\tau=1$ sにおけるσ_2の値は$\sigma_2\leqq1\times10^{-12}$であり**2**．の(1)に示した条件を満たしていることがわかる。

次に**2**．の(2)に示した第2レーザーの周波数可変範囲をしらべた結果をFig. 8 に示す。Fig. 8 はFig. 1 中の周波数シンセサイザーの出力周波数を掃引回路(Frequency sweep controller)を用いて5 sごとに10kHz ステップで掃引した結果を示し，これによるとビート周波数f_1-f_2もそれに追随して掃引されていることがわかる。Fig. 8 でのビート周波数の可変範囲は2 MHz$\leqq f_1-f_2\leqq$20MHz であった。従って第2レーザーの周波数可変範囲は18MHz であり，これは**2**．の(2)に示した条件を満たしている。$f_1-f_2<2$ MHz の範囲では位相比較器の利得が小さくなり制御がかかりにくい。またこの範囲でf_1-f_2を小さくしていくとビート信号検出用の検出器の窓面などからの反射により2台のレーザー間で注入同期の現象が生じ，周波数安定度が劣化す

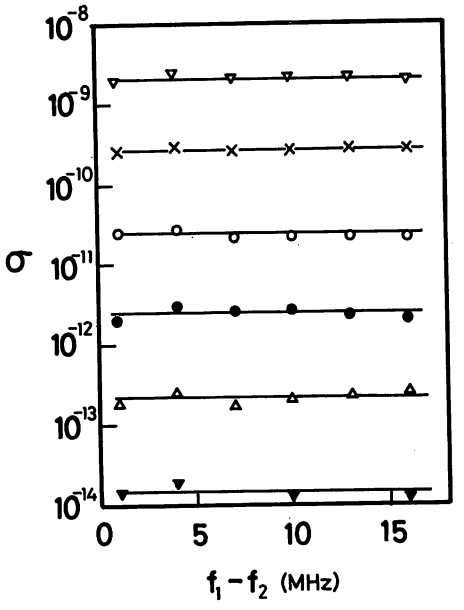

Fig. 9. The relation between the value of σ and the value of the beat frequency f_1-f_2 between the first and second lasers, where σ represents the same quantity as that shown in Fig. 7. The same PZT driver was used as for the curve B in Fig. 7. ▽: τ= 1 ms, N= 100, ×: τ=10 ms, N= 100, ○: τ= 100 ms, N= 100, ●: τ= 1 s, N= 100, △: τ=10s, N=20, ▼: τ= 100 s, N=10.

る。一方f_1-f_2>20MHz ではビート信号レベルが小さくなりFig. 1 中のディスクリミネータでアナログ信号からTTL 信号への変換が不可能になるため周波数オフセットロックがかからなくなっている。従って今回の結果よりさらに周波数可変範囲をひろげるにはまずより高速の光検出器を用いビート信号を高感度増幅することが最も大切である。さて，この周波数可変範囲内でのビート周波数f_1-f_2のそれぞれの値においてf_1-f_2の安定度を測定した結果をFig. 9 にに示す。Fig. 9 ではf_1-f_2をFig. 8 の周波数可変範囲内のいくつかの値に設定して周波数オフセットロックを施し，そのときのf_1-f_2の安定度をf_1-f_2の設定値に対してプロットしたものでありパラメータはτである。Fig. 9 によるとFig. 8の周波数可変範囲内ではf_1-f_2の安定度はf_1-f_2の設定値によらないこと，従ってそれはFig. 7 に示した結果をもって代表して表わしうることがわかる。

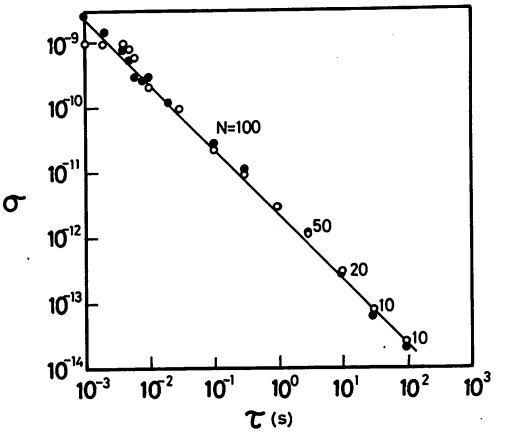

Fig. 10. The square root of the Allan variance σ^2 of the frequency fluctuations of the beat signal between the first and second lasers when the second laser is frequency-offset-locked to the first laser. The value of σ is normalized to the He-Xe laser frequency at 3.51 μm. The same PZT driver was used as for the curve B in Fig. 7. ○: The frequency of the first laser only was modulated. Therefore, the beat frequency was modulated. ●: The frequency of the second laser was modulated synchronously with that of the first laser. Tkerefore, the beat frequency was not modulated.

次に**2**．の(3)の周波数変調に関する実験の結果について記す。第1 レーザーの周波数を安定化するときにはH_2CO の反転ラムくぼみの微分波形を得るためにレーザーの周波数を変調していた。[5),6)]それはPZT に交流電圧を加えることにより行なうがFig. 6 の結果を得たときは変調周波数f_m は 500 Hz，変調の最大周波数偏移$\Delta\nu_m$は1.15 MHz(peak-to-peak 値）であった。この第1 レーザーを用いて第2 レーザーに周波数オフセットロックを施した実験(Figs. 7 ～9 ）では第2 レーザーは周波数変調をかけていなかった。そこで第2 レーザーの周波数に変調をかけた場合，および無変調の場合につきビート周波数f_1-f_2の安定度を測定した結果をFig. 10

に示す。Fig. 10ではFig. 7の曲線Bと同様PZT用電源内の積分増幅器とフィルター，比例増幅器に微分増幅器を併用している。図中白丸はFig. 7と同様第1レーザーの周波数のみが変調され，第2レーザー周波数は無変調の場合の結果を示す。すなわちこの場合ではビート周波数f_1-f_2は変調されている。一方黒丸は第2レーザー周波数を第1レーザー周波数に同期して変調した場合の結果を示す。この場合スペクトラムアナライザのブラウン管画面上で観測されるビート信号スペクトルの幅が両レーザー周波数とも無変調の場合のビート信号スペクトルの幅と同等の値まで狭くなるように第2レーザー用のPZTに加える交流電圧の振幅と位相を調節した。白丸と黒丸の結果を比較すると両者に差異はみられず第2レーザー周波数が変調，無変調にかかわらず同等の安定度で周波数オフセットロックが可能であることがわかる。従って**2**．の(3)の条件が満たされていることが確認される。上記のような変調を加えた場合変調周波数f_mの逆数に相当する積分時間$\tau=2$ msでσは変調の最大周波数偏移$\Delta\nu_m$の値に依存する値を有するはずであるから，変調，無変調の場合を比較すると$\tau=2$ msの付近でのσの値に差が生じると予想される。しかしながらFig. 10に示す実験結果でその差が現われていないのは次の理由による：周波数オフセットロックの制御系では位相比較器が使われており，これは文字どおり信号の位相を検出する回路である。位相は周波数を時間積分した量であるので位相比較器は周波数オフセットロック制御系の中で積分増幅器として働き，従ってその利得は高周波数領域では低い。すなわちこの制御系では変調周波数f_mの値付近の周波数領域では制御利得は小さく，周波数変調により生ずる周波数変動量に対しては十分な制御がかかっていないため，変調，無変調の場合に対して$\tau=2$ ms付近ではσの値には互いに差が生じないものと考えられる。もし周波数オフセットロックの制御系の制御帯域をより高周波数領域までのばすことができればレーザーの周波数変調，無変調の場合に対しσの値は$\tau=2$ ms付近で互いに差を生ずるはずである。そしてこの場合は今回の結果よりもより高周波領域まで（すなわち，よりτの小さい範囲まで）高い周波数安定度が得られると考えられる。

以上により**2**．の(1)〜(3)で示された条件を満足する性能の周波数オフセットロックレーザーを実現することができ，当初の目標であるH_2COの高分解能分光に使用しうることが確認された。さらに高速のPZTを使い，PZT用電源の制御周波数帯域を広げることにより周波数安定度を向上させることができ，より高速の光検出器を用いることで周波数可変範囲も拡大しうると期待される。

4．結論

3.51 μm帯でのH_2COの高分解能レーザー分光を行なうために周波数オフセットロックHe−Xeレーザーを開発した。積分，比例，微分増幅器を有するPZT用電源を用いてレーザー周波数を制御したとき次の結果を得た。

(1)　第1レーザー，すなわち周波数基準となるH_2CO安定化He-Xeレーザーの周波数安定度は

$$\sigma=1.0\times10^{-14}\ (\tau=100\ \mathrm{s}\ \text{で}) \qquad (4)$$

であった。

(2)　第1レーザー周波数に対する第2レーザーすなわち周波数オフセットロックレーザーの周波数追随度は

$$\sigma=8.0\times10^{-13}\cdot\tau^{-1}\quad(10\ \mathrm{ms}\leqq\tau\leqq100\ \mathrm{s}) \qquad (5)$$

であった。

(3)　第2レーザーの周波数可変範囲は18 MHzであった。すなわち第1，第2レーザー間のビート周波数f_1-f_2の可変範囲は

$$2\ \mathrm{MHz}\leqq f_1-f_2\leqq20\ \mathrm{MHz} \qquad (6)$$

であった。この範囲内で第1レーザーに対する

第2 レーザーの周波数追随度はビート周波数の値には依存しなかった。

(4) 第1 レーザーに対する第2 レーザーの周波数追随度の値は周波数変調の影響を受けなかった。

謝 辞

実験に協力いただいた本学大学院修士課程小山亮平氏（現在旭化成株式会社）葛城誠一氏（現在東京芝浦電気株式会社）に感謝します。なお，本研究の一部は文部省科学研究費特定研究の補助により行なわれたものである。

参 考 文 献

1) R.L.Barger and J.L.Hall: Phys. Rev.Letters **22** (1969) 4.
2) G.R.Hanes and K.M.Baird: Metrologia **5** (1969) 32.
3) C.Freed and A. Javan: Appl.phys.Letters **17** (1970) 53.
4) D.W.Allan: Proc.IEEE **54** (1966) 2.
5) M.Ohtsu, R.Koyama and T.Tako: Jpn.J.Appl. **18** (1979) 1621.
6) M.Ohtsu, S.Katsuragi and T. Tako: submitted to IEEE J. Quantum Electron.
7) 椎尾一郎，大津元一，田幸敏治：電子通信学会論文誌Cに投稿中
8) M.Ohtsu, R.Koyama, A.Kusnowo and T. Tako: Jpn.J.Appl.phys.**18** (1979) 1619.

JAPANESE JOURNAL OF APPLIED PHYSICS
VOL. 19, NO. 9, SEPTEMBER, 1980 pp. 1683–1688

Wavelength Measurement of an H_2CO-Stabilized He–Xe Laser at 3.51 μm

Toshiharu TAKO, Motoichi OHTSU, Seiichi KATSURAGI, Misao OHI† and Yoshiaki AKIMOTO†

Research Laboratory of Precision Machinery and Electronics, Tokyo Institute of Technology, 4259 Nagatsuta-cho, Midori-ku, Yokohama, Kanagawa 227
†National Research Laboratory of Metrology, 1–4, 1-chome, Umezono, Sakura-mura, Niihari-gun, Ibaraki 305

(Received March 28, 1980)

The vacuum wavelength of an H_2CO ($5_{1,5}$(ground state)→$6_{0,6}$($v_5=1$))-stabilized He–Xe laser was measured with respect to the CH_4-stabilized He–Ne laser at 3.39 μm by using a pressure-scanning Fabry-Perot interferometer. The average value $\bar{\lambda}_{H_2CO}$ of the vacuum wavelength obtained was 3 507 979.48 pm. The standard deviation σ_{n-1} was 0.39 pm with an accuracy of $\sigma_{n-1}/\bar{\lambda}_{H_2CO}=1.1\times10^{-7}$. The estimated values of the systematic errors were $-0.24\text{ pm}\leqq\Delta\lambda_{H_2CO,1}\leqq0$, $\Delta\lambda_{H_2CO,2}=0.004$ pm, and $\Delta\lambda_{H_2CO,3}=0.02$ pm, respectively, where $\Delta\lambda_{H_2CO,1}$, $\Delta\lambda_{H_2CO,2}$, and $\Delta\lambda_{H_2CO,3}$ represent the errors caused by diffraction, nonparallelism between the interferometer mirrors, and nonparallelism between the two laser beams, respectively.

§1. Introduction

The authors (M. O. and T. T. of T. I. T.) have carried out experiments on the frequency stabilization of an He–Xe laser at 3.51 μm by using the inverted Lamb dip in H_2CO ($5_{1,5}$ (ground state)→$6_{0,6}$ ($v_5=1$)).[1,2] The frequency or wavelength of this laser should be precisely measured so that it may be used as a new frequency or wavelength standard in the infrared band around 3.5 μm. The frequency of the free-running He–Xe laser has been measured,[3] but no measurement has been carried out for the H_2CO-stabilized He–Xe laser. Sakurai *et al.* have estimated the vacuum wavelength of the absorption line in H_2CO ($5_{1,5}$ (ground state)→$6_{0,6}$($v_5=1$)) as 3.507993 μm by using its wavenumber value of 2850.633 cm^{-1}.[4]

We report here the result of the wavelength measurement of the H_2CO-stabilized He–Xe laser. This result was obtained by the coincidence method using pressure-scanning Fabry-Perot interferometers, which have been used to measure the wavelengths of He–Ne lasers at 3.39 μm and 633 nm.[5,6]

§2. Experimental Apparatus

The frequency stability σ of the H_2CO-stabilized He–Xe laser was 1.6×10^{-14} at $\tau=$ 100 s, and $\sigma\leqq1.0\times10^{-10}$ for $\tau\geqq10$ ms, where σ and τ represent the square root of the Allan variance σ^2 of the frequency fluctuations[7] and the integration time, respectively. Therefore, the frequency is stable enough to get the value of the wavelength with nine or ten significant digits. Further details of the frequency stabilization will be reported elsewhere.

The experimental apparatus for the wavelength measurement is shown in Fig. 1. A CH_4-stabilized He–Ne laser at 3.39 μm was used as a wavelength reference and was constructed by the authors (M. O. and Y. A. of N. R. L. M.). The frequency stability σ of this laser is 1.8×10^{-12} at $\tau=30$ s,[8] and its vacuum wavelength

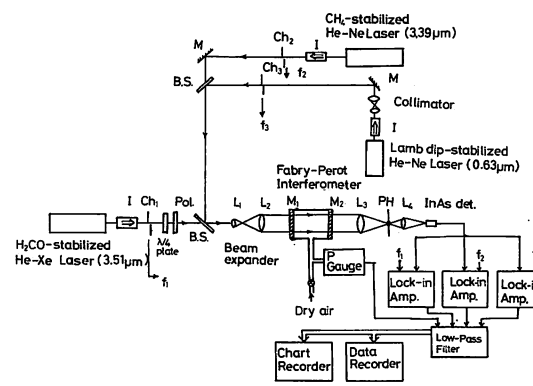

Fig. 1. Experimental apparatus: f_1, f_2, and f_3 represent three different frequencies of the choppers (*Ch*) used with lock-in amplifiers. *I* represents the optical isolator.

λ_{CH_4} is 3 392 231.40 pm.[9] The interference fringes of He–Xe and He–Ne lasers were simultaneously measured by a pressure-scanning Fabry-Perot interferometer, and then the value of the vacuum wavelength of the He–Xe laser was obtained from these results by the coincidence method. Two Al-coated flat mirrors were used for the Fabry-Perot interferometer. The Al-film of the mirror was also coated with SiO_2-film for protection. The reflectance of each mirror was 85% in the infrared region around 3.5 μm, i.e., the finesse of the interferometer was 20. Two fused quartz cylinders about 10 and 20 cm long were used as the interferometer spacers. The spacer length of the interferometer was preliminarily measured by using a laser interferometer (HP5526A) within an error of 0.5 μm, and the result was used as auxiliary data when the orders of interference were found by the coincidence method. Furthermore, a Lamb-dip-stabilized He–Ne laser at 633 nm (SP-119) was also used as an auxiliary wavelength reference to find the orders of interference in a simpler way.

The intensities of the He–Xe and He–Ne (3.39 μm) lasers were about 10 μW at the incident point of the interferometer. Because of the low intensities of these lasers, the signal-to-noise ratios of the recorded interference fringes were low. Therefore, a large value of the time constant of the lock-in amplifier, 1s, was used to suppress the noise accompanying the low laser intensity measurement. As the noise suppression was not sufficient, a low-pass filter with a cut-off frequency of 3.3 Hz was used at the next stage of the lock-in amplifier, and the output signal from the filter and the signal from the pressure gauge for the interferometer were recorded with a data recorder. The playback signals from the data recorder, after A/D conversion, were then fitted into the Lorentzian curves by the least-squares method. The order of interference m for each laser was obtained at the peak of the fitted Lorentzian curve by the coincidence method, and the wavelength λ_{H_2CO} of the He–Xe laser was calculated from eq. (1):

$$\lambda_{H_2CO} = \lambda_{CH_4} \cdot m_{CH_4}/m_{H_2CO}, \qquad (1)$$

where m_{H_2CO} and m_{CH_4} represent the values of m of the He–Xe and He–Ne (3.39 μm) lasers, respectively.

§3. Experimental Results

Figure 2 shows the interference fringes of three lasers traced on a chart recorder. It took 25 minutes to trace these fringes. Table I shows the values of the vacuum wavelength of the He–Xe laser obtained from the results of Fig. 2. Four series of experiments were carried out on

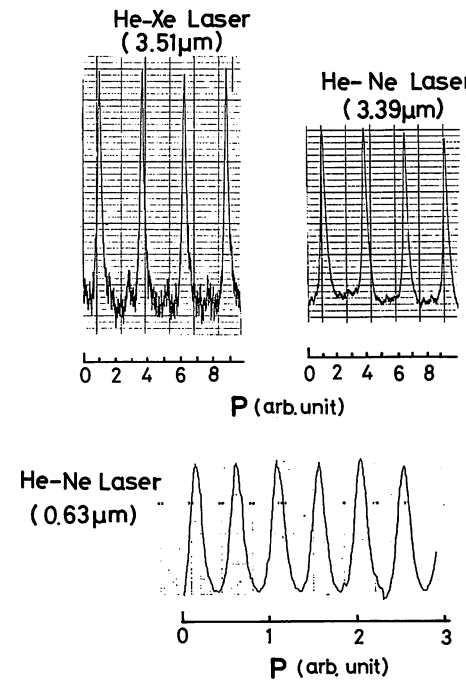

Fig. 2. Interference fringes of three lasers. P represents the pressure of dry air in the interferometer.

Table I. Experimental results obtained by using the interferometers of 10 cm and 20 cm length. L, n, $\bar{\lambda}_{H_2CO}$, and σ_{n-1} represent the length of the interferometer, the number of data, the average value of the vacuum wavelength, and the standard deviation, respectively.

	L	n	$\bar{\lambda}_{H_2CO}$ (pm)	σ_{n-1} (pm)	$\sigma_{n-1}/\bar{\lambda}_{H_2CO}$
A-(1)	10 cm	10	3 507 978.87	0.12	3.4×10^{-8}
A-(2)	10 cm	3	3 507 978.79	0.10	2.9×10^{-8}
B-(1)	20 cm	6	3 507 979.15	0.21	6.0×10^{-8}
B-(2)	20 cm	5	3 507 979.16	0.20	5.7×10^{-8}

different days. A-(1) and A-(2) represent the results when the interferometer of length 10 cm was used, and the number of data are 10 and 3, respectively. The accuracies of these results are about 3×10^{-8}. B-(1) and B-(2) represent the results when the interferometer of length 20 cm was used, and the numbers of data are 6 and 5, respectively. The accuracies of these results are about 6×10^{-8}.

A difference of about 0.3 pm can be seen between the average value $\bar{\lambda}_{H_2CO}$ of the wavelength of series A and that of series B. This is caused by the dispersion of the phase change at the reflection on the mirrors of the interferometer. The virtual spacer method was used to compensate for this dispersion effect,[10] i.e., the order of interference for the virtual spacer was calculated by subtracting the order of interference for the 10 cm length interferometer from that of the 20 cm length interferometer. Then the wavelength λ_{H_2CO} was calculated from eq. (2):

$$\lambda_{H_2CO}=\lambda_{CH_4}\cdot(m_{CH_4,20}-m_{CH_4,10})/(m_{H_2CO,20}-m_{H_2CO,10}), \quad (2)$$

where the suffices 10 and 20 represent the quantities for the 10 cm and 20 cm length interferometers, respectively.

By using the results of Table I and eq. (2), the final result was obtained:

$$\bar{\lambda}_{H_2CO}=3\,507\,979.48 \text{ pm},$$
$$\sigma_{n-1}=0.39 \text{ pm}, \quad (3)$$

where the number of data n is 143 because 13 data for the 10 cm length interferometer and 11 data for the 20 cm length interferometer were combined. As the value of the standard deviation σ_{n-1} in eq. (3) is 0.39 pm, the accuracy of the final result is

$$\sigma_{n-1}/\bar{\lambda}_{H_2CO}=1.1\times10^{-7}. \quad (4)$$

Figure 3 shows the distribution of the 143 combined data.

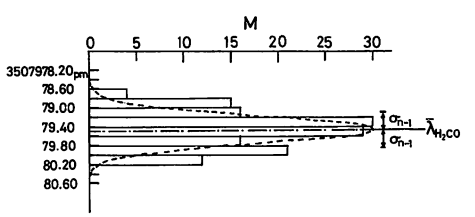

Fig. 3. Distribution of 143 combined data. M represents the numbers of data found in intervals of 0.20 pm. The broken line represents the Gaussian probability function whose average value and standard deviation is equal to $\bar{\lambda}_{H_2CO}$ and σ_{n-1} of eq. (3), respectively.

§4. Discussions

The value of $\bar{\lambda}_{H_2CO}$ in eq. (3) contains systematic errors. The possible sources of systematic errors are;

(1) The effect of diffraction,

(2) nonparallelism between the planes of the two mirrors of the interferometer,

(3) nonparallelism between the He–Xe and He–Ne (3.39 μm) laser beams. The values of systematic errors due to these sources are estimated in this section.

(1) Figure 4 shows the experimental results of the interference fringes and the least-squares-fitted Lorentzians for the three lasers. Comparing two curves for each laser, it can be seen that the experimental curves are asymmetric. One of the sources of this asymmetry is that higher-order transverse modes were generated in the interferometer by diffraction and the fringes of these modes were superposed on that of the (0, 0) transverse mode. The other possible source is discussed in (2). As the line shape of the interference fringe is asymmetric, the value of the order of interference at the peak of the fringe is shifted from the true value. Therefore, a systematic error occurs. The value of this error is estimated in the following.

As the intensity of the (0, 1) mode is the highest among those of higher-order transverse modes, and as the contributions to the value of this error from other modes were estimated to be about a few percent of that from

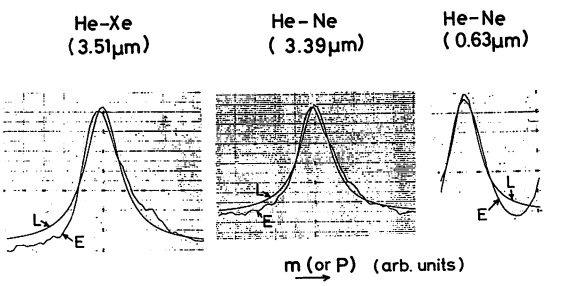

Fig. 4. Line shapes of the experimental result of the interference fringe (E) and the least-squares-fitted Lorentzian (L) for each laser. P represents the pressure in the interferometer and m the order of interference.

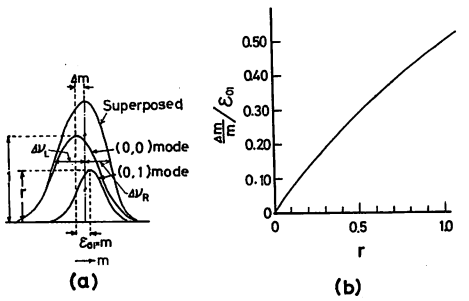

Fig. 5. (a) The definition of Δm, r, ε_{01}, $\Delta\nu_L$, and $\Delta\nu_R$ for the interference fringe composed of the fringes of the (0, 0) and (0, 1) modes. Δm: The difference between the order of interference at the peak of the superposed fringe and that of the (0, 0) mode. r: The ratio of the peak height of the fringe of the (0, 1) mode to that of the (0, 0) mode. $\varepsilon_{01}\cdot m$: The difference between the orders of the interference fringes of the (0, 0) and (0, 1) modes. $\Delta\nu_L$ and $\Delta\nu_R$: The half width at the half maximum on the left and right of the superposed fringe.
(b) The calculated result of the relation between Δm and r.

the (0, 1) mode, only the (0, 1) mode is considered in the following discussion. Figure 5(b) shows the calculated result of the shift Δm of the order of interference at the peak of the fringe which is composed of the fringes of the (0, 0) and (0, 1) modes. In this figure, r represents the ratio of the peak height of the fringe of the (0, 1) mode to that of the (0, 0) mode, and $\varepsilon_{01}\cdot m$ represents the difference of the order of interference between the fringes of these modes. ε_{01} is expressed as

$$\varepsilon_{01}=\frac{9}{128}(\lambda/A)^2, \tag{5}$$

where λ and A represent the wavelength and the radius of the laser beam, respectively.[11] It was necessary to estimate the value of r in order to find the value of Δm. This was done as follows: first, the ratio of $\Delta\nu_L$ to $\Delta\nu_R$ was obtained for the calculated asymmetric interference fringe, where $\Delta\nu_L$ and $\Delta\nu_R$ represent the values of the half-width at the half-maximum on the left and right of the fringe respectively, as shown in Fig. 5(a) This value of the ratio $\Delta\nu_L/\Delta\nu_R$ was then compared with that of the experimental result of the fringe. From this comparison, the value of r was estimated to be $0\leqq r\leqq 0.3$ for the He–Xe and He–Ne (3.39 μm) lasers. It was rather difficult to estimate this value more accurately because of the noise contained in the line shapes of the fringe. From this value, the value of Δm was estimated to be $0\leqq\Delta m\leqq 0.19\ \varepsilon_{01}\cdot m$ by using Fig. 5(b). Therefore, by using eq. (5), the values of $\Delta m/m$ for the He–Xe and He–Ne (3.39 μm) lasers were estimated to be

$$0\leqq\Delta m_{H_2CO}/m_{H_2CO}\leqq 7.2\times10^{-8},$$
$$0\leqq\Delta m_{CH_4}/m_{CH_4}\leqq 8.4\times10^{-9}, \tag{6}$$

respectivety, where $A=1.5$ mm was used for the He–Xe laser and $A=4.3$ mm was for the He–Ne laser (3.39 μm).

Since the final result of eq. (3) was obtained from the results obtained using the 10 cm and 20 cm length interferometers, the systematic errors contained in these results have to be used to estimate the systematic error in the final result. This is done in the following. The systematic error $\Delta\lambda_{H_2CO}$ in λ_{H_2CO} of eq. (2) is expressed as

$$\Delta\lambda_{H_2CO}/\lambda_{H_2CO}$$
$$=(\Delta m_{CH_4,20}-\Delta m_{CH_4,10})/(m_{CH_4,20}-m_{CH_4,10})$$
$$-(\Delta m_{H_2CO,20}-\Delta m_{H_2CO,10})$$
$$/(m_{H_2CO,20}-m_{H_2CO,10}). \tag{7}$$

By substituting the following relations

$$m_{CH_4,20}\cong 2\cdot m_{CH_4,10},$$
$$m_{H_2CO,20}\cong 2\cdot m_{H_2CO,10}, \tag{8}$$

into eq. (7) and using eq. (1), the value of $\Delta\lambda_{H_2CO}/\lambda_{H_2CO}$ is expressed as

$$\Delta\lambda_{H_2CO}/\lambda_{H_2CO}\cong 2(\Delta\lambda_{H_2CO}/\lambda_{H_2CO})_{20}$$
$$-(\Delta\lambda_{H_2CO}/\lambda_{H_2CO})_{10}, \tag{9}$$

where $(\Delta\lambda_{H_2CO}/\lambda_{H_2CO})_{20}$ and $(\Delta\lambda_{H_2CO}/\lambda_{H_2CO})_{10}$ represent the values of the systematic errors in the results obtained by using the 10 cm and 20 cm length interferometers, respectively. As these values are calculated to be

$$-6.8\times10^{-8}\leqq(\Delta\lambda_{H_2CO}/\lambda_{H_2CO})_{20}$$
$$=(\Delta\lambda_{H_2CO}/\lambda_{H_2CO})_{10}\leqq 0, \tag{10}$$

by using eqs. (1) and (6), the value of the systematic error, represented now as $\Delta\lambda_{H_2CO,1}$ caused by diffraction is estimated to be

$$-0.24\ \text{pm}\leqq\Delta\lambda_{H_2CO,1}\leqq 0, \tag{11}$$

by using eqs. (9) and (10). This is the final result of the estimation.

(2) When the planes of the two mirrors of the interferometer are not parallel, the line shapes of the fringe are asymmetric, and a systematic

error would appear in the orders of interference at the peaks of the fringes. The relation between the value of this error Δm and the angle α between the two mirrors has already been calculated.[12] In the present work, the values of α were measured as 4×10^{-4} rad for both lengths of interferometers by using a laser interferometer (HP5526A). Using these values of α and the relation calculated in ref. 12, the value of Δm was easily estimated, and then, the value of the systematic error $\Delta\lambda_{H_2CO,2}$ was found to be

$$\Delta\lambda_{H_2CO,2}=0.004\text{ pm}. \tag{12}$$

Equation (9) was also used in this estimation.

(3) When the optical axes of the He–Xe and He–Ne (3.39 μm) lasers are not parallel, a systematic error occurs because the length of the interferometer is different for the two laser beams. In experiments A-(1), A-(2), B-(1), and B-(2) in Table I, the values of $1-\cos\theta$ were measured as 4.82×10^{-9}, 5.06×10^{-9}, 4.90×10^{-9}, and 5.16×10^{-9}, respectively, where θ represents the crossing angle between the two laser beams. This angle was measured by scanning the position of the InAs detector of the 0.02 mm^2 active area. By using these results, the value of the systematic error $\Delta\lambda_{H_2CO,3}$ was found to be

$$\Delta\lambda_{H_2CO,3}=0.02\text{ pm}, \tag{13}$$

where eq. (9) was also used.

In the present experiment, as shown in Fig. 4 of §2, the signal-to-noise ratio of the interference fringe was rather low because of the low intensities of the laser beams. Therefore, it can be seen that the main cause of the accidental error in the value of $\bar{\lambda}_{H_2CO}$ of eq. (3) was this noise. However, a full quantitative estimation of the accidental error caused by this noise has not yet been done. If the intensities of the lasers are increased while their high-frequency stabilities are maintained, the accidental error would be decreased and, as a result, the value of σ_{n-1} in eq. (3) would be decreased. Furthermore, the value of $\Delta\lambda_{H_2CO,1}$ of eq. (11) would be more accurately estimated.

The frequency estimated by using the value of $\bar{\lambda}_{H_2CO}$ of eq. (3) is

$$\nu_{H_2CO}=85\ 460\ 151.6\text{ MHz}, \tag{14}$$

where 299 792 458 m/s[9] was taken as the speed of light. Therefore, the difference between this value and the frequency ν_{Xe} of the free-running He–Xe laser is

$$\nu_{H_2CO}-\nu_{Xe}=155\text{ MHz}, \tag{15}$$

where

$$\nu_{Xe}=85\ 459\ 997\text{ MHz}.^{3)} \tag{16}$$

As the value of this difference reported by M. Takami and K. Shimoda is about 180 MHz,[13] the value of eq. (15) agrees with it within the difference caused by the pressure shift in ν_{Xe}.

§5. Conclusion

The average value $\bar{\lambda}_{H_2CO}$ of the vacuum wavelength of the H_2CO-stabilized He–Xe laser was 3 507 979.48 pm. The standard deviation σ_{n-1} was 0.39 pm and, therefore, the accuracy $\sigma_{n-1}/\bar{\lambda}_{H_2CO}$ was 1.1×10^{-7}. It was estimated that the values of the systematic error were

$$-0.24\text{ pm}\leqq\Delta\lambda_{H_2CO,1}\leqq0,$$
$$\Delta\lambda_{H_2CO,2}=0.004\text{ pm},$$
$$\Delta\lambda_{H_2CO,3}=0.02\text{ pm},$$

where $\Delta\lambda_{H_2CO,1}$, $\Delta\lambda_{H_2CO,2}$, and $\Delta\lambda_{H_2CO,3}$ represent the errors caused by diffraction, nonparallelism between the interferometer mirrors, and nonparallelism between the two laser beams, respectively. It was discussed that the main cause for the accidental error was the noise in the low laser intensity measurements. The value of σ_{n-1} will decrease if this noise is suppressed while the high-frequency stabilities are maintained.

Acknowledgements

The authors are much indebted to Prof. Dr. A. Toyama and Dr. A. Shimokobe of Tokyo Institute of Technology for their help with the preliminary measurements of the spacer length of the interferometer.

This work was partially supported by a Grant-in-Aid for Scientific Research from the Ministry of Education, Science and Culture.

References

1) M. Ohtsu and T. Tako: Jpn. J. Appl. Phys. **17** (1978) 2169.
2) M. Ohtsu, R. Koyama and T. Tako: Jpn. J. Appl. Phys. **18** (1979) 1621.
3) D. A. Jennings, F. R. Petersen and K. M. Evenson: Appl. Phys. Lett. **26** (1975) 510.
4) K. Sakurai, K. Uehara, M. Takami and K.

Shimoda: J. Phys. Soc. Jpn. **23** (1967) 103.
5) G. R. Hanes and K. M. Baird: Metrologia **5** (1969) 31.
6) R. L. Barger and J. L. Hall: Appl. Phys. Lett. **22** (1973) 196.
7) D. W. Allan: Proc. IEEE **54** (1966) 221.
8) M. Ohi and Y. Akimoto: Jpn. J. Appl. Phys. **15** (1976) 1853.
9) Comité Consultatif pour la Définition du Mètre: 5e Session, Rapport, (Bureau Internationale des Poids et Mesures, Sèveres, France, 1973).
10) N. Ito and K. Tanaka: Metrologia **14** (1978) 47.
11) N. Ito and K. Tanaka: Rep. NRLM **28** (1979) 63.
12) K. Toyoda and Y. Sakurai: Rep. NRLM **20** (1971) 23.
13) M. Takami and K. Shimoda: Jpn. J. Appl. Phys. **11** (1972) 1648.

Reprinted from **Applied Optics,** Vol. 19, page 1227, April, 1980

Measurement of the saturated absorption signal of CH_4 at 3.39 μm using a He–Ne laser and a multipath cell

Anung Kusnowo, Motoichi Ohtsu, Naoki Kobayashi, and Toshiharu Tako

Tokyo Institute of Technology, Research Laboratory of Precision Machinery & Electronics, 4269 Nagatsuta-cho, Midori-ku, Yokohama, Kanagawa 227, Japan

Received 26 November 1979.
0003-6935/80/081227-03$00.50/0.

We report the results of measurement of the saturated absorption signal of CH_4 at 3.39 μm using an external absorption cell in a multipath (White-cell)[1] configuration. The laser used was a pressure-shifted He–Ne laser at 3.39 μm.[2] Measurement of the saturated absorption signal in an external cavity with a White-cell configuration has been carried out before for phosphine.[3] In this experiment, we investigated the case of CH_4. We measured the dip height (ΔI) and width ($\Delta\nu$, FWHM) to be compared with the calculated predictions as a function of ϕ, the crossing angle between the two oppositely propagating beams; G, the saturation parameter; and $r_{1/e}$, the beam radius.

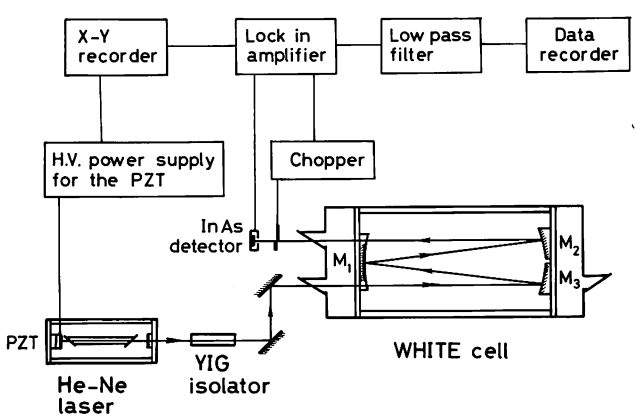

Fig. 1. Experimental setup.

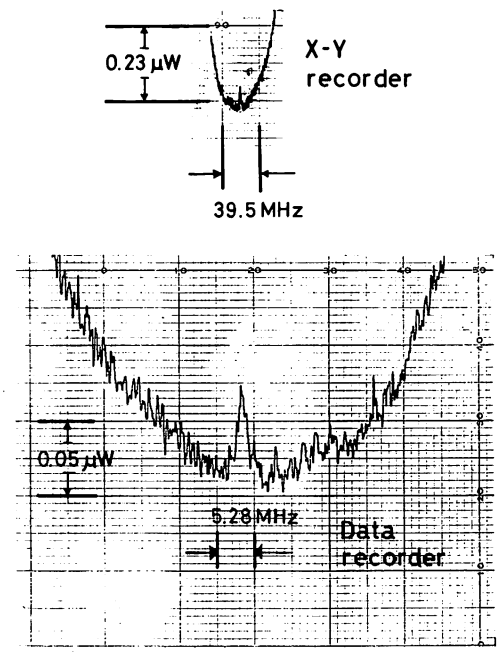

Fig. 2. An example of the experimental result of the dip, from playback of the data recorder.

The experimental apparatus is shown in Fig. 1. The laser was sealed off at a total pressure of 6 Torr and He:Ne = 10:1; under these conditions, the CH_4 absorption line nearly coincides with the laser line. The laser was operated under free-running conditions; typical stability is $\Delta\nu/\nu = 1 \times 10^{-10}$ at 1-sec integration time.[4] The power output of this laser at a discharge current of 8 mA was about 650 μW. To prevent the reflected beam from disturbing the stability of the discharge, we used a YIG optical isolator. The White cell was a Pyrex tube 18 cm in diameter and 160 cm in length. The distance between mirrors M_1 and M_2 or M_3 was set at 1 m, the same length as the radius of curvature of the mirrors.

The dip was observed by scanning the laser line around the center frequency of the CH_4 line. A typical result of the inverted Lamb dip is presented in Fig. 2. The height of the inverted Lamb dip is determined by the intensity of the laser beam and the number of the absorbing molecules in the standing-wave region where the two opposing beams cross.

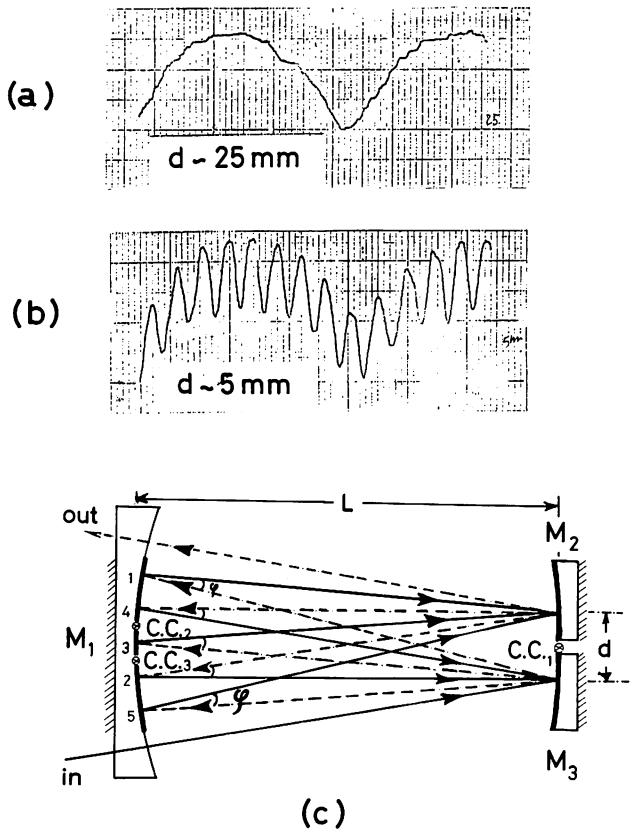

Fig. 3. (a), (b) Interference patterns for d = 25 and 5 mm, respectively. (c) Trajectory for N = 6. ϕ is the crossing angle; $C.C._1$, $C.C._2$, and $C.C._3$ are the center curvature of M_1, M_2, and M_3. Bold and dashed lines correspond to the right and left directions, respectively.

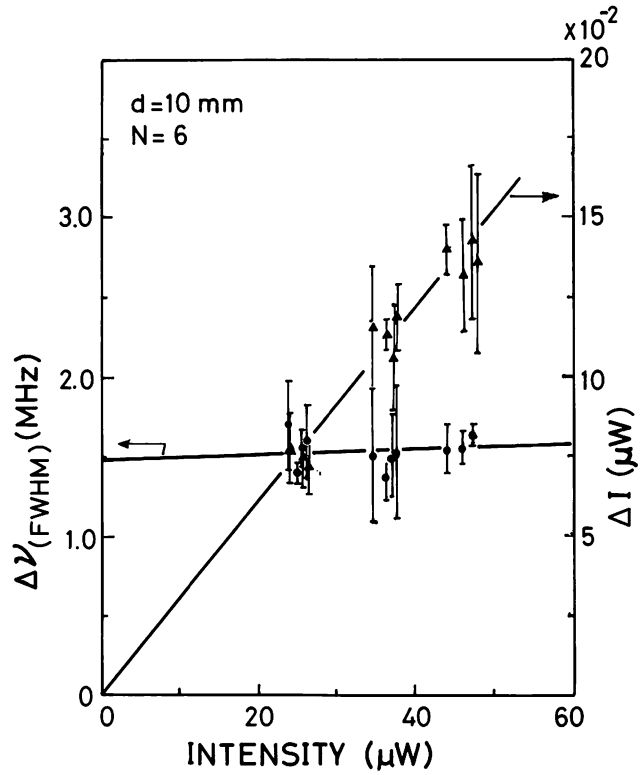

Fig. 4. Width $\Delta\nu$ (FWHM) and height ΔI of the inverted Lamb dip as a function of the intensity. Solid lines represent least-squares fit of the experimental data.

The dip height is inversely proportional to the square of the crossing angle ϕ and the beam radius $r_{1/e}$.[5] The crossing angle ϕ [see Fig. 3(c)] can be expressed as $\phi \approx (d/L)$ rad, where L is the distance between M_1 and M_2 or M_3, and d is the distance between the two beam spots at M_2 and M_3. However, in an attempt to reduce ϕ, i.e., to make d small we observed that when d was less than ~6–8 mm, there will be an interference pattern in the output power of the tuning curve, possibly because of the interference between the first reflected beam (no. 1) and the output beam, as can be seen in Fig. 3(c). This effect did not happen for N = 2 or 4, where N is the number of passes between the mirrors in the White cell. The interference patterns for several values of d are presented in Fig. 3.

Experimental results of $\Delta\nu$ and ΔI are presented in Fig. 4. To calculate the peak contrast $H = (\Delta I)/I$, where I is the laser intensity, we have to know the saturation parameter G, defined as $G \equiv P/P_s$, where P and P_s are the laser power and the saturation power, respectively. The saturation power can be expressed as[6]

$$P_s = \frac{\epsilon_0 c \hbar^2 \gamma A}{2\mu_s^2 \tau}, \tag{1}$$

where A is the cross section of the laser beam; γ and τ are the transverse and longitudinal relaxation rate, respectively; μ_s is the dipole moment of the transition; c is the speed of light, $\hbar$ is the Planck constant, and ϵ_0 is the permittivity of free space. In this experiment the average beam radius was calculated to be 1.3 mm. Assuming that $\gamma = \tau^{-1}$ and using the value of $\gamma = \tau^{-1} = 7 \times 10^5$ rad/sec for p = 7.5 mTorr[6] and the dipole moment μ_s = 0.03 D, from Eq. (1) P_s was found to be 3.69 mW. Since at pressure p = 7.5 mTorr the laser power was 23.9 μW, the saturation parameter G was 6.5×10^{-3}. The peak contrast H for the case of oppositely directed waves can be expressed as[7]

$$H = 1 - (1 + G)^{-1/2}. \tag{2}$$

Therefore, using G as calculated above, H was found to be 0.32%. From the experimental result we found that H at p = 7.5 mTorr was 0.3%, which agrees well with the calculated prediction.

For calculation of the width $\Delta\nu$, there are several contributions that must be considered.

(1) Because of the saturation, the resonance width is broadened, which can be expressed as[7]

$$\Delta\nu_{(\mathrm{FWHM})} = \frac{1}{2\pi}\Delta\omega = \frac{2\Gamma}{2\pi} f_p, \tag{3}$$

where 2Γ represents the homogeneous FWHM of the transition, and f_p is the power-broadening factor, which can be expressed approximately as[7]

$$f_p = (1 + G)^{1/2}. \tag{4}$$

For $G = 6.5 \times 10^{-3}$, $f_p \sim 1 + \frac{1}{2}G = 1.003$. Using the value of $2\Gamma = 4 \times 10^5$ rad/sec at p = 7.5 mTorr,[8] $\Delta\nu$ is calculated to be 64 kHz.

(2) Since in this experiment the beam radius $r_{1/e} = 1.3$ mm, the transit time broadening, which can be expressed as[7]

$$\Delta\nu_{tr} = \frac{1}{2\pi}\Delta\omega_{tr} = \frac{0.58u}{\pi r_{1/e}}, \tag{5}$$

was calculated to be 79 kHz by using the average speed of the CH_4 molecule at 20°C as $u = 5.57 \times 10^4$ cm/sec.

(3) The geometrical broadening was dominant because of the large value of ϕ,

$$\Delta\nu_g = \frac{1}{2\pi}\Delta\omega_g = \frac{u}{\lambda}\phi, \tag{6}$$

where λ is the wavelength of the laser. For $d = 10$ mm, the crossing angle ϕ was 10 mrad, and $\Delta\nu_g$ was found to be 1.64 MHz. The total contributions to the broadening were $\Delta\nu$ = (1.640 + 0.079 + 0.064) MHz = 1.78 MHz.

As presented in Fig. 4, we observed that $\Delta\nu = (1.50 \pm 0.19)$ MHz, which agrees quite well with the prediction; the difference may be due to the inaccuracy in the determination of d.

To summarize, we have reported here our results on the measurement for the first time of the inverted Lamb dip in an external absorption cell with a dip width of $\Delta\nu_{(FWHM)}$ = 1.50 MHz at CH_4 pressure of 7.5 mTorr. This result can be applied to laser frequency stabilization.

This work was partially supported by a Grant-in-Aid for Scientific Research from the Ministry of Education, Japan. A scholarship from the Ministry of Education, Japan, given to one of the authors (A.K) during this work is gratefully acknowledged.

References

1. J. U. White, J. Opt. Soc. Am. **32,** 285 (1942).
2. M. Ohi, Jpn. J. Appl. Phys. **12,** 1377 (1973).
3. F. Shimizu, H. Shwe, and T. Tamayama, J. Appl. Phys. **46,** 258 (1975).
4. K. Shimoda and T. Tako, in *Proceedings, Second Frequency Standards & Metrology Symposium, Copper Mt. U.S.A.* (1976), p. 187.
5. F. Shimizu, Jpn. J. Appl. Phys. **14,** 521 (1975).
6. K. Shimoda, Jpn. J. Appl. Phys. **12,** 1222 (1973).
7. V. S. Letokhov, in *High-Resolution Laser Spectroscopy,* K. Shimoda, Ed. (Springer, New York, 1976).
8. S. N. Bagaev, E. V. Baklanov, and V. P. Chebotayev, Pis'ma Zh. Eksp. Teor. Fiz. **16,** 15 (1972).

報　文 2

3.51 μm He-Xe レーザーの発振特性
——ファブリー・ペロー共振器型および導波路型——

大津元一・三田村一郎*・田幸敏治

東京工業大学精密工学研究所　横浜市緑区長津田 4259（〒 227）
* 現在は東京工業大学電子物理工学科，東京都目黒区大岡山 2-12-1（〒152）

(1979年8月27日受理)

Oscillating Characteristics of He-Xe lasers at 3.51 μm
—A Fabry-Perot Resonator-Type and Waveguide-Type—

Motoichi OHTSU, Ichiro MITAMURA* and Toshiharu TAKO

Research Laboratory of Precision Machinery and
Electronics, Tokyo Institute of Technology,
4259 Nagatsuta, Midori-ku, Yokohama 227
* Now at Department of Physical Electronics, Tokyo Institute of Technology, 2-12-1
O-okayama, Meguro-ku, Tokyo 152

(Received August, 1979)

By using a Ti cold-cathode and a gas return path, stable laser oscillation was obtained in a Fabry-Perot resonator-type and a waveguide He-Xe lasers at 3.51 μm. The relations between the laser output power and the total gas pressure, the pressure ratio of Xe gas to the total gas, and the discharge current were measured for the both type of lasers. It became clear that lower pressure and higher discharge current were required for the waveguide laser than for the Fabry-Perot resonator-type laser to get the highest output power when the same value of the pressure ratio was used.

Two types of waveguide laser were constructed by considering the coupling efficiency of the EH_{11} mode at the edge of the hollow waveguide. The oscillating characteristics of these two types of waveguide laser were measured and compared with each other.

1. まえがき

Xe の 5d-6p 遷移は波長 2.03 μm から 5.58 μm の範囲で数本のレーザー発振が可能であることが知られている[1]．とくにこのうちの 3.51 μm 発振線に関しては He を Xe に混合するとペニング効果[2]などによりレーザー出力が増加するので，しばしば He を混合して用いられている．この He-Xe レーザーの出力特性や発振機構については多くの報告があるが[3-6]，このレーザーは必ずしも広く用いられていない．この理由としてはとくに，直流放電中に起こる He-Xe との分離，さらに管壁面への Xe の clean-up による出力変動が挙げられる．従来は高周波放電を用いて分離を防ぎ[1]，また Xe ガスだめを用いて clean-up による Xe 圧力の減少分を補なっていたが[4]，装置が大がかりになること，出力変動の抑制がまだ不十分であることなどの欠点があった．

このレーザーを分光用光源として用いるときには長時間にわたり一定出力で発振する必要があるので少なくともまず上記のガス分離，clean-up の効果を消去する必要がある．さらに出力の低雑音化，高出力化，周波数変

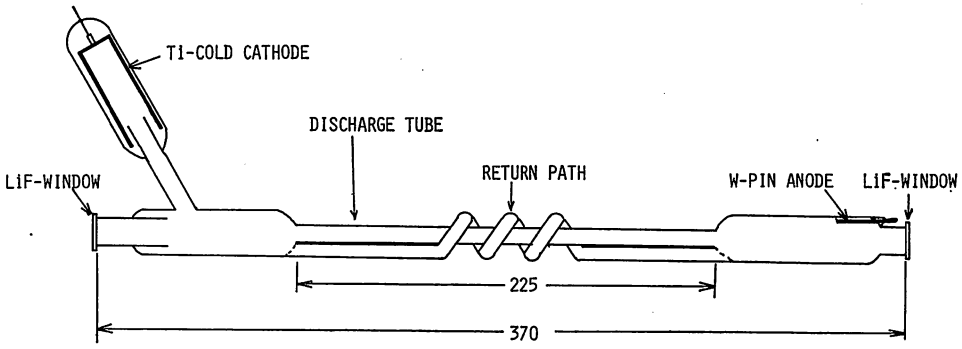

Fig. 1. The discharge tube for the Fabry-Perot resonator-type laser.

動の低減，なども実現しなければならず，そのためにはレーザー管の改良，および出力と各種放電パラメータとの関係を明らかにする必要がある．

本論文では H_2CO の反転ラムくぼみ測定[7]，それを用いた He-Xe レーザー周波数の安定化[8-10]，などを行なうために製作した He-Xe レーザーの発振特性について報告する．ここではファブリー・ペロー共振器型のレーザーの特性，および導波路型レーザーの特性について述べる．特に後者については 10.6 μm CO_2 レーザー[11]など主に赤外，遠赤外領域での報告がすでに多くあり，その特長は小型ながらも高出力が得られることである．3.51 μm He-Xe レーザーでも導波路型のものができれば小型のために周囲環境の変動（温動変化，空気の対流，機械的振動など）の影響をうけにくく，かつ高出力の発振をするものができる可能性がある．導波路型 He-Xe レーザーについてはその発振の報告があるが[12]，出力と各種放電パラメータとの関係についての報告は十分でない．そこで本論文では上記のようにファブリー・ペロー共振器型のレーザーとともに，導波路型レーザーを製作しその特性を測定したのでその結果について述べた後，両者を比較する．

2. ファブリー・ペロー共振器型レーザー

2.1 実験装置

製作したレーザー管の形を Fig. 1 に示す．放電部分の内径は 3 mm，長さ 225 mm である．直流放電中の He と Xe との分離を防ぐために放電管両端をむすぶリターンパスを設けた．その形状は内径 3 mm，長さ 320 mm のらせん管である．陽極は直径 1 mm のタングステン (W) 棒である．陰極は内径 16 mm，外径 19 mm，長さ 60 mm のチタン (Ti) 管を用いた冷陰極である．このレーザーは H_2CO の反転ラムくぼみ測定[7]，それを用いた周波数安定化[8-10]のために作られたものであり，レーザー管軸方向に約 130 G の直流磁場を加えて円偏光を得る必要があるので[13]レーザー管両端の窓板は光軸と垂直になっている．この窓板は厚さ 2 mm の LiF である．ファブリー・ペロー共振器を構成する 2 枚の反射鏡は曲率半径 2 m の熔融石英基板上に 3.51 μm の光に対する反射率が 100%，90% となるように誘電体多層膜を蒸着したものを用いた．これらは直径 20 mm のインバー棒 4 本によって構成されたレーザー架台の両端のフランジ上に対面して設置された．共振器長は 55 cm である．放電は直流安定化電源 (FLUKE 415 B) を用いて行なった．レーザー出力はパワーメーター（日本高周波 LPM-1 K) で校正された InAs 検出器 (Judson J-12 LD 受光面積 0.02 mm^2)，400 Hz チョッパ，およびロックインアンプを用いて測定した．共振器を構成する 2 枚の反射鏡の一方は電歪素子 (PZT) 上に設置し，これに電圧を加えることによりレーザーの出力同調曲線を測定した．そしてこの出力同調曲線の中心周波数での出力 I の値と放電電流 i_d，気体全圧力 P_T，P_T に対する Xe 圧力の割合 k との関係を測定した．なお，本報告の測定の際には管軸方向の直流磁場は加えていない．

2.2 実験結果

リターンパスのないレーザー管を用いると直流放電開始直後すぐ He と Xe との分離が始まり，5 分以内に放電の色が陽極側と陰極側とで異なってくる様子が肉眼で観察された．これに伴ない放電電流，レーザー出力の値も減少した．しかし Fig. 1 に示すようなリターンパスを用いるとそのような色の変化は肉眼では認められなくなり，He と Xe との分離を防ぐことは一応解決された．しかし He と Xe との分離の問題が解決されても clean-up の効果により放電電流，レーザー出力の値はやはり時間とともに減少する．従来の報告[1]では clean-

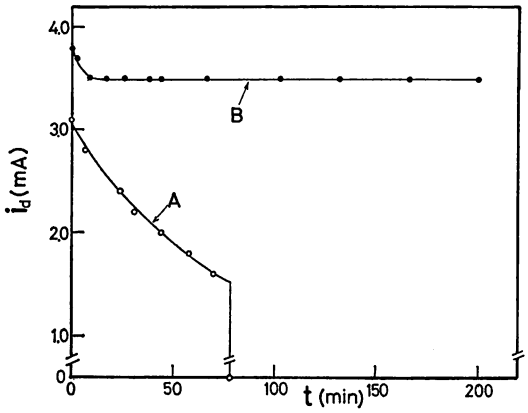

Fig. 2. The time dependence of a discharge current i_d.

A: The result when an Al-cold cathode was used.

B: The result when a Ti-cold cathode was used.

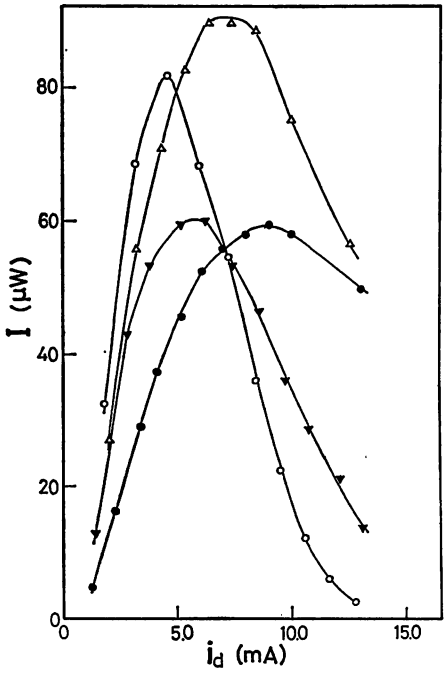

Fig. 3. The relation between the laser power intensity I and the discharge current i_d. The ratio k of Xe gas pressure to the total gas pressure P_T was 0.021.

●; P_T=2.50 Torr, △; P_T=4.60 Torr,
▼; P_T=7.30 Torr, ○; P_T=9.84 Torr.

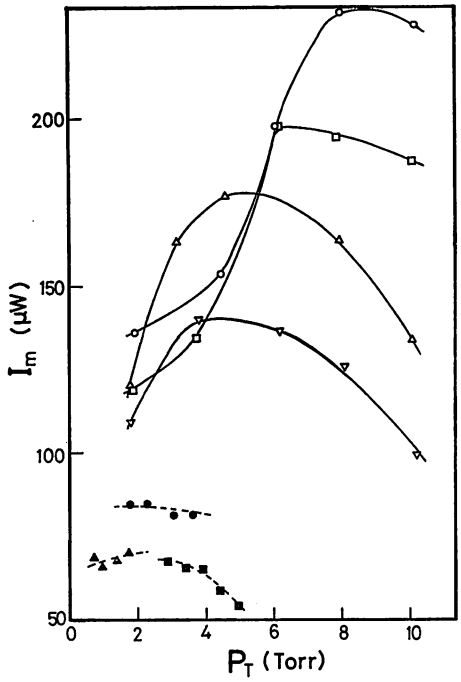

Fig. 4. The relation between I_m and the total gas pressure P_T, where I_m represents the peak value on the curve of I vs. i_d as in Fig. 3. The solid and broken lines represent the results for the Fabry-Perot resonator-type laser and for the waveguide laser (II), respectively.

▽; k=0.003, ○; k=0.005, □; k=0.009,
△; k=0.016, ■; k=0.009, ●; k=0.002,
▲; k=0.046.

up の効果により放電開始後放電電流は単調に減少し，従ってレーザー出力も減少して 30 分後にはレーザー出力は放電開始直後の 1/10 の値になるという例もある．著者らの場合の例として Fig. 1 に示すレーザー管に対し Al の冷陰極（その形状は **2.1** に示した Ti のものと同じ）を用いたときの放電電流の時間変化の測定結果を Fig. 2 の曲線 A に示す．これによると単調減少のようすが明らかであり，レーザー出力も同様に単調減少し，clean-up の影響を受けていることがわかる．しかし Al のかわりに Ti を用いると Fig. 2 の曲線 B に示すように放電開始後約 10 分で放電電流は一定値に達し，それに伴ないレーザー出力も一定になった．Ti を用いるとなぜ clean-up の効果の影響がなくなり，放電電流が一定になるのかは現在ではまだ不明であるが，結果的には Ti 冷陰極を用いることにより安定なレーザー発振を得ることができた．

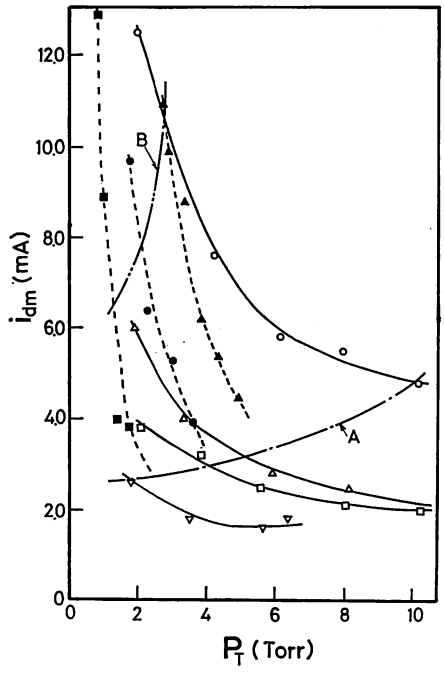

Fig. 5. The relation between i_{dm} and P_T, where i_{dm} represents the discharge current for the peak value of I (i. e., I_m) on the curve of I vs. i_d. The solid and broken lines are for the Fabry-Perot resonator-type laser and the waveguide laser (II), respectively.

○; k=0.010, △; k=0.021, □; k=0.074, ▽; k=0.097, ▲; k=0.009, ●; k=0.020, ■; k=0.046.

The curves A and B represent the relation between i_{dm}, P_T, and k at which I_m takes the peak value I_{mo} on the curve of I_m vs. P_T.

A: The Fabry-Perot resonator-type laser.

B: The waveguide laser (II).

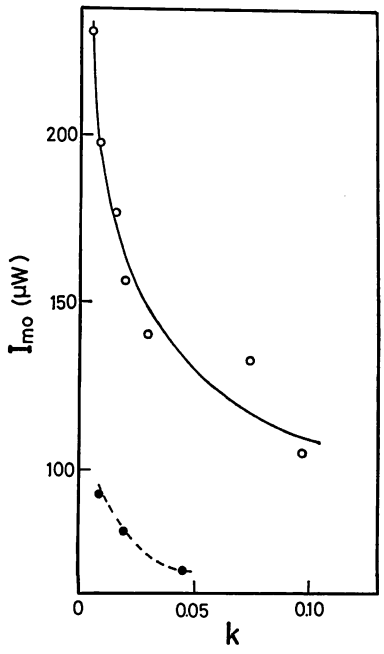

Fig. 6. The relation between I_{mo} and k, where I_{mo} represents the peak value on the curve of I_m vs. P_T. The solid and broken lines are for the Fabry-Perot resonator-type laser and for the waveguide laser (II), respectively.

次にこのレーザーの出力 I と i_d, P_T, k との関係の測定結果を示す. ここでの測定に使用した i_d, P_T, k の値の範囲は次のとうりである.

$$\left.\begin{array}{c} i_d \leqq 18\ \mathrm{mA} \\ 2\ \mathrm{Torr} \leqq P_T \leqq 12\ \mathrm{Torr} \\ 0.003 \leqq k \leqq 0.100 \end{array}\right\} \qquad (1)$$

(1) の範囲外では出力 I に含まれる雑音が大きいか, または出力 I の値が小さくて定量的な測定が不可能であった. Fig. 3 には k=0.021 のときの I と i_d との関係を P_T をパラメータとして示した. Fig. 3 の各曲線では i_d のある値 i_{dm} において I は最大値 I_m をとるのでこの I_m と P_T との関係を k をパラメータとして Fig. 4 に示した. また i_{dm} と P_T との関係を k をパラメータとして Fig. 5 に示した. なお, Fig. 4 の各曲線でも P_T のある値 P_{Tm} において I_m が最大値 I_{mo} をとる. そのときの P_{Tm} と i_{dm}, k との関係を Fig. 5 中の曲線 A で示した. また, I_{mo} と k との関係を Fig. 6 に示した.

また, 出力 I に含まれる雑音の大きさを定性的に調べた. これは XY レコーダ上に記録した出力同調曲線に含まれる雑音の振幅の値 ΔI_n から判断したものであるが次のような傾向が得られた.

(A) ΔI_n の値は k の値に反比例する.

(B) $i_d \leqq 3$ mA, 12 mA$\leqq i_d$ の範囲, または $P_T \geqq 8$ Torr の範囲では次式が成り立つ.

$$\Delta I_n / I \geqq 0.02 \qquad (2)$$

2.3 考 察

Fig. 5, Fig. 6 により高出力を得るための i_d, P_T, k の値の間の相互関係が明らかになる. すなわち Fig. 5

により

$$i_{dm} \propto P_T^{-l} \quad (3)$$

$$i_{dm} \propto k^{-m} \quad (4)$$

$$P_{Tm} \propto k^{-n} \quad (5)$$

が成り立ち，また Fig. 6 より

$$I_{mo} \propto K^{-p} \quad (6)$$

が成り立つことがわかる．ここで右辺の l, m, n, p の値は Fig. 5, Fig. 6 により，ほぼ1に近い値であると考えられる．

(6) 式に従い，I_{mo} の値を大きくするため k の値を小さくすると **2.2** の (A) に示したように雑音の振幅も大きくなる．従って，たとえば H_2CO の飽和吸収スペクトルを測定する場合のように高出力かつ低雑音発振を実現するには k の値を適切に選ぶことが重要である．H_2CO の飽和吸収信号の最大値はレーザー出力 I のほぼ1%であり．このような小信号を観測するために著者ら[7]は

$$k=0.020 \quad (7)$$

とし，さらに $P_T=4.0$ Torr, $i_d=4\sim6$ mA の値を用いた．

3. 導波路型レーザー

3.1 実験装置

まず，導波路型レーザーの設計方法について述べる．中空導波路を伝搬する光の横モードが最低次のモード，すなわち EH_{11} モードとなるために，このモードの伝搬損失を最小にするような中空導波路の材質としては屈折率 $n<2.02$ であればよいことが知られている[14]．ここではそのような材質としてパイレックスガラスを用いた．そしてこの中空導波路を共振器内に設置したとき，反射鏡からの光が中空導波路に入射する際の結合効率を最大にする方針で中空導波路，共振器を設計した．

中空導波路の内半径 a，共振器用の円形反射鏡の面半径 b，曲率半径 c，中空導波路端と反射鏡との距離 d の関数としての結合効率の値がすでに Degman と Hall によって数値計算されている[15]．すなわち結合効率の値は $\alpha\ (=ka^2/c)$, $\beta\ (=d/c)$, $\gamma\ (b/a)$ (ただし k は光の波数) の値に依存しており，文献 15 の Fig. 2 では α の値をパラメータとしてこの結合率の値を β の関数として示している．それによると β の値に対し結合効率の値が極大となる場合が次に示すように3つある．

(I) $\beta=1.0$； 結合効率の値は $\beta=1.0$ で鋭いピークをもつ．

(II) $\beta=0.05$； 結合効率の値は $\beta=0.5$ の付近ではゆるやかに変化する．

(III) $\beta=0$； 結合効率の値は $\beta=0$ で鋭いピークをもつ．

このうち (III) は $d=0$，すなわち内部鏡型共振器の場合であるがこれは製作上の困難さ（中空導波路端と反射鏡との接着，反射鏡面の光軸調整など）が伴なうので本研究の場合には採用せず，残りの2つの場合に従って2種類のレーザーを製作した．

Xe 気体の放電による小信号利得は放電管径に反比例し[3]，中空導波路中の光の伝搬損失は中空導波路内径の3乗に反比例する[16]．従って小信号利得と伝搬損失との差，すなわち導波路型レーザーの正味の利得を最大にする中空導波路内半径の a 値が存在する．しかし 3.51 μm の発振線については両者の値と a との関係式中の係数の値が不明であるので a の最適値は直ちに求めることはできない．そこで従来発振の報告がなされている導波路型レーザー (3.39 μm He-Ne レーザー[17], 10.6 μm CO_2 レーザー[11,18,19], 5 μm CO レーザー[20], 3.51 μm He-Xe レーザー[12]) に採用されている a の値を参考にした．それらによると

$$42 \leqq a/\lambda \leqq 314 \quad (8)$$

であり，とくに $a/\lambda=70$ の付近で用いているものが多い．ここで λ は光の波長である．そこでまず上記の(I)の型のレーザーに関し $a \cong 70\lambda$ ($\lambda=3.51$ μm) となるように a の値を設定し $a=250$ μm とした．次にパラメータ α の値を変化させたとき $\beta=1.0$ における結合効率がほぼ最大になるように α の値を選び，その値と a の値とから反射鏡の曲率半径 $c=20$ cm とした．そして β と c の値より中空導波路端と反射鏡との距離 $d=20$ cm とした．一方，共振器長 L はこのレーザーが出力同調曲線の中心周波数付近では単一たてモードで発振するような値に設定した．すなわち，**3.2** で示される出力同調曲線中心周波数では単一たてモードでの値になるようにした．波長 3.51 μm での Xe のドプラー幅 $\Delta\nu_D$ (半値半幅) は約 150 MHz であり，原子間衝突による幅 $\Delta\nu_c$ (半値半幅) は He と Xe との全圧力 P_T (Torr) によって

$$\Delta\nu_c=(3.7+19P_T) \ \text{(MHz)} \quad (9)$$

と与えられている[12]ので **3.2** に示す実験での圧力範囲 ($P_T \leqq 14$ Torr) では $\Delta\nu_c \leqq 270$ MHz である．以上の $\Delta\nu_D$, $\Delta\nu_c$ の値からレーザー媒質のスペクトル線幅は約 300 MHz (半値半幅，$P_T \leqq 14$ Torr) 以下[21]と推定できる．従

	a	c	d	l	α	β
(I)	0.25mm	20cm	20cm	15cm	0.56	1.0
(II)	0.50mm	20cm	10cm	25cm	2.24	0.5

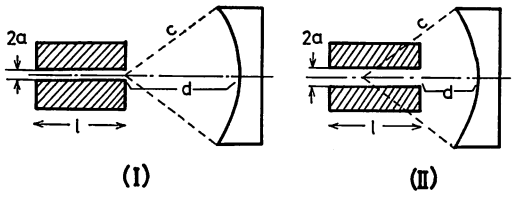

Fig. 7. Waveguide and mirror parameters for the waveguide lasers (I) and (II). a; inner radius of the hollow waveguide, c; radius of curvature of the mirror, d; distance between the hollow waveguide edge and the mirror, l; length of the hollow waveguide, k; wavenumber of the light. $\alpha=ka^2/c$. $\beta=d/c$.

って今の目的では共振器長 L の値は約 50 cm 以下であればよいことがわかる．そして，これを満足するように中空導波路の長さ l $(=L-2d)$ を決めた．

一方（II）の型のレーザーについては（I）と同じ反射鏡 ($c=20$ cm) を使用した．そして $\beta=0.5$ においてパラメータ α の値をかえたとき結合効率の値がほぼ最大になるように α の値をえらび，これにより $a=500\,\mu$m とした．なお，a については（I）と同じく $a/\lambda=70$ の条件から $a=250\,\mu$m とすると $\beta=0.5$ における結合効率の値をほぼ最大にするためには $c=5$ cm, $d=2.5$ cm となる．これは曲率半径 5 cm の反射鏡を中空導波路端から 2.5 cm の位置に置くことを意味し，これはレーザー管端の光学窓と中空導波路端との距離が約 8 cm (Fig. 8 参照) であるため無理な値である．そこで c の値としては（I）と同じく 20 cm とし上記のように $a=500\,\mu$m とした．このとき $a/\lambda=142$ でありこれは (8) 式を満足している．次に $\beta=0.5$ より $d=10$ cm とし，最後に（I）の場合と同様共振器長 L, 中空導波路長 l の値を決めた．（I），（II）の型のレーザー各部の寸法についての以上の結果を Fig. 7 に示す．Fig. によると α の値は（I），（II）の場合に対してそれぞれ 0.56, 2.24 であり，文献 15 の Fig. 2 によるとこのとき結合効率はほぼ 95% であることがわかる．

以上のようにして設計したレーザー管の形状を Fig. 8 に示す．この図は（II）の型のレーザー管に対するものである．**2.** の場合と同様に Ti の冷陰極とリターンパス（内径 4 mm, 長さ 120 cm）とを用いた．なお，この場合，発振を容易にするためにレーザー管の両端の光学窓（溶融石英，厚さ 3 mm）は **2.** の場合と異なりブルースター角で接着し，反射損失を抑えている．従ってこのレーザー出力 I の値を **2.** の場合と比較するには光学窓での反射損失の差を考慮する必要がある．しかし I と P_T, k, i_d との関係について両者を比較する際にはその必要

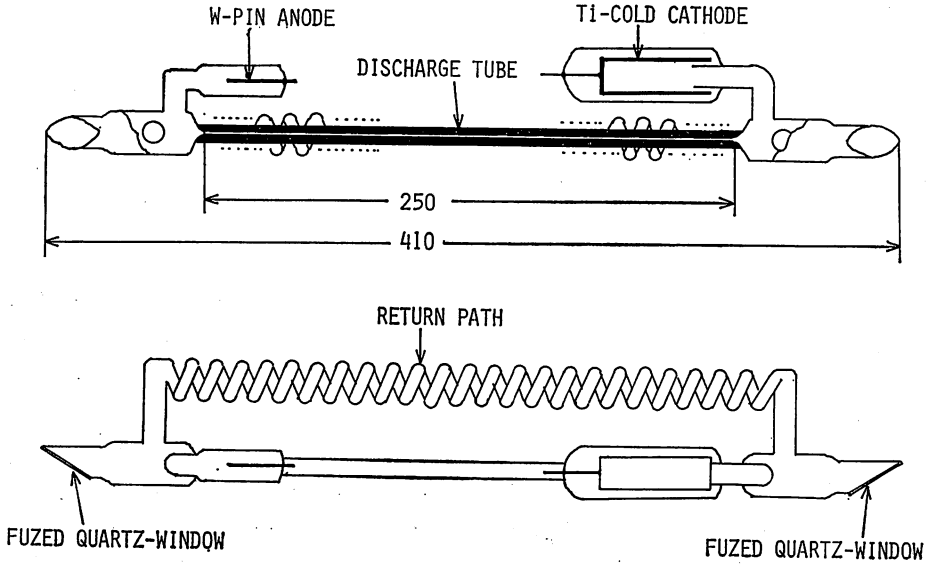

Fig. 8. The discharge tube for the waveguide laser (II).

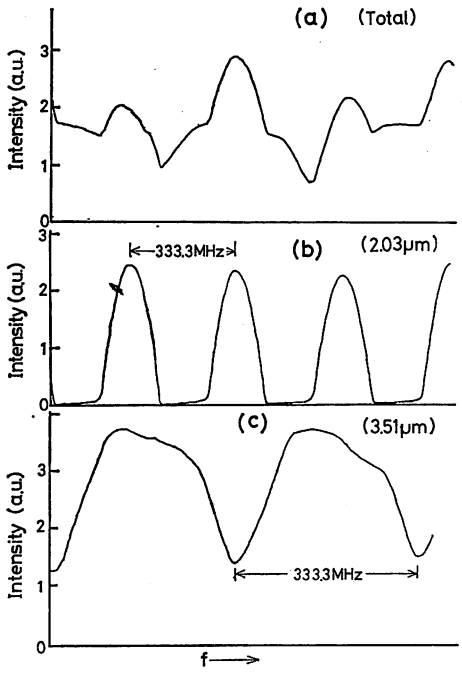

Fig. 9. Power detuning curves of the waveguide laser (II).
(a) Total power detuning curve.
(b) Detuning curve for the 2.03 μm line.
(c) Detuning curve for the 3.51 μm line.

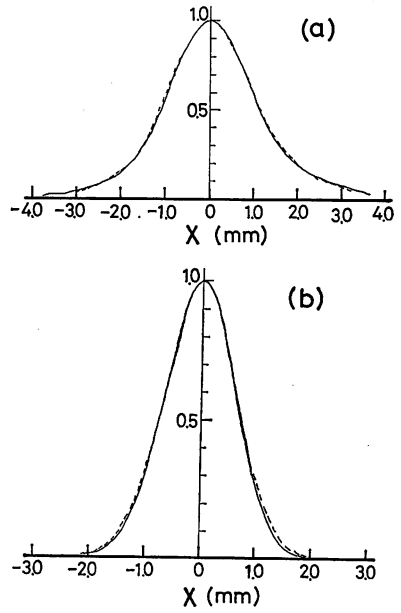

Fig. 10. Intensity distribution of the output beam of the waveguide laser.
(a) The waveguide laser (I).
(b) The waveguide laser (II).
The solid and broken lines are for the horizontal and vertical distributions, respectively. The distance D between the output mirror of the resonator and the detector was 38 cm.

はないと考えられる．反射鏡は波長 3.51 μm の光に対し反射率 100% および 90% の誘電体多層膜蒸着鏡を用いた．2 枚の反射鏡は **2.** で用いたレーザー架台に設置し，一方の反射鏡は PZT 上に設置し出力同調曲線を測定しその中心周波数での出力 I の値を求めた．この測定については **2.** で用いた測定装置と同じものを用いている．

波長 3.51 μm の光の発振特性の測定に先だち，他の波長の光の発振の可能性をしらべるために回折格子分光器を用いた．波長 3.51 μm の光は反射率 90% の反射鏡をとおして 3.51 μm 用干渉フィルターを用いて検出した．他の発振線は反射率 100% (波長 3.51 μm の光に対して) の反射鏡をとおしてとり出し回折格子分光器によってそれらの波長を測定した．なお，**3.2** に示す 2.03 μm の光に対するこの反射鏡の反射率は測定の結果約 50% であることが確認された．

波長 3.51 μm の光の出力同調曲線の中心周波数付近でレーザーが単一たてモード発振をしていることを確かめるため PZT 掃引ファブリー・ペロー干渉計 (平面鏡からなる．自由スペクトル域 750 MHz，フィネス 30) を用いた．

3.2 実験結果

レーザー (II) の出力曲線を Fig. 9 に示す．Fig. 9 (a) は全出力に対する結果であり，回折格子分光器を用いて調べた結果波長 3.51 μm の光と同時に 2.03 μm の光が発振していることが確認された．そこでこれらの光に対する出力同調曲線をそれぞれ測定した結果を同図 (b), (c) に示した．またファブリー・ペロー干渉計を用いて測定した結果，これらの光の出力調同曲線の中心周波数付近では単一たてモード発振が起っていることが確認された．

レーザー (I), (II) について波長 3.51 μm の光の光束断面の強度分布を Fig. 10 に示す．同図 (a) はレーザー (I), (b) はレーザー (II) についての結果であり両方ともほぼガウス形の強度分布をしていることから EH_{11} モードで発振していると考えられる．両図の曲線から求められるスポットサイズの値と共振器端から InAs 検出器までの距離 D との関係を Fig. 11 に示す．

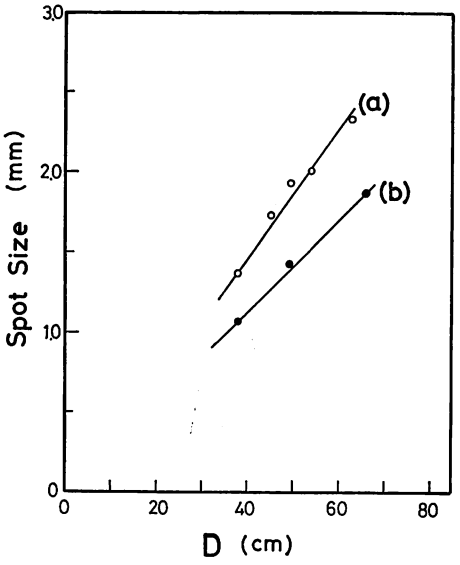

Fig. 11. The relations between the spot size of the beam and the distance D. Curves a and b are for the waveguide laser (I) and (II), respectively.

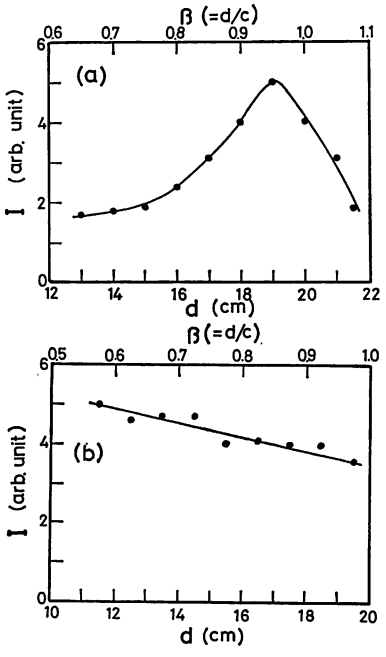

Fig. 12. The relation between the laser power intensity I and the distance d.
(a) The waveguide laser (I).
(b) The waveguide laser (II).

Fig. 11 の直線の傾きからレーザー（I），（II）の光束のスポットサイズの発散角はそれぞれ 4.2 mrad, 3.0 mrad であり，これは共振器長 50 cm の共焦点系のファブリー・ペロー共振器型レーザーの光束のスポットサイズの発散角の計算値 (3.2 mrad) と同程度の値になっていることがわかる．

次に中空導波路端と反射鏡との距離 d の値に対するレーザー（I），（II）の出力 I の値の変化の測定結果を Fig. 12 に示す．Fig. 12 (a) では Fig. 7 に示したレーザー（I）に対する d の値 ($=20$ cm) からずれるに従い，出力は急激に減少し，Fig. 12 (b) では Fig. 7 に示したレーザー（II）に対する d の値 ($d=10$ cm) からずれるに従い，出力はレーザー（I）の場合よりもゆるやかに減少している．これらの特性は **3.1** の（I），（II）に示した結合効率の特性（文献 15 の Fig. 2）とほぼ一致しいる．このことから d の変化に対する出力の変化は結合効率が変化することによると推定される．

次にレーザーの出力 I と i_d, P_T, k との関係の測定結果を示す．まず，レーザー出力 I と P_T との関係の測定結果を Fig. 13, Fig. 14 に示す．両図はレーザー（I），（II）に対する結果であり，実線，破線はそれぞれ波長 3.51 μm, 2.03 μm の光に対するものである．パラメータは i_d, k である．両図によると波長 3.51 μm の

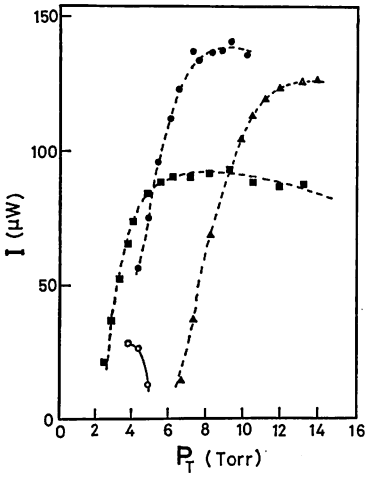

Fig. 13. The relation between I and P_T for the waveguide laser (I). The solid and broken lines represent the results of the 3.51 μm line and 2.03 μm line, respectively. $i_d=6$ mA.
○; $k=0.008$, ●; $k=0.011$,
■; $k=0.016$, ▲; $k=0.032$.

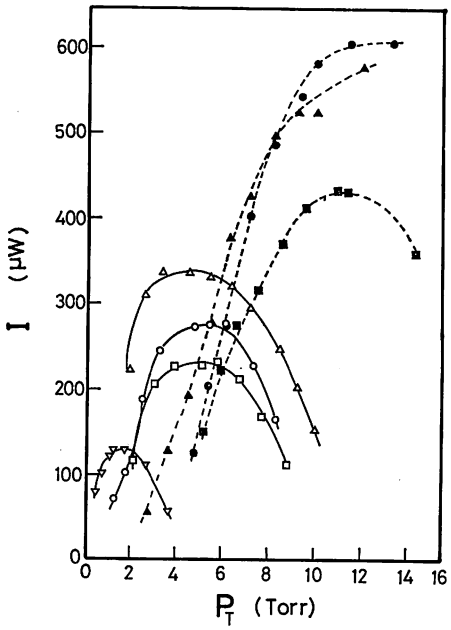

Fig. 14. The relation between I and P_T for the waveguide laser (II). The solid and broken lines are for the 3.51 μm and 2.03 μm lines, respectively. i_d=4 mA.
□, ■; k=0.012, ○, ●; k=0.016,
△, ▲; k=0.024, ▽; k=0.048.

光は低圧力側に，2.03 μm の光は高圧力側に出力の最大値をもつ．また，レーザー(II)にくらべレーザー(I)では波長 3.51 μm の光の発振する P_T の値の範囲がせまく，その出力の値も小さい．従って波長 3.51 μm の光の出力 I と i_d, P_T, k との関係を測定するにはレーザー（II）を用いた方が有利であり，以後はレーザー（II）に対する測定結果を示す．Fig. 15 に I と i_d との関係を示す．パラメータは P_T であり，ここでは k=0.020 の場合を示す．Fig. 15 は **2.2** のファブリー・ペロー共振器型レーザーの測定結果 (Fig. 3) に相当するものである．この I と i_d との関係の測定結果をもとに **2.2** で示したように I_m と P_T との関係，i_{dm} と P_T との関係，I_{mo} と k との関係を求め，その結果をそれぞれ Fig. 4, Fig. 5, Fig. 6 中に破線で示した．

3.3 考 察

レーザー（I），（II）を比較するとまず Fig. 13, Fig. 14 によりレーザー（I）にくらべレーザー（II）の方が波長 3.51 μm の光の発振する P_T の値の範囲が広く，またその出力 I の値も大きいことがわかる．また，Fig. 12 によると中空導波路端と反射鏡との距離 d の値の変

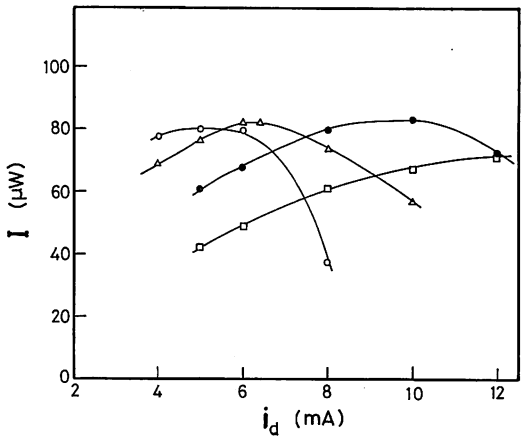

Fig. 15. The relation between I and i_d for the waveguide laser (II). k=0.020.
□; P_T=1.32 Torr, ●; P_T=1.78 Torr,
△; P_T=2.27 Torr, ○; P_T=3.06 Torr.

化に対しレーザー（II）の出力変動は小さく，従って機械的振動による d の値の変化の影響を受けにくい．さらにレーザー（I）にくらべレーザー（II）の d の値は 1/2 なのでレーザー（II）の方が中空導波路と反射鏡の間の光路中の空気の屈折率変動の影響を受けにくい．以上の点を考慮すると外部環境の変動の影響を受けにくく，出力の大きい波長 3.51 μm の導波路型 He-Xe レーザーとしてはレーザー（I）にくらべレーザー（II）の方がすぐれていると考えられる．

4. ファブリー・ペロー共振器型および導波路型レーザーの比較

2. で示したファブリー・ペロー共振器型レーザーではレーザー管両端の光学窓が光軸に垂直であるのに対し **3.** の導波路型レーザーではブリュースタ角になっているので両者のレーザー出力の値を比較するには光学窓での光の反射損失の差を考慮する必要があるがレーザー出力 I の i_d, P_T, k への依存性の特性を比較するときはその差は考慮する必要はないと考えられる．そしてこれらの特性についての結果を示す Fig. 4, Fig. 5, Fig 6 によるとファブリー・ペロー共振器型レーザーについて成り立つ関係式（(3)～(6)）が導波路型レーザーについてもやはり成り立つことがわかる．これらの特性を最終的にまとめた図が Fig. 5 であるといえるといえるが，この図の曲線 A と B とを比較するとレーザー出力の最大値 I_{mo} を与える条件は k の値が両者等しいときは導波路型レーザーの方がファブリー・ペロー共振器型レーザ

ーよりも全圧力 P_T が低く，放電電流 id が大きいことがわかる．

レーザー光束断面に関しては導波路型レーザーはガウス型の強度分布をしており，ファブリー・ペロー共振器型レーザーの TEM_{00} モードと類似の強度分布になっていることがわかる．また，そのスポットサイズの発散角の値も共焦点系のファブリー・ペロー共振器型レーザーの場合の計算値とほぼ同等であることが示された．これらの点により，光の空間的な指向特性について今回製作した導波路型レーザーはファブリー・ペロー共振器型レーザーに比較的よく類似していると考えられる．

両レーザーの出力についていえば導波路型レーザーの方が光学窓での反射損失が少ないにもかかわらずFig. 4, Fig. 6 からわかるように導波路型レーザーよりファブリー・ペロー共振器型レーザーの方が高出力が得られており，現在のところ導波路型レーザーの利点である小型・高出力という特長を十分得ているとはいえない．そのような特長を得るためには中空導波路断面の半径 a の値の設定方法や共振器用の反射鏡の反射率の最適値などをさらに検討する必要があろう．また導波路型レーザー（II）にくらべ導波路型レーザー（I）の方がなぜ 3.51 μm 発振線の出力が小さく，その発振可能な全圧力 P_T の値の範囲がせまいのかについてもさらにしらべる必要があると考えられる．

5. 結　　論

ファブリー・ペロー共振器型および導波路型の 3.51 μm He-Xe レーザーを設計，製作し，その発振特性を測定して両者を比較した．両方のレーザー管とも Ti 冷陰極とガスリターンパスとを使用することにより安定なレーザー発振を得ることができた．両方のレーザーに対しレーザー出力と放電電流，気体全圧力，気体全圧力に対する Xe の分圧比との関係を測定した．その結果を比較すると Xe の分圧比が等しい場合には出力の最大値を与える条件は導波路型レーザーの方がファブリー・ペロー共振器型レーザーよりも低圧力，大放電電流であることが示された．

導波路型レーザーに関しては2種類のレーザーを設計，製作し，相互比較した結果，波長 2.03 μm の光の同時発振時における 3.51 μm の光の発振する全圧力の範囲，出力の値，および反射鏡の位置変動による出力減少の特性を考慮するとレーザー(II)の方がレーザー(I)よりも優れていることが示された．

謝　　辞

ファブリー・ペロー共振器型レーザーの設計に関し有益な助言を頂きました理化学研究所高見道生博士に感謝します．なお，本研究の一部は文部省科学研究費特定研究の補助により行なわれたものである．

文　　献

1) 大和田芳子，田幸敏治： 光学 **3**, 93 (1976).
2) C. S. Willet: *Introduction to Gas Lasers; Population Inversion Mechanisms* (Pergamon Press, Oxford, 1974).
3) E. B. Aleksandrov, V. N. Kulyasov and A. B. Marnyrin: Opt. & Spectrosc. **31**, 170 (1971).
4) G. J. Linford: IEEE J. Quantum Electron. **QE-8**, 477 (1972).
5) P. O. Clark: IEEE J. Quantum Electron. **QE-1**, 109 (1965).
6) R. J. Freiberg and L. A. Weaver: J. Appl. Phys. **38**, 250 (1967).
7) M. Ohtsu and T. Tako: Tako: J. Appl. Phys. **50**, 599 (1979).
8) M. Ohtsu and T. Tako: Jpn. J. Appl. Phys. **17**, 2169 (1978).
9) M. Ohtsu, R. Koyama and T. Tako: Jpn. J. Appl. Phys. **18**, 1621 (1979).
10) M. Ohtsu, R. Koyama, A. Kusnowo and T. Tako **18**,: Jpn. J. Appl. Phys. 1619 (1979).
11) T. J. Bridges, E. G. Burkhardt and P. W. Smith: Appl. Phys. Lett. **20**, 403 (1972).
12) P. W. Smith and P. J. Maloney: Appl. Phys. Lett. **22**, 667 (1973).
13) M. Ohtsu and T. Tako: Jpn. J. Appl. Phys. **17**, 177 (1978).
14) E.A.J. Marcatili and R. A. Schmeltzer: Bell. Syst. Tech. J. **43**, 1783 (1964).
15) J. J. Degnan and D. R. Hall: IEEE J. Quantum Electron. **QE-9**, 901 (1973).
16) E. A. J. Marcatili: Bell Syst. Tech. J. **48**, 2071 (1969).
17) P. W. Smith: IEEE J. Quantum Eiectron. **QE-2**, 77 (1966).
18) R. E. Jensen and M. S. Tobin: Appl. Phys. Lett. **20**, 509 (1972).
19) J. J. Degnan, H. E. Walder, J. H. McElroy and N. McAvoy: IEEE J. Quntum Electron. **QE-9**, 489 (1973).
20) R. Yusek and G. Lockhart: IEEE J. Quantum Electron. **QE-9**, 694 (1973).
21) K. Shimoda: *High Resolution Laser Spectroscopy*, ed. K. Shimoda (Springer, 1976) p. 25, Fig. 2. 4

BULL. P.M.E. (T.I.T.), *No. 44, 1979*

621.373.8

Theoretical Study of Mode Competition in the 3.51μm He-Xe Laser in an Axial Magnetic Field

By

Motoichi Ohtsu*, Seiichi Katsuragi**, and Toshiharu Tako***

(Received May 17, 1979)

The results of the numerical analysis is dealt with the mode competition between two oppositely circularly polarized Zeeman components (the σ_+ and σ_- modes) of a He-Xe laser at 3.51μm in an axial magnetic field. The third-order theory of a gas laser was used by considering the intracoherence and the relaxation constants between Zeeman-sublevels. After a parameter M was defined to express the strength of the mode competitions, the cause of the pressure dependence of M was quantitatively investigated by comparing with the experimental results obtained in the previous work. As a result, it was shown that the increase of M with increasing the gas pressure was due to the increase of population exchange between Zeeman-sublevels and to the preservation of the intracoherence between them. Furthermore, it was shown that the value of M was independent of the characteristics of the dispersion of the active medium, and that it decreased because of isotope effects.

1. Introduction

Competition phenomena between polarized lights of a gas laser in an axial magnetic field have been measured by several authors. The competition phenomenon in a He-Xe laser at 2.65μm ($J = 1 \rightarrow 0$) has been studied by Culshaw and Kanneland[1], and those in a He-Ne laser at 1.52μm ($J = 1 \rightarrow 0$) and at 0.633μm ($J = 1 \rightarrow 2$) have been studied by Tomlinson and Fork[2].

The theory of a gas laser in a magnetic field has been given[3], and has been used to discuss experimental results[2]. In these papers, however, the number of participated Zeeman sublevels is small (i. e., the values of J in upper and lower energy levels of the transition are small), and the pressure dependence of competition phenomena has not yet been investigated in detail.

The competition phenomenon between two oppositely circularly polarized Zeeman components of a He-Xe laser at 3.51μm ($J = 3 \rightarrow 2$) in an axial magnetic field has been measured by the authors[4]. The result has been applied for the measurement of the inverted Lamb dip in H_2CO[5] and for the frequency stabilization[6]. One of these components (the σ_+ mode) is shifted toward the higher frequency and the other (the σ_- mode) toward the lower by an axial magnetic field. In this case, the numbers of Zeeman sublevels in the upper and the lower energy level are 7 and 5, respectively and are bigger than those in the previous works[1,2]. It was also observed that the competition characteristics between the σ_+ and σ_- modes were pressure dependent[6]. These two features are different from those of the previous works[1,2]. In the present paper, the third-order theory of a gas laser[3] is applied to the 3.51μm He-Xe laser, and the pressure dependence of the competition characteristics measured in the previous experiment[4] is investigated.

A parameter is defined for the following discussion to represent the strength of the mode

* Associate, Dr. Eng.
** Graduate student
*** Professor, Dr. Sci.

Published by Research Laboratory of Precision Machinery and Electronics, Tokyo Institute of Technology, Nagatsuta, Midori-ku, Yokohama 227, Japan

competition between the σ_+ and σ_- mode by using the results obtained previously[4]: The detuning curves of the σ_+ and σ_- modes were measured in the previous experiment[4] by varying the cavity length. One of the results is shown in Fig. 1.*) The solid lines in Fig. 1 represent

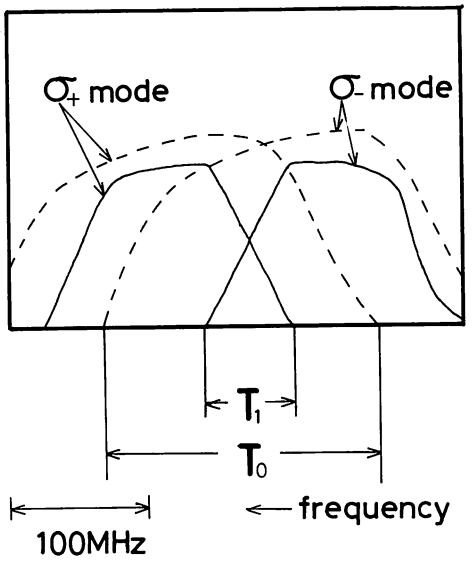

Fig. 1 The detuning curves of the σ_+ and σ_- modes in an axial magnetic field.[4] The solid lines represent the experimental results in which the mode competition occurs. The broken lines represent the results in which the mode competition does not occur. The value of total gas pressure P_T and that of magnetic field strength H are 8.17 Torr and 26.6 G, respectively. For the meanings of T_0 and T_1, refer to the text.

the experimental results in which the mode competition occurs. The broken lines represent the results in which the mode competition does not occur, which were estimated by using the detuning curves at $H = 0$. The value of the frequency interval in which the σ_+ and σ_- modes oscillate simultaneously are represented as T_1 (solid lines) and T_0 (broken lines), respectively.

The value of T_1 is smaller than T_0 because of the mode competition between the σ_+ and σ_- modes. Since the center frequencies ω_+ and ω_- of the gain curves of the σ_+ and σ_- modes are shifted in proportion to the magnetic field strength H, both values of T_0 and T_1 also proportionally depend on the value of H. Therefore, the value of the parameter M which is defined by eq. (1) is expected to be independent of the value of H.

$$M = 1 - T_0/T_1 \qquad (1)$$

It is obvious from eq. (1) that $0 \leqq M \leqq 1$, and M can be considered as the parameter which represents the strength of the mode competition. The relation between M and the total gas pressure P_T can be derived by using the experimental results of the previous work[4], and is shown in Fig. 2. In Fig. 2, it can be said the value of M is independent of the value of H, and

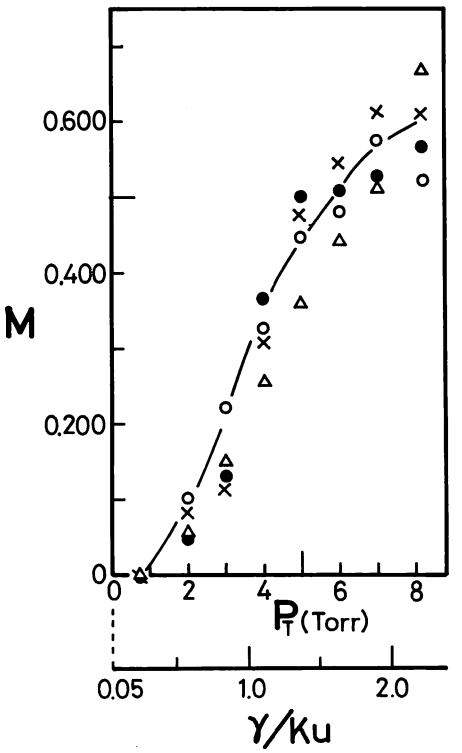

Fig. 2 The relation between M and the total gas pressure P_T. The value of γ/Ku was derived by eq. (21) in §2.
○ : H=15.0 G, △ : H=26.6 G,
× : H=63.3 G, ● : H=130.0 G

*) The block of H=26. 6G in Fig. 5 of reference 4, is shown here again.

it is clear from this figure that the mode competition becomes stronger with increasing the total gas pressure P_T. The value of γ/Ku in Fig. 2 is derived by eq. (22) in 2. In the followng chapter, the pressure dependence of the parameter M shown in Fig. 2 is investigated by using a simple model.

In 2, the model used in the present paper is given, and relaxation constants for the 3.51μm Xe transition are defined. The amplitude and frequency-determining equations for the σ_+ and the σ_- modes are given in 3. The calculated result of the relation between the parameter M and the total gas pressure P_T is described in 4. The effect of the dispersion of the active medium on the value of M is discussed in 5. The isotope effect of naturally available Xe gas on the value of M is discussed in 6. The results obtained in the present work are discussed in 7 and the conclusion is given in 8.

2. The Model Used for Numerical Calculation

Transitions of the Xe $(3d_4-2p_9)$ in an axial magnetic field are shown in Fig. 3. Each relaxation constant is also shown in this figure. The longitudinal relaxation constants of the upper and lower levels are expressed as γ_a and γ_b, respectively. The transverse relaxation constant between upper and lower levels is expressed as γ. Furthermore, γ_{al} and γ_{at} represent the longitudinal and the transverse relaxation constants between Zeeman-sublevels in the upper levels due to collision between atoms, respectively. Those in the lower levels are expressed as γ_{bl} and γ_{bt}, respectively. These four constans (γ_{al}, γ_{at}, γ_{bl}, and γ_{bt}) have not been explicitly considered in the previous paper[3]. In the present case, however, these constants should be considered since the number of Zeeman-sublevels is large and the transition probability between these sublevels must be large. This can be shown more clearly by the following estimation: The energy difference between adjacent Zeeman-sublevels was smaller than 1.33×10^{-25} J in the previous experiment[4] because the value of magnetic field strength H was lower than 133G.

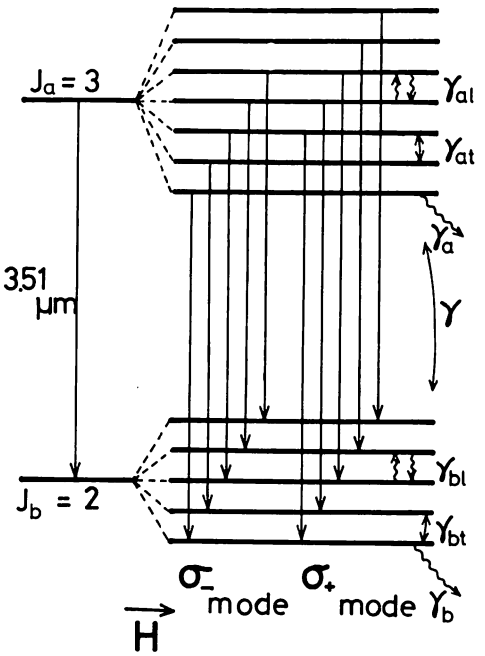

Fig. 3 Transitions of the 3.51μm Xe line $(3d_4\text{-}2p_9)$ in an axial magnetic field. The symbol of each relaxation constant is also shown. The definitions of these relaxation constants are given in the text.

Therefore, the collision between atoms must occurs frequently because this value of the energy difference is 2×10^{-5} times smaller than that of the thermal energy kT(=6.9×10^{-21} J at T=500K) of a Xe atom.

The relations given by following equations must hold for the relaxation constants shown in Fig. 3.

$$\gamma_a/\gamma_b < 1 \quad (2)$$

$$(\gamma_a + \gamma_b)/2\gamma \leqq 1 \quad (3)$$

$$\gamma_{al}/\gamma_{bl} \cong 1, \quad \gamma_{at}/\gamma_{bt} \cong 1 \quad (4)$$

$$\gamma_{al}/\gamma_{at} \leqq 1 \quad (5)$$

$$\gamma_{bl}/\gamma_{bt} \leqq 1 \quad (6)$$

Equation (2) represents the condition for the population inversion to be built. Equation (3) holds because of some collision processes such as phase-changing and population-changing collisions[7]. The values of the relaxation constants for the Zeeman-sublevels in the upper level is nearly equal to those in the lower level because the value of the energy difference between

adjacent Zeeman-sublevels in the upper level is nearly equal to that in the lower level, and so, eq. (4) holds. Equations (5) and (6) represent the relations which correspond to eq. (3) on the transitions between the Zeeman-sublevels in the upper and lower levels.

The parameters k, ℓ, k_a, and k_b are defined by the following equations.

$$k = \gamma_A / \gamma_B \tag{7}$$

$$\ell = (\gamma_A + \gamma_B) / 2\gamma \tag{8}$$

$$k_a = \gamma_A / \gamma_{at} \tag{9}$$

$$k_b = \gamma_B / \gamma_{bt} \tag{10}$$

, where

$$\begin{cases} \gamma_A = \gamma_a + \gamma_{al} \\ \gamma_B = \gamma_b + \gamma_{bl} \end{cases} . \tag{11}$$

Two constants, γ_A and γ_B, will appear in eqs. (48) and (49) in **3**. The ranges of the values of those four parameters are shown in the following:

According to eqs. (2), (7), and (11),

$$k < 1 \tag{12}$$

for $\gamma_a \gg \gamma_{al}$ and $\gamma_b \gg \gamma_{bl}$. According to eqs. (4), (7), and (11),

$$k \cong 1 \tag{13}$$

for $\gamma_a \ll \gamma_{al}$ and $\gamma_b \ll \gamma_{bl}$. However, the value of k is always smaller than unity because of eq. (4). Equations (12) and (13) mean that the value of k increases and approaches unity when the rate of the population exchange between the Zeeman sublevels increases by the collision between atoms. According to eqs. (3), (8), and (11),

$$\ell < 1 \tag{14}$$

for $\gamma_a \gg \gamma_{al}$ and $\gamma_b \gg \gamma_{bl}$, and

$$\ell \cong 1 \tag{15}$$

for $\gamma_a \cong \gamma_{al}$ and $\gamma_b \cong \gamma_{bl}$. Furthermore,

$$\ell > 1 \tag{16}$$

for $\gamma_a < \gamma_{al}$ and $\gamma_b < \gamma_{bl}$ if the value of γ_{al} and γ_{bl} are so large that

$$(\gamma_{al} + \gamma_{bl}) / 2\gamma > 1 - (\gamma_a + \gamma_b) / 2\gamma \tag{17}$$

Equations (14), (15), and (16) represent that the value of ℓ increases with increasing the rate of the population exchange between the Zeeman-sublevels, as well as k, and can become larger than unity. According to eqs. (5), (9), and (11), k_a takes the following values

$$k_a > 1 \text{ for } \gamma_a > \gamma_{al} \text{ and } \gamma_{at} \cong \gamma_{al}, \tag{18}$$

$$k_a \cong 1 \text{ for } \gamma_a < \gamma_{al} \text{ and } \gamma_{at} \cong \gamma_{al}, \tag{19}$$

$$k_a < 1 \text{ for } \gamma_a > \gamma_{al} \text{ and } \gamma_{at} \gg \gamma_{al}, \tag{20}$$

$$k_a \ll 1 \text{ for } \gamma_a < \gamma_{al} \text{ and } \gamma_{at} \gg \gamma_{al}. \tag{21}$$

It is easily shown from the previous discussions on k and ℓ that $k < 1$ and $\ell < 1$ when eqs. (18) and (20) hold and that $k \cong 1$ and $\ell \geqq 1$ when eqs. (19) and (21) hold. The relation $\gamma_{at} = \gamma_{al}$ means the presence of the coherence between Zeeman-sublevels, i. e., "intracoherence" as descirbed by Wang et. al.[8]. Equations (18) and (19) represent this situation. The relation $\gamma_{at} \gg \gamma_{al}$ means the absence of the intracoherence, and eqs. (20) and (21) represent this situation. The same discussion can be carried out on k_b if the suffix b is used in eqs. (18) ~ (21) instead of a.

Only the pressure dependence of γ has been experimentally known[9] and is represented by the following equation.

$$\gamma = 3.7 + 1.9\, P_T \,(\mathrm{MH_Z}), \tag{22}$$

where P_T represents the total gas pressure of He and Xe mixture expressed in Torr. Equation (22) holds for $P_T < 10$ Torr. Parameters k, ℓ, k_a and k_b are used in the following discussion together with eq. (22) because the pressure dependences of other relaxation constants have not been known. If the calculated results agree with the experimental results shown in Fig. 2 can be ensured, the cause of the experimental results can be discussed and the pressure dependences of other relaxation constants can be estimated by using the value of parameters k, ℓ, k_a, and k_b used for calculation and by eqs. (7)~(10), and (22).

3. Derivation of Equations Used

To describe the position of the laser, the direction of the Cartesian coordinates is chosen such that the z axis is parallel to and the x and y axes are perpendicular to the optical axis of the laser. If the direction of the applied magnetic field vector is toward the $+z$ axis, the polarizations of the σ_+ and σ_- modes are right- and left-handed, and the electric field vectors $E_+(z, t)$ and $E_-(z, t)$ of these modes are represented as

$$E_\pm(z, t) = \frac{1}{2} \boldsymbol{\varepsilon}_\pm E_\pm(t)\, e^{-i(\nu_\pm t + \phi_\pm)}\, U_\pm(z) + \text{c.c.}, \tag{23}$$

respectively. In eq. (23), $U_+(z)$ and $U_-(z)$ represent the normal mode functions of the σ_+ and σ_- modes which are expressed as

$$U_\pm(z) = \sin K_\pm z. \tag{24}$$

The wave numbers K_+ and K_- of both modes are related to the angular frequencies of the longitudinal modes Ω_+ and Ω_- by the following equation:

$$\Omega_\pm = K_\pm c, \tag{25}$$

where c represents the speed of light. The vectors $\boldsymbol{\varepsilon}_+$ and $\boldsymbol{\varepsilon}_-$ represent the complex unit vectors for circular polarization of the σ_+ and σ_- modes which are expressed as

$$\boldsymbol{\varepsilon}_\pm = \frac{1}{\sqrt{2}}(\boldsymbol{x} \mp i\boldsymbol{y}), \tag{26}$$

where $\boldsymbol{x}$ and $\boldsymbol{y}$ represent the unit vectors for x and y Cartesian coordinates, respectively. The amplitude $E_+(t)$ and phase $\phi_+(t)$ vary slowly in an optical frequency period, and $\nu_+ + \mathrm{d}\phi_+/\mathrm{d}t$ corresponds to the oscillation angular frequency of the σ_+ mode. Those for the σ_- mode are expressed as $E_-(t)$, $\phi_-(t)$, and $\nu_- + \mathrm{d}\phi_-/\mathrm{d}t$, respectively. In the following discussion, suffices + and − are used in the symbols to express the physical quantities of the σ_+ and σ_- modes, respectively, as were in eqs. (23) ~ (26). If the electric field in the resonator is expressed as

$$\boldsymbol{E}(z, t) = \boldsymbol{E}_+(z, t) + \boldsymbol{E}_-(z, t), \tag{27}$$

then the induced polarization of the medium can be written as

$$\boldsymbol{P}(z, t) = \boldsymbol{P}_+(z, t) + \boldsymbol{P}_-(z, t), \tag{28}$$

where

$$\boldsymbol{P}_\pm(z, t) = \frac{1}{2}\boldsymbol{\varepsilon}_\pm P_\pm(t)\, \mathrm{e}^{-i(\nu_\pm t + \phi_\pm)} U_\pm(z) + \mathrm{c.c.}, \tag{29}$$

In eq. (29), $P_+(t)$ and $P_-(t)$ are the complex, slowly varying components of the polarizations for both modes. By substituting eqs. (22) and (29) into Maxwell's equations, the self-consistency equations are obtained and expressed as

$$\frac{\mathrm{d}E_\pm}{\mathrm{d}t} + \frac{1}{2}\frac{\nu}{Q_\pm}E_\pm = -\frac{1}{2}\frac{\nu}{\epsilon_0}\,\mathrm{Im}(P_\pm), \tag{30}$$

and

$$\nu_\pm + \frac{\mathrm{d}\phi_\pm}{\mathrm{d}t} = \Omega_\pm + \frac{1}{2}\frac{\nu}{\epsilon_0}\frac{1}{E_\pm}\,\mathrm{Re}(P_\pm), \tag{31}$$

where ϵ_0 and ν represent the permittivity of vacuum and the laser oscillation angular frequency at 3.51μm, respectively. The real and the imagenary parts of $P_\pm$ are expressed as $\mathrm{Re}(P_\pm)$ and $\mathrm{Im}(P_\pm)$. The cavity quality factors for both modes are expressed as Q_+ and Q_- which are equal to the reciprocals of the diagonal elements g_{++} and g_{--} of the conductivity matrix,[10] respectively. It was experimentally shown in the previous work[4] that the cavity anisotropy had not effects upon the oscillation spectra of both modes, therefore the off-diagonal elements g_{+-} and g_{+-} of the conductivity matrix were set to be zero in eqs. (30) and (31).

The equations of motion for the density matrix are given by the following equations to obtain the values of $P_+(t)$ and $P_-(t)$ in eqs. (30) and (31):

$$\frac{\mathrm{d}}{\mathrm{d}t}\rho_{a'a'} = -\gamma_a\rho_{a'a'} - \gamma_{al}\rho_{a'a'} - \gamma_{al}\frac{1}{2J_a}\sum_{a''(\neq a')}\rho_{a''a''} + \frac{i}{\hbar}\sum_{b''}(V_{b''a'}\rho_{a'b''} - V_{a'b''}\rho_{b''a'}) + \lambda_a \tag{32}$$

$$\frac{\mathrm{d}}{\mathrm{d}t}\rho_{a'a''} = -(i\omega_{a'a''} + \gamma_{at})\rho_{a'a''} + \frac{i}{\hbar}\sum_{b''}(V_{b''a''}\rho_{a'b''} - V_{a'b''}\rho_{b''a''}) \tag{33}$$

$$\frac{\mathrm{d}}{\mathrm{d}t}\rho_{b'b'} = -\gamma_b\rho_{b'b'} - \gamma_{al}\rho_{b'b'} - \gamma_{bl}\frac{1}{2J_b}\sum_{b''(\neq b')}\rho_{b''b''} + \frac{i}{\hbar}\sum_{a''}(V_{a''b'}\rho_{b'a''} - V_{b'a''}\rho_{a''b'}) + \lambda_b \tag{34}$$

$$\frac{\mathrm{d}}{\mathrm{d}t}\rho_{b''b'} = -(i\omega_{b''b'} + \gamma_{bt})\rho_{b''b'} + \frac{i}{\hbar}\sum_{a''}(V_{a''b'}\rho_{b''a''} - V_{b''a''}\rho_{a''b'}) \tag{35}$$

$$\frac{\mathrm{d}}{\mathrm{d}t}\rho_{a'b'} = (i\omega_{a'b'} + \gamma)\rho_{a'b'} + \frac{i}{\hbar}\sum_{a''}V_{a''b'}\rho_{a'a''} - \frac{i}{\hbar}\sum_{b''}V_{a'b''}\rho_{b''b'} \tag{36}$$

The Bohr angular frequency between energy levels p and q (= a', a'', b', and b'') is expressed as ω_{pq} in eqs. (32) ~ (36) which is written as $\omega_\pm$ for $p = q \pm 1$ and are used to express the center angular frequencies of the gain curves of the σ_+ and σ_- modes. The relations between $\omega_\pm$ and the axial magnetic field strength H are

$$\omega_{\pm} = \omega_0 \pm 2\pi \cdot 1.40 \cdot gH \text{ (Mrad)}, \quad (37)$$

where ω_0 and g(=1.114) represent the value of $\omega_{\pm}$ at H=0 G and Landé g-factor, respectively. Suffices a', a'' express the numbers of the Zeeman sublevels in the upper level, and b', b'', are for the lower level. Therefore,

$$a', a'' = -J_a, -J_a + 1, \ldots, J_a - 1, J_a = -3, -2, \ldots, 2, 3, \quad (38)$$

$$b', b'' = -J_b, -J_b + 1, \ldots, J_b - 1, J_b = -2, -1, \ldots, 1, 2, \quad (39)$$

where J_a and J_b represent the quantum numbers of the angular momenta for the upper and lower levels. The numbers of atoms per second-per volume excited to the upper and lower levels are expressed as λ_a and λ_b, respectively. $V_{a'b'}(z, t)$ in eqs. (32) ~ (36) represents the matrix element of the electric-dipole interaction energy, and is expressed as

$$V_{a'b'}(z, t) = -\frac{1}{2}\sqrt{2}\, p_{a'b'} E_{a'b'}(t) e^{-i(\nu_{a'b'} t + \phi_{a'b'})} U_{a'b'}(z) \quad (40)$$

$$= \begin{cases} -\frac{1}{2}\sqrt{2} p_{b'+1,b'} E_+(t) e^{-i(\nu_+ t + \phi_+)} U_+(z) \\ \quad (\text{for } a' = b' + 1), \quad (41) \\ -\frac{1}{2}\sqrt{2} p_{b'-1,b'} E_-(t) e^{-i(\nu_- t + \phi_-)} U_-(z) \\ \quad (\text{for } a' = b' - 1), \quad (42) \\ 0 \\ \quad (\text{for } a' \neq b' \pm 1), \quad (43) \end{cases}$$

where $p_{a'b'}$ represents the electric-dipole element between levels a' and b'. Because $J_a = J_b + 1$(=3) in the present case,

$$p_{a'b'} = \begin{cases} -\frac{1}{2} p \sqrt{(J_a + b')(J_a + b' + 1)} \\ = -\frac{1}{2} p \sqrt{(3 + b')(4 + b')} \\ (\text{for } a' = b' + 1) \\ \frac{1}{2} p \sqrt{(J_a - b')(J_a - b' + 1)} \\ = \frac{1}{2} p \sqrt{(3 - b')(4 - b')} \\ (\text{for } a' = b' - 1), \quad (44)^{11} \end{cases}$$

where the value of p is independent on the values of a' and b'. The third term in the right-side of eq. (32) represents the number of atoms per second which are excited to the level a' from the other Zeeman-sublevels in the upper level. The corresponding term in eq. (34) represents the number of atoms for the lower level. In these terms, γ_{al} and γ_{bl} are used. These terms represent the transition between Zeeman-sublevels due to atomic collisions, and have not been considered yet in the previous work[3]. Equation (33) represents the time dependence of the intracoherence between Zeeman-sublevels a' and a'' in the upper level. Equation (35) represents the time dependence of the intracoherence for the lower level. In these equations, γ_{at} and γ_{bt} are used, which have not been used yet in the previous work[3].

The solution of eq. (36) to the first-and the third-order in the perturbation $V_{a'b'}(z, t)$ is obtained by using eqs. (32) ~ (36). A Maxwell-Boltzmann distribution

$$W(v) = \frac{1}{\sqrt{\pi}\, u} \exp[-(v/u)^2] \quad (45)$$

will be assumed for the component v of velocity of the Xe atom along the laser (z) axis, where u represents the most probable speed of the atom. Using eqs. (36), (40), and (45), one has for the first-order contribution to $\rho_{a'b'}$

$$\rho^{(1)}_{a'b'}(v, z, t) = -\frac{1}{2}\sqrt{2}\, \frac{i}{\hbar} W(v) N(z, t) p_{a'b'} E_{a'b'} \exp[-i(\nu_{a'b'} t + \phi_{a'b'})] \cdot \int_0^{\infty} d\tau' \exp[-(i\omega_{a'b'} - i\nu_{a'b'} + \gamma)\tau'] \cdot U_{a'b'}(z - v\tau'), \quad (46)$$

where $N(z, t)$ represents the population inversion density, The value of $U_{a'b'}$ is equal to U_+ or U_- in eq. (24) for $a' = b' + 1$, $b' - 1$. The third-order contribution is expressed as

$$\rho^{(3)}_{a'b'}(v, z, t)$$

$$= -\frac{i}{\hbar^3} W(v) N(z, t) \int_0^\infty d\tau' \int_0^\infty d\tau'' \int_0^\infty d\tau'''$$

$$\exp[-(i\omega_{a'b'} + \gamma)\tau']$$

$$\cdot \sum_{a''} \sum_{b''} \Big[V_{a''b'}(z', t') \exp[-(i\omega_{a'a''} + \gamma_{a'})\tau''] \cdot \{ V_{b''a''}(z'', t'') \cdot V_{a'b''}(z''', t''') \cdot$$

$$\exp[-(i\omega_{a'b''} + \gamma)\tau'''] + V_{a'b''}(z'', t'') \cdot V_{b''a''}(z''', t''') \cdot$$

$$\exp[-(i\omega_{b''a''} + \gamma)\tau'''] \} + V_{a'b''}(z', t')$$

$$\exp[-(i\omega_{b''b'} + \gamma_{b'})\tau''] \{ V_{a''b'}(z'', t'') \cdot V_{b''a''}(z''', t''') \cdot$$

$$\exp[-(i\omega_{b''a''} + \gamma)\tau'''] + V_{b''a''}(z'', t'') \cdot V_{a''b'}(z''', t''') \cdot$$

$$\exp[-(i\omega_{a''b'} + \gamma)\tau'''] \} \Big] \quad . \tag{47}$$

Two relaxation constants, $\gamma_{a'}$ and $\gamma_{b'}$, in eq. (47) have the following values

$$\gamma_{a'} = \begin{cases} \gamma_A & (\text{for } a'' = a') \\ \gamma_{at} & (\text{for } a'' \neq a') \end{cases} , \tag{48}$$

$$\gamma_{b'} = \begin{cases} \gamma_B & (\text{for } b'' = b') \\ \gamma_{bt} & (\text{for } b'' \neq b') \end{cases} , \tag{49}$$

where γ_A and γ_B are given by eq. (11). In eqs. (46) and (47), three τ's (τ', τ'', τ'',) and three z's (z', z'', z'',) are expressed as

$$\begin{cases} \tau' = t - t' \\ \tau'' = t' - t'' \\ \tau''' = t'' - t''' \end{cases} \tag{50}$$

$$\begin{cases} z' = z - v\tau' \\ z'' = z - v\tau'' \\ z''' = z - v\tau''' \end{cases} \tag{51}$$

Because $\rho^{(3)}_{a'b'}(v, z, t)$ in eq. (47) is composed of four terms, one can express it as

$$\rho^{(3)}_{a'b'}(v, z, t) = \sum_{m=1}^{4} \rho^{(3)}_{a'b'(m)}(v, z, t) \tag{52}$$

Using $\rho_{a'b'}(v, z, t)$, polarizations $P_+(t)$ and $P_-(t)$ in eq. (29) are expressed as

$$P_\pm(t) = 2\sqrt{2} \exp[i(\nu_\pm t + \phi_\pm)] \frac{1}{\aleph} \int_0^L dz U^*_\pm(z) \int_{-\infty}^{\infty} dv \sum_{a'} \sum_{b'} \rho_{a'b'}(v, z, t) p_{b'a'} \delta_{a', b' \pm 1} \quad , \tag{53}$$

where $\aleph$ is defined as

$$\aleph = \int_0^L dz \, |U_\pm(z)|^2 \quad . \tag{54}$$

Furthermore, L, $U^*_\pm(z)$, and δ represent the cavity length, the complex conjugate of $U_\pm(z)$, and the Kronecker delta function, respectively. Substituting $\rho^{(1)}_{a'b'}$ in eq. (46) into eq. (53), the first-order contributions to $P_+(t)$ and $P_-(t)$ are obtained, and are expressed as

$$P^{(1)}_{\pm(t)} = -\frac{\bar{N}}{\hbar K u} \sum_{b'=-2}^{2} |p_{b'\pm 1, b'}|^2 E_\pm Z[\upsilon_\pm] \quad , \tag{55}$$

where

$$\bar{N} = \frac{1}{\aleph} \int_0^L N(z, t) \quad . \tag{56}$$

And, $Z[\upsilon]$ is the plasma dispersion function which is defined as

$$Z[\upsilon] = \frac{iK}{\sqrt{\pi}} \int_{-\infty}^{\infty} dv \exp[-(v/u)^2] \frac{1}{\upsilon + iKv} \quad . \tag{57}$$

Furthermore, υ_+ and υ_- are expressed as

$$\upsilon_\pm = i(\omega_\pm - \nu_\pm) + \gamma \quad . \tag{58}$$

Substituting $p_{a'b'}$ of eq. (44) into eq. (55), $P^{(1)}_+(t)$ and $P^{(1)}_-(t)$ are expressed as

$$P^{(1)}_\pm(t) = -\frac{35\bar{N}p^2}{2\hbar K u} E_\pm Z[\upsilon_\pm] \quad . \tag{59}$$

Substituting $\rho^{(3)}_{a'b'}$ in eq. (47) (or in eq. (52)) into eq. (53), one has for the third-order contributions to $P_+(t)$ and $P_-(t)$, which are composed of four terms and are expressed as

$$P_{\pm}^{(3)}(t) = \sum_{m=1}^{4} P_{\pm m}^{(3)}(t)$$

$$= \sum_{m=1}^{4} \frac{\bar{N}p^4}{128\hbar^3 Ku} E_{\pm} [1484E_{\pm}^2 J_{m1}^{\pm}$$

$$+ 504E_{\mp}^2 J_{m2}^{\pm} + 84E_{\mp}^2 J_{m3}^{\pm}] \quad . \qquad (60)$$

Equation (44) was used to get eq. (60). In eq. (60), J_{mn}^{+} and J_{mn}^{-}(m=1~4, n=1~3) are expressed as

$$J_{mn}^{\pm} = n_{\alpha}^{\pm} \frac{1}{v_2^{\pm}} \frac{Z[v_1^{\pm}] + Z[v_3^{\pm}]}{v_1^{\pm} + v_3^{\pm}}$$

$$+ n_{\beta}^{\pm} \frac{1}{v_2^{\pm}} \frac{Z[v_1^{\pm}] - Z[v_3^{\pm}]}{v_1^{\pm} - v_3^{\pm}}$$

$$+ n_{\gamma}^{\pm} \frac{1}{2} \frac{1}{v_1^{\pm} - v_2^{\pm}/2} \left\{ \frac{Z[v_1^{\pm}] - Z[v_3^{\pm}]}{v_1^{\pm} - v_3^{\pm}} \right.$$

$$\left. - \frac{Z[v_3^{\pm}] - Z[v_2^{\pm}/2]}{v_3^{\pm} - v_2^{\pm}/2} \right\} , \qquad (61)$$

where the values of $v_p^{\pm}$ (p=1~3) and $n_q^{\pm}$ (q=α,β,γ) are shown in Table 1. $v_{\pm}$, v_a, v_b, and n_2 in Table 1 are expressed as

$$\begin{cases} v_{\pm} = i(\omega_{\pm} - \nu_{\pm}) + \gamma \\ v_a = i(\omega_{a',a'-2} + \nu_- - \nu_+) + \gamma_{at} \\ v_b = i(\omega_{b'+2,b'} + \nu_- - \nu_+) + \gamma_{bt} \\ n_2 = N_2/\bar{N} \end{cases} , \qquad (62)$$

where

$$N_2 = \frac{1}{N} \int_0^L dz N(z, t) \cos 2(K_+ - K_-)z \quad . \qquad (63)$$

The following assumptions were used to get eq. (60) by using eq. (47): Because $V_{a'b'}(z,t)$ in eq. (40) is proportional to $U_{a'b'}(z)$, it is known from eqs. (47) and (53) that the integrand in the time integrations in eq. (53) is composed of the products of four U's. In this integrand, the term which are composed of odd functions in v and rapidly varying in z are averaged out in the integrations over v and z after substituting eq. (47) into eq. (53). Therefore, these terms in eq. (47) can be discarded. For example, the approximation

$$U_+^*(z) \cdot U_{a''b'}(z - v\tau') \cdot U_{b''a''}(z - v\tau' - v\tau'')$$

$$\cdot U_{a'b''}(z - v\tau' - v\tau'' - v\tau''')$$

$$\cong \frac{1}{8} \{ \cos(K_+ - K_{a''b'} - K_{b''a''} + K_{a'b''})z$$

$$\cdot \cos Kv(\tau' - \tau''')$$

$$+ \cos(K_+ - K_{a''b'} + K_{b''a''} - K_{a'b''})z$$

$$\cdot \cos Kv(\tau' + \tau''')$$

$$+ \cos(K_+ + K_{a''b'} - K_{b''a''} - K_{a'b''})z$$

$$\cdot \cos Kv(\tau' + 2\tau'' + \tau''') \} \qquad (64)$$

Table 1. The values of $v_p^{\pm}$(p=1~3) and $n_q^{\pm}$(q=α, β, γ). The symbol * is used to express the complex conjugate.

σ_+ mode

m	n	v_1^+	v_2^+	v_3^+	n_α^+	n_β^+	n_γ^+
1	1	v_+	γ_A	v_+	1	1	1
〃	2	〃	v_a	v_+	n_2	1	1
〃	3	〃	γ_A	v_-	1	1	n_2
2	1	v_+	γ_A	v_+^*	1	1	1
〃	2	〃	v_a	v_-^*	1	n_2	1
〃	3	〃	γ_A	v_-^*	1	1	n_2
3	1	v_+	γ_B	v_+^*	1	1	1
〃	2	〃	γ_B	v_-^*	1	1	n_2
〃	3	〃	v_b	v_-^*	1	n_2	1
4	1	v_+	γ_B	v_+	1	1	1
〃	2	〃	γ_B	v_-	1	1	n_2
〃	3	〃	v_b	v_+	n_2	1	1

σ_- mode

m	n	v_1^-	v_2^-	v_3^-	n_α^-	n_β^-	n_γ^-
1	1	v_-	γ_A	v_-	1	1	1
〃	2	〃	v_a^*	v_-	n_2	1	1
〃	3	〃	γ_A	v_+	1	1	n_2
2	1	v_-	γ_A	v_-^*	1	1	1
〃	2.	〃	v_a^*	v_+^*	1	n_2	1
〃	3	〃	γ_A	v_+^*	1	1	n_2
3	1	v_-	γ_B	v_-^*	1	1	1
〃	2	〃	γ_B	v_+^*	1	1	n_2
〃	3	〃	v_b^*	v_+^*	1	n_2	1
4	1	v_-	γ_B	v_-	1	1	1
〃	2	〃	γ_B	v_+	1	1	n_2
〃	3	〃	v_b^*	v_-	n_2	1	1

were used to get $P_{\pm}^{(3)}(t)$.

Because each $P_{\pm m}^{(3)}(t)$ in eq. (60) is composed of the sum of three terms, as is the right side of eq. (64), J_{mn}^{+} and J_{mn}^{-} given by eq. (61) are composed of three terms. The absolute value of the first term is the largest among three terms in the right side of eq. (61), and that of the third term is the smallest. Though the dependency of the third term on the strength H of the magnetic field is the clearest among the three terms, J_{mn}^{+} and J_{mn}^{-} do not clearly depend on H because the third term does not give a large contribution to J_{mn}^{+} and J_{mn}^{-}. Accordingly, the value of the parameter M calculated by using $J_{mn}^{\pm}$ must not clearly depend on H. This fact is consistent with the characteristics of the experimental results in Fig. 2.

Substituting $P_{\pm}^{(1)}(t)$ and $P_{\pm}^{(3)}(t)$ of eqs. (59) and (60) into eqs. (30) and (31), one has

$$\frac{dI_{\pm}}{dt} = 2I_{\pm}(\alpha_{\pm}-\beta_{\pm}I_{\pm}-\theta_{\pm\mp}I_{\mp}) \tag{65-a}$$

$$\nu_{\pm}+\frac{d\phi_{\pm}}{dt} = \Omega_{\pm}+\sigma_{\pm}-\rho_{\pm}I_{\pm}-\tau_{\pm\mp}I_{\mp}\ , \tag{65-b}$$

where

$$I_{\pm}=\frac{P^2}{2\hbar^2\gamma_A\gamma_B}\cdot E_{\pm}^2 \tag{66}$$

and are dimensionless intensities for the σ_+ and σ_- modes. Each coefficient in eq. (65) is expressed as

$$\sigma_{\pm}+i\alpha_{\pm}=\frac{35}{4}\kappa\left[Z\left[\frac{\nu_{\pm}-\omega_{\pm}}{Ku},\frac{\gamma}{Ku}\right]\right]$$
$$-i\cdot\frac{1}{\bar{N}_{\pm}}\cdot Im\left[Z\left[0,\frac{\gamma}{Ku}\right]\right] \tag{67}$$

$$\rho_{\pm}+i\beta_{\pm}=\frac{1484}{128}\kappa\cdot\gamma_A\cdot\gamma_B\sum_{m=1}^{4}J_{m1}^{\pm} \tag{68}$$

$$\tau_{\pm\mp}+i\theta_{\pm\mp}$$
$$=\frac{1}{128}\kappa\gamma_A\gamma_B\sum_{m=1}^{4}(504J_{m2}^{\pm}+84J_{m3}^{\pm})\ , \tag{69}$$

where

$$\kappa=\frac{\nu\bar{N}p^2}{\epsilon_0\hbar Ku}\ . \tag{70}$$

In eq. (67), $\bar{N}_+$ and $\bar{N}_-$ represent the relative excitations of the σ_+ and σ_- mode which are expressed as

$$\bar{N}_{\pm}=\bar{N}/\bar{N}_{th\pm}\ . \tag{71}$$

Here, $\bar{N}_{th+}$ and $\bar{N}_{th-}$ in eq. (71) represent the values of the population inversions $\bar{N}_+$ and $\bar{N}_-$ at threshold which are expressed as

$$N_{th\pm}=\frac{\nu}{2Q_{\pm}}/\frac{35\nu p_2}{4\epsilon_0\hbar Ku}\cdot Im\,[Z[0,\gamma/Ku]]\ . \tag{72}$$

The relations between $J_{mn}^{\pm}(m=1\sim4,\ n=1\sim3)$ in eqs. (68) and (69) and $\nu_{\pm}$ are shown in Fig. 4. However, only the relations for $Im(J_{mn}^{+})$ are shown in Fig. 4 for simplicity. The values of relaxation constants which satisfied the conditions expressed by eqs. (2)~(6) were used to draw Fig. 4. If different values are used, the line shapes in Fig. 4 do not remarkably change. Among all the curves in Fig. 4, those for $\mathrm{Im}[J_{12}^{+}]$ and $\mathrm{Im}[J_{43}^{+}]$ show dispersive shapes and those for others appear to be combinations of a Lorentzian and a Gaussian. Because the components $\rho_{a'a''}$ and $\rho_{b'b''}$ in eqs. (32)~(36), i.e., the intracoherence, were considered, the functions $\mathrm{Im}[J_{12}^{+}]$ and $\mathrm{Im}[J_{43}^{+}]$ (as well as $\mathrm{Im}[J_{22}^{+}]$ and $\mathrm{Im}[J_{33}^{+}]$) appeared, and it can be seen from Fig. 4 that the absolute values of those functions are not negligibly smaller than those of other $\mathrm{Im}[J_{mn}^{+}]$'s.

The frequency dependences of each coefficient in eqs. (67)~(69) are shown in Fig. 5. In Fig. 6, the frequency dependence of the coupling parameter C is shown, which is defined as

$$C=\theta_{+-}\theta_{-+}/\beta_{+}\beta_{-}\ . \tag{73}$$

The following parameter k_{ab} was used in eqs. (68) and (69) for simplicity to draw Figs. 5 and 6 instead of using k_a and k_b because this approximation gave answers within 1×10^{-4} of the exact values:

$$k_{ab}=k_a=k_b\ . \tag{74}$$

It will be known from the discussion in §4 ((A), (B), and (C) in **4.2**) that the values of parameters (k=ℓ=k_{ab}=1) used for drawing Figs.5 and 6 correspond to the large value of M, i.e., the case in which the mode competition is clearly observed.

The value of $Z[x, y]$ in eqs. (67)~(69) was

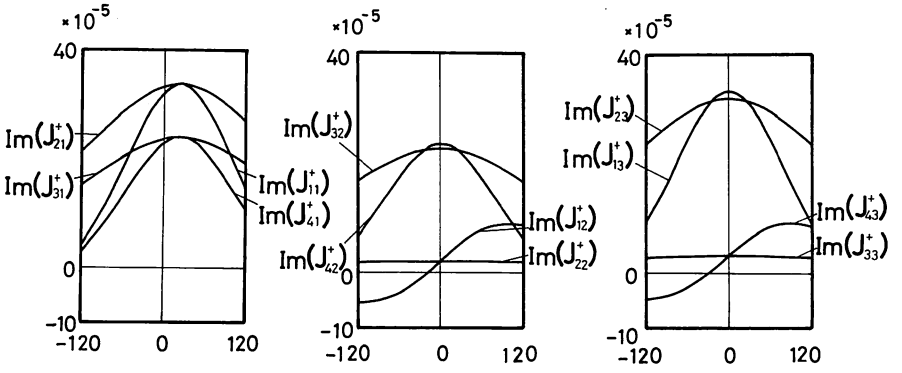

Fig. 4 The relation between $\mathrm{Im}[J^{+}_{mn}]$ and ν_{+}.
H=15 G, γ/Ku=2.2,
$\gamma_A=\gamma_{at}$=15.54MHz,
$\gamma_B=\gamma_{bt}$=22.2MHz

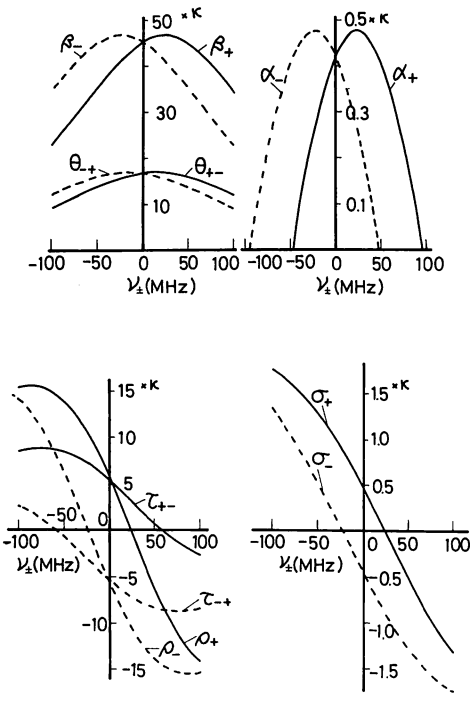

Fig. 5 The relation between each coefficient in eq. (65) and $\nu_{\pm}$. H=15 G, γ/Ku=2.2, $k=\ell=k_{ab}$=1.

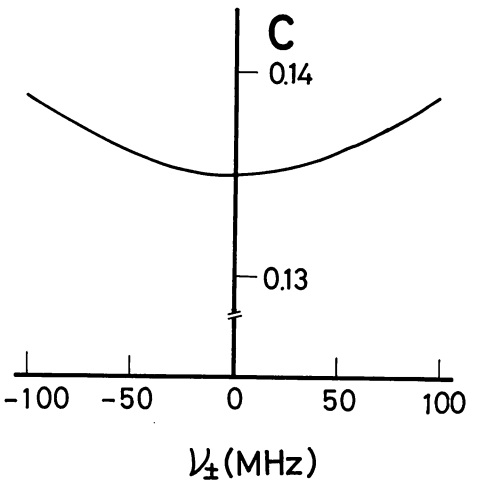

Fig. 6 The relation between the coupling parameter C and $\nu_{\pm}$. The same value of each parameter as in Fig. 5 was used.

calculated by using a numerical table.[12]

The value of $Z[x, y]$ for arbitary values of x and y in the range of $0 \leqq x, y \leqq 10$ was calculated by polinomial approximation and the values given in the plasma dispersion function table.[12]

Especially, the value for $0 \leqq x \ll 1$ and $y > 0$ was calculated by the continued fraction (given in IV of ref. 12). As the value of the relative error of calculated $Z[x, y]$ was smaller than 1×10^{-5}, those of I_{+} and I_{-} calculated from eq. (65) were smaller than 1×10^{-4}.

4. Calculated Results

4.1 The case of low pressure (P_T<1Torr)

The values of the relaxation constants at

P_T<1Torr have been experimentally given,[13~15] i.e.,

$$\begin{cases}\gamma_a = 0.73\text{MHz} \\ \gamma_b = 22.2\text{MHz}\end{cases} . \quad (75)$$

The value of the Doppler broadening constant used in **4** is

$$Ku = 71.6\text{MHz}, \quad (76)$$

which is the average of those of Xe isotopes shown in Table 6 in **6**. For the case of P_T=0.6Torr, one has

$$\gamma/Ku = 0.2 \quad (77)$$

by eqs. (22) and (76). Furthermore, if we choose H=6.7G and $\mathfrak{N}_\pm$=1.15, the relation between $I_+(I_-)$ and $\nu_+(\nu_-)$ can be obtained by eqs. (65) and (67)~(69). The results are shown in Fig. 7. Curves I'_+ and I'_- in Fig. 7 represent the results by substituting zero into θ_{+-} and θ_{-+} in eq. (65), i.e., the results in the absence of the mode competition. The value of T_0 in eq. (1) is obtained by the curves I'_+ and I'_-. The curves I_+ and I_- represent the results exactly calculated from eq. (65) without substituting zero into θ_{+-} and θ_{-+}. As the value of M in Fig. 7 is 0.029 which is much smaller than unity, it is known that the mode competition between the σ_+ and σ_- modes will be weak at low pressure (P_T<1 Torr). This result qualitatively agrees with the experimental result in the previous work (section **3.1** in ref. 4).

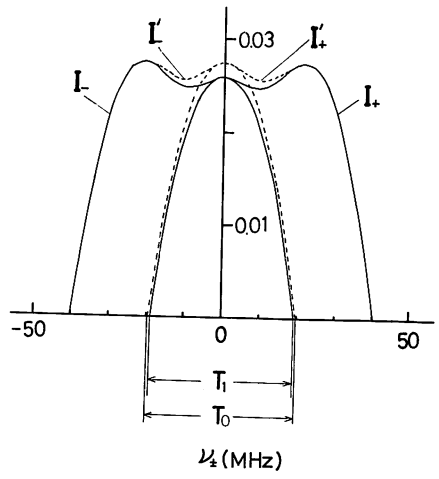

Fig. 7 The relation between the intensity $I_+(I_-)$ of the $\sigma_+(\sigma_-)$ mode and $\nu_+(\nu_-)$. Curves I'_+ and I'_- represent the results in the absence of the mode competition. In this figure, the value of M is found to be 0.029.
H=6.7 G, P_T=0.6 Torr, γ/Ku=0.2, $\gamma_A = \gamma_{at}$=0.73MHz, $\gamma_B = \gamma_{bt}$=22.2MHz, $\mathfrak{N}_\pm$=1.15

4.2 The relation between the parameter M and the pressure P_T

As the value of each relaxation constant has not been experimentally given at $P_T \geqq 1$Torr except for γ in eq. (22), the relation between M and P_T was obtained by substituting several values into the parameters in eqs. (7)~(10) and by using eq. (22). The results are shown in Fig. 8. The equation (74) was used for Fig. 8 as was for Figs. 5 and 6. Though it is known by eqs. (16) and (18) that ℓ, k_a, and k_b can take values larger than unity, the characteristics of the relation between M and P_T can be inferred by using the results at ℓ, k_a, $k_b \leqq 1$ because the values of eqs. (65), (67)~(69) are monotonously varied with ℓ, k_a, and k_b also at ℓ, k_a, $k_b > 1$. Therefore, the relation between M and P_T was shown only at ℓ, $k_{ab} \leqq 1$ in Fig. 8. The values of H, $\mathfrak{N}_+$, and $\mathfrak{N}_-$ were conveniently selected to be 15G, 1.15, and 1.15 because the calculated value of M was not strongly depend on those values. The results at $P_T \leqq$8Torr are shown in Fig. 8 because the experiment was carried out for the pressure lower than about 8Torr[4], as shown in Fig. 2. According to eqs. (22) and (75), the value of γ/Ku is equal to 2.2 for P_T = 8Torr. The relation between the characteristics of curves in Fig. 8 and the values of parameters k, ℓ, and k_{ab} are as follows; (A) On all the curves for $\ell < 1/2$, the value of M monotonously decreases with increasing P_T. It requires that $\ell \geqq 1/2$ for the value of M to increase monotonously with increasing P_T, as was shown by the experimental results in Fig. 2. According to the discussion on ℓ in **2** (eqs. (14)~(16)), it can be said that the range $\ell \geqq 1/2$ correspond to the situation of increasing in the rate of population exchange between Zeeman-sublevels and, therefore, $\gamma_{a1} \leqq \gamma_{a1}$ and $\gamma_b \leqq \gamma_{b1}$. (B) It requires that $k_{ab} \geqq 1/2$(i.e., k_a, $k_b \geqq 1/2$) as well as $\ell \geqq 1/2$ for the value of M to increase

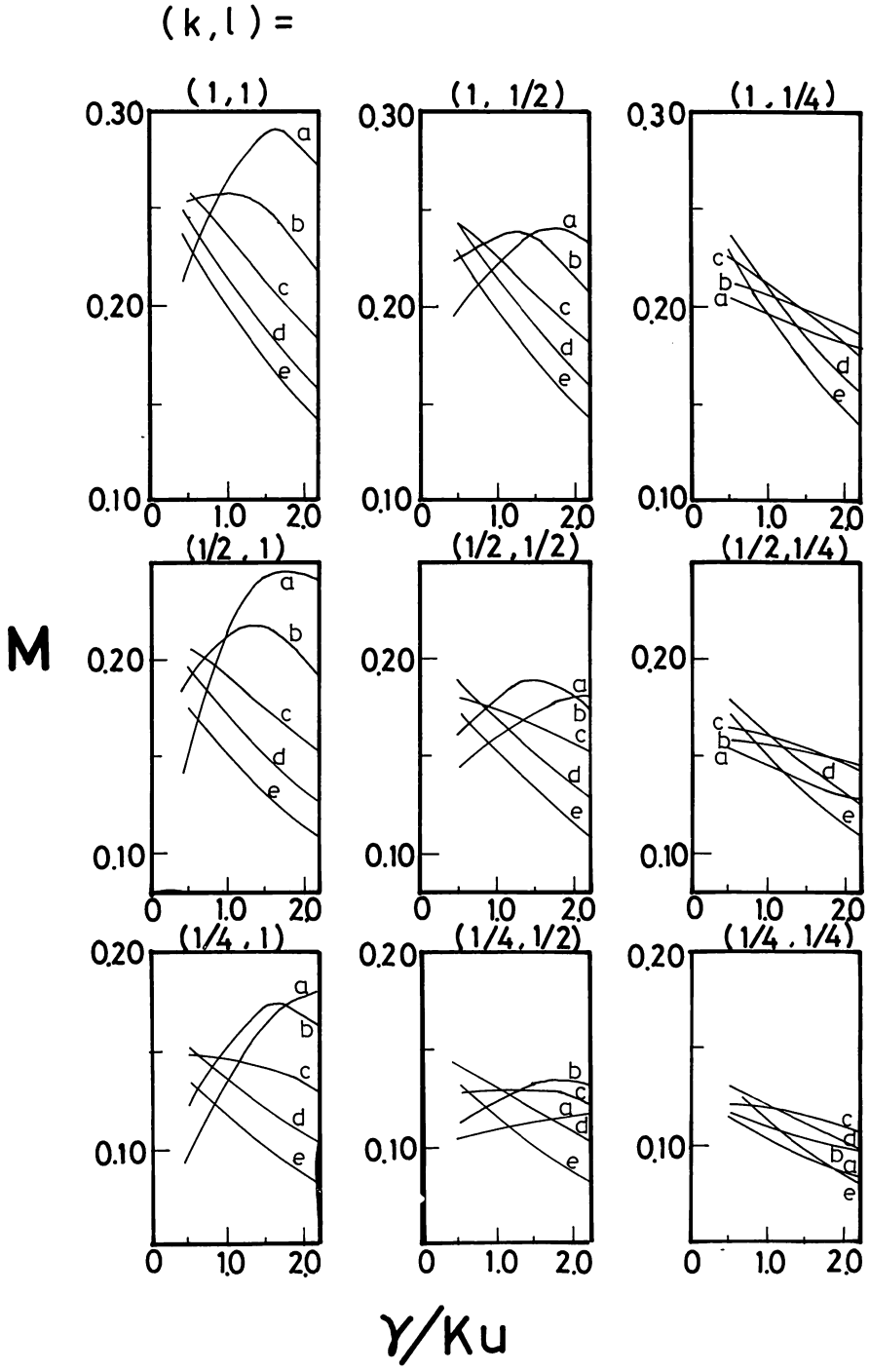

Fig. 8 The relation between the parameter M and γ/Ku. The pair of numbers in a parenthesis on each block represents the value of k and ℓ. The values of k_{ab} used for five curves in each block are (a) $k_{ab}=1$, (b) $k_{ab}=1/2$, (c) $k_{ab}=1/4$, (d) $k_{ab}=1/10$, (c) $k_{ab}=0$

monotonously with increasing P_T, as were the results shown in Fig. 2. According to the discussion on k_a in **2** (eqs. (18)~(21)), the range $k_a \geqq 1/2$ corresponds to eqs. (18), (19), and (20). However, among these equations, only eq. (19) satisfies also the conditions $\ell \geqq 1/2$. Therefore, together with the conditions shown in (A), it can be said that the value of M monotonously increases with increasing P_T if $\gamma_{at} \cong \gamma_{al}$, i.e., if the intracoherence between Zeeman-sublevels are preserved. The same discussion on k_b holds true if the suffices a and b are interchanged in the discussion described above.

(C) Though the values of M in Fig. 8 are smaller than those in Fig. 2 at each value of P_T, they increase with increasing k and approaches those in Fig. 2. That is, it is desirable for the value of k to be large so that the values of M in Fig. 8 approach those in Fig. 2. However, according to the discussion on k in **2** (eqs. (12) and (13)), k takes the values of about unity, i.e., a large value, when the condition (A) ($\gamma_a \leqq \gamma_{al}$, $\gamma_b \leqq \gamma_{bl}$) holds true. Therefore, this condition is compatible with the condition (A).

Because these three condition are compatible with each other and overlap with each other, they can be summarized. That is, two conditions described below are required so that the calculated result of the relation between M and P_T has qualitatively the same characteristics as those of the experimental results shown in Fig. 2:

(I) Increasing the rate of population exchange between Zeeman-sublevels, and, equivalently, $\gamma_a \leqq \gamma_{al}, \gamma_b \leqq \gamma_{bl}$.

(II) Preserving the intracoherence between Zeeman-sublevels, and, equivalently, $\gamma_{at} \cong \gamma_{al}$, $\gamma_{bt} \cong \gamma_{bl}$.

It can be interpreted that these two points are the causes of the characteristics of the experimental results shown in Fig. 2. Especially, for the case of k_{ab}=0(i.e., $\gamma_{at}, \gamma_{bt} \to \infty$) as shown by the curve e in each block of Fig. 8, the value of M monotonously decreases with increasing P_T whatever the values of ℓ and k are. That is, the characteristics of the calculated results will be completely contrary to those of the experimental results if the intracoherence between Zeeman-sublevels is neglected, as was in the conventional theory[3]. Therefore, it is necessary to introduce the intracoherence into the model used for calculation in such a manner as done in the present work.

In additions, the pressure dependences of other relaxation constants than γ can be, if desired, immediately estimated by using the range of k, ℓ, k_{ab} as shown in (A), (B), and (C), and by eqs. (7)~(11), and (22).

5. The Effect of Dispersion on the Parameter M

In **4**, the value of M was obtained by the calculated result of the relations between $I_\pm$ and $\nu_\pm$. On the other hand, the value of M was experimentally obtained by the detuning curves measured in the previous work[4], i.e., by the relations between $I_\pm$ and $\Omega_\pm$. Therefore, if the relations between $\nu_\pm$ and $\Omega_\pm$ are nonlinear, the results in **4** must be compared with those in Fig. 2 after some corrections. In this section, the relations between $\nu_\pm$ and $\Omega_\pm$, ie., the dispersion of the medium, are discussed to know whether these corrections are required.

The values of ν_+ and ν_- are obtained as functions of Ω_+ and Ω_- from eqs. (65-a) and (65-b) by the following method: As the first step, the values of I_+ and I_- are calculated by substituting Ω_+ and Ω_- into ν_+ and ν_- in eq. (65-a). These values of I_+ and I_- have already been obtained in **4**. The values of ν_+ and ν_- are obtained by substituting these values of I_+ and I_- into eq. (65-b). As the next step, more exact values of I_+ and I_- are obtained by substituting these values of ν_+ and ν_- into eq. (65-a), and, finally, more exact values of ν_+ and ν_- are calculated from eq. (65-b). Though this procedure can be iterated, this iteration was carried only one stage in the present work because the first step gave answers within 1×10^{-4} of the exact values of ν_+ and ν_-.

It is necessary to know the value of κ in eq. (65-b) when the values of ν_+ and ν_- are calculated from eqs. (65-a) and (65-b). The values of κ was obtained from the experimental results by the following method: The value of the width of the power detuning curve measured

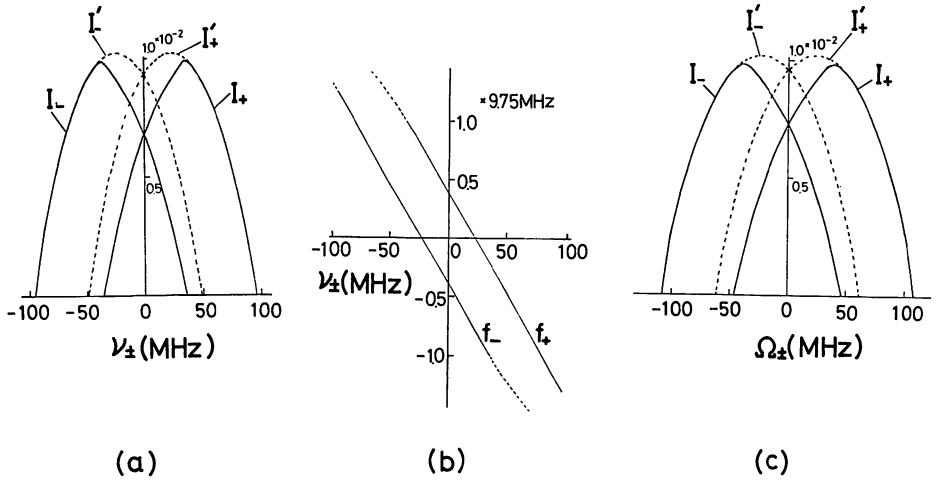

Fig. 9 (a) The relations between $I_{\pm}$ and $\nu_{\pm}$ in which the effect of dispersion is not considered. Curves I_+ and I_- represent the results in the absence of the mode competition. In this figure, the value of M is found to be 0.271.
(b) The relations between $f_{\pm}$ and $\nu_{\pm}$, i.e., the dispersion characteristics of the active medium. The values of f_+ and f_- are given in eq. (78). The value of κ used is 9.75MHz.
(c) The relations between $I_{\pm}$ and $\Omega_{\pm}$ in which the effect of dispersion is considered by using Fig. 9 (b). In this figure, the value of M is found to be 0.271.
In Figs. 9 (a)~(c), the values of parameters used are H=15 G, P_T=8.1 Torr, γ/Ku=2.2, Ku=71.6MHz, k=ℓ=k_{ab}=1, and $\aleph_{\pm}$=1.15.

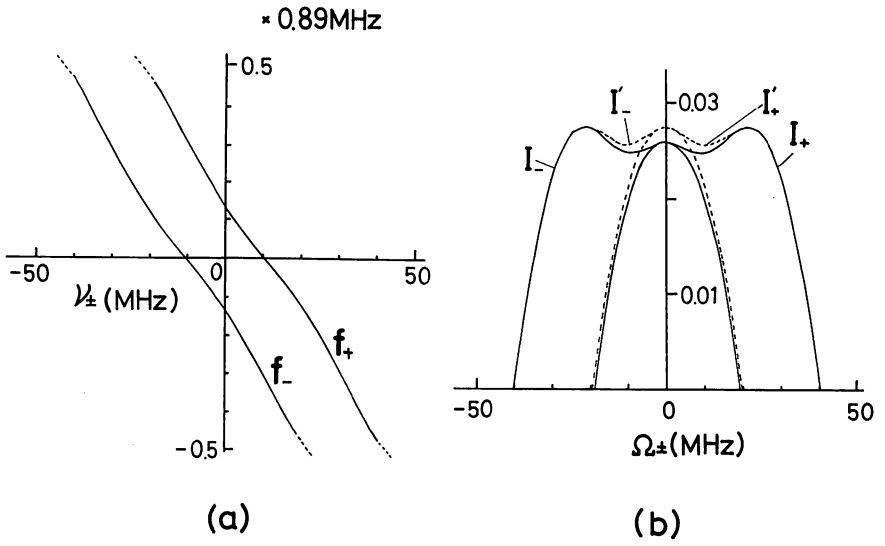

Fig. 10 The results for the case of low pressure. In these figures, the same values of parameters were used as in Fig. 7.
(a) The relations between $f_{\pm}$ and $\nu_{\pm}$, i.e., the dispersion characteristics of the active medium. κ=0.89MHz.
(b) The relations between $I_{\pm}$ and $\Omega_{\pm}$ by using Figs. 7 and 10 (a). In this figure, the values of M is found to be 0.029.

in the experiment[4] was larger than that of a longitudinal-mode interval. This difference is due to the effect of frequency-pulling.

The ratio between these values are tentatively represented as $r(>1)$ in this section. Then, the values of κ is determined so that the ratio between the widths of the curves $I_\pm$ vs $\Omega_\pm$ calculated in this section and those of $I_\pm$ vs. $\nu_\pm$ calculated in **4** will be equal to r.

Calculated results are shown in Figs. 9 and 10. Curves in Fig. 9 correspond to the case of the greatest value of M in Fig. 8, i.e., the case when the mode competition is clearly observed. The values of the three parameters (k, ℓ, and k_{ab}) are unity. Figure 9 (a) represents relations between $I_\pm$ and $\nu_\pm$, which have been already obtained in **4**. The value of M is known to be 0.271 from this figure. Figure 9(b) represents relations between $f_\pm$ and $\nu_\pm$, where f_+ and f_- are defined as

$$f_\pm = \sigma_\pm - \rho_\pm I_\pm - \tau_{\pm\mp} I_\mp \qquad (78)$$

from eq. (65-b). The value of κ used was 9.75MHZ, which was calculated from the experimental results by using the method described above. Figure 9(c) represents the relations between $I_\pm$ and $\Omega_\pm$ which were obtained by the relations in Figs. 9(a) and 9(b). The value of M obtained from Fig. 9(c) is 0.271 which is equal to that of Fig. 9(a), i.e., it is found that the values of M in Fig. 9 is independent of the dispersion of the medium. This is because the relations between $f_\pm$ and $\nu_\pm$ are linear. Fig. 10 represents the calculated results for the case of low pressure, in which the same values of parameters were used as in Fig. 7. Figure 7 represents relations between $I_\pm$ and $\nu_\pm$ as shown in Fig. 9 (a), and the value of M obtained from Fig. 7 is 0.029. Figure 10 (a) represents relations between $f_\pm$ and $\nu_\pm$, in which the value of κ used is 0.89MHz. Figure 10(b) represents the relations between $I_\pm$ and $\Omega_\pm$ which were obtained from the relations in Figs. 7 and 10 (a). The value of M is 0.029 in Fig. 10 (b), which is equal to that of Fig. 7. Though one may notice the nonlinearity in relations between $f_\pm$ and $\nu_\pm$ in Fig. 10 (a), it is known that this nonlinearity is not so clear as to give any effects on the value of M.

The highest value of P_T on Fig. 8 was used for Fig. 9 (c), and the lowest value was for Fig. 10 (b). It was known that the value of M was independent of the dispersion at other values of P_T in Fig. 8., and therefore, the results in **4** can be directly compared with those shown in Fig. 2 without considering the effect of the dispersion.

6. Isotope Effects of Xe on the Parameter M

It has been assumed that Xe gas contained only one isotope in the previous sections. However, naturally available Xe gas was used in the experiment[4], which has many kinds of isotope. Therefore, isotope effects on the value of M will be discussed in this section.

The physical quantities of each isotope in naturally available Xe (Xe^{nat}) are given in Table 2[16]. The values of I_+ and I_- are obtained after calculating each coefficient in eq. (65) for Xe^{nat} which is the superposition of those of all the isotopes by using Table 2. Each coefficient is expressed as

Table 2. The physical quantities of each isotopes in Xe^{nat}.

M_j : The mass constant of the jth isotope.
a_j : The fractional abundance of the jth isotope.
Δf_j : The frequency shift of the jth isotope from the center frequency of the 3.51μm laser line.[16]
Ku_j : The Doppler broadening constant of the jth isotope.

M_j		124	126	128	129	130	131	132	134	136
a_j	(%)	0.096	0.09	1.92	26.44	4.08	21.18	26.8	10.44	8.87
Δf_j	(MHz)	/	/	-88	12	-34	-64	12	52	92
Ku_j	(MHz)	74.7	74.1	73.6	73.3	73.0	72.7	72.4	71.9	71.4

$$\sigma_{\pm n} + i\alpha_{\pm n} = \left[\sum_j a_j \frac{35}{4}\kappa_j \left\{ Z\left[\frac{\nu_\pm - \omega_\pm - \Delta f_j}{Ku}, \frac{\gamma}{Ku}\right] - i\frac{1}{\aleph_{\pm n}} \cdot \mathrm{Im}\left[Z\left[\frac{\nu_{\pm M} - \omega_\pm - \Delta f_j}{Ku}, \frac{\gamma}{Ku}\right]\right]\right\}\right] / \sum_j a_j \quad (79)$$

$$\rho_{\pm n} + i\beta_{\pm n} = \left\{\sum_j a_j \frac{1484}{128}\kappa_j \gamma_A \gamma_B \sum_{m=1}^{4} J_{m1}^{\pm}\left[\frac{\nu_\pm - \omega_\pm - \Delta f_j}{Ku}, \frac{\gamma}{Ku}\right]\right\} / \sum_j a_j \quad (80)$$

$$\tau_{\pm\mp n} + i\theta_{\pm\mp n} = \sum_j a_j \frac{1}{128}\kappa_j \gamma_A \gamma_B \left[\sum_{m=1}^{4}\left\{504 J_{m2}^{\pm}\left[\frac{\nu_\pm - \omega_\pm - \Delta f_j}{Ku}, \frac{\gamma}{Ku}\right] + 84 J_{m3}^{\pm}\left[\frac{\nu_\pm - \omega_\pm - \Delta f_j}{Ku}, \frac{\gamma}{Ku}\right]\right\}\right] / \sum_j a_j \quad (81)$$

where

$$\kappa_j = \frac{\nu \bar{N}_n p^2}{\epsilon_0 \hbar K u_j} \quad . \quad (82)$$

The values of ν_+ and ν_- at which the second term of the right-side of eq. (79) takes the maximum value are expressed as ν_{+M} and ν_{-M}, respectively. The notes a_j, Δf_j, and Ku_j represent the fractional abundance, the isotope shift, and the Doppler broadening constant of the jth isotope, respectively. Calculated results are shown in Figs. 11 and 12. The values of parameters used in Fig. 11 are the same as in Fig. 9. Figure 11 (a) represents the relations between $I_\pm$ and $\nu_\pm$. The value of M obtained from this figure is 0.250, which is smaller than that from Fig. 9. Figure 11 (b) represents the relations between $f_\pm$ and $\nu_\pm$, i.e., the dispersion characteristics of the medium. Curves f_+ and f_- are linear, as those in Fig. 9 (b), and it is confirmed that the value of M is also independent of dispersion. Curves in Fig. 12 were obtained by using the same values of parameters as was used in Figs. 7 and 10. Figure 12 (a) represents the relations between $I_\pm$ and $\nu_\pm$. The values of M obtained from this figure is 0.012, and is smaller

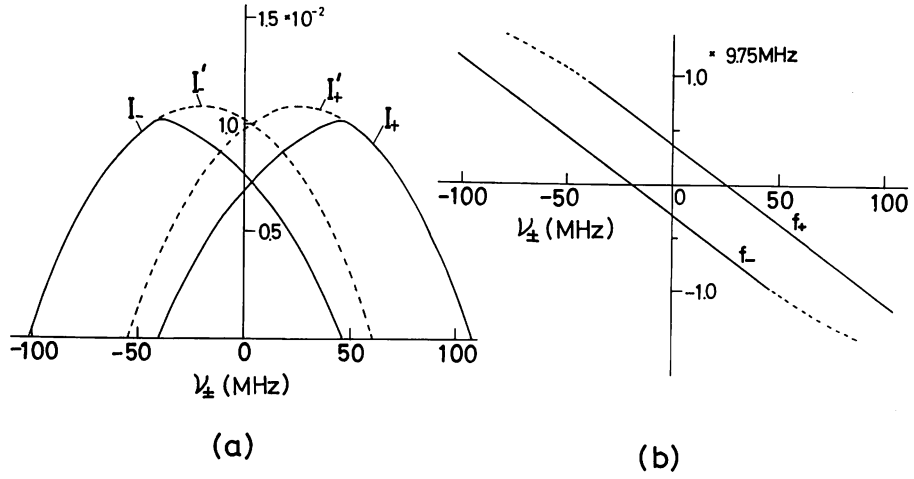

Fig. 11 Calculated results in which the isotope effect was considered. In these figures, the same values of parameters were used as in Fig. 9.
(a) The relations between $I_\pm$ and $\nu_\pm$. In this figure, the value of M is found to be 0.250.
(b) The relations between $f_\pm$ and $\nu_\pm$. κ=9.75MHz.

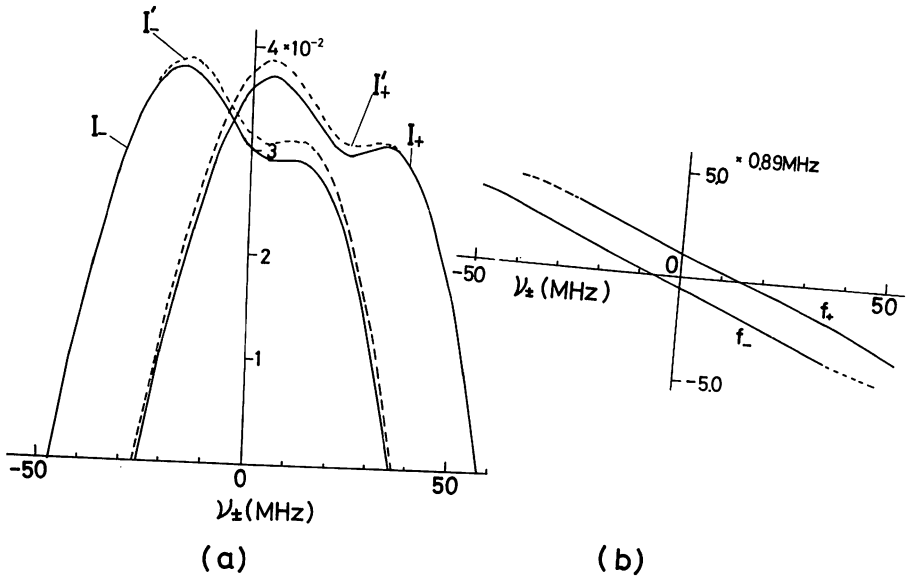

Fig. 12 Calculated results for the low pressure. The isotope effect was considered. In these figures, the same values of parameters were used as in Fig. 7.
(a) The relations between $I_{\pm}$ and $\nu_{\pm}$. In this figure, the value of M is found to be 0.012.
(b) The relations between $f_{\pm}$ and $\nu_{\pm}$. κ=0.89MHz.

than that from Fig. 7. Figure 12 (b) represents the relation between $f_{\pm}$ and $\nu_{\pm}$. It is also confirmed that the value of M is independent of the dispersion shown in Fig. 12 (b).

According to the discussion above, it was shown in the range of P_T in Fig. 8 that the value of M decreased if the isotope effects were considered, and the amount of decrease was between 0.017 and 0.021. That is, the mode competition is suppressed by isotope effects. On the other hand, it was shown that the value of M was independent of the effect of dispersion even if isotope effects was considered.

7. Discussion

The coherence between Zeeman-sublevels (intracoherence) has not been considered in the previous works.[1~3] In the present work, it was considered and the calculated results were obtained which agree with the experimental results. However, this agreement is not quantitatively accurate, e.g., the value of M obtained by the experiment is slightly higher than that by the calculation. Furthermore, the shape of the detuning curve experimentally obtained has some differences with that of calculated one. It is necessary to use a model which includes more precise mechanisms of atomic collisions and relaxation to reduce these disagreements. In the present work, however, the calculated results were obtained in which the sign of dM/dP_T agrees with that of the experimental results by using the simple model and by using the pressure dependence of the relaxation constants. That is, it was shown by the calculation as well as by the experiment that the strength of the mode competition increased with increasing P_T. Therefore, it can be said that one method of explaining the cause of the experimental results was obtained by the present study. The developments of a more precise model and better formulations are remained to be solved.

8. Conclusion

In the present paper, the results of the numerical calculation were given which dealt with the mode competition between two oppositely circularly polarized Zeeman components (the σ_+ and σ_- modes) of a He-Xe laser at 3.51μm in an axial magnetic field.

A parameter M was defined to express the strength of the mode competition. Then, the cause of the pressure dependence of M was discussed by comparing the calculated and the experimental results. The results obtained here can be summarized as follows:

(1) It was interpreted that the increase of M with increasing of the gas pressure P_T was due to the increase of population exchange between Zeeman-sublevels ($\gamma_a \leqq \gamma_{a1}$, $\gamma_b \leqq \gamma_{b1}$) and to the preservation of the intracoherence between them ($\gamma_{at} \cong \gamma_{a1}$, $\gamma_{bt} \cong \gamma_{b1}$),

(2) It was shown that the value of M was independent of the characteristics of the dispersion of the active medium.

(3) It was shown that the value of M decreased because of the isotope effects by several kinds of isotopes in naturally available Xe gas, and the amount of decrease was between 0.017 and 0.021. Furthermore, it was shown that the value of M was still independent of the characteristics of the dispersion when isotope effects were considered.

Acknowlegements

The authors are much indebted to Dr. T. Akahane of their laboratory for his valuable discussion.

This work was partially supported by the Grant-in-Aid for Scientific Research from the ministry of Education.

References

1) W. Culshaw and J. Kanneland: Phys. Rev. **156** (1967) 308
2) W. J. Tomlinson and R. L. Fork: Phys. Rev. **164** (1967) 466
3) M. Sargent III, W. E. Lamb, Jr., and R. L. Fork: Phys. Rev. **164** (1967) 436, 450
4) M. Ohtsu and T. Tako: Jpn. J. Appl. Phys. **17** (1978) 177
5) M. Ohtsu and T. Tako: J. Appl. Phys. **50** (1979) 599
6) M. Ohtsu and T. Tako: Jpn. J. Appl. Phys. **17** (1978) 2169
7) K. Shimoda: *High-Resolution Laser Spectroscopy*, ed. K. Shimoda (Springer, Berlin, 1976) p. 22, eq. (2.25)
8) C. H. Wang, W. J. Tomlinson, and R. T. George, Jr.: Phys. Rev. **181** (1969) 125
9) P. W. Smith and P. J. Maloney: Appl. Phys. Lett. **22** (1973) 667
10) M. Sargent III, M. O. Scully, and W. E. Lamb, Jr.: *Laser Physics* (Addison-Wesley. Reading, 1974) p184
11) E. U. Condon and G. H. Shortley: *The Theory of Atomic Spectra* (Cambridge University Press, New York, 1935) p. 63
12) B. D. Fried and S. D. Conte: *The Plasma Dispersion Function* (Academic Press, New York 1961)
13) H. R. Schlossberg and A. Jawan: Phys. Rev. Lett. **17** (1966) 1242
14) R. J. Freiberg and L. A. Weaver: J. Appl. Phys. **38** (1967) 250
15) M. Tsukakoshi and K. Shimoda: J. Phys. Soc. Jpn. **26** (1969) 758
16) J. Nella, S. Y. Szeto, P. Rabinowitz, and J. T. Latourrette: IEEE J. Quantum Electron. **QE-12** (1976) 543

JPN. J. APPL. PHYS. Vol. 18 (1979), No. 8

Improvements in the Long-Term Frequency Stability of the He–Xe Laser at 3.51 μm

Motoichi OHTSU, Ryohei KOYAMA and Toshiharu TAKO

Research Laboratory of Precision Machinery and Electronics, Tokyo Institute of Technology, 4259 Nagatsuta-cho, Midori-ku, Yokohama, Kanagawa 227

(Received April 26, 1979)

The authors have carried out an experiment on the frequency stabilization of an He–Xe laser at 3.51 μm by using the inverted Lamb dip in H_2CO.[1] However, it is necessary to improve the long-term frequency stability* of this laser to use it as an optical frequency standard or a light source for spectroscopic studies. In the present work, the results of the improvement are reported.

The laser tube used was the same as in the previous work,[1] with a more rigid cavity to avoid mechanical vibrations. Furthermore, the previous PZT (Lansing 21.837) was replaced by a Burleigh PZ-81 to construct a new type of PZT driver. The other parts of the apparatus were the same as in the previous work.[1]

The curve A in Fig. 1 represents the frequency stability of the laser, which has previously been measured.[1] The PZT driver used for this experiment incorporated an integrating amplifier. On curve A,

$$\sigma = 6.6 \times 10^{-12} \quad \text{at} \quad \tau = 10\ \text{s}, \qquad (1)$$

where σ and τ represent the square root of the Allan variance[2] σ^2 and the integration time, respectively. For $\tau > 10$ s, σ increases with increasing τ because the drift due to thermal expansion of the cavity length could not be compensated. In the present work, however, as a filter (-7 dB/decade) was connected at the next stage of the integrating amplifier, the thermal drift could be compensated, and the result shown by curve B in Fig. 1 was obtained. On curve B,

$$\sigma \propto \tau^{-1/2} \quad \text{for} \quad 100\ \text{ms} \leqq \tau \leqq 1000\ \text{s}, \qquad (2)$$

*In the present paper, this term is used to represent the frequency stability for $\tau \geqq 1$ s, where τ represents the integration time.

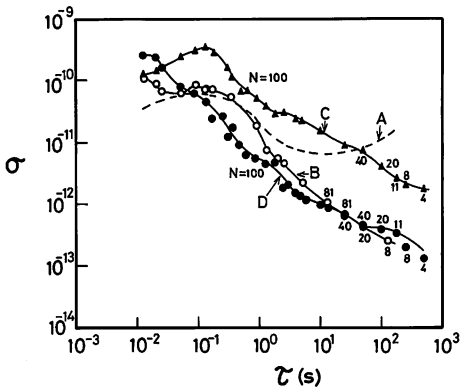

Fig. 1. The square root of the Allan variance σ^2 of the frequency fluctuations. τ and N represent the integration time and the number of data, respectively.
A: The result of the previous work.[1]
B: The result of the present work using the PZT driver with an integrating amplifier and a filter (-7 dB/decade).
C: The result obtained by the same apparatus as for curve B. However, the signal-to-noise ratio of the first derivative signal of the inverted Lamp dip was lower than that of curve B.
D: The result obtained under almost the same conditions as that of curve C. The difference was, a proportional amplifier was added parallel to the integrating amplifier in the PZT driver.

and

$$\sigma = 2.8 \times 10^{-13} \quad \text{at} \quad \tau = 100\ \text{s}. \qquad (3)$$

The signal-to-noise ratio of the first derivative signal of the inverted Lamb dip was sometimes low because of the instability of the discharge in the laser tube. Such a signal is shown in Fig. 2(a). For comparison, the signal obtained under a stable discharge condition is shown in Fig. 2(b). Curve B in Fig. 1 was obtained by using the signal of Fig. 2(b). Curve C in Fig. 1 represents the result using the signal of Fig. 2(a). On curve C,

$$\sigma = 4.8 \times 10^{-12} \quad \text{at} \quad \tau = 100\ \text{s}, \qquad (4)$$

which is 17 times larger than that of eq. (3). A proportional amplifier was added parallel to the integrating amplifier in the PZT driver to get a smaller value of σ than that of eq. (4) under such an unstable discharge condition. The block diagram of the PZT driver used is shown in Fig. 3. Figure 4 represents the time dependence of the laser frequency fluctuations obtained by using the signal of Fig. 2(a). Part A in this figure represents the result obtained

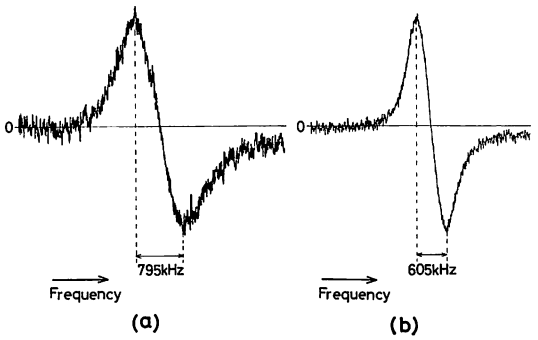

Fig. 2. The first derivative signal of the inverted Lamb dip in H_2CO traced on a chart recorder.
(a): The signal in which the signal-to-noise ratio is lower than that of (b) because of the instability of the discharge in the laser tube. By using this signal, curves C and D in Fig. 1 were obtained.
(b): The signal obtained under a stable discharge condition. By using this signal, curve B in Fig. 1 was obtained.

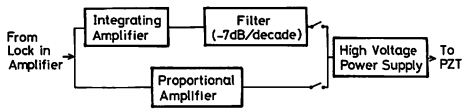

Fig. 3. The block diagram of the PZT driver used in the present work.

without using the proportional amplifier in Fig. 3.

Parts B and C represent the results using the proportional amplifier. The voltage gain of the proportional amplifier for part C is higher than that for part B. It can be seen that the frequency fluctuations of parts B and C are lower than those of part A. The relation between σ and τ for part C is shown by curve D in Fig. 1. On this curve,

$$\sigma = 3.7 \times 10^{-13} \quad \text{at} \quad \tau = 100\ \text{s}. \qquad (5)$$

This value is smaller than that of eq. (4) and is

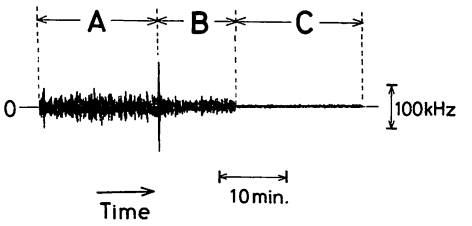

Fig. 4. The time dependence of the frequency fluctuations traced on a chart recorder. A: The result obtained without using the proportional amplifier in the PZT driver of Fig. 3.
B: The result obtained by connecting the proportional amplifier with a low voltage gain to the PZT driver.
C: The result obtained by connecting the proportional amplifier with a high voltage gain to the PZT driver.

nearly equal to that of eq. (3). From eq. (5), it can be confirmed that σ can be kept smaller than 1×10^{-12} at $\tau = 100$ s by using the proportional amplifier along with the integrating amplifier. Furthermore, it can be seen from Fig. 1 that the values of σ on curves C and D are smaller than that on curve A for $\tau \geqq 1$ s. This is an improvement in the long-term frequency stability compared with the previous result.[1)]

Higher stability can be expected by developing a low-noise laser tube and by increasing the response speed of the controlling electronic circuit.

This work was partially supported by a Grant-in-Aid for Scientific Research from the Ministry of Education, Science and Culture.

References

1) M. Ohtsu and T. Tako: Jpn. J. Appl. Phys. **17** (1978) 2169.
2) D. W. Allan: Proc. IEEE **54** (1966) 2.

JPN. J. APPL. PHYS. Vol. 18 (1979), No. 8

Development of a Frequency-Offset-Locked He–Xe Laser at 3.51 μm

Motoichi OHTSU, Ryohei KOYAMA, Anung KUSNOWO and Toshiharu TAKO

Research Laboratory of Precision Machinery and Electronics, Tokyo Institute of Technology, 4259 Nagatsuta-cho, Midori-ku, Yokohama, Kanagawa 227

(Received April 26, 1979)

Frequency-offset-locking techniques of gas lasers have been used to construct a light source for high-resolution laser spectroscopy.[1] The frequency of the offset-locked laser can be varied while a very high frequency stability can be maintained. In the present work, a frequency-offset-locked He–Xe laser was constructed and its frequency stability was measured.

The experimental apparatus is shown in Fig. 1. In this figure, the frequency of the first laser is stabilized by using the inverted Lamb dip in H_2CO, and its stability is shown in Fig. 2.[2] In Fig. 2,

$$\sigma = 3.7 \times 10^{-13} \quad \text{at} \quad \tau = 100\,\text{s}, \qquad (1)$$

where σ and τ represent the square root of the Allan variance[3] σ^2 and the integration time, respectively. The second laser was frequency-offset-locked by using the first laser as a reference laser. The beat frequency between the first and the second laser, (i.e., the reference

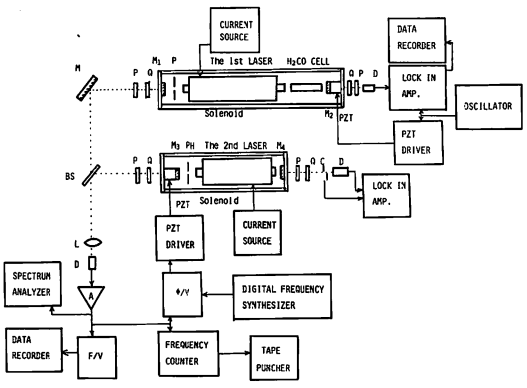

Fig. 1. Experimental apparatus.
ϕ/V: The phase-to-voltage converter used to control the beat frequency. F/V: The analog frequency-to-voltage converter used to measure the beat frequency for $\tau < 1$ s. BS: Beam splitter. C: Chopper. D: Detector. L: Lens. M: Mirror. P: Polarizer. PH: Pinhole. Q: Quarter-wave plate.

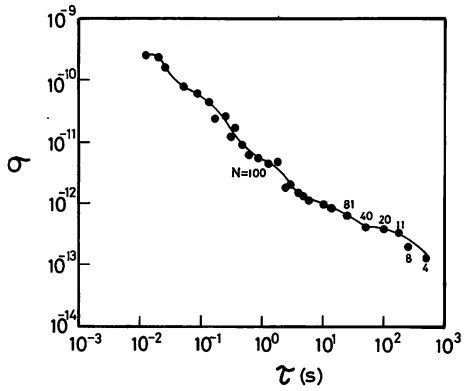

Fig. 2. The square root of the Allan variance σ^2 of the frequency fluctuations of the first laser (the reference laser). τ represents the integration time, N the number of data.

laser and the frequency-offset-locked laser) was locked to the output frequency of a digital frequency synthesizer. The phase-to-voltage converter (ϕ/V converter) shown in Fig. 1 was used to convert the time-integrated value of the beat frequency into voltage. The experimental results of the frequency fluctuations of the locked beat signal are shown in Fig. 3. In this figure, the value of σ represents the frequency fluctuations of the beat signal which are normalized to the frequency of the He–Xe

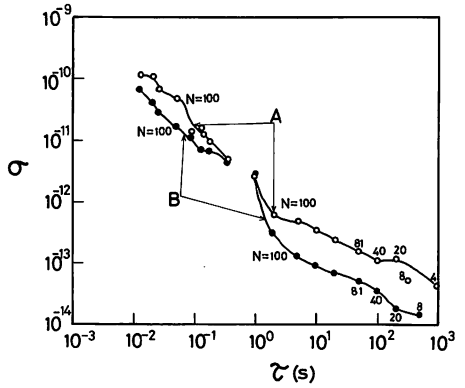

Fig. 3. The square root of the Allan variance σ^2 of the frequency fluctuations of the beat signal between the two lasers. The value of σ is normalized to the He–Xe laser frequency. For $\tau < 1$ s, σ was measured by using an analog frequency-to-voltage converter, and for $\tau \geqq 1$ s, by a frequency counter.
A: A PZT driver with a proportional amplifier and a filter (−7 dB/decade) was used to get the results represented by this curve.
B: A PZT driver with a proportional amplifier, an integrating amplifier, and a filter (−7 dB/decade) was used here.

laser at 3.51 μm. These results can be interpreted as representing the traceability of the frequency of the second laser to that of the first laser. In Fig. 3, the values of σ for $\tau<1$ s were calculated from the data measured by an analog frequency-to-voltage converter, while a frequency counter was used for $\tau\geqq 1$ s. Curve A in Fig. 3 represents the experimental result in which the output signal of the ϕ/V converter was applied to a PZT driver with a proportional amplifier and a filter (−7 dB/decade). In curve B, on the other hand, the PZT driver with a proportional amplifier, an integrating amplifier, and a filter (−7 dB/decade) was used. It can be shown that higher stability was obtained on curve B than on curve A. In this figure, on curve A,

$$\sigma=1.1\times10^{-13} \quad \text{at} \quad \tau=100\ \text{s}, \tag{2}$$

and on curve B,

$$\sigma=3.8\times10^{-14} \quad \text{at} \quad \tau=100\ \text{s}. \tag{3}$$

In the experiment with the results shown in Fig. 3, the frequency of the first laser was modulated but that of the second laser was not; consequently, the beat frequency was modulated. Figure 4 represents the experimental results of the effect of frequency modulation on the frequency stability of the beat signal. Curve A in Fig. 4 represents the result in which the frequency of the first laser only was modulated, as it was in Fig. 1. Curve B represents the experimental result in which the frequency of the second laser was modulated synchronously with the first laser. This synchronous modulation can have no effect on the beat frequency, i.e., the beat frequency was not modulated. In all of the experiments described here, the values of the modulation frequency and the maximum frequency deviation of the modulation were 501 Hz and 877 kHz, respectively. It can be concluded from these results that the stability of the beat frequency is independent of frequency modulation for 10 ms$\leqq\tau\leqq$1000 s because the shape of curve A in Fig. 4 is similar to curve B in this range of τ.

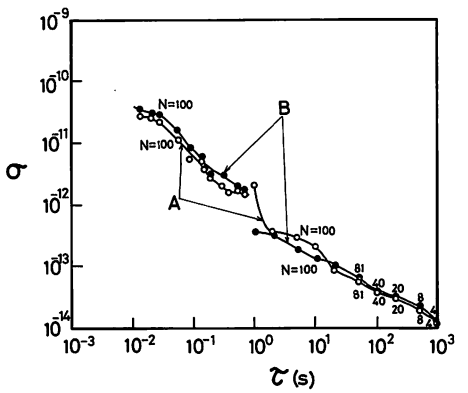

Fig. 4. The square root of the Allan variance σ^2 of the frequency fluctuations of the beat signal between the two lasers. The same PZT driver was used as for curve B in Fig. 3.
A: The frequency of the first laser only was modulated. Therefore, the beat frequency was modulated. The values of the modulation frequency and the maximum frequency deviation of the modulation were 501 Hz and 877 kHz, respectively. These values were used for all of the experiments in the present work.
B: The frequency of the second laser was modulated synchronously with that of the first laser. Therefore, the beat frequency was not modulated.

In Figs. 3 and 4, the average value f_b of the beat frequency was 4.0 MHz. This value of f_b can be varied by changing the frequency of the digital frequency synthesizer. The variable range in which the beat frequency was locked was 5.8 MHz, i.e., 0.8 MHz$\leqq f_b\leqq$6.6 MHz. In this range, the characteristics of the relation between σ and τ were independent of the value of f_b, and were similar to those in Figs. 3 and 4.

Because the value of σ on curves A and B in Fig. 3 (or those of eqs. (2) and (3)) are smaller than that on the curve in Fig. 2 (or that of eqs. (3) and (5)), it can be said that the frequency stability of the second laser is nearly equal to that of the first laser.

By improving the performances of the preamplifier for the beat signal, the ϕ/V converter, and the PZT driver, the frequency stability of the second laser can be improved, and its application to several kinds of measurements can be expected.

The authors wish to express their gratitude to Dr. M. Ohi and Mr. Y. Akimoto of the National Research Laboratory of Metrology for their useful discussions.

This work was partially supported by a Grant-in-Aid for Scientific Research from the Ministry of Education, Science and Culture.

References

1) R. L. Barger and J. L. Hall: Phys. Rev. Lett. **22** (1969) 4.
2) M. Ohtsu, R. Koyama and T. Tako: Jpn. J. Appl. Phys. **18** (1979) 1621.
3) D. W. Allan: Proc. IEEE **54** (1966) 2.

Measurement of the width of the inverted Lamb dip in H_2CO at 3.51 μm

Motoichi Ohtsu and Toshiharu Tako

Research Laboratory of Precision Machinery and Electronics, Tokyo Institute of Technology, 4259 Nagatsuta, Midori-ku, Yokohama 227, Japan

(Received 19 May 1978; accepted for publication 13 July 1978)

The width of the inverted Lamb dip in H_2CO at 3.51μm [$5_{1,5}$ (ground state)$\rightarrow 6_{0,6}(v_5=1)$] was measured by using a low-noise He-Xe laser in an axial magnetic field as the light source. To measure the dip width it was necessary to determine first the range of the magnetic field strength and the maximum frequency deviation of the laser frequency modulation. Based on these results, the power-broadening characteristics were measured. Finally, the relation between the dip width free from the power broadening and the pressure of H_2CO was obtained. The dip width (HWHM) was $\Delta\nu_h=(123\pm24)+(155\pm31)P_F$ (kHz), where P_F represents the H_2CO pressure expressed in Pascal.

PACS numbers: 35.80.+s, 07.65.Gj, 42.65.Gv, 42.60.—v

I. INTRODUCTION

The high-resolution spectroscopy of atoms and molecules recently has been improved by the saturated absorption method using highly stabilized lasers. For example, the saturated absorption signal in CH_4 at 3.39 μm [1,2] has been precisely measured and has been applied to stabilize the frequency of He-Ne laser oscillation. The inverted Lamb dip in H_2CO [the vibration-rotation transition: $5_{1,5}$ (ground state)$\rightarrow 6_{0,6}(v_5=1)$] at 3.51-$\mu$m has been first observed in the infrared-microwave double-resonance experiment.[3] However, the pressure dependence of its width has not been reported yet. One of the main reasons is due to the difficulty in getting a low-noise 3.51-μm He-Xe laser light source. In the present work, this dependence was measured with a low-noise 3.51-μm He-Xe laser developed by the authors.

II. EXPERIMENTAL APPARATUS

The experimental apparatus is shown in Fig. 1. The cavity length of the laser was 149 cm and the length of the H_2CO absorption cell was 42 cm. A laser tube with a discharge part of 0.6 cm inner diameter and 75 cm length was used. A stable and low-noise laser oscillation was obtained with a return path and a titanium cold cathode. The output power was 0.5 mW when the total gas pressure was $P_t=4$ Torr (533 Pa), the pressure ratio of He and Xe being $P_{He}/P_{Xe}=49$, and the discharge current was $i_d=6$ mA. Since the absorption-line frequency of H_2CO was about 180 MHz higher than the center of the gain curve of a He-Xe laser, an axial magnetic field of about 130 G was applied to the laser tube to compensate for this frequency gap. A quarter-wave plate and a polarizer were used to separate the higher-frequency component (the σ_+ mode)of the laser output from the lower (the σ_- mode).[4] One of the cavity mirrors was mounted on a piezoelectric transducer (PZT) to control the laser frequency by applying a dc or ac voltage to the PZT. The inverted Lamb dip in H_2CO was observed on the laser power tuning curve and its width was measured by varying the dc voltage on the PZT.

III. DETERMINATION OF THE MAGNETIC FIELD STRENGTH

A. Procedures

The longitudinal-mode frequency interval was 100.7 MHz and was narrower than the width of the laser gain curve which was estimated to be about 150 MHz. Under this situation, two-mode oscillation occurred at the tail of the tuning curve. Therefore, when the inverted Lamb dip appears at the tail of the tuning curve at a certain strength of the magnetic field, the measured value of the dip width will be affected by the characteristics of the two-mode oscillation. This is due to the fact that the linear relationship between the laser frequency and the cavity tuning (the abscissa of the tuning curve) is not valid in the case of the two-mode oscillation. This is because of the frequency pushing between both modes. Therefore, it is necessary for the present experiment to determine first the range of the magnetic field strength in which the relationship is linear.

This is accomplished through the following method: The frequency ν of a single-mode laser is expressed as [5]

$$\nu=(\omega_+ + S\Omega)/(1+S), \tag{1}$$

where ω_+, Ω, and S represent the center frequency of the gain

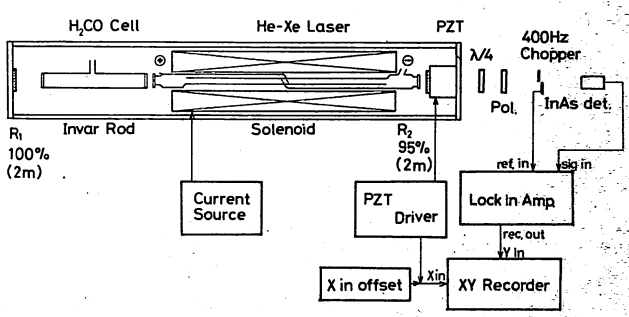

FIG. 1. Experimental apparatus: "X in offset" was used to expand the value of the abscissa of the tuning curve.

 0021-8979/79/020599-03$01.10

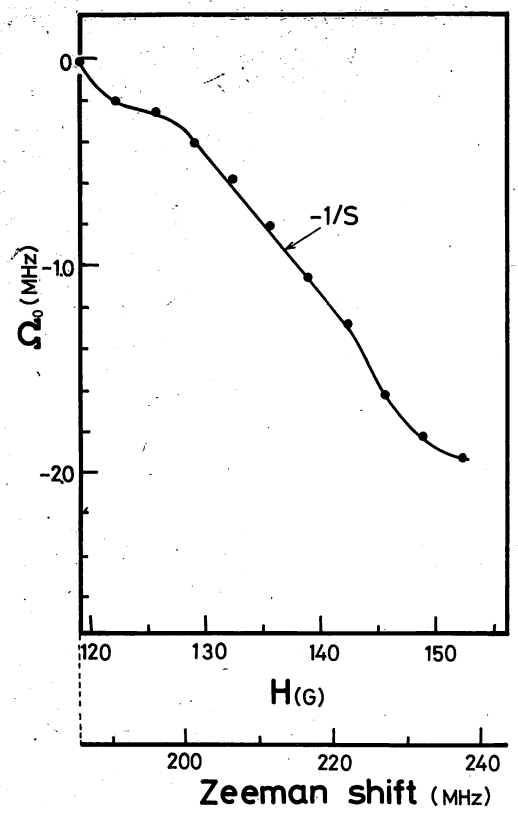

FIG. 2. The relation between Ω_0 and H: The position of the zero point on the ordinate was arbitrarily selected because it was necessary to measure only the change of Ω_0 with respect to H to obtain the right-hand side of Eq. (4).

curve of the σ_+ mode, the longitudinal-mode frequency, and the constant known as the "stabilization factor"[4], respectively.

The value of the longitudinal-mode frequency Ω_0 which corresponds to the center frequency ν_0 of the inverted Lamb dip is given from Eq. (1) as

$$\Omega_0 = -\omega_+/S+(1+S)(\nu_0/S). \tag{2}$$

Furthermore, ω_+ can be expressed as a function of the magnetic field H as

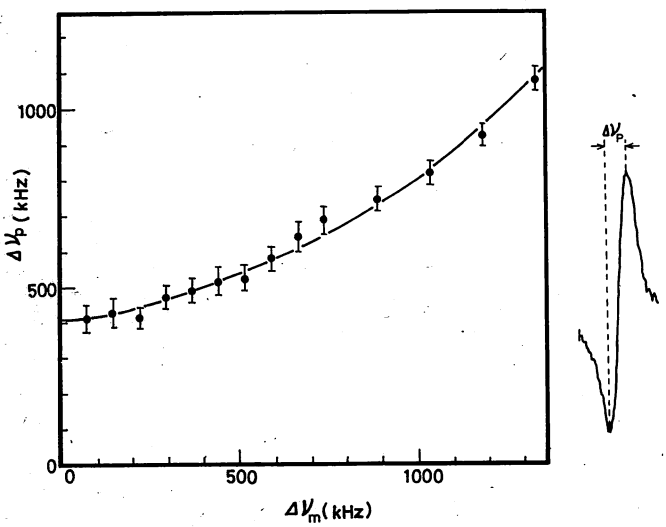

FIG. 3. The relation between $\Delta\nu_p$ and $\Delta\nu_m$: $P_F = 2.1$ mTorr (0.28 Pa).

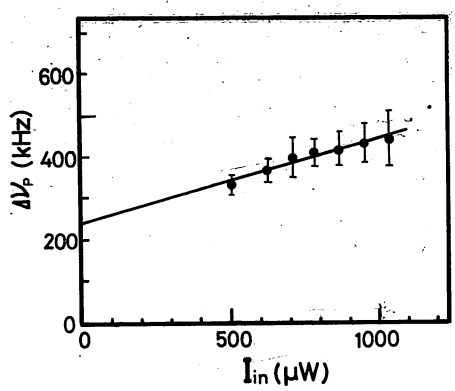

FIG. 4. The relation between $\Delta\nu_p$ and I_{in}: $P_F = 3.9$ m Torr (0.52 Pa).

$$\omega_+ = \omega_0 + 1.4gH, \tag{3}$$

where ω_0 represents ω_+ at $H = 0$, and $g(= 1.114)$ represents the Landé g factor of the Xe transition at 3.51 μm. From Eqs. (2) and (3),

$$\frac{d\Omega_0}{dH} = -1.4g/S. \tag{4}$$

Consequently, it is clear from Eq. (4) that the relationship between Ω_0 and H is linear in the case of the single-mode oscillation. On the other hand, if Eq. (1) is used to express the frequency of one mode in the case of the two-mode oscillation, the value of S will be affected by the other mode and by the frequency pushing effect between both modes. Thus, S is no longer a constant because of its dependence on the frequency, and the linear relationship between Ω_0 and H will not be valid. Hence, if $d\Omega_0/dH$ is measured and the range of H in which this value remains constant is found out, then it will be confirmed that the single-mode oscillation occurs. In this range, the relationship between the laser frequency and the cavity tuning is linear.

B. Results

Figure 2 shows the experimental result. From Fig. 2, it

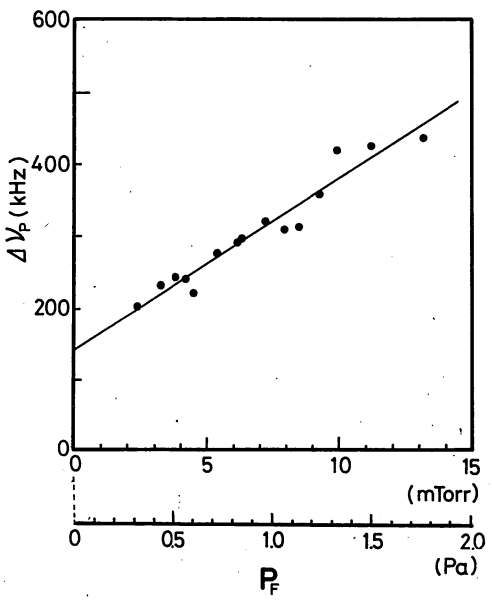

FIG. 5. The relation between $\Delta\nu_p$ free from the power-broadening and P_F.

can be seen that the value of Eq. (4) remains constant for $129 < H < 143$ G. Therefore, H is fixed within this range in the experiments which followed. In this range, S is found to be 23.9. From Eq. (1),

$$\frac{d\nu}{d\Omega} = S/(1+S) = 0.96. \quad (5)$$

Equation (5) shows that the dip width expressed in the frequency unit is 0.96 times measured on the tuning curve. This conversion factor is used to determine the final result [Eqs. (6) and (7)].

IV. EXPERIMENTAL RESULTS

To measure the width of the inverted Lamb dip precisely, the first derivative line shape of dip was traced on an X-Y recorder. Figure 3 shows the results. It was observed that the peak-to-peak width $\Delta\nu_p$ of the signal increased with increasing the maximum frequency deviation $\Delta\nu_m$ of the laser frequency modulation.

Because $\Delta\nu_p$ remained constant within the experimental error (less than 10%) for $\Delta\nu_m < 200$ kHz, $\Delta\nu_m$ was fixed at 140 kHz for the following experiments. In the next experiment, the dependence of $\Delta\nu_p$ on the laser power intensity in cavity I_{in}, i.e., power-broadening characteristics, was measured. In the range of $3.5 < i_d < 10$ mA, I_{in} was linearly proportional to i_d and the noise level on the first derivative signal of the dip was low enough to enable the measurement of the dip width.

The result is shown in Fig. 4. From Fig. 4, it was observed that $\Delta\nu_p$ was linearly proportional to I_{in}. The power-broadening coefficient was 0.2 kHz/μW. This linear dependence means that $I_{in} << I_s$ in this experiment, where I_s represents the saturation parameter of H_2CO. The extrapolation of I_{in} to zero in Fig. 4 made $\Delta\nu_p$ free from the power broadening. Figure 5 shows the dependence of the extrapolated value of $\Delta\nu_p$ on the pressure P_F of H_2CO for $P_F \leq 13$ m Torr (1.73 Pa). The inverted Lamb dip could not be observed for $P_F > 13$ m Torr (1.73 Pa) because the laser power was too low due to the linear absorption by H_2CO. In Fig. 5, the relationship between $\Delta\nu_p$ and P_F (the pressure broadening) can be well expressed by the following linear equation (least-square fitted):

$$\Delta\nu_p = (142 \pm 28) + (179 \pm 36)P_F \text{ (kHz)}; \quad (6)$$

P_F in Pa. Assuming that the inverted Lamb dip has the Lorentzian line shape, its half-width at half-maximum (HWHM) $\Delta\nu_h$ can be expressed as [from Eq. (6)]

$$\Delta\nu_h = \tfrac{1}{2}\sqrt{3}\Delta\nu_p$$

$$= (123 \pm 24) + (155 \pm 31)P_F \text{ (kHz)}; \quad (7)$$

P_F in Pa. The value of $\Delta\nu_h$ in Eq. (7) includes the transit-time broadening of 55 kHz which is determined by the flight time of an H_2CO molecule through the light beam; therefore, if the beam diameter is enlarged, $\Delta\nu_h$ will become smaller.

V. CONCLUSION

In the present experiment, the width of the inverted Lamb dip in H_2CO was measured. The results of the present work can be applied to the frequency stabilization of a He-Xe laser which might be used for the development of a new frequency standard.

[1] R.L. Barger and J.L. Hall, Phys. **22**, 4 (1969).
[2] J.L. Hall, C.J. Bordé, and K. Uehara, Phys. Rev. Lett. **37**, 1339 (1976).
[3] M. Takami and K. Shimoda, Jpn. J. Appl. Phys. **11**, 1648 (1972).
[4] M. Ohtsu and T. Tako, Jpn. J. Appl. Phys, **17**, 177 (1978).
[5] M. Sargent III, M.O. Scully, and W.E. Lamb, Jr., *Laser Physics* (Addison-Wesley, Reading, Mass., 1974), p. 110.

JAPAN. J. APPL. PHYS. Vol. 17 (1978), No. 12

Frequency Stability of an H_2CO-Stabilized He–Xe Laser in an Axial Magnetic Field

Motoichi OHTSU and Toshiharu TAKO
Research Laboratory of Precision Machinery and Electronics, Tokyo Institute of Technology, 4259 Nagatsuta-cho, Midori-ku, Yokohama 227

(Received July 4, 1978)

Frequencies of several lasers have been stabilized by using saturated absorption spectra in atoms or molecules to develop new wavelength standards.[1-3] We report here the results of frequency stabilization of the 3.51 μm He–Xe laser in an axial magnetic field by using the inverted Lamb dip, that is, the saturated absorption in H_2CO.

The experimental apparatus is shown in Fig. 1. A laser tube with a discharge part of 0.6 mm inner diameter and 75 cm length was used. The total pressure was 533Pa. The pressure ratio of He to Xe was 49. The discharge current was 6 mA. Since the absorption line frequency of H_2CO was about 200 MHz higher than the center frequency of the gain curve of a He–Xe laser, an axial D.C. magnetic field of 129.8G was applied to the laser tube to compensate for this frequency gap. In this case, as the center frequency of the gain curve of the σ_+ mode (one component between two oppositely circularly polarized Zeeman components of the laser oscillation) coincides with the absorption line frequency of H_2CO, this mode was used in the present work. The frequency of the σ_- mode (the other Zeeman component) was about 400 MHz lower than the absorption line frequency of H_2CO under this magnetic field. A quarter-wave plate and a polarizer were

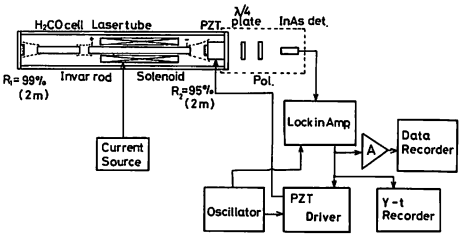

Fig. 1. Experimental apparatus: Broken lines represent plastic tubes used to reduce the effect of air flow.

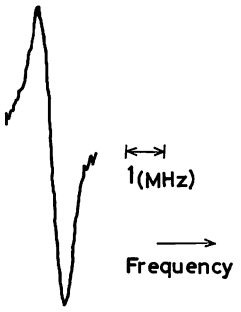

Fig. 2. The first derivative signal of the inverted Lamb dip in H_2CO.

used to separate the σ_+ mode from the σ_- mode. One of the mirrors, R_2, was mounted on a piezoelectric transducer (PZT) for frequency tuning and modulation. The laser oscillated with one longitudinal-mode in the frequency range on the tuning curve in which the inverted Lamb dip appeared.[4] The first derivative signal of the inverted Lamb dip is shown in Fig. 2. A. C. voltage of 10 V (peak-to-peak) was applied to the PZT to modulate the laser frequency. The modulation frequency f_m was 794 Hz. The frequency deviation corresponding to the value of 10 V was 1.48 MHz. This value is comparable to the width of the inverted Lamb dip. For frequency stabilization, however, it was necessary to use this value to obtain the first derivative signal with high signal-to-noise ratio. The linear part between the two peaks of this signal was used as a frequency discriminator to control the laser frequency. The control system consisted of a lock-in amplifier and a PZT driver with an integrator. The time constant τ_L of the low-pass filter in the output stage of the lock-in amplifier was 3 ms. The laser cavity was placed on an optical bench with air dampers.

Error signals from the lock-in amplifier were proportional to the fluctuations of the laser frequency and were recorded by means of a data recorder. The square root of the Allan variance[5] σ^2, which is the measure of frequency stability, and the power spectral density S of the laser frequency fluctuations were calculated from these signals after analog-to-digital conversion.

The result for σ is shown in Fig. 3. τ and N represent the integration time and the number of data, respectively. Curves F_{Xe} and S_{Xe} are for the free running laser and for the stabilized

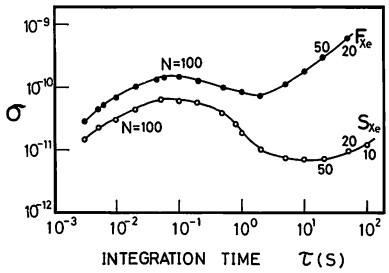

Fig. 3. The square root of the Allan variance σ^2 of the frequency fluctuations. τ and N represent integration time and the number of data, respectively: Curves F_{Xe} and S_{Xe} are for the free running laser and for the stabilized laser, respectively.

laser, respectively. The value of σ on the curve F_{Xe} increases proportional to $\tau^{1/2}$ for $\tau > 2$s. It is due to the thermal expansion of the cavity length. As for the curve S_{Xe}, this increase is suppressed by the feedback control. The minimum value of this curve is

$$\sigma = 6.6 \times 10^{-12} \qquad (1)$$

at $\tau = 10$ s. For $\tau < 50$ ms, curves F_{Xe} and S_{Xe} must be proportional to τ^{-n} with n about 1/2 because of the white-noise generated in the frequency control loop. This relation has been found not only in gas lasers[6,7] but also in dye lasers.[8] However, curves F_{Xe} and S_{Xe} are proportional to $\tau^{1/2}$ for $\tau < 50$ ms as shown in Fig. 3. This is because of the effect of the low-pass filter in the output stage of the lock-in amplifier. Though this effect has been expected to appear for $\tau < 3$ ms ($=\tau_L$), it appeared for $\tau <$ 50 ms in the present experiment. If two equally stabilized He–Xe lasers are available, the value of σ for $\tau < 50$ ms can be measured more precisely by using the beat frequency between them.

Results for the power spectral density, S, are shown in Fig. 4. S is smaller in S_{Xe} than in F_{Xe}. The dip at $f = 0.1$ Hz in S_{Xe} represents the effect of the integrator in the PZT driver. This dip corresponds to the minimum value (eq. (1)) of the curve S_{Xe} in Fig. 3. There are peaks at $f = 50$ Hz in both curves S_{Xe} and F_{Xe}. These peaks represent voltage fluctuations of the power supplies used in the present experiment. Several peaks for $f > 100$ Hz of the curve S_{Xe} are caused by the response characteristics of the frequency control loop.

The frequency stability was improved in the present work as compared to a free running

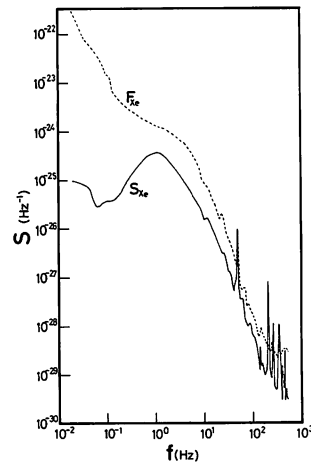

Fig. 4. Power spectral density S of frequency fluctuations. Curves F_{Xe} and S_{Xe} represent the results for the free running laser and the stabilized laser, respectively.

He–Xe laser. The minimum value of σ given by eq. (1) is comparable to CH_4-stabilized 3.39 μm He–Ne lasers (2×10^{-12} at $\tau = 10$ s)[9] which have been carefully constructed by the authors for frequency stabilization. Higher stability can be expected by improving the laser tube, the cavity, and the controlling electronic circuit, and by using the results given in Figs. 3 and 4.

The authors are much indebted to Dr. M. Ohi and Mr. Y. Akimoto of the National Research Laboratory of Metrology for their help with the experiments.

References

1) R. L. Barger and J. L. Hall: Phys. Rev. Letters **22** (1969) 4.
2) G. R. Hanes and K. M. Baird: Metrologia **5** (1969) 32.
3) F. R. Peterson, D. C. McDonald, J. D. Cupp and B. L. Danielson: Phys. Rev. Letters **31** (1973) 573.
4) M. Ohtsu and T. Tako: to be published in J. appl. Phys. **49** (1978).
5) D. W. Allan: Proc. IEEE **54** (1966) 2.
6) H. Hellwig, H. E. Bell, P. Kartaschoff and J. C. Bergquist: J. appl. Phys. **43** (1972) 450.
7) V. S. Letokhov and V. P. Chebotayev: *Nonlinear Spectroscopy* (Springer-Verlag, Berlin, Heidelberg, and New York, 1977) p. 390.
8) R. L. Barger, M. S. Sorem and J. L. Hall: Appl. Phys. Letters **22** (1973) 573.
9) K. Shimoda and T. Tako: *Proc. of the 2nd Frequency Standards and Metrology Symposium Copper Mt., USA, 1976* (National Bureau of Standards, Colorado, 1976) p. 187.

Birefringence of *n*-Type Nematic Liquid Crystals Due to Electrically Induced Deformations of Vertical Alignment

Motoichi OHTSU, Tadashi AKAHANE and Toshiharu TAKO

Research Laboratory of Precision Machinery and Electronics, Tokyo Institute of Technology, O-okayama, Meguro-ku, Tokyo

(Received August 8, 1973)

The transmission of monochromatic light through the sandwich cell of MBBA (a typical *n*-type liquid crystal) with vertical alignment is investigated. When the cell is set in crossed Nicol and controlled by a.c. voltages, the transmissivity is zero at any voltage V below the threshold value V_{th}. When $V > V_{th}$, it shows nearly a sinusoidal variation with V. This phenomenon is observed even with fairly thick cells (50 μm). The threshold voltage V_{th} is shown to be independent of the cell's thickness and about 4.0 V (r.m.s.) at 24.0 °C for $f < 10$ kHz. The orientation angles of molecules and the phase differences of the light beams are calculated theoretically by using the static continuum theory of liquid crystals. The experimental results agree well with the theoretical calculations.

§1. Introduction

The birefringence of nematic liquid crystals with a negative dielectric anisotropy ($\varepsilon_p - \varepsilon_n < 0$; N_n liquid crystals) occurs when they are vertically aligned in a glass cell and a.c. voltages are applied. For the mixture of MBBA and EBBA, these phenomena have been investigated by Schiekel and Fahrenchen,[1] Soref and Rafuse,[2] Kahn,[3] Hareng *et al.*[4], but their measurement were restricted to thin cells ($d \lesssim 10$ μm).

In this experiment, birefringence of MBBA cells for wide range of the thickness ($d = 12$ μm ~ 50 μm) are measured to investigate the phenomenon from the electro-optical point of view. The results are then analyzed quantitatively by using the static continuum theory of liquid crystals.[5-7]

The similar analysis has been performed for the N_n liquid crystal cells with the magnetic field,[8] but because of practical considerations, quantitative explanations are needed when the electric field is applied. Hareng *et al.*[4] did not compare their calculations with experimental results. Gruler and Meier,[9] using quite thick cells of azo-C_7 as N_n liquid crystals, have measured its birefringence at high temperatures and high voltages, and have analyzed these results under the approximation that the applied voltage is not much greater than the threshold value.

In this paper a different approximation from that of Gruler and Meier[9] is used and the results which hold for wide range of voltages are obtained. Then, calculated values of the orientation angle of MBBA and that of the phase difference of the light are compared with experimental results.

§2. Measurement Procedure

The birefringence of MBBA was measured with an arrangement shown in Fig. 1. A He-Ne gas laser ($\lambda_0 = 632.8$ nm) and a mercury lamp with an interference filter ($\lambda_0 = 546.1$ nm) were used as the light source. A polarizer and an analyzer (Polaroid film HN 38) formed the

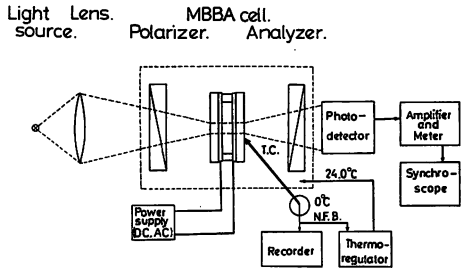

Fig. 1. Experimental set-up; By a convex lens, the light beam in the cell is made to be collimated and its diameter to be small. Polaroid films (HN 38) are used as a polarizer and an analyzer, and form the crossed Nicol. The light sources are a He-Ne gas laser ($\lambda_0 = 632.8$ nm) and a mercury lamp with an interference filter ($\lambda_0 = 546.1$ nm).

crossed Nicol. A photoelectric tube and a phototransistor were used as detectors. When the cell was set at the focal point of a convex lens, the light beam was made to be parallel and to have a small diameter in the cell because of the depth of focus. In this method, the diameter of the He-Ne gas laser beam was about 10 μm in the cell, which was the same order of cell's thickness, while that of the beam from the mercury lamp was about 0.1 mm. The applied voltage was a sinusoidal wave from 0 to 10 V and its frequency f was from 0 to 200 kHz. In all the measurements, the sample cells were kept at 24.0°C ($\pm$0.1°C) in a thermobath.

When a birefringent material is in the crossed Nicol, as in Fig. 1, the transmissivity T is given by a well known formula[10]

$$T=\sin^2 2\psi\cdot\sin^2\frac{\delta}{2}, \qquad (1)$$

where ψ is the angle between the incident light polarization (optical E vector) and that of the extraordinary light and δ is the phase difference between the ordinary light and the extraordinary light in the material. When the voltage is applied to the MBBA cell, the induced electric dipole moment of the molecule receives the torque from the electric field, and the molecular orientation will change. And when the alignment of molecules in the cell is varied, the phase velocities of the light are modulated. Then the value of δ in eq. (1) is controlled by the applied voltage. On the other hand, the value of ψ in eq. (1) is not controlled by the applied voltage, but determined only by the relative orientation of the cell to the crossed Nicol. Therefore the value of ψ is independent of the applied voltage V.

In this experiment, MBBA of high purity (99.8%)* was used as a N_n liquid crystal sample, and was vertically aligned in the clean, humidity-free transparent electrodes. The NESA coat glasses were used as the transparent electrodes, which is coated with SnO_2 film (surface resistivity is 500 Ω, and glass thickness is 2 mm). These glasses were cleaned in the following way: (1) Cleaning with the laboratory detergent. (2) Immersing for 24 hours in a solution of chromic acid. (3) Cleaning with flowing water for 1 hour and with the distilled water for 10 minutes. (4) Removing the humidity in a desiccator. (5) Cleaning in the ethylalcohol by using the ultrasonic cleaner for 1 hour. (6) Cleaning with hot trichloroethylene and with hot ethylalcohol for 10 minutes respectively. After this procedure, the value of surface resistivity of SnO_2 film did not change.

It is known that when the lecithine is coated on the glass walls, molecules of MBBA are vertically aligned because of the dispersion force between the lecithine and the butyl group ($-C_4H_9$) of MBBA.[11] We dissolved lecithine made from soy beans in ethylether to the extent of about 1 mg/cm^3 and coated it on the SnO_2 film of glass plates. The thickness of this lecithine film was less than 150 nm. Next, Myler films of uniform thickness (d=12, 25, 50 μm) were put between two glasses as spacers, and the sandwich cell was formed. In this cell, MBBA was sucked up with capillarity at 24.0°C. Finally, it can be confirmed with a conoscope that the molecules of MBBA align vertically in the cell. We obtained easily the cross image which is characteristic of the uniaxial crystal. When these cells were sealed with the epoxy adhesive agent and kept in the desiccator, it was confirmed that the characteristics of birefringence did not change for, at least, a week.

§3. Experimental Results

Figure 2 shows the relation between the transmissivity T and the applied voltage V when 632.8 nm and 546.1 nm light beams were normally incident on the 12 μm cell. The transmissivity has the threshold voltage V_{th}, as is clear in Fig. 2. The value of V_{th} is determined by the extrapolation in the plot of the relation between δ and V which is obtained from the relation between T and V by eq. (1). For the case of Fig. 2, the values of V_{th} obtained by this method are 4.00 V (r.m.s.) for λ_0=632.8

*This value was obtained by measuring precisely the melting point of MBBA at the Government Chemical Industrial Research Institute, Tokyo.

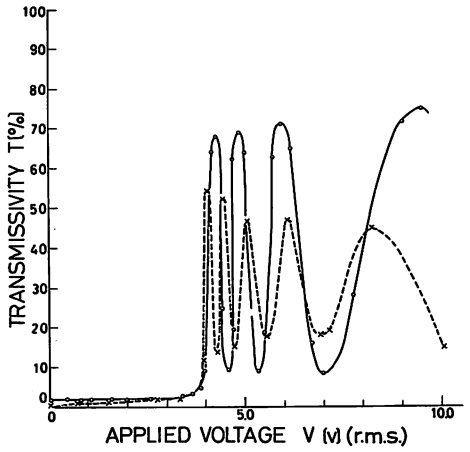

Fig. 2. The relations between the transmissivity T and the applied a.c. voltage V; $d=12\ \mu m$, $f=100$ Hz, (a)—○— $\lambda_0=632.8$ nm, (b) —×— $\lambda_0=546.1$ nm.

nm and 3.94 V (r.m.s.) for $\lambda_0=546.1$ nm. The phase difference δ increases monotonically with V ($V>V_{th}$), and the rate of increase is almost inversely proportional to the wavelength of the incident light beam. Therefore, when the white light is incident on this cell, each wavelength is selectively transmitted for $V>V_{th}$. In fact, the outgoing colour were green at 4.04 V, red at 4.30 V, blue-green at 4.58 V, yellow at 4.95 V and red at 5.97 V for the same cell as of Fig. 2. These results agree precisely with the characteristics in Fig. 2. Figure 3 shows the transmissivity of the 50 μm cell. Because the diameter of the incident light beam was made small, similar characteristics

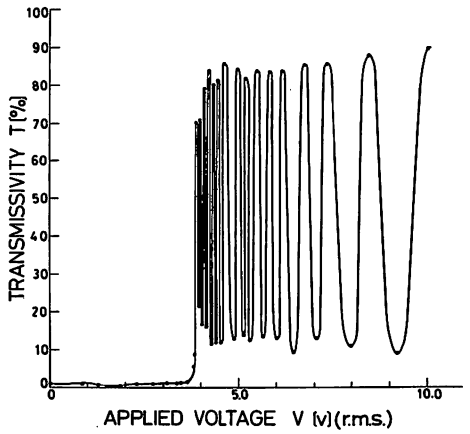

Fig. 3. The relation between T and V; $d=50\ \mu m$, $f=50$ Hz, $\lambda_0=632.8$ nm.

as in Fig. 2 were obtained even for such a thick cell. The threshold voltage in Fig. 3, obtained by the same method as in Fig. 2, is 3.88 V (r.m.s.). For several results of the relation between T and V, the values of V_{th} are obtained by the same way as in Figs. 2 and 3, then from these values the relation between δ and V/V_{th} are obtained by using (1), as shown in Figs. 4 and 5. In these figures, solid lines are the results of the theoretical analysis obtained in §4. The dependency of V_{th} on the frequency f is shown

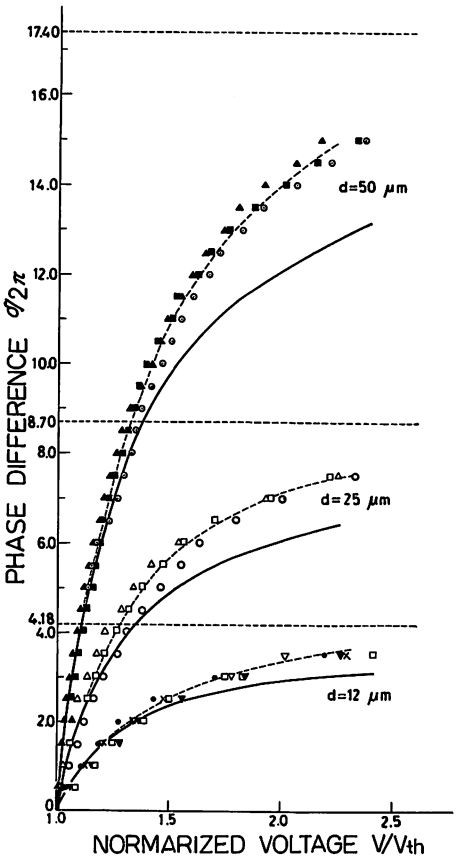

Fig. 4. The relations between the phase difference $\delta/2\pi$ and the normalized voltage V/V_{th}; $\lambda_0=632.8$ nm, (a) $d=50\ \mu m$: ■; $f=20$ Hz, $V_{th}=3.90$ V. ◉; $f=50$ Hz, $V_{th}=3.88$ V. ▲; $f=10$ kHz, $V_{th}=4.33$ V. (b) $d=25\ \mu m$: △; $f=20$ Hz, $V_{th}=3.88$ V. ▣; $f=50$ Hz, $V_{th}=3.85$ V. ○; $f=1$ kHz, $V_{th}=3.70$ V. (c) $f=12\ \mu m$: ●; $f=20$ Hz, $V_{th}=4.00$ V □; $f=50$ Hz, $V_{th}=4.00$ V. ×; $f=100$ Hz, $V_{th}=4.00$ V. ▼; $f=1$ kHz, $V_{th}=3.87$ V. ▽; $f=10$ kHz, $V_{th}=4.09$ V.

The solid lines are the results of theoretical analysis of §4, and for these lines the following values have been used: $\kappa=-0.20$, $\varepsilon_n=5.84\ \varepsilon_0$F/m, $\varepsilon_p=4.49\ \varepsilon_0$F/m.

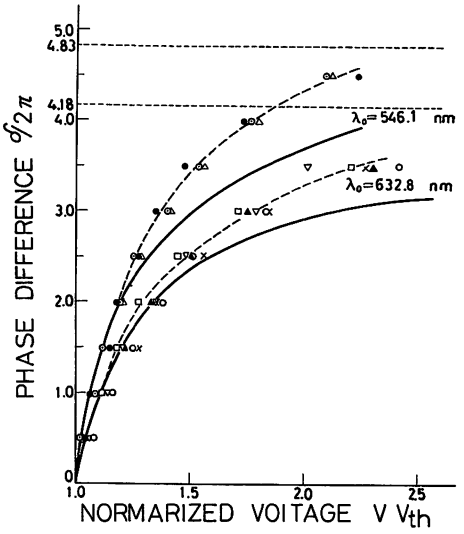

Fig. 5. The relations between $\delta/2\pi$ and V/V_{th}; $d=12\ \mu$m, (a) $\lambda_0=632.8$ nm: □; $f=20$ Hz, $V_{th}=4.00$ V. ○; $f=50$ Hz, $V_{th}=4.00$ V. ▲; $f=100$ Hz, $V_{th}=4.00$ V. ×; $f=1$ kHz, $V_{th}=3.87$ V. ▽; $f=10$ kHz, $V_{th}=4.09$ V. (b) $\lambda_0=546.1$ nm: ●; $f=20$ Hz, $V_{th}=4.00$ V. ◉; $f=100$ Hz, $V_{th}=3.94$ V. △; $f=1$ kHz, $V_{th}=3.85$ V.

The solid lines are the results of §4, and here $\kappa=-0.20$, $\varepsilon_n=5.48\ \varepsilon_0$F/m and $\varepsilon_p=4.49\ \varepsilon_0$F/m have been used.

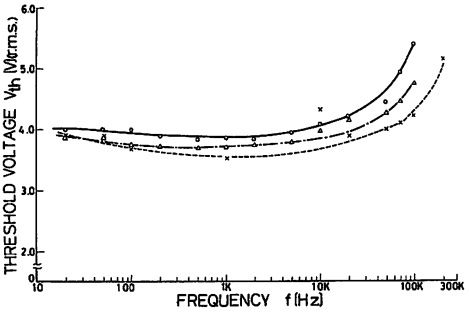

Fig. 6. The relations between the threshold voltage V_{th} and frequency f; $\lambda_0=632.8$ nm, (a) —○— $d=12\ \mu$m, (b) —·—△—·— $d=25\ \mu$m, (c) —×— $d=50\ \mu$m.

in Fig. 6. In Fig. 6, the values of V_{th} are nearly constant for $f\leqq 10$ kHz, but increase gradually for $f\geqq 10$ kHz, as was measured by Soref and Rafuse.[2] In the same figure, the values of V_{th} for thin cells are rather higher than those of thick ones, but it is considered that V_{th} is independent of the cell's thickness since this difference is less than that caused by the individuality of each cells. The value of V_{th} is independent of d due to the following reason; when d increases, the amplitude of the electric field decreases at a given voltage, but since the chains of MBBA molecules whose ends are fixed on glass walls become long, the central part of this chain becomes flexible with the weak electric field. The value of V_{th} for the pure MBBA obtained in this experiment was about 4.0 V (r.m.s.) while these values for several mixtures of MBBA and EBBA measured by Soref and Rafuse[2] were about 8.0 V (r.m.s.).

When d.c. voltages were applied, V_{th} was about 4.20 V, but the transmissivity T deviates from the regular behaviour of eq. (1) for $V>V_{th}$. Soref and Rafuse[2] obtained the results which obeyed eq. (1) for d.c. voltages, too. Since we used lecithine which is different from the case of Soref and Rafuse,[2] it may be considered that lecithine was electrolized by d.c. voltages and the resulting electric current perturbed the regular alignment of the liquid crystal molecules.

The dependency of T on ψ in eq. (1) as shown in Fig. 7 was measured by rotating the crossed Nicol about the direction of the light beam and keeping the value of δ constant by applying a fixed voltage V ($>V_{th}$). In Fig. 7, the shape of solid line (a) for the thin cell agrees well with

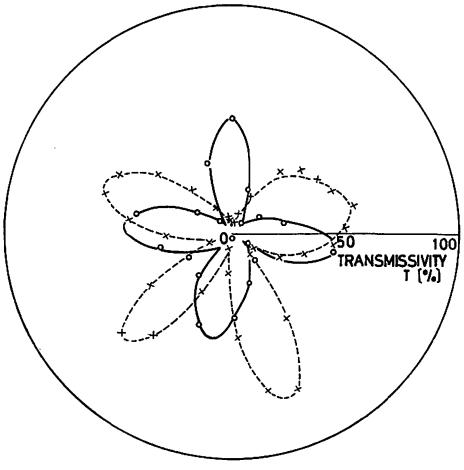

Fig. 7. The relations between T and ψ; These results were obtained by applying the constant voltage V ($>V_{th}$) and by rotating the crossed Nicol along the light beam. $\lambda_0=632.8$ nm, $f=1$ kHz. (a) —○— $d=12\ \mu$m, $V=4.87$ V (r.m.s.). (b) —×— $d=50\ \mu$m, $V=5.69$ V (r.m.s.).

eq. (1). Though the dashed line (b) for the thick cell has a slightly distorted shape, four maxima and minima appear even in this case.

§4. Theoretical Analysis

In this section, the experimental results obtained in §3 are explained by using the static continuum theory formulated by Oseen,[5] Zocher[6] and Frank.[7] The Cartesian coordinate system is determined in the cell, as in Fig. 8, and the orientation angle $\phi(x)$ which expresses the direction of the longer axis of a molecule is defined. Furthermore, the unit vector $\boldsymbol{n}$ which shows the direction of the longer axis is defined. Then, from the formula of the continuum theory, the elastic term of the free energy per unit volume is

$$f_{el}=\tfrac{1}{2}k_{11}(\nabla\cdot\boldsymbol{n})^2+\tfrac{1}{2}k_{22}\{\boldsymbol{n}\cdot(\nabla\times\boldsymbol{n})\}^2+\tfrac{1}{2}k_{33}\{\boldsymbol{n}\times(\nabla\times\boldsymbol{n})\}^2-\tfrac{1}{2}(k_{22}+k_{24})\times\{(\nabla\cdot\boldsymbol{n})^2+(\nabla\times\boldsymbol{n})^2-\nabla\boldsymbol{n}:\Delta\boldsymbol{n}\}. \quad (2)$$

In eq. (2), the elastic constants k_{11}, k_{22} and k_{33} come from "splay", "twist" and "bend" modes of the deformation of molecules respectively, and $k_{11}\geqq k_{33}\approx 10^{-11}$ N for nematic liquid crystals. The fourth term in eq. (2) vanishes when it is integrated over the volume. On the molecule, the electric dipole moment is induced by the applied electric field. When the dielectric tensor is indicated as $[\varepsilon]$, the polarization $\boldsymbol{P}$ is

$$\boldsymbol{P}=[\varepsilon-\varepsilon_0]\boldsymbol{E}=(\varepsilon_P-\varepsilon_0)(\boldsymbol{E}\cdot\boldsymbol{n})\boldsymbol{n}+(\varepsilon_n-\varepsilon_0)\times[\boldsymbol{E}-(\boldsymbol{E}\cdot\boldsymbol{n})\boldsymbol{n}], \quad (3)$$

where ε_n and ε_p are the dielectric constants perpendicular and parallel to the longer axis and ε_0 is that of vacuum. Then, the dielectric term of the free energy per unit volume is

$$f_{diel}=-\tfrac{1}{2}\boldsymbol{P}\cdot\boldsymbol{E}=\tfrac{1}{2}(\varepsilon_n-\varepsilon_0)(\boldsymbol{E}\cdot\boldsymbol{n})^2-\tfrac{1}{2}(\varepsilon_n-\varepsilon_0)\boldsymbol{E}^2\equiv\tfrac{1}{2}\varepsilon_a(\boldsymbol{E}\cdot\boldsymbol{n})^2-\tfrac{1}{2}(\varepsilon_n-\varepsilon_0)\boldsymbol{E}^2, \quad (4)$$

where
$$\varepsilon_a\equiv\varepsilon_n-\varepsilon_p. \quad (5)$$

For N_n liquid crystals such as MBBA, the value of ε_a is positive.

Considering the two-dimensional model, the orientation angle ϕ is the function of x, then the vectors $\boldsymbol{E}$ and $\boldsymbol{n}$ are expressed as $\boldsymbol{E}=(E, 0, 0)$ and $\boldsymbol{n}=(\cos\phi(x),\ 0,\ \sin\phi(x))$. Substituting these expressions, then eqs. (2) and (4) are written as

$$f_{el}=\frac{1}{2}\left(\frac{d\phi}{dx}\right)^2(k_{11}\sin^2\phi(x)+k_{33}\cos^2\phi(x)) \quad (6)$$

and

$$f_{diel}=\frac{1}{2}\varepsilon_a E^2\cos\phi(x), \quad (7)$$

where the term independent of $\phi(x)$ in eq. (7) is eliminated because it has no effect on the following discussions. The free energy per unit area of the glass wall is, from eqs. (6) and (7),

$$F=\int_{-d/2}^{d/2}(f_{el}+f_{diel})dx=\int_{-d/2}^{d/2}\left[\left(\frac{d\phi}{dx}\right)^2(k_{11}\sin^2\phi+k_{33}\cos^2\phi)+\varepsilon_a E^2\cos\phi\right]dx. \quad (8)$$

Because the realized state is such that F takes the minimum value, the following nonlinear differential equation is obtained by minimizing F with respect to ϕ;

$$(\kappa\sin^2\phi+1)\frac{d^2\phi}{dx^2}+\kappa\sin\phi\cos\phi\left(\frac{d\phi}{dx}\right)^2+\left(\frac{\varepsilon_a E^2}{k_{33}}\right)\sin\phi\cos\phi=0, \quad (9)$$

where
$$\kappa\equiv\frac{k_{11}-k_{33}}{k_{33}} \quad (10)$$

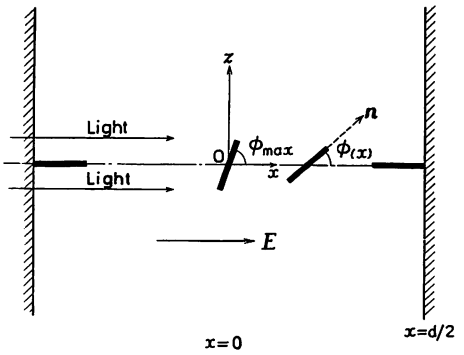

Fig. 8. The definitions of coordinates and the orientation angle $\phi(x)$ of a molecule; The symbols $\boldsymbol{E}$ and $\boldsymbol{n}$ denote the applied electric field and the unit vector in the direction of the longer axis of the molecule. At the center of the cell ($x=0$), the angle ϕ takes the maximum value ϕ_{max} and $d\phi/dx=0$ by the symmetry. Corresponding to the experiment, the angle $\phi=0$ at $x=\pm d/2$.

Since it is clear that $\phi(x)=\phi(-x)$ by the symmetry of the cell, only the region $x\geqq 0$ is considered hereafter. The boundary conditions are

$$\phi=0 \quad \text{at } x=\frac{d}{2} \quad \text{(on the glass wall)},$$

$$\phi=\phi_{max} \text{ and } \frac{d\phi}{dx}=0 \quad \text{at } x=0 \quad \text{(at the center of the cell)}.$$

Under these conditions, the first integral obtained from eq. (9) is

$$d\phi\{(1+\kappa \sin^2\phi)/(k^2-\sin^2\phi)\}^{\frac{1}{2}} = -(\varepsilon_a E^2/k_{33})^{\frac{1}{2}}dx \ (x\geqq 0), \tag{11}$$

where $$k\equiv \sin\phi_{max}. \tag{12}$$*

As it was previously described, $|\kappa|\ll 1$ and $\kappa<0$ because $k_{11}\approx k_{33}$ and $k_{11}>k_{33}$. Therefore eq. (11) is approximated for κ and to give

$$d\phi\left(1+\frac{\kappa}{2}\sin^2\phi\right)/(k^2-\sin^2\phi)^{\frac{1}{2}} = -(\varepsilon_a E^2/k_{33})^{\frac{1}{2}}\,dx \ (x\geqq 0). \tag{13}$$

Equation (13) is easily integrated and expressed as

$$\left(1+\frac{\kappa}{2}\right)F(\alpha, k)-\frac{\kappa}{2}E(\alpha, k) = \frac{1}{2}(\varepsilon_a/k_{33})^{\frac{1}{2}}V\left(1-\frac{2}{d}x\right) \ (x\geqq 0), \tag{14}$$

where $F(\alpha, k)$ and $E(\alpha, k)$ are the elliptic integrals of the first and second kind respectively and

$$\alpha=\sin^{-1}\left(\frac{\sin\phi}{k}\right). \tag{15}$$

In eq. (14), electric field E was considered to be uniform in the cell and the value $E\cdot d$ was substituted by the applied voltage V. The value of V is the root-mean-square value (r.m.s.) in the case of a.c. voltages, which is clear from eq. (4). By putting $x=0$ and $\phi=\phi_{max}$ in eq. (14), one may obtain

$$\left(1+\frac{\kappa}{2}\right)\cdot K(k)-\frac{\kappa}{2}\cdot E(k)=\frac{1}{2}(\varepsilon_a/k_{33})^{\frac{1}{2}}V, \tag{16}$$

where $K(k)$ and $E(k)$ are the complete elliptic integrals of the first and second kind respectively. The value of V in eq. (16) at $k=0$ ($\phi_{max}=0$) is, when it is rewritten as V_{th}.

$$V_{th}\equiv\pi(k_{33}/\varepsilon_a)^{\frac{1}{2}}. \tag{17}$$

Equation (16) has no solution for k when V is lower than such a value as given by eq. (17) because the left-hand side of eq. (16) is a monotonically increasing function of k. Therefore the dependence of the orientation angle ϕ on the voltage V has the "threshold", and its value is given by eq. (17). This is the theoretical value of the threshold voltage which appeared in the experimental results in §3. By using eq. (17), one may rewrite eqs. (14) and (16) as

$$\left(1+\frac{\kappa}{2}\right)\cdot F(\alpha, k)-\frac{\kappa}{2}\cdot E(\alpha, k) = \frac{\pi}{2}\cdot(V/V_{th})\cdot\left(1-\frac{2}{d}x\right) \ (x\geqq 0) \tag{18}$$

and

$$\left(1+\frac{\kappa}{2}\right)\cdot K(k)-\frac{\kappa}{2}\cdot E(k)=\frac{\pi}{2}(V/V_{th}). \tag{19}$$

Equation (18) expresses the dependence of ϕ on x and V, and eq. (19) expresses that of ϕ_{max} on V.

Figure 9 shows the relation between ϕ_{max} and

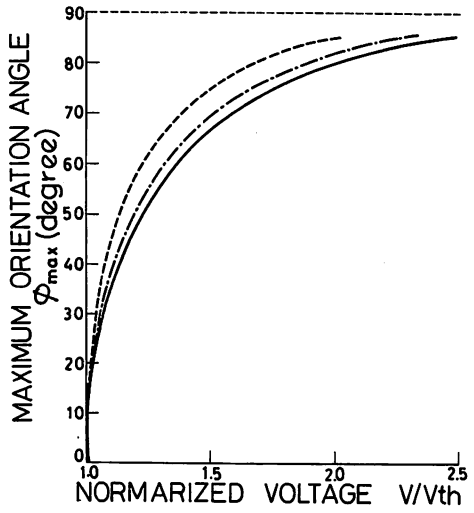

Fig. 9. The relations between the maximum orientation angle ϕ_{max} and the normalized voltage V/V_{th} numerically calculated from eq. (19); (a) — $\kappa=0$, (b) —·— $\kappa=-0.20$, (c) ---- $\kappa=-0.50$.

*Hareng *et al.*[4] defined k as $1/\sin\phi_{max}$. But by this definition, it is inadequate to use k as the index of the elliptic integral because $|k|\geqq 1$.

V/V_{th} obtained from eq. (19) for several small and negative values of κ. In Fig. 9, little difference between the curves for $\kappa=0$ and that for $\kappa=-0.20$ is recognized. In the case of $\kappa=-0.20$, the dependence of ϕ on x and V obtained from eq. (18) is shown in Fig. 10. As shown in Figs. 9 and 10, the value of ϕ, in the region $V>V_{th}$, increases rapidly at first and then the rate of increase becomes small. Accordingly, the value of δ in eq. (1) may increase in the similar way and the transmissivity T oscillates sinusoidally in the region $V>V_{th}$. Its oscillating period is small at first but gradually increases, which agrees with the experimental results as in Fig. 2. To explain this inclination quantitatively, the expression for δ in eq. (1) is required. This is calculated from the orientation angle obtained from eqs. (18) and (19).

As shown in Fig. 11(a), a thin film of MBBA which is between x and $x+dx$ is considered. When the light beam of wavelength λ_0 is incident on this film as in Fig. 11(a), the situation is equivalent to that of Fig. 11(b) in which the same beam comes at an angle $\phi(x)$ with respect to the normal to the uniaxial crystal plate. Two refractive indices of this uniaxial crystal for this beam are[10]

$$\left.\begin{aligned} &n_o=\sqrt{\mu\varepsilon_n} \\ &\text{and} \\ &n_e=\{\mu\varepsilon_n\varepsilon_p/(\varepsilon_p\cos^2\phi(x)+\varepsilon_n\sin^2\phi(x))\}^{\frac{1}{2}}, \end{aligned}\right\} \quad (20)$$

where μ is the magnetic permeability. Accordingly, the phase difference $\delta(x, V)$ caused by MBBA molecules between x and $x+dx$ is, from eq. (20),

$$\delta(x, V)=\frac{2\pi dx}{\lambda_0}(n_o-n_e). \quad (21)$$

Then the total phase difference due to the cell is, from eqs. (20) and (21),

$$\begin{aligned}\delta(V)&=\int_{-d/2}^{d/2}2\pi dx(n_o-n_e)/\lambda_0 \\ &=\frac{4\pi}{\lambda_0}\sqrt{\mu\varepsilon_n}\left\{d/2-\int_0^{d/2}\left(1+\frac{\varepsilon_n-\varepsilon_p}{\varepsilon_p}\times\sin^2\phi(x)\right)^{-\frac{1}{2}}dx\right\}.\end{aligned}$$

Changing the integral variable from x to ϕ by

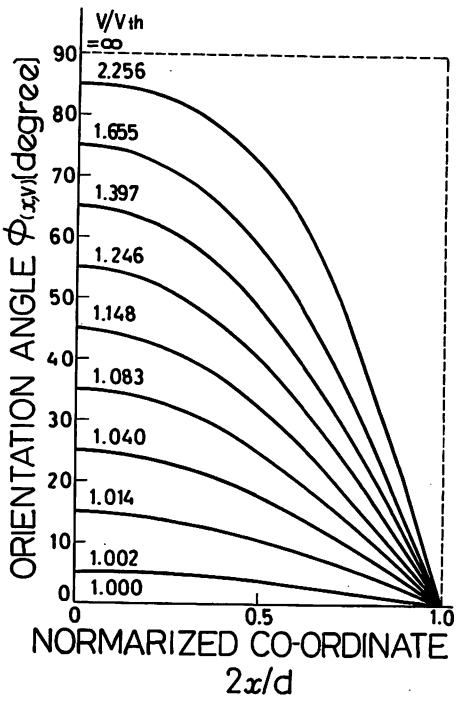

Fig. 10. The relation between the orientation angle ϕ and x, V/V_{th} numerically calculated from eq. (18); $\kappa=-0.20$. The angle ϕ approaches 90° when V/V_{th} goes to ∞.

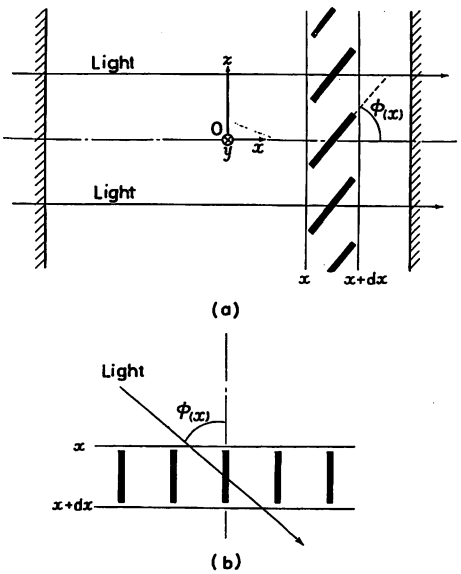

Fig. 11. The model for calculating the phase difference δ in eq. (1); (a) In this model, the uniaxial crystal plates of dx thickness are considered to be piled with their optical axes inclined. (b) The situation equivalent to (a); The light beam coming at the incident angle $\phi(x)$ to the uniaxial crystal plate of thickness dx.

using eq. (11), one may obtain

$$\delta(V)=\frac{4\pi d}{\lambda_0}\sqrt{\mu\varepsilon_n}\left[\frac{1}{2}-\frac{1}{\pi}\frac{V_{th}}{V}\int_0^{\phi_{max}}\left(1+\frac{\varepsilon_n-\varepsilon_p}{\varepsilon_p}\times\sin^2\phi\right)^{-\frac{1}{2}}\left\{(1+\kappa\sin^2\phi)/(k^2-\sin^2\phi)\right\}^{\frac{1}{2}}d\phi\right]. \quad (22)$$

Equation (22) shows the dependence of δ on the applied voltage V, but this relation is not clear because it is expressed in the form of an integral. Slightly intelligible expression is obtained from eq. (22) by using the following approximation; as Conners and Paxton[12] used in their calculation, the values of ε_n and ε_p, for MBBA, are about $5.3\,\varepsilon_0$ F/m and $4.7\,\varepsilon_0$ F/m respectively, so that $|(\varepsilon_n-\varepsilon_p)/\varepsilon_p|\approx 0.1\approx|\kappa|$. Since the results in Fig. 9 have little difference between each value of κ as previously mentioned, the approximation may be performed here with respect to $(\varepsilon_n-\varepsilon_p)/\varepsilon_p$ and κ. Then one may obtain a slightly easier equation from eq. (22),

$$\delta(V)=\frac{2d}{\lambda_0}\sqrt{\mu\varepsilon_n}\frac{\varepsilon_n-\varepsilon_p}{\varepsilon_p}\frac{V_{th}}{V}\left[\left(1+\frac{\kappa}{3}+\frac{\kappa k^2}{6}\right)\cdot K(k)-\left(1+\frac{\kappa}{3}+\frac{\kappa k^2}{3}\right)\cdot E(k)\right]. \quad (23)$$

For $V/V_{th}\approx 1$, *i.e.* $k=\sin\phi_{max}\ll 1$, the value of k is, from eq. (19),

$$k\approx\frac{2}{\sqrt{1+\kappa}}\sqrt{\frac{V}{V_{th}}-1}.$$

Substituting this into eq. (23), one may obtain

$$\delta(V)\approx\frac{2\pi d}{\lambda_0}\sqrt{\mu\varepsilon_n}\frac{\varepsilon_n-\varepsilon_p}{\varepsilon_p}\frac{k_{33}}{k_{11}}\left(\frac{V}{V_{th}}-1\right), \quad (24)$$

which is the linear relation between $\delta(V)$ and V/V_{th} and holds for the small values of ϕ_{max}. Furthermore, when V/V_{th} is eliminated from eq. (22) by using eq. (11), then

$$\delta(V)\to\frac{2\pi d}{\lambda_0}(\sqrt{\mu\varepsilon_n}-\sqrt{\mu\varepsilon_p}) \text{ for } k=\sin\phi_{max}\to 1, \quad (25)$$

which is natural, because molecules in the cell align perfectly parallel to the glass walls when V/V_{th} goes to infinity.

For $\lambda_0=632.8$ nm the relations between $\delta/2\pi$ and V/V_{th} of the 12 μm, 25 μm and 50 μm cells can be now calculated numerically from the value of κ, ε_n, ε_p and μ. The solid lines in Fig. 4 show these calculated values from eq. (22) by using $\kappa=-0.20$, $\varepsilon_n=5.48\,\varepsilon_0$ F/m, $\varepsilon_p=4.49\,\varepsilon_0$ F/m and $\mu=\mu_0$ H/m (magnetic permeability of vacuum), which were determined by those used by Conners and Paxton[12]. Figure 4 shows simultaneously the experimental results for several frequencies of applied voltages. By eq. (25), $\delta/2\pi$ goes to 4.18, 8.70 and 17.40 for the 12 μm, 25 μm and 50 μm cells respectively when V/V_{th} goes to infinity. Figure 4 shows these limits, too. The solid lines in Fig. 5 show the calculated relations obtained from eq. (22) for the case of $\lambda_0=632.8$ nm and 546.1 nm for the 12 μm cell, in which the same values of κ, ε_n, ε_p and μ as in Fig. 4 were used. By eq. (25), $\delta/2\pi$ goes to 4.18 and 4.83 for $\lambda_0=632.8$ nm and 546.1 nm when V/V_{th} goes to infinity, and these values are shown in Fig. 5 simultaneously.

In eq. (22), the values of elastic constants, dielectric constants, applied voltage and cell's thickness appear all in forms of the ratio such as $(k_{11}-k_{33})/k_{33}(=\kappa)$, $(\varepsilon_n-\varepsilon_p)/\varepsilon_p$, V/V_{th} and d/λ_0. Therefore one cannot know the absolute values of k_{11}, k_{33}, ε_n and ε_p from experimental results of δ. These values are estimated from the experimental results of V_{th} because V_{th}, as given by eq. (17), is determined by these absolute values. By substituting previously reported values $\varepsilon_a\approx 0.8\,\varepsilon_0$ F/m,[12] $k_{33}\approx 10^{-11}$ [7] N into eq. (17), one may obtain $V_{th}\approx 4.0$ V, which agrees with our experimental results.

In this section we used the two-dimensional and static model, and it is adequate to use it for $f\leqq 10$ kHz by considering the results of Figs. 6 and 7. But for $f\geqq 10$ kHz, this model cannot be used because, in this region, V_{th} gradually increases as in Fig. 6. To explain this phenomena, the hydrodynamic model must be used which involves the space charges and diffusion currents in the cell as adopted by Dubois-Violette *et al.*[13] The theoretical analysis for this phenomenon is a remained problem to be solved.

§5. Conclusion

When MBBA was set in the crossed Nicol

and controlled by a.c. voltages, the transmissivity was zero at any voltage V below the threshold value V_{th}. When $V > V_{th}$, it showed nearly sinusoidal variation with V. This phenomenon was observed even with fairly thick cells (50 μm). The threshold voltage V_{th} was shown to be independent of the cell's thickness and about 4.0 V (r.m.s.) at 24.0°C for $f \lesssim 10$ kHz, which was smaller than that of the mixed liquid crystals (MBBA+EBBA). Furthermore, we obtained the relation between T and ψ as in eq. (1) even for the 50 μm cell which was four times thicker than that of Soref and Rafuse.[2] This was caused by the fact that molecules were aligned quite regularly by lecithine and that the diameter of the incident light beam was small.

Theoretically, the orientation angles of molecules and the phase differences of the light beams were calculated by using the static continuum theory of liquid crystals. The experimental results agreed well with the theoretical calculations.

Due to this agreement, the validity of the static continuum model was assured.

Acknowledgements

The authors wish to express their gratitudes to Mr. S. Nagai of National Research Laboratory of Metrology for his helpful advice and to the members of authors' laboratory for their cooperation.

References

1) M. F. Schiekel and K. Fahrenschen: Appl. Phys. Letters **19** (1971) 391.
2) R. A. Soref and M. J. Rafuse: J. appl. Phys. **43** (1972) 2029.
3) F. J. Kahn: Appl. Phys. Letters **20** (1972) 199.
4) M. Hareng, E. Leiba and G. Assouline: Molec. Cryst. Liq. Cryst. **17** (1972) 361.
5) C. W. Oseen: Trans. Faraday Soc. **29** (1933) 883.
6) H. Zocher: Trans. Faraday Soc. **29** (1933) 945.
7) F. C. Frank: Disc. Faraday Soc. **25** (1958) 19.
8) A. Saupe: Z. Naturforsch. **15a** (1960) 15.
9) H. Gruler and G. Meier: Molec. Cryst. Liq. Cryst. **16** (1972) 299.
10) M. Born and E. Wolf: *Principles of Optics* (Pergamon Press, London, 1970) 4th ed., Chap. 14.
11) T. Uchida, H. Watanabe and M. Wada: Japan. J. appl. Phys. **11** (1972) 1559.
12) G. H. Conners and K. B. Paxton: J. appl. Phys. **43** (1972) 2959.
13) E. Dubois-Violette, P. G. de Gennes and O. Parodi: J. Phys. (France) **32** (1971) 305.

NOISES AND COHERENCE IN SEMICONDUCTOR LASERS

MOTOICHI OHTSU

International Cooperation Center for Science and Technology, Tokyo Institute of Technology, 2-12-1 O-okayama, Meguro-ku, Tokyo 152, Japan

Abstract

The spectral width of 0.8μm AlGaAs laser, derived from the experimental results of FM noise measurements, was less than 10MHz. The power-independent width was also estimated from 1/f noises which was 2.0MHz. Several frequency controlling techniques of 0.8μm AlGaAs and 1.5μm InGaAsP lasers were demonstrated to improve their long-term frequency stabilities. The stabilities were about 1000 times improved then that of the free-running lasers. It was confirmed that the long-term stability of AlGaAs laser was almost equal to the theoretical limit. Several examples of application of these highly stabilized lasers were demonstrated in the field of coherent optical measurements i.e., Rb and Cs atomic clocks, pollutant gas monitoring, and fiber-gyroscope.

1. Introduction

Due to the increasing demand in optical communication industries for better characteristics of semiconductor laser, several remarkable improvements in performances of 0.8μm AlGaAs and 1.5μm InGaAsP lasers have been successfully carried out recently. If these lasers are used for coherent optical measurements, their spectral purities and long-term frequency stabilities (for integration time longer than 1μs), have to be improved. From these points of view, the author has tried to measure the spectral widths and to improve the long-term frequency stabilities of these lasers. In this paper, these results and several examples of applications to coherent optical measurements are shown.

There are several lateral mode stabilized AlGaAs lasers at 0.8μm. Among them, Channeled-Substrate-Planar (CSP) type lasers[1] are used in the present study because they have larger stripe width, that is, the cavity Q is larger, which means they show narrower spectral widths and lower quantum noises.

As for 1.5μm InGaAsP lasers. Plano-Convex-Waveguide (PCW) type lasers[2] were employed here. which are similar to CSP lasers.

2. Spectral Width Measurements of 0.8μm AlGaAs Lasers

The spectral width $\Delta\nu$ (FWHM) has been conveniently expressed by the following modified Schawlow-Townes formula[3].

$$\Delta\nu = 2\cdot\frac{h\nu_0}{16\pi P_0}\left(\frac{c}{nL}\right)^2(\ln R-\alpha_\ell L)(\ln R)n_{sp}(1+\alpha^2) \quad (1)$$

Here. α represents the broadening by the extra FM noises induced by the carrier density fluctuations. which also corresponds to the ratio of the real and imaginary parts of the change of the complex refractive indices by the carrier density fluctuations[4]. The spectral width of CSP lasers with 300μm long has been measured in Japan as being less than 10MHz[5.6]. On the other hand. the values reported in other countries are sometimes as large as100MHz, which is about ten times larger than Japanese results (see. for example [3]). As the other outstanding results. the power-independent spectral width has been observed for TJS lasers, which is 1.9MHz at room temperature[3]. while this value for the CSP lasers has been reported as being 0.6 - 0.9MHz[7]. Following these results. there are two problems to be solved. namely ; the real value of the spectral width and the origin of the power-independent spectral width. In this section. the experimental results are shown about these problems.

There are several techniques of measuring the spectral width. That is. measuring the beat spectrum between the two lasers. using a high resolution Fabry-Perot interferometer[5]. and using an optical fiber which is called as the delayed self heterodyne technique[8]. However. these techniques have several difficulties in them. i.e.. the extra FM noises are induced by the light reflected back from the mirror surface of the interferometer or the end of the optical fibers. These FM noises also induces extra spectral broadening. or sometimes. narrowing. To avoid this effect. an indirect method was employed in the present experiment. i.e.. the spectral width was estimated from the measured value of the FM noises. The experimental setup is shown in Fig. 1. As a tilted Fabry-Perot interferometer can be used as a frequency discriminator for FM noise measurements because the finesse does not have to be high enough in this case. the reflected light does not come back into the laser cavity. Therefore. no extra noises are induced. and this method can be safe enough to estimate the intrinsic spectral width.

The spectra profile $I(\nu)$ can be given by the Fourier transformation of the autocorrelation function $R(\tau)$ of the amplitude $E(t)$ of the electric field of the laser light.As given

by eq.(2), the amplitude E(t) contains the fluctuating phase $\phi(t)$ in it.

$$E(t) = \exp\,[\,-i\,(2\pi\nu_0 t + \phi(t))]. \qquad (2)$$

The time derivative of this fluctuating phase gives the frequency fluctuations (FM noises) $y(t)$ ($= d\phi/dt/2\pi\nu_0$). The autocorrelation function $R(\tau)$ is, then, expressed by the second-order moment of the phase fluctuations $\langle \delta\phi^2(\tau) \rangle$. which is expressed by eq.(3).

$$\begin{aligned} R(\tau) &= \langle E(t)\cdot E(t+\tau)^* \rangle / E_0^2 \\ &= \exp\,[\,i\,(2\pi\nu_0\tau + \phi(t+\tau) - \phi(t))] \\ &= \exp\,[\,i\,(2\pi\nu_0\tau + \delta\phi(\tau))] \\ &= \exp\,[\,i2\pi\nu_0\tau - \langle \delta\phi^2(\tau) \rangle /2]. \end{aligned} \qquad (3)$$

where τ represents the integration time for the fluctuation measurements. The second-order moment of the phase fluctuations $\langle \delta\phi^2(\tau) \rangle$ is proportional to that of the frequency fluctuations $\langle \delta\nu^2(\tau) \rangle$. as is expressed in eq.(4). Here, $\langle \delta\nu^2(\tau) \rangle$ can be also expressed by a measure known as the Allan variance $\sigma_y^2(\tau)$ [9].

$$\begin{aligned} \langle \delta\phi^2(\tau) \rangle &= (2\pi\tau)^2 \langle \delta\nu^2(\tau) \rangle \\ &= (2\pi\tau)^2 \cdot \nu_0^2 \cdot \sigma_y^2(\tau). \end{aligned} \qquad (4)$$

Therefore, $R(\tau)$, $I(\nu)$, and the spectral width $\Delta\nu$ can be given by the Allan variance (eqs.(5) and (6)) :

$$R(\tau) = \exp[\,i2\pi\nu_0\tau - 2(\pi\nu_0\tau)^2 \cdot \sigma_y^2(\tau)]. \qquad (5)$$

$$I(\nu) = \int_0^\infty \exp\,[\,i2\pi(\nu_0 - \nu)\tau - 2(\pi\nu_0\tau)^2 \cdot \sigma_y^2(\tau)]d\tau + \text{c.c.} \quad . \qquad (6)$$

The Allan variance is a convenient measure. which has been proposed by D. Allan. and is defined by eq.(7) [9].

$$\sigma_y^2(\tau) = \lim_{N\to\infty} \frac{1}{N-1} \sum_{k=1}^{N-1} (y_{k+1} - y_k)^2/2 . \qquad (7)$$

Here, y_k represents the frequency fluctuations which is averaged over the integration time τ. The Allan variance can be also derived from the power spectral density of the frequency fluctuations $S_y(f)$ by eq.(8).

$$\sigma_y^2(\tau) = 2 \int_0^\infty S_y(f) \frac{\sin^4(\pi f \tau)}{(\pi f \tau)^2} \, df. \qquad (8)$$

By these procedures, the spectral width can be derived by measuring the Allan variance or the power spectral density of the frequency fluctuations, i.e., FM noises.

Figure 2 shows the experimental result of the power spectral density of FM noises at T = 293K. In the Fourier frequency range higher than 5MHz, the noise is governed by the quantum noises, i.e., the spontaneous emission and carrier density fluctuations. These quantum noises are the white noises, and in the case of the single longitudinal mode oscillation, this magnitude is inversely proportional to the injection current I, which is expressed as

$$S_y(f) = A_0 (I/I_{th} - 1)^{-1} \qquad (Hz^{-1}) \qquad (9)$$

$$A_0 = 2.8 \times 10^{-24} \qquad (Hz^{-1})$$

where I_{th} represents the threshold value of the current. When the value of the proportional constant A_0 is derived, one should be careful not to use the values of the FM noises in the multimode oscillation region. If these data are used, the proportional constant is overestimated. In the case of the present experiment, the intensity of the satellite longitudinal modes were only less than 1% of that of the main mode in this region. Even by such weak satellite modes, the extra FM noises can be induced and the deviation from this linear relation can be seen, which is illustrated by Fig. 3. This can be also said for direct measurement of the spectral width. If the spectral width is measured in this region, which is slightly multimode, its value can be overestimated because of the mode competition. This may be one of the reason why sometimes the value of the spectral width is measured as large as 100MHz. By using this proportional constant, the spectral width can be estimated by the procedure shown above. The broken line in Fig. 4 shows the result, which corresponds to the modified Schawlow-Townes formula. The conclusion obtained from this line is that the spectral width is less than about 10MHz in the single mode region, which is consistent with the results previously reported in Japan [5,6].

On the other hand, Kikuchi and Okoshi [10] pointed out that a power-independent 1/f noise appears in the power spectral density of FM noises, which can be formulated as :

$$S_y(f) = A_1 \cdot f^{-1} \qquad (Hz^{-1}) \tag{10}$$

$$A_1 = 3.4 \times 10^{-18}$$

It can be said that one of the origin of the power-independent spectral width is this noise. To estimate the effect of this noise, calculations were done by adding this value to eq. (9). The solid curve in Fig. 4 shows the result[11]. It is deviated from the modified Schawlow-Townes formula (the broken line), and has the power-independent spectral width of 2.0MHz at room temperature. This value is almost equal to the result for TJS laser[3], while it is about two times larger than those reported for CSP lasers[7]. Though there are several differences between each value, the power-independent 1/f noise can be one of the origin of the power-independent spectral width because the existence of this noise is quite possible, as has been popularly observed in the current fluctuations and mobility fluctuations in conventional semiconductor devices[12].

3. Frequency Control and Stabilization of 0.8μm AlGaAs Lasers

To improve the long-term frequency stability of the 0.8μm AlGaAs lasers, it has to be known how the frequency shift is induced. The frequency shift is due to the carrier density change and the temperature change by the injection current, and is also due to the change of the ambient temperature. The frequency shifts by the unit change in the injection current and temperature have been measured as being -2.5GHz/mA and -25GHz/K, respectively, for the CSP lasers. As the laser frequency is controlled by the injection current in the present experiments, its response charecteristics to the injection curremt should be checked first. It has been known that the phase characteristics of the response can be expressed as

$$\arg\left(\frac{\delta\nu}{\delta I(f)}\right) = -0.32 \log_{10} f + 1.03 \quad (rad)$$

$$\text{for } f < 10MHz. \tag{11}$$

which shows the phase lag for the current frequency f up to 10MHz[13]. Therefore, to improve the long-term frequency stability within this range of the current frequency (i.e., $\tau \geq 1$ μs), the phase-lead compensation is required. That is, a differentiator has to be used to control the current. Furthermore, a proportional amplifier and integrator have to be

also added to reduce a very slow frequency drift. Therefore, PID control is required for long-term frequency stabilization for $\tau \gtrsim 1\mu s$. Figure 5 shows the frequency characteristics of the gains of the PID controller employed.

A very stable frequency standard has to be prepared for the stabilization. Then, the laser frequency is locked to this standard frequency by controlling the injection current. At the same time, the Allan variance or the power spectral density of the residual frequency fluctuations (FM noises) are measured. To suppress the frequency fluctuations for $\tau \gtrsim 1\mu s$, a stable atoms or molecules can be used as a frequency standard.

3.1. Improvements of the stability for $\tau \gtrsim 1$ ms

To suppress the slow fluctuations for $\tau \gtrsim 1$ms, several frequency standards can be used. The first example is the Fabry-Perot interferometer which is stabilized by a He-Ne laser with a higher frequency stability. The experimental setup is shown in Fig. 6[14]. The second example is the absorption spectra in H_2O vapor, which has a great number of spectral lines due to the rotational structure of the combination tones of the vibration transition around 0.8μm wavelength region. If these spectra are used, the experimental setup becomes simpler than that of Fig. 6, which is illustrated in Fig. 7 [15].

The third example is the Rb-D_2 line which shows stronger absorption than that by the H_2O vapor. The absorption spectra observed is shown in Fig. 8 [16]. Figure 9 shows the result of the frequency stabilization using these three standard, where $\sigma_y(\tau)$ is the square root of the Allan variance of the residual frequency fluctuations. The frequency stability was about 1000 times improved than that of the free-running lasers. Especially, by using the Rb-D line, the minimum of $\sigma_y(\tau)$ obtained was

$$\sigma_y(\tau) = 1.4 \times 10^{-12} \quad \text{at} \quad \tau = 100\ \text{s}. \tag{12}$$

3.2. Improvements of the Stability for $\tau < 1$ms

As the next step, to improve the stability for $\tau < 1$ms, a Fabry-Perot interferometer made of a rigid quartz block can be used as a frequency standard. In this case, several differentiators have to be connected to expand the bandwidth of the phase-lead compensation. Figure 10 shows the frequency characteristics of the gains of these differentiators designed by the author's colleague[17]. As shown by the curve C of Fig. 11, the frequency stability was improved also for $5\mu s \lesssim \tau \lesssim 1$ms by this stabilization. This figure also shows the summary of the experimental results obtained above. The frequency stability for $\tau \gtrsim 5\mu s$ was about 1000 times improved by the stabilization, which is almost equal to the theoretical limits. Here, the theoretical limit was estimated by using the semiclassical Langevin's

equation including spontaneous emission, carrier density fluctuations, current fluctuations, etc[18]. On the other hand, for $\tau < 1\mu s$, it can be seen from this figure that the frequency stability of the free-running lasers (the curve D) is already almost equal to the theoretical limit. This result means that frequency stability within this range of τ can not be improved any more even if the stabilization is employed. However, if one wish to improve the stability for $\tau <$ $1\mu s$ (i.e., the short-term stability), the laser structure itself has to be changed. One of the effective way for this purpose is th increase the cavity Q by adding an external grating as shown by Fig. 12, the stability of the free running laser was actually improved, and further improvements were obtained by the stabilization.
The results are given by Fig. 13[19]. Though they are still preliminary results, it can be expected that this technique is really effective to improve the short-term stability.

4. Frequency Control and Stabilization of 1.5μm InGaAsP Lasers

As 1.5μm InGaAsP lasers are rather new type laser, some of their oscillating characteristics are still unknown. However, by several experiments, it has been known that the frequency shifts by the unit change in the injection current and temperature are -1.0GHz/mA and -11GHz/K, respectively[20]. Furthermore, it was found that absorption spectra in NH_3 and H_2O vapor can be used as the frequency standards for the long-term frequency stabilization[21]. Figure 14 shows the results of the stabilization[21]. The stability was improved about 1000 times than that of the free-running lasers. The minimum of $\sigma_y(\tau)$ was

$$\sigma_y(\tau) = 2.1 \times 10^{-11} \quad \text{at} \quad \tau = 200 \text{ s}. \tag{13}$$

5. Applications of Frequency Controlled Lasers

One of the most important applications of 0.8μm AlGaAs lasers if the optically pumped Rb atomic clock, which will be used for communication, navigation, astronomy, etc [22]. That is, these lasers are used for optical pumping of Rb vapor to get a stable microwave signal of 6.8GHz. As a preliminary experiment, the Doppler-free saturated absorption spectra in Rb-D_2 line has been measured by the author, which is shown by Fig. 15[16].

The second example is the optically pumped Cs atomic clock which shows a higher frequency stability than that of Rb atomic

clock, and can be used as a primary standard of time[23]. The aukthor's colleagues have already succeeded in fabricating a stable single mode CW laser (S-MIS type AlGaAs laser) used for this experiment[24]. Several laser fabrications are now in progress by the author's group to get a better wavelength coincidence with the Cs or Rb resonant lines for optical pumping.

The third example is the pollutant gas monitoring by 1.5μm InGaAsP lasers and optical fibers. The remote sensing of the local concentration of pollutant gases can be done by using the optical fiber as a transmission line. The experimental apparatus is shown by Fig. 16[21]. Figure 17 shows the relation between the signal-to-noise ratio of the observed NH_3 spectral shape and the NH_3 vapor pressure. The minimum detectable concentration was estimated as being 3ppm from this result.

The last example is the fiber gyroscope composed of a 1.5μm InGaAsP laser and optical fibers. Figure 18 is the schematic diagram of the gyroscope proposed by the author, which is composed of a ring Fabry-Perot interferometer[25]. It was estimated that the sensitivity, shown by Fig. 19 , of this gyro is as high as the one limited by the detector-shot noises. which is more sensitive than a conventional Mach-Zender interferometer-type fiber-gyro. The experiments are now in progress by following this design.

6. Summaries

The results of the spectral width measurements and long-term frequency stabilizations of 0.8μm AlGaAs and 1.5μm InGaAsP lasers were presented. These highly stabilized lasers may be used as reliable light sources for coherent optical measurements in the future. As examples of such application, several results for Rb and Cs atomic clock, pollutant gas monitoring, and fiber-gyro were also described.

Acknowledegements

The author would like to express his thanks to Profs. T. Tako and Y. Suematsu of his institute for their encouragements during this study.

References

[1] K. Aiki, M. Nakamura, T. Kuroda, J. Umeda, R. Ito, N. Chinone and M. Maeda : IEEE J. Quantum Electron., QE-14 (1978) 89

[2] Y. Noda, K. Sakai and Y. Matsuyama : Electron. Lett., 17 (1981) 226
[3] D. Welford and A. Mooradian : Appl. Phys. Lett., 40 (1982) 865
[4] C. Henry: IEEE J. Quantum Electron., QE-18 (1982) 259
[5] T. Takakura, K. Iga and T. Tako : Jpn. J. Appl. Phys., 19 (1980) L725
[6] Y. Yamamoto, S. Saito and T. Mukai : IEEE J. Quantum Electron., QE-19 (1983)47
[7] W. Elsasser, E. O. Gobel and J. Kuhl : IEEE J. Quantum Electron., QE-19 (1983) 981
[8] T. Okoshi, K. Kikuchi and A. Nakayama : Electron. Lett., 16 (1980) 630
[9] D. Allan : Proc. IEEE, 54 (1966) 221
[10] K. Kikuchi and T. Okoshi : Electron. Lett., 19 (1983) 812
[11] M. Ohtsu and S. Kotajima : Jpn. J. Appl. Phys., 23 (1984) 760
[12] T. J. Boem, H. R. Bilger and J. 1. Tandon : Proc. Symposium on 1/f fluctuations, p62, Tokyo, July 1977
[13] M. Ito : Ph.D. Thesis, Tokyo Institute of technology, February 1982 (in Japanese)
[14] H. Tsuchida, M. Ohtsu and T. Tako : Jpn. J. Appl. Phys., 20 (1981) L403
[15] H. Tsuchida, M. Ohtsu and T. Tako : Jpn. J. Appl. Phys., 21 (1982) L1
[16] H. Tsuchida, M. Ohtsu,1 T. Tako, N. Kuramochi and N. Oura : Jpn. J. Appl. Phys., 22 (1983)1543
[17] H. Tsuchida and T. Tako : Jpn. J. Appl. Phys., 22 (1983)L258
[18] M. Ohtsu,1 H. Fukada, T. Tako and H. Tsuchida : Jpn. J. Appl. Phys., 22 (1983) 1157
[19] S. Sampei, H. Tsuchida, M. Ohtsu and T. Tako : Jpn. J. Appl. Phys., 22 (1983) L258
[20] M. Ohtsu, H. Tagawa and H. Kotani : Jpn. J. Appl. Phys., 22 (1983) 1876
[21] M. Ohtsu, H. Kotani and H. Tagawa : Jpn. J. Appl. Phys., 22 (1983) 1553
[22] L.L. Lewis and M. Feldman : Proc. 35th Annual Symposium on Frequency Control, p.612, Ft. Monmouth, May 1981
[23] M. Arditi and J.L. Picque : J. Phys. Lett., (Paris), 41 (1980) L379
[24] K. Kishino, S. Kinoshita, S. Konno and T. Tako : Jpn. J. Appl. Phys., 22 (1983) L473
[25] M. Ohtsu and Y. Otsuka : Proc. Meeting on Opto-Quantum Electronics, IECE Japan, OQE83-61, September 1983 (in Japanese

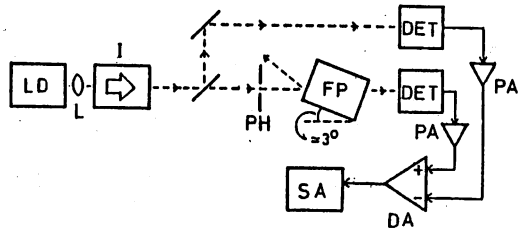

Fig. 1. Experimental setup for FM noise measurements [11].

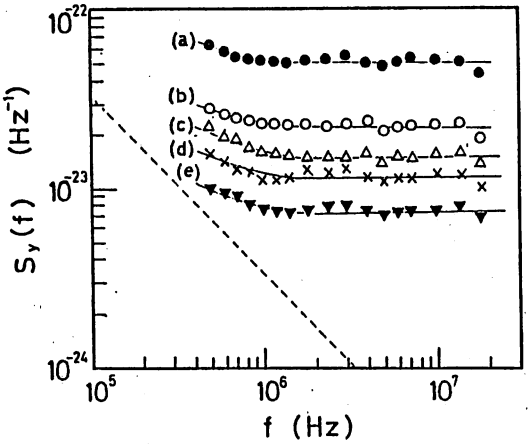

Fig. 2. Experimental results of the power spectral density of the FM noises at T = 293K [11].
$(I/I_{th} - 1)^{-1}$ = 11.1 (a), 8.3 (b), 5.9 (c), 4.2 (d), 2.9 (e).
--------: Power-independent 1/f noise by Kikuchi and Okoshi [10].

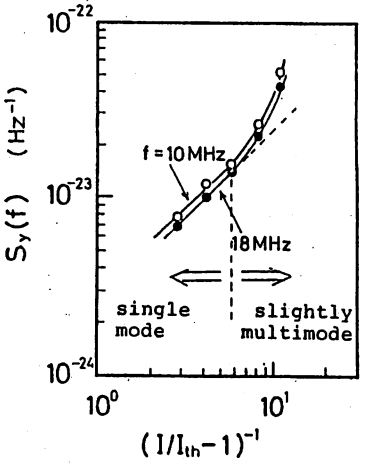

Fig. 3. The relation between the power spectral density and the injection current [11].

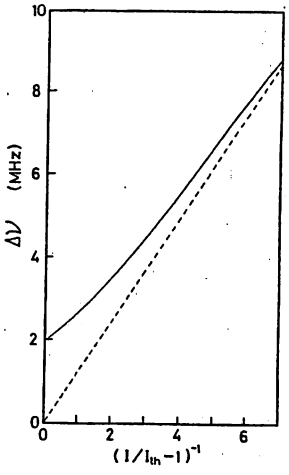

Fig. 4. The relation between the estimated spectral width and the injection current [11].
———— : The results obtained by considering also the 1/f noises.
------ : The result obtained by neglecting the 1/f noises.

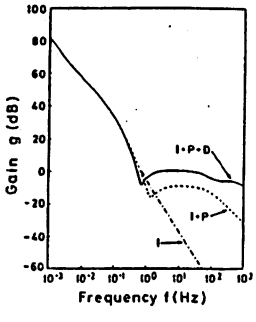

Fig. 5. The frequency characteristics of the gains of the PID controller

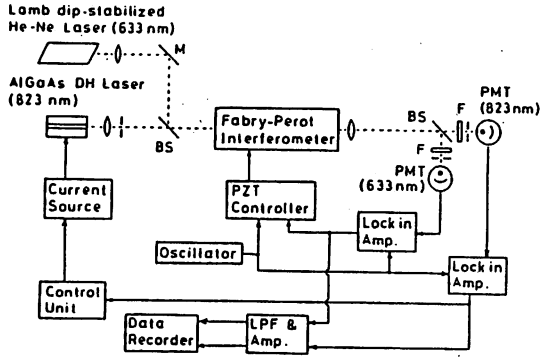

Fig. 6. Experimental setup of the frequency stabilization using a Fabry-Perot interferometer as a frequency standard, which is also stabilized by a He-Ne laser [14].

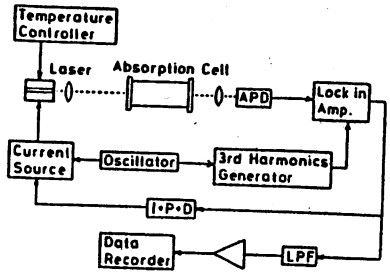

Fig. 7. Experimental setup of the frequency stabilization using an absorption line in H_2O vapor as a frequency standard [15].

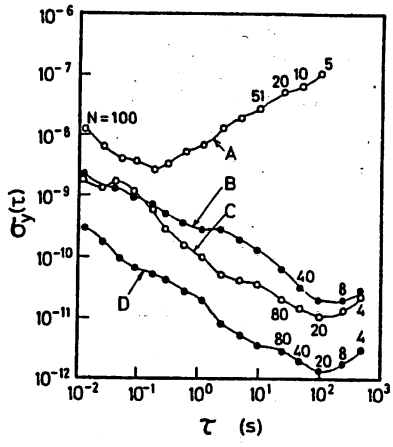

Fig. 9. The results of the frequency stabilization.
A : Free-running laser.
B : Stabilized laser by the stabilized Fabry-Perot interferometer.
C : Stabilized laser by H_2O
D : Stabilized laser by $^{85}Rb\text{-}D_2$ line.

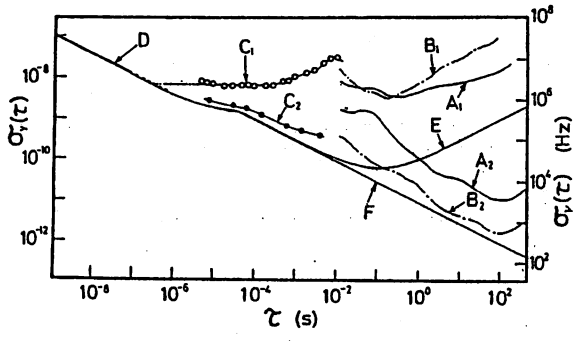

Fig. 11. Comparison between the experimental results of frequency stabilization and the theoretical limits.
A_1, B_1, C_1, D : Free-running.
A_2 : Stabilized by H_2O [15].
B_2 : Stabilized by $^{85}Rb\text{-}D_2$ [16].
C_2 : Stabilized by a rigid Fabry-Perot interferometer [17].
E : Theoretical limit for the free-running laser [18].
F : Theoretical limit for the stabilized laser [18].

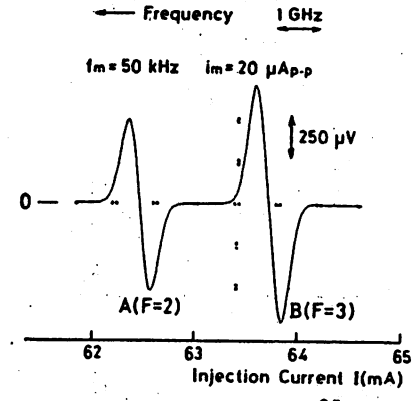

Fig. 8. Absorption spectra of $^{85}Rb\text{-}D_2$ line used as the frequency standard [16].

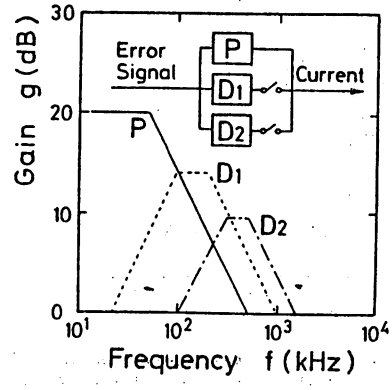

Fig. 10. Frequency characteristics of the gains of the differentiators used to expand the bandwidth of the phase-lead compensation [17].

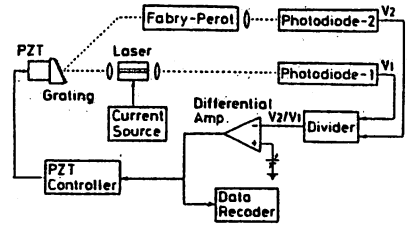

Fig. 12. Experimental setup of the frequency stabilization of the laser with an external grating [19].

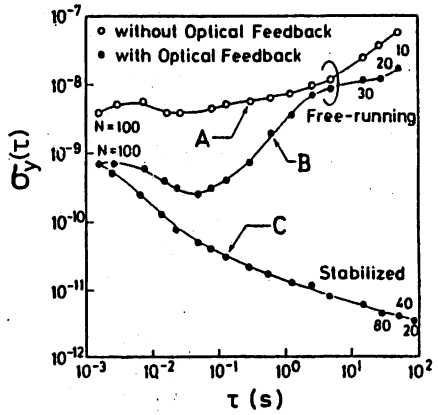

Fig. 13. Experimental results of the stabilization of the laser with an external grating [19].

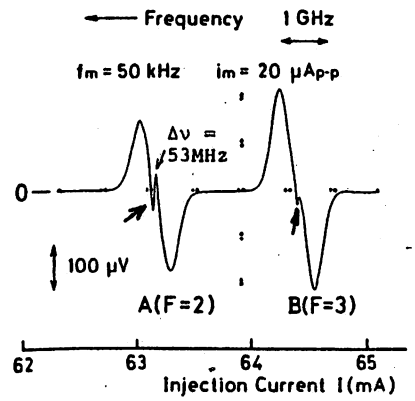

Fig. 15. Saturated absorption spectra in ^{85}Rb-D$_2$ lines, which are indicated by arrows in the figure [16].

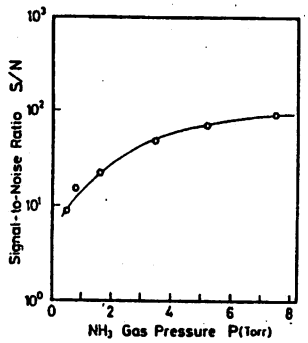

Fig. 17. The experimental results of the relation between the S/N value of the NH_3 spectral shape and its vapor pressure [21].

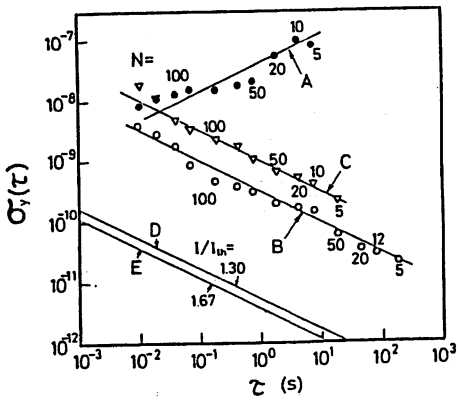

Fig. 14. Experimental results of the frequency stabilization of 1.5μm InGaAsP lasers [21].
A : Free-running.
B : Stabilized by NH_3 spectra.
C : Stabilized by H_2O spectra.
D, E : Theoretical limits.

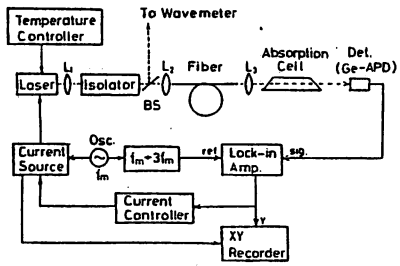

Fig. 16. Experimental setup of the pollutant gas monitoring using a 1.5μm InGaAsP laser [21]. The fiber length was 50 m .

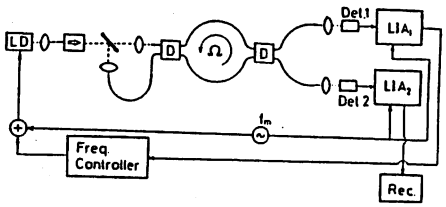

Fig. 18. Fiber-gyroscope which is composed of a ring Fabry-Perot interferometer [25].

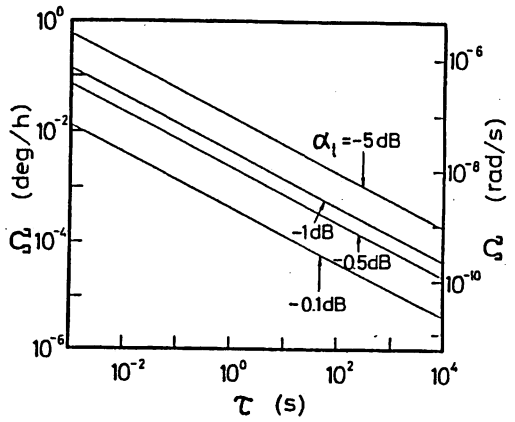

Fig. 19. Estimated sensitivity of the fiber-gyro of Fig. 18 [25].
α_t represents the total loss of the fiber and directional coupler D.

LIMIT OF FREQUENCY STABILITY IN SEMICONDUCTOR LASERS

T. Tako, M. Ohtsu* and H. Tsuchida**
Department of Physics, Faculty of Science and Technology, Science University of Tokyo, Noda, Chiba 278
* International Cooperative Center for Science and Technology, Tokyo Institute of Technology, O-okayama, Meguro-ku, Tokyo 152
** Electrotechnical Laboratory, Sakura-mura, Niihari-gun, Ibaraki 305

Semiconductor lasers during free-running operation exhibit large frequency fluctuations due to the high sensitivity of the active layer refractive index to temperature and injection current variations. For instance, the frequency change per unit temperature and injection current changes are -20 GHz/°C and -3 ~ -7 GHz/mA,in AlGaAs lasers. Therefore, these frequency fluctuations should be reduced for such applications as precise optical metrology, high resolution spectroscopy, coherent optical transmission systems. There have been several reports on frequency stabilization in semiconductor lasers using a Fabry-Perot etalon and atomic or molecular absorption lines as stable frequency references.

1. Frequency Stabilization Using a Fabry-Perot Etalon

A Fabry-Perot etalon is used as a frequency reference to improve the short-term ($\tau < 1$ s) stability. This method has an advantage in that the laser frequency can be easily stabilized regardless of its wavelength. However, long-term stability is limited mainly by the thermal drift of the length of the etalon. Figure 1 shows the frequency stability of an AlGaAs laser (I_{th} = 57 mA, λ= 815 nm, I/I_{th} = 1.25). The solid line represents the theoretical stability determined by the quantum noise of the laser, which is calculated by taking account of the spontaneous emission coupled to a lasing mode, carrier and current modulation noises. Curves A and B represent the frequency stability of the free-running and the stabilized lasers, respectively. The value of σ_y on the Curve B is nearly proportional to $\tau^{-\frac{1}{2}}$. The results of the experiment are in good agreement with theoretical stability, which indicates that the stability obtained with this method is limited by the quantum noise of lasers. To obtain higher stability it is necessary to decrease the quantum noise, that is, to use the laser with a higher Q-value.

2. Frequency Stabilization Using an Atomic or Molecular Absorption Line

Atomic or molecular absorption lines have been used for frequency stabilization to improve long-term stability and reproducibility. In this method, it necessay that the wavelength of the laser to be stabilized coincides with that of the absorption line and that the laser frequency (or absorption line freq.)

is modulated to obtain the derivative signal of the absorption spectrum, which can be used as a frequency discriminator. Figures 2 and 3 show the frequency stability of the stabilized AlGaAs lasers using the ^{85}Rb-D_2 line at 780 nm (strong absorption) and using the vibration-rotation spectrum of water vapor at 824 nm (weak absorption), respectively. The stabilities are seen to be limited by both the quantum noise and noise of the photodetector in Fig. 2 and by the effects of the noise of the detector and the frequency modulation in Fig.3. To obtain higher stability with this method, it is necessary to increase the amount of the absorption and the signal to noise ratio.

References

1) M. Ohtsu, H. Fukada, T. Tako and H. Tsuchida: Jpn. J. Appl. Phys. 22 (1983) 1157

2) H. Tsuchida and T. Tako: Jpn. J. Appl. Phys. 22 (1983) 1870

3) T. Tako and H. Tsuchida: JARECT Vol. 11. Optical Devices & Fibers (1984) (ed. Y. Suematsu) Ohmsha LTD. and North-Holland Pub. Co. p. 46

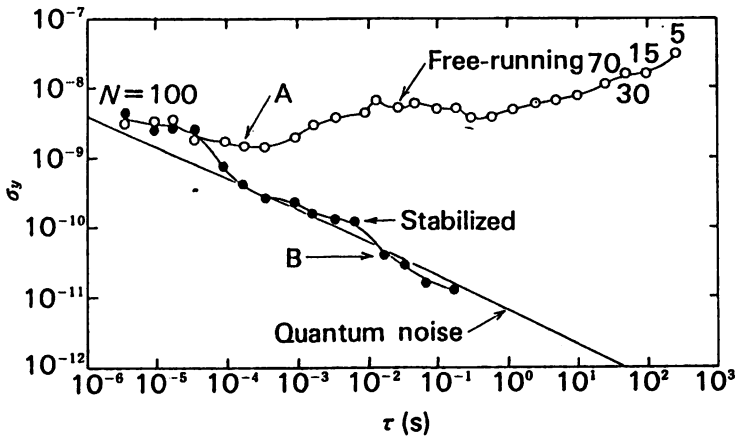

Fig. 1 The frequency stability of the lasers, where σ_y, τ and N represent the square root of the Allan variance, integration time and number of data, respectively. Curves A and B correspond to the free-running and the stabilized lasers. Solid line represents the theoretical stability determined by the quantum noise of the laser. [3]

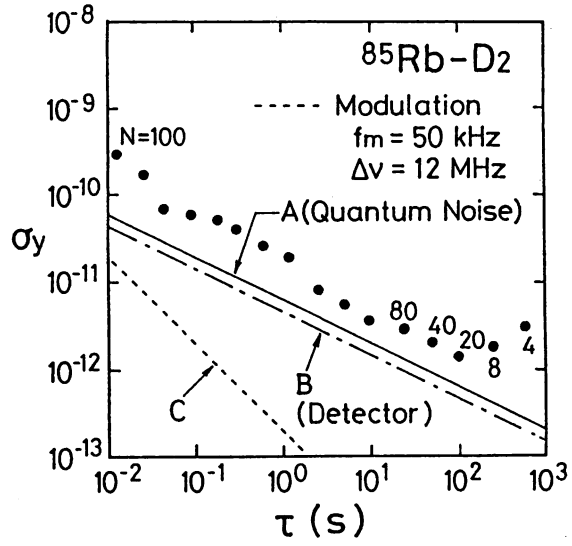

Fig. 2 Frequency stability of the laser stabilized using the $^{85}Rb\text{-}D_2$ line. Curves A, B and C represent the theoretical stabilities determined by the quantum noise, noise of a photodetector and frequency modulation, respectively.[2)]

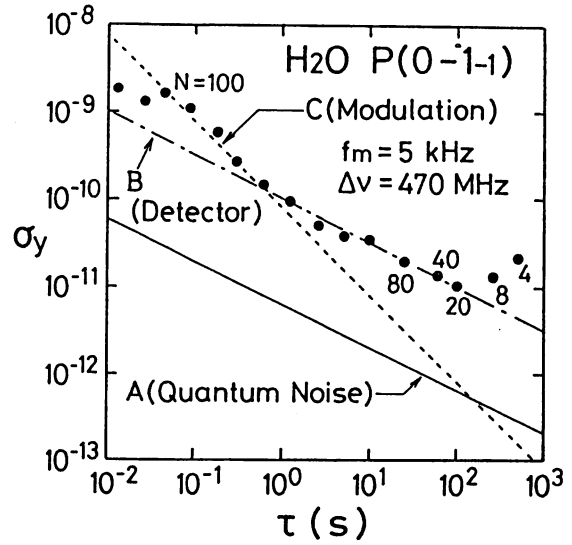

Fig. 3 Frequency stability of the laser stabilized using the vibration-rotation spectrum of water vapor. Curves A, B and C represent the theoretical stabilities determined by the quantum noise, noise of a photodetector and frequency modulation, respectively. [2)]

SPECIFIC INSTABILITIES IN SEMICONDUCTOR LASERS INDUCED BY REFLECTED LIGHT

Y.Teramachi* and M.Ohtsu**

* Graduate School at Nagatsuta, Tokyo Institute of Technology, Yokohama, Kanagawa 227, JAPAN

** International Cooperation Center for Science and Technology, Tokyo Institute of Technology, Meguro-ku, Tokyo 152, JAPAN

It has been experimentally found that a large level of intensity instability appears in a semiconductor laser when the delayed reflected light is injected into the laser. The characteristics of this instability is investigated by analog computer simulation in this study.

The laser oscillation was described by van der Pol equation, to which a term representing a reflected light was added. Coefficients in this equation were derived from one of the most precise model for semiconductor [1] so that a detailed comparison with previously reported experimental results can be done. Since these coefficients are proportional to the number of active carriers in the laser, the temporal variation variation of this number had to be simutaneously considered.

As the results of the simulation, it was found that a relaxation oscillation in carrier number gave a specific instability of laser oscillation. Figures 1,2 and 3 give power spectral density fluctuation for three levels of reflected light intensity. When the reflected light intensity is low (Fig. 1), a resonant peak by the influence of the relaxation oscillation can be clearly seen. For the medium level of reflected light intensity (Fig. 2), it is seen that this resonant peak is enhanced by the reflected light, and wideband incoherent fluctuations are also induced. This profile of power spectral density means that the laser intensity fluctuation shows a chaotic behavior. Furthermore, for a larger intensity of a light (Fig. 3), resonant peaks corresponding to even order harmonics of the relaxation oscillation were induced, which is a specific phenomenon of the semiconductor lasers.

It can be concluded from these results that the chaotic behavior and harmonics of relaxation oscillation in semiconductor lasers are strongly

influenced by temporal variations of the number of active carriers and its relaxation oscillation phenomenon.

Reference:
(1) M.Yamada and Y.Suematsu; IEEE Journal of Quantum Electron., QE-16 (1980) 347

Figure Captions:

Fig.1 Power spectral density S(f) of intensity fluctuation for $K=1.5\times10^{9}(\ s^{-1}\ )$, where K represents the coupling coefficient of the reflected light into the laser cavity.

Fig.2 S(f) for $K=7.5\times10^{9}(\ s^{-1}\ )$.

Fig.3 S(f) for $K=6.0\times10^{10}(\ s^{-1}\ )$.

Fig.1

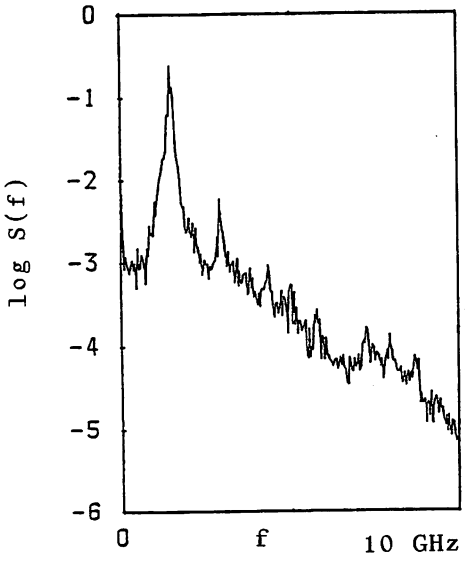

Fig.2

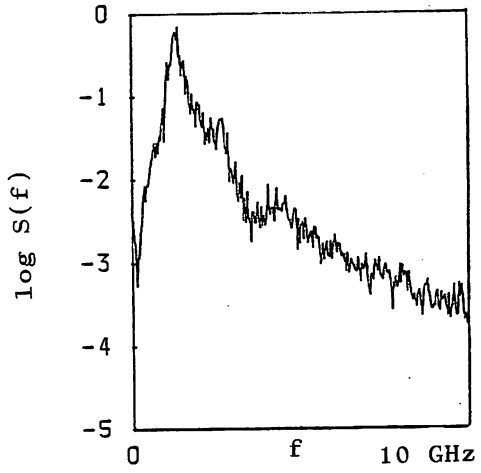

Fig.3

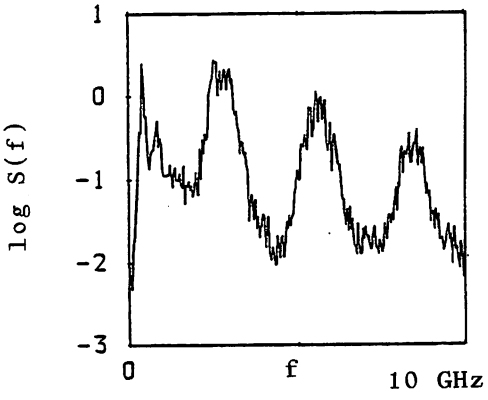

Title will be announced.

R. L. Byer

Ginzton Laboratory, Stanford University
Stanford, CA 94305

JOURNAL DE PHYSIQUE
Colloque C8, supplément au n°12, Tome 42, décembre 1981 *page* C8-83

FREQUENCY STABILIZATION OF AlGaAs LASERS BASED ON THE H_2O AND Rb-D_2 LINES

T. Tako, M. Ohtsu and H. Tsuchida

Research Laboratory of Precision Machinery and Electronics, Tokyo Institute of Technology, 4259 Nagatsuta-cho, Midori-ku, Yokohama, Kanagawa 227, Japan.

Abstract: Recent works on frequency stabilization of AlGaAs DH lasers based on absorption lines of H_2O vapor at 0.81 — 0.83μm or 85Rb-D_2 line at 0.78μm are reported. The minimum values of the square root of Allan variance are 1.0×10^{-11} and 1.4×10^{-12} at 100s of averaging time, respectively.

§1. Introduction

Recently, spectral properties of semiconductor lasers have been improved. A stable single longitudinal and transversal mode oscillation has been obtained for AlGaAs double heterostructure (DH) lasers and the spectral widths of these lasers have been estimated to be narrower than 1 MHz by interferometric measurements[1]. The frequency stability as well as the spectral width is a very important factor for many applications, such as heterodyne-type optical communication, high resolution spectroscopy, precise metrology and so on.

There have been several reports on the frequency stabilization of semiconductor lasers by using a Fabry-Perot imterferometer as a frequency reference.[2-7] In our previous work,[7] the frequency of AlGaAs lasers was stabilized at the resonant frequency of a

interferometer, which was controlled by a Lamb dip stabilized 633nm He-Ne laser. By controlling the injection current, the frequency stability of $2.1\times10^{-9} \geqq \sigma \geqq 2.0\times10^{-11}$ for $10ms \leqq \tau \leqq 500s$ was obtained, where σ and τ represent the square root of the Allan variance and integration time, respectively.

Direct frequency locking of semiconductor lasers based on atomic or molecular lines is important for the use of frequency standards. Ohi reported the frequency stabilization of a PbSnTe laser to methane absorption lines in the ν_4 band at about 7.7μm[8] and Yabuzaki et al. reported the frequency stabilization of a GaAlAs laser to the Cs-D_2 line at 852.1nm.[9]

In this paper the frequency stabilization of AlGaAs lasers based on the absorption lines of water vapor and the hyperfine components of ^{85}Rb-D_2 line are presented.

§2. Frequency stabilization based on H_2O lines

H_2O molecule has a vibration-rotation band (0,0,0)-(2,1,1) at 0.81 -- 0.84μm. Figure 1 represents the assignment and relative intensity of the main lines of this band reported by Baumann and Mecke[10].

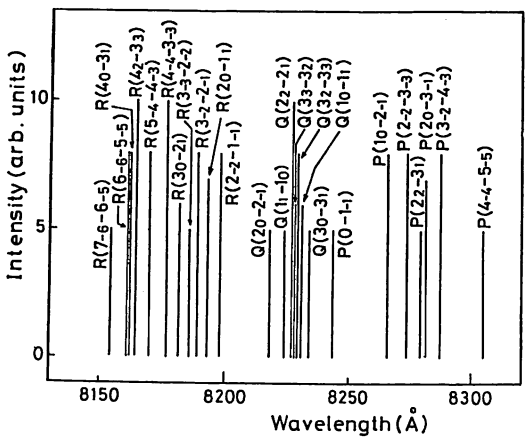

Fig. 1.

A single mode AlGaAs DH laser (CSP type[11]) was used. The threshold current was about 80 mA. The dependence of the laser frequency on the injection current was measured to be (-2.75) GHz/mA by using an interferometer. The laser frequency was tuned in the range of 822.5 — 824.5nm by the temperature change of heat sink of 17 — 23°C.

An absorption cell of 10cm length with pure water drop was used at room temperature (the corresponding vapor pressure being about 20 Torr). The laser beam was focused on an APD after passing through the absorption cell. The first, second, and third derivative signals of the transmission spectrum of H_2O vapor was obtained by synchronously detecting with a lock-in amplifier.

Figure 2 shows typical examples of records. The upper and lower traces represent the first and second derivative signals of the transmission spectrum, respectively. The lines marked (o) correspond to that assigned by Baumann and Mecke and the lines marked (x) are unassigned. At present we have found several tens unknown lines.

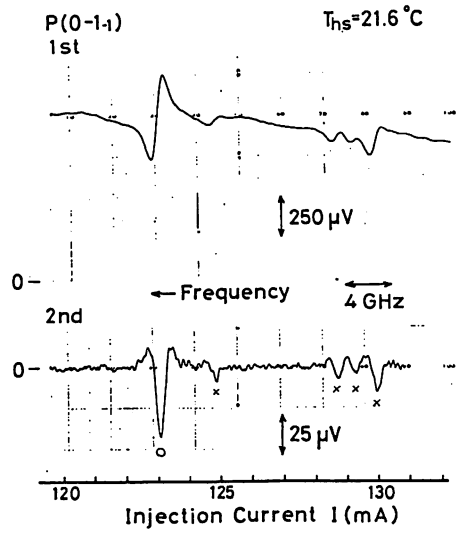

Fig. 2.

Next, the frequency of AlGaAs DH lasers have been stabilized in refer to one of H_2O absorption lines, $P(0\text{-}1_{-1})$. The third derivative signal shown in Fig. 3 was used as a frequency discriminator. The square root of the Allan variance σ^2 is shown at Curve A in Fig. 4. Curves A and B represent the stabilities of the free reunning laser and the stabilized laser by using a Fabry-Perot interferometer and a Lamb dip stabilized 633nm He-Ne laser for comparison.[7] The value of σ on curve A is better than that of curve B and is nearly proportional to $\tau^{-1/2}$. The minimum value on this curve is

$$\sigma = 1 \times 10^{-11} \quad \text{at } \tau = 100\text{s}$$

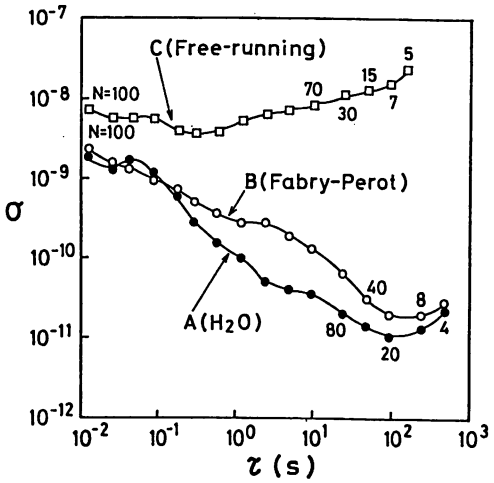

Fig. 4

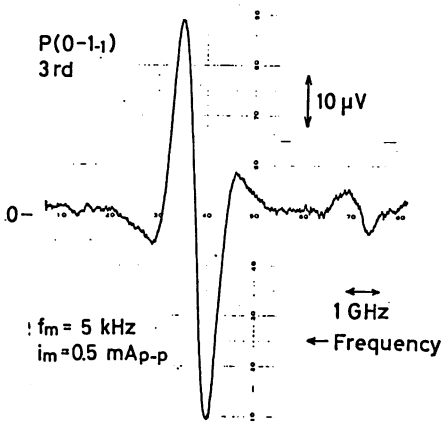

Fig. 3

§3. Freuquency stabilization to Rb-D_2 line

Preliminary experiments are carried out on the frequency stabilization of another AlGaAs laser to a hyperfine component of Rb-D_2 line at 780.0nm. Figure 5 represents the spectral profile (the upper trace) and the first derivative (the lower trace) in case of linear absorption for a 85Rb cell without buffer gas at room temperature (the corresponding vapor pressure of Rb being

-10^{-5} Torr). Figure 6 represents the result on the freuqency stabilization to the F=3 components. The minimum value of σ is

$$\sigma = 1.4 \times 10^{-12} \text{ at } \tau = 100\text{s}$$

and is several times better than the results on the H_2O stabilized laser in Fig. 4.

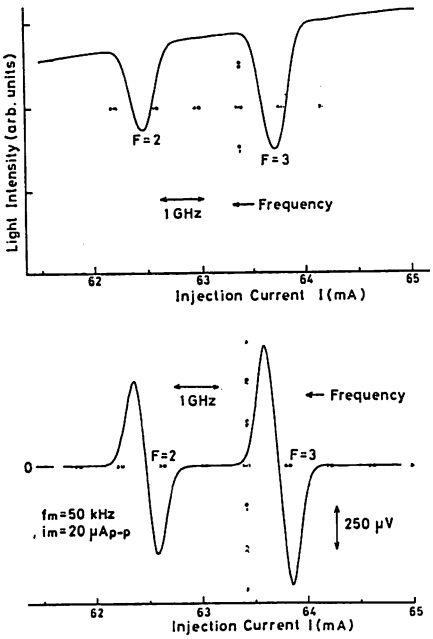

Fig. 5.

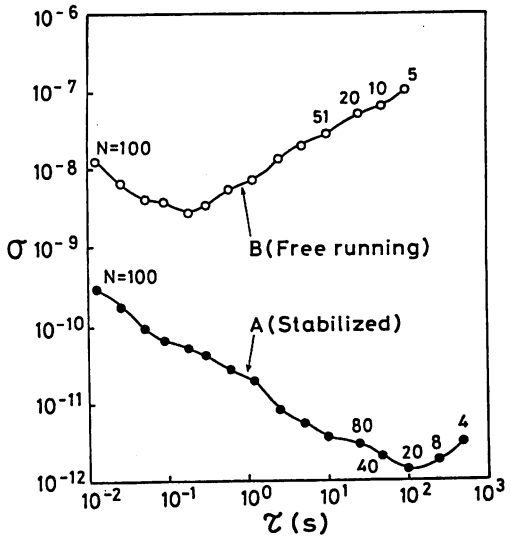

Fig. 6.

The saturated absorption spectrum of Rb-D_2 line was also observed as shown in Fig. 7 and the stabilization experiment to this spectrum is in progress.

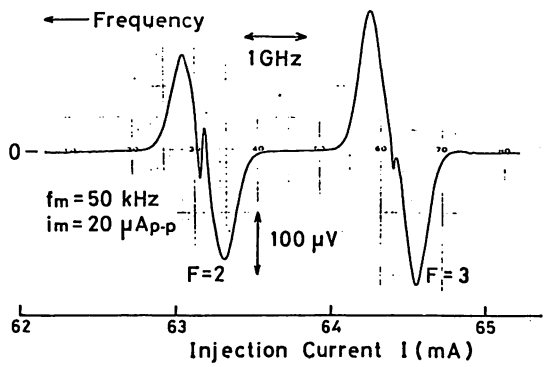

Fig. 7.

References

1) T. Takakura, K. Iga and T. Tako: Jpn. J. Appl. Phys. 19 (1980) L725.

2) Yu. A. Bykovskii, V. L. Velichanskii, I. G. Goncharov and V. A. Masrov: Sov. Phys.-Semicond. 4(1970) 580.

3) J. L. Picque and S. Roizen: Appl. Phys. Lett. 27(1975) 340.

4) T. Okoshi and K. Kikuchi: Electron. Lett. 16(1980) 179.

5) F. Favre and D. Le Guen: Electron. Lett. 16(1980) 709.

6) H. Tsuchida, S. Sanpei, M. Ohtsu and T. Tako: Jpn. J. Appl. Phys. 19(1980) L721.

7) H. Tsuchida, M. Ohtsu and T. Tako: Jpn. J. Appl. Phys. 20 (1981) L403.

8) M. Ohi: Jpn. J. Appl. Phys. 19(1980) L541.

9) T. Yabuzaki, T. Ibaragi, H. Hori, M. Kitano and T. Ogawa: Jpn. J. Appl. Phys. 20(1981) L451.

10) W. Baumann and R. Mecke: Zeit. Physik. 81(1933) 445.

11) K. Aiki, M. Nakamura, T. Kuroda, J. Umeda, R. Ito, N. Chinone and M. Maeda: IEEE J. Quantum Electron., QE-14 (1978) 89.

H_2CO STABILIZED He-Xe LASER, AND ITS APPLICATION TO H_2CO MOLECULAR BEAM SPECTROSCOPY

Toshiharu Tako
Motoichi Ohtsu

Research Laboratory of Precision
Machinery and Electronics,
Tokyo Institute of Technology,
4259 Nagatsuta, Midori-ku,
Yokohama 227, Japan

ABSTRACT: A highly stabilized frequency-offset-locked He-Xe laser system at 3.51μm was constructed for the saturated absorption and molecular beam spectroscopies of H_2CO. A H_2CO-stabilized He-Xe laser was used as a frequency reference, and its vacuum wavelength was measured to be 3 507 979.48 pm. Its frequency stability was 1.0×10^{-14} at τ = 100 s. The frequency traceability of the frequency-offset-locked laser to this laser was $8.0 \times 10^{-13} \cdot \tau^{-1}$ for 10 ms $\leq \tau \leq$ 100 s. Its frequency variable range was 19 MHz. As an example of its application to the high resolution laser spectroscopy, the H_2CO molecular beam spectroscopy and its experimental apparatus will be demonstrated at the session.

OPTICAL RAMSEY RESONANCE

K. Shimoda

Department of Physics, University of Tokyo
Hongo, Bunkyo-ku, Tokyo 113, Japan
Telephone: 03/812-2111 ext.4164

ABSTRACT: The optical Ramsey resonance signal of two-level molecules in three separated fields produced by a corner reflector is studied. The transition probability of a molecule that traverses the three interaction regions is calculated. It is then integrated over distributions of molecular velocities and positions to evaluate the signal observed with a gas cell. The result is applied to compute the optical Ramsey resonance signal in the absoption line of CH_4 at 3.39μm, which is under experimental investigation. The pressure dependence and the power dependence of the signal are numerically obtained in order to find the optimal condition of experiment.

解　説 2

1.1, 7.3

原子分子ビーム・レーザー分光

田幸敏治・大津元一

東京工業大学精密工学研究所　〒227 横浜市緑区長津田 4259

(1978年4月26日　受理)

1. はじめに

原子分子ビームの最初の実験はすでに60年以上前の1911年にDunoyer[1]によって行なわれ，Na原子ビームの飛行軌跡が調べられた．それ以後原子分子ビームは気体運動論，化学平衡の研究手段として使われるとともに，原子の磁気モーメントの測定がまずSternとGerlach[2]によって1924年に行なわれ，その後，1938年にRabiら[3]によって原子分子ビーム共鳴法が核，原子，分子の特性の精密測定に導入されたのを契機に原子分子ビームの歴史は主に共鳴法の歴史であるといえるほど磁気共鳴法，マイクロ波分光法に盛んに用いられるようになった．そしてこの分野の一つの応用として現在時間標準として知られているCsビーム標準器が開発された．また，NH_3分子ビームメーザー[4]，H原子ビームメーザー[5]，さらにミリ波，サブミリ波領域でのHCN[6,7]，H_2CO[8]分子ビームメーザーに原子分子ビーム法が使用されている．

いっぽう，光領域でも高分解能分光の分野で原子分子ビームが使用され，当時の波長標準としてのCd赤線の分光に利用されたり[9]，また可干渉距離が1m以上の光源としてのCa[10]，^{198}Hg[11]，Cd, Ar[12]などの原子ビーム光源の研究が行なわれた．さらにレーザーの出現以来，レーザーと原子分子ビームとの併用によって気体原子，分子の分光の分解能向上に寄与した．また，原子分子ビームは最近注目されているレーザー同位体分離においても基本的技術として重要である．

本稿では高分解能レーザー分光への原子分子ビームの応用を主題として解説を試みる．なお，本稿とほぼ同じ主題に関する1975年以前の研究についての優れた解説がJacquinot[13]によってなされているが本稿ではJacquinotのふれていない点，1975年以後の研究例についても述べたい．さらに磁気共鳴法を主題とした原子分子ビームの解説としては有名なRamseyの著書[14]があり，生成実験技術については楠[15]による解説があることを付記する．なお，本稿では原則としてイオンビームは除外したい．

2. 原子分子ビーム分光法の特徴

レーザー分光に原子分子ビームを用いる理由の一つとして実験技術的なものがある．すなわち，たとえばNa, Ca, Csなどの金属原子は試料セル中で温度調節により一定蒸気圧の金属蒸気として使うよりもむしろ原子ビームとして使った方が容易な場合がある．しかしこの他にも他の方法とくらべて優れた点があるので本章では原子分子ビーム分光法の特徴について記す．

2.1 ドプラー幅の消去

原子分子ビームの飛行方向と直角方向からレーザー光を入射させたとき原子分子ビームのスペクトルのドプラー幅は原子ビームの発散角に比例する．したがって発散角が小さいときには線形分光法でも不均一拡がりであるドプラー形スペクトルを消去し，均一拡がりをもったスペクトルを測定することができる．ドプラーフリーの他の分光法として代表的なものに飽和吸収分光法，2光子分光法がある．両者は非線形光学効果にもとづく方法であることによりいくつかの欠点をもっているが[16]，原子分子ビーム分光法は線形分光であるので得られるスペクトルの形は単純である．

2.2 衝突数の減少

一般に使用されている原子分子ビームの密度は低いので原子分子の間での衝突数は他の分光法で用いられる試料セル中での衝突数よりも少ない，さらに原子分子ビーム中での各原子分子はほぼ同一方向に飛行するので同一密度の試料セル中よりもさらに衝突数は少ない．したがって原子分子ビームを用いるとスペクトルの衝突幅（圧力幅），圧力シフトを減少させることができる．また，高励起準位では主量子数nの2乗に比例する大きな衝突半径をもっているので衝突に対して敏感であり，したがってこの準位の研究には原子分子ビーム法は有力な手段である．

2.3 軌跡の偏向

原子分子ビーム中の原子分子のうちで光と共鳴相互作用をしたものはフォトンとの運動量の移動によりその飛

行軌跡が偏向する[17~20]．また，常磁性原子分子が光と相互作用することによりその磁気副準位が変化すればその原子分子ビームの飛行軌跡は不均一磁場によって偏向する[21~23]．偏向したこれらの原子分子ビーム中の原子分子数をイオン検出器で測定すれば光との相互作用についての情報が得られる．このように従来の分光法とちがい情報の担い手がフォトンではなく原子分子にもなりうることは原子分子ビーム分光法の独特な特徴である．

2.4 原子分子ビームの飛行軌跡上での時間-空間変換

原子分子ビーム中の原子分子の位置はその飛行速度を比例定数として時刻に比例しているのでその原子分子からの放出光の時間変化は空間的変化としてとらえることができる．これを使うと量子ビート[24]，radiative decay などの時間的現象を空間的現象に変換して測定できる．

3. 検出方法

光領域での原子分子ビームスペクトル測定のための信号検出法について記す．

3.1 光の吸収，自然放出光（螢光）測定による検出

入射光の吸収率を測定する方法では原子分子ビームの密度が低いときには入射光のうちの微小部分が吸収されるのみであり，透過光強度と入射光強度の差が小さいので S/N 値を大きくできない．そこで吸収率を増す方法としては **5.3** で示す multiparallel channel を使って原子分子ビーム断面積を増すこと，White's cell[25] などのくりかえし反射鏡を用いること，原子分子ビームをレーザー共振器中で流すことによって原子分子ビーム中でのレーザー光路長を長くすることが挙げられる．いっぽう原子分子ビームからの自然放出光(螢光)を測定する場合放出光強度は弱くても吸収率測定の場合と異なりバックグラウンドである入射光とは分離して測定できるので S/N 値が高くなる．吸収率測定，自然放出光（螢光）測定の場合の S/N 値をそれぞれ $(S/N)_{abs.}$, $(S/N)_{fl.}$ と書くと両者の比は次式で与えられる[13]．

$$(S/N)_{fl.}/(S/N)_{abs.}=\sqrt{\frac{1}{a}\cdot\frac{\Omega}{4\pi}} \qquad (1)$$

ここで a は吸収率測定の場合の入射フォトンの吸収率，Ω は自然放出光の発光源からの検出器の受光面を見込んだ立体角である．ふつう $a=10^{-6}$～10^{-8} の値をとるので $\Omega=10^{-2}$ sr 程度の値でも(1)式の値は 8～80 となり，自然放出光測定の有利さがわかる．**4.** に示す可視域での実験の多くは自然放出光測定の方法を用いている．

3.2 軌跡の偏向を用いる検出

これは **2.3** の性質を用いる方法である．フォトンとの運動量の移動による飛行軌跡の偏向角はふつう 10^{-5} rad 程度であり小さいが偏向後の原子分子ビームの飛行距離を長くとることによりイオン検出器で偏向原子分子の数を計数しうる．**3.1** で示した自然放出光を測定する方法では空間的に均一に放出される自然放出光の一部が光検出器の中に入るにすぎないが，本節の方法では偏向した原子分子を全部イオン検出器に入射させることが可能であるので測定効率がよい．Ashkin[17] はこの方法を同位体分離に応用することを提案した．次に，不均一磁場を用いた偏向の方法では磁場強度と磁場の位置とにより偏向角の値は自由にかえられるが検出方法としてはフォトンとの運動量の移動による偏向の例と同じであり，Duong ら[21] によって NaD_2 線の微細構造が，Duong と Vialle[23] によって NaD_1 線のそれが測定された．

3.3 光電離による検出

この方法は第1のレーザー光により原子分子を励起し，それにさらに第2のレーザー光を照射してイオン化し，イオン化された原子分子の数を検出するものである．イオン計数法は高効率であるので原子分子ビーム密度が低くても S/N 値は大きい．この場合は通常上準位からの光電離確率が下準位から上準位への励起確率より小さいのでここの検出方法の効率は光電離確率で決まる．これはレーザー同位体分離の代表的な方法で[26]，たとえば Tuccio ら[27] によって ^{235}U の，Brinkmann ら[28] によって ^{40}Ca の同位体分離が行なわれた．

以上の検出方法のうち光電離によるものは2台のレーザーを用いるのでやや特殊であるがその他について比較すると，寿命の短かい励起準位にはレーザー光と原子分子ビームとの交点での自然放出光（螢光）の検出がもっとも簡単な方法であり，また，寿命の長い励起準位には磁場（または電場）による偏向法が適していると考えられる．吸収検出法は高密度原子分子ビームが得られるならば使用可能である．ただしこのとき衝突数の増加を抑えるように注意が必要である．

4. 原子分子ビーム分光法の現状

現在までに行なわれている研究例のうち主なものを以下にまとめて示す．

4.1 原子ビーム分光

CW 色素レーザーを用いて Na 原子の微細構造の測定がよく行なわれている．まず Lange ら[29] は発散角 2 mrad, 残留ドプラー幅 5 MHz の Na 原子ビームを生成し螢光検出により D_2 線の2組，各3本の微細構造線を分離測定した　その結果を **Fig. 1** に示す．**Fig. 1** 中の各スペクトル線の幅は約 15 MHz である．また Hartig ら[30] は Lange らと同時期に，分解能はやや劣るが NaD_1, D_2 線の微細構造線を測定し，D_1 線の微細構造線の1つ ($F=2\rightarrow2$) に色素レーザー周波数を固定して周波数変動

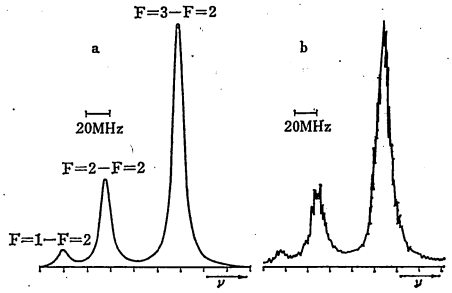

Fig. 1 The hyperfine structure of the Na D_2-line observed in a fluorescence experiment by using a tunable dye laser and a Na atomic beam (Lange *et al.*[29]).
(**a**) Calculated signal curve for comparison with the experimental results ((**b**)).
(**b**) The hyperfine structure observed in this experiment.

を ±1.5 MHz におさえた．同様の実験は Schuda ら[31]によっても行なわれ，Wu ら[32]は D_2 線からの螢光をファブリ・ペロー干渉計によって解析し，非弾性散乱光による $F'=2\rightarrow F=3$ の線のスペクトルのサイドバンドを測定した．また Jacquinot ら[33]はレーザー光による原子ビームの飛行軌跡の偏向を用いて D_1, D_2 線の微細構造線を測定し，Lange ら[29]の実験結果とほぼ同程度の分解能を得ている．この場合，原子ビームの発散角は 0.1 m rad と非常に小さく，流量も $10^7\,s^{-1}$ と低いのが特長である．また，Griffith ら[34]は D_1 線の2本の微細構造線 ($F=2\rightarrow1, F=2\rightarrow2$) に2台の色素レーザー周波数を固定し，両者のビート周波数から2本の微細構造線の周波数差を 188.93 (±0.02) MHz と測定している．Na 以外では Träger ら[35]が波長 657.3 nm の Ca の禁制 intercombination 線 ($4s^2\,{}^1S_0-4s4p\,{}^3P_1$) スペクトルを測定した．この場合 $4s4p\,{}^3P_1$ 準位の寿命は長い (0.4 ms) ので螢光の観測位置は励起用色素レーザー光と Ca 原子ビームとの交差点からはなれており，迷光の影響を少なくすることができた．また，Ca 原子ビームはレーザー共振器内で流しているので測定感度が高く，^{nat}Ca 中の含有率の少ない ^{43}Ca, ^{46}Ca によるスペクトル線が分離測定可能であった．この他に原子ビーム分光法を適用した原子としては Yb, Ne, Li などがある[13]．

次に，すでにマイクロ波領域で行なわれていた実験に対応するものを光領域での原子ビーム分光法を用いて行なった実験を2つ挙げる．

第1の例は Bergquist ら[36]によって行なわれた Ramsey fringe の観測である．この実験では準安定状態の $^{20}Ne^*$ ($1s_5$) の原子ビームが使われている．これはあらかじめ Ne^+ ビームを加速して作っているので平均速度

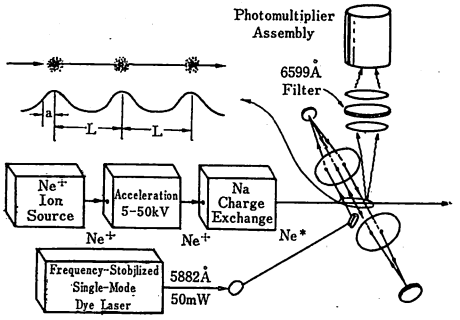

Fig. 2 Schematic diagram of the experiment to observe the Ramsey's interference fringes in the optical region by using a tunable dye laser and a Na atomic beam (Bergquist *et al.*[36]).

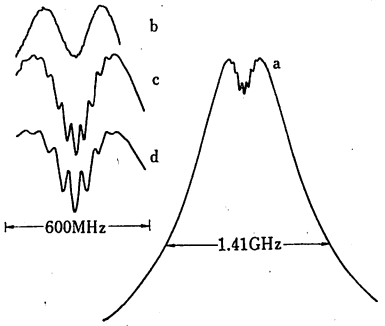

Fig. 3 Fluorescence signals observed wtih the experimental apparatus shown in Fig. 2 (Bergquist *et al.*[36]).
(**a**) The Doppler profile of the Na atomic beam spectrum (full width at half-maximum of 1.4 GHz) showing saturation dip and Ramsey fringes.
(**b**) Saturation dip observed with two separated laser beams.
(**c**) Ramsey fringes and saturation dip with three laser beams.
(**d**) Ramsey fringes and saturation dip with four laser beams.

は 3×10^5 m/s，速度分布のひろがりは $\Delta v/v\cong10^{-4}$，発散角は 2 m rad の“単一速度”の原子ビームである．これは本稿の対象としては例外的な原子ビームであるが高分解能分光として特記すべき内容であるのでここに記す．**Fig. 2** に示すようにこの原子ビームを出力 50 mW の周波数安定化単一モード色素レーザー光（波長 588.2 nm）と3回交差させ，$1s_5\rightarrow2p_2$ 遷移の飽和を起こさせるとともに飽和によって生ずる $2p_2\rightarrow1s_2$ 遷移（波長 659.9 nm）の螢光スペクトル中のラムくぼみの上に **Fig. 3** に示す Ramsey fringe を出現させた．なお，誘起分極の位相コヒーレンス長はこの場合約 1.6 cm であり光束間距

離は0.5 cmである．このfringeは核磁気共鳴におけるマイクロ波領域のRamsey fringe[14,37]に対応するものである．マイクロ波領域では原子と2つのマイクロ波磁場との相互作用によって原子ビームが両磁場間を飛行する時間に反比例する幅をもつRamsey fringeが得られているが，光領域では光の波長が光束直径などの実験上の寸法より非常に小さく，また光の進行方向への原子の熱運動速度 v_z によるドプラー効果が無視できないので状況はマイクロ波の場合と異なり複雑である．**Fig. 2** に示す第1の光束と原子との線形相互作用によって生じる誘起分極は v_z の速度分布について平均すると0になるが，その後第2の光束との非線形相互作用により，誘起分極を生じた原子群の v_z の速度分布には $\lambda/2T$ (λ: 光の波長，T: 光束間の平均飛行時間) を周期とする周期構造が生じ[38]誘起分極は v_z について平均するとこの周期構造のためにもはや0とならず第3の光束をプローブ光としてこれら原子群に吸収させて得られるスペクトルにはに T 反比例したRamsey fringeが現われる．このように光領域でのRamsey fringeには空間的に分離した光束が3本以上必要でありBergquistらはキャッツアイのリトロレフレクターを用いて平面波の光束を3本作った．このうち第2の光束は定在波である．こうして **Fig. 3 (c)** に示すような対称性のよいRamsey fringeを観測した．さらに光束を4本にし **Fig. 3 (d)** に示すRamsey fringeを得た．このfringeは原子の誘起分極によって原子のもつ位相情報が各光束間を輸送されることによって生ずるものであり，原子のもつ位相は原子が光束間を飛行している間，すなわち光と相互作用していないときにも時間とともにすすんでいくためRamsey fringeはpower broadeningを受けにくい点がある．また，飽和吸収法ではtransit-time幅を小さくするために直径の大きい光束を用いる必要があるがこの場合は直径の大きい光束を使うことなくTに反比例する幅のせまい共鳴信号が得られるのでこの方法は今後の高分解能分光での有力な手段となりうると考えられる．

第2の例はWuら[39]による2準位系原子による光の増幅の観測である．まず色素レーザーからの光ポンピングによってNa原子ビームの D_2 線内の1組のエネルギー準位間の遷移を2準位系として用意し，それに固定周波数の飽和用の強い色素レーザー光 (589 nm) とプローブ用の弱い色素レーザー光とを同時に照射してプローブ光に対する吸収スペクトルを測定した．その結果飽和用の光強度が強くなると **Fig. 4 (a) (iii)〜(v)** に示すように負の吸収が生じた．すなわちあらかじめ反転分布を用意することなしに強く飽和した2準位系で光の増幅が起った．これはすでにミリ波領域[40]，マイクロ波領域[41]で観測されていたものである．**Fig. 4** は飽和用の光周波数を共鳴周波数に一致させた場合の結果であり，この場合には飽和光による反跳効果のために共鳴周波数が0〜2MHzシフトするので原子ビームと光束とを直角から1 mradずらして交差させドプラーシフトを用いてそれを補償している．さらに，**Fig. 4** の場合より高い増幅率を得るためには飽和用の光周波数は $\Omega/3$ (Ω: 飽和光によるラビ周波数) ほど離調すればよいことが認められた．これはつよい飽和光強度による原子のエネルギー準位のシフトが原因であると解釈された[39]．**Fig. 4** に示す実験結果は従来の螢光のスペクトルの形[42]と非常に異なっており，この方法は光強度によるエネルギー準位のシフト量の精密測定に使用しうると考えられる．

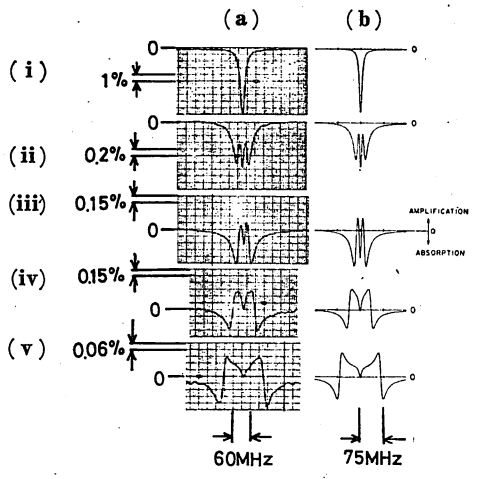

Fig. 4 Spectral line shapes of the two-level atomic system in the presence of saturation field (Wu *et al.*[39]). A CW dye laser (5890 Å) and a Na atomic beam were used in this experiment.
(**a**) Experimental results. The ordinates of each figure represent percent change of probe light intensity. Saturation field intensities are (**i**) no saturation field; (**ii**) 26 mW/cm²; (**iii**) 47 mW/cm²; (**iv**) 130 mW/cm²; (**v**) 560 mW/cm².
(**b**) Theoretical line shapes calculated for comparison with the measured line shapes in (**a**).

4.2 分子ビーム分光

I_2 の分子ビーム分光がEzekielら[43]によって行なわれている．光源として Ar^+ レーザー (波長 514.5 nm) を用い，その利得曲線内に入る $^{127}I_2$ の $^1\Sigma_g^+$(X)と $^3\Pi_{ou}^+$(B) 電子状態間の P (13) (43-0) と R (15) (43-0) 遷移線を測定した[44,45]．I_2 分子ビームの発散角は約 0.5 mrad であり，螢光測定の結果得られた各スペクトル線の幅は

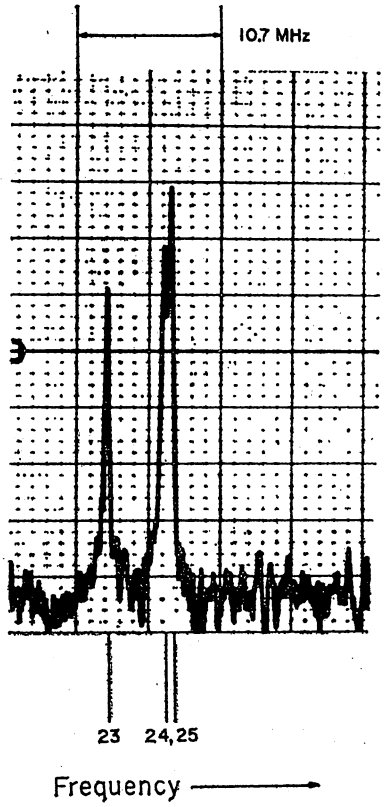

Fig. 5 Three lines of 42 hyperfine components of the P (13) (43–0) and the R (15) (43–0) lines between $^1\Sigma_g^+$(X) and $^3\Pi_{ou}^+$(B) electronic states in the $^{127}I_2$ molecular beam spectrum observed with an Ar^+ laser (5145 Å) (Ruben *et al.*[45]). The numbers 23, 24 and 25 in this figure are numbered consecutively by Ruben et al.[45] for the purpose of identification. The width of the line 23 is 300 kHz (HWHM).

Fig. 5 に示すように 300 kHz (FWHM) であった[45]．これは分解能 5×10^{-10} に相当する．I_2 分子ビームによる寿命測定の結果 I_2 の自然幅は約 100 kHz であるが[46]原子間の小角度衝突，レーザー周波数変動，レーザー光束と分子ビームとの非直交性によりこの実験のように幅が 300 kHz までひろがったと考えられる．つぎに色素レーザー（波長 580 nm）を光源として用い測定を行なった[47]．レーザー周波数は外部のファブリ・ペロー干渉計の共振周波数に固定することによりその短時間安定度を向上させている．原子ビームの発散角 0.5 mrad は残留ドプラー幅 200 kHz に相当する．得られたスペクトル線の幅 (HWHM) は 350 kHz であり，これはレーザー周波数変動をはじめ線幅をひろげる実験上の原因を考慮すると寿命測定から得られる結果とよく一致した．I_2 は寿命が長く，重い分子なので 2 枚の thin orifice (**5.3** 参照) を用いるのみで発散角の小さい分子ビームを得ることができ，その螢光を測定することで高い分解能が得られた．いっぽう，赤外域に共鳴線をもつ有機分子に対する分子ビーム分光の例は少ない．これは信号検出に必要な流量を有する，指向性のよい分子ビームを得るのが可視域の場合ほど技術的に容易でないからである．次にその成功例を示す．Chu と Oka[48]は波長 9.4 μm 帯の N_2O レーザーの P (13) 枝，CO_2 レーザーの P (32) 枝を光源として用い，NH_3 分子ビームの Q (8, 7) 遷移，$^{13}CH_3F$ 分子ビームの R (4, 3) 遷移の吸収スペクトルを測定した．NH_3, $^{13}CH_3F$ は共に軽い分子なので thin orifice を使ったのでは十分な指向性を得られず，したがって半径 5 μm，長さ 0.18 cm のガラス管を束ねた multiparallel channel を用いて分子ビームを生成した．また，これらの分子にシュタルク変調を加えることにより吸収率測定の感度を向上させた．その測定結果を **Fig. 6** に示す．この場合分子ビーム源内圧力が 100 m Torr のとき分子ビーム中の NH_3 分子密度は 1.3×10^{13} cm^{-3} と推定された．**Fig. 6** のスペクトル線の幅の最小値は分子ビーム源内圧力 10 m Torr のときの 1.3 MHz であり，これから分子ビームの発散角を推定すると 44 mrad である．この角度は計算による予測値 14 mrad より大きいが排気速度の大きい真空ポンプを用いて浮遊分子数をへらし，長い光路長を用いて測定感度を上げることにより発散角を予測値に近づけることができる．しかし現状では **4.1** の例および I_2 分子ビームの場合にくらべこの場合の吸収率測定法は感度が悪く，分子ビームの指向性も劣ってい

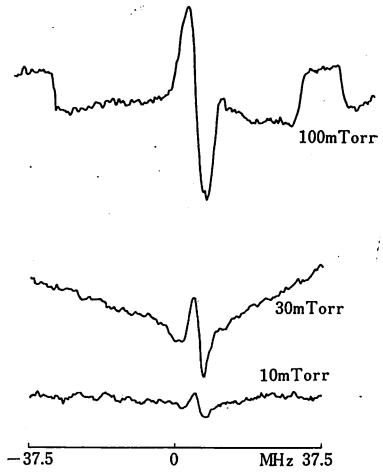

Fig. 6 The first derivatives of the absorption lines of Q (8, 7) transition (927.4 cm^{-1}) in NH_3 molecular beam observed with a N_2O laser (Chu and Oka[48]). The values in the figure represent the source pressure of the molecular beam.

る．いっぽう，Gough ら[49]は測定感度を上げるために吸収率測定とは異なる方法を用いた．すなわち，レーザー光と相互作用した分子ビームをクライオボロメータにあててレーザー光の吸収によるボロメータの抵抗値の変化を検出した．分子ビームは CO でありその赤外域の $v=0\rightarrow1, J=1\rightarrow2$ 遷移のスペクトルを測定している．この励起準位の寿命は長いので吸収されたレーザー光のエネルギーは分子ビーム中の CO 分子によってボロメータの位置まで十分輸送され，スペクトルの測定が可能であった．ここではノズルとスキマーとによって発散角 3×10^{-4} sr の超音速ジェットの分子ビームを作り市販の PbS_xSe_{1-x} 半導体レーザーを光源として用いた．得られた分子ビームスペクトルの幅は 20 MHz で吸収セル中の CO スペクトルの幅 150 MHz より小さい値となっている．分子ビームの発散角の値から推定される残留ドプラー幅は 4.6 MHz であるがレーザー光と分子ビームとの非直交性，レーザー周波数変動によってスペクトル幅は 20 MHz に留まっており Chu と Oka[48]の場合にくらべ分解能は悪い．現在の分子ビームの流量は $10^{15}\,s^{-1}$ であるが Gough らはより高感度のボロメータを使い，分子ビーム中のレーザー光路長を増すことにより $10^{7}\,s^{-1}$ まで流量値を下げても検出可能であると予測している．

4.3　レーザー周波数の安定化

原子分子ビームスペクトルは原子分子間衝突による衝突幅，衝突シフトが無視できるのでこれを周波数基準としてレーザーの周波数安定化に応用すると高安定度が期待できる．Ezekiel ら[43,47,50,51]は **4.2** に示した $^{127}I_2$ 分子ビームを用い Ar^+ レーザーと色素レーザーの周波数安定化を行なっている．まず Ar^+ レーザー周波数[51]の短時間安定度を向上させるためにレーザー周波数を高いフィネスを持つファブリ・ペロー干渉計の共振周波数に固定し，さらに長時間安定度を向上させるためにこのファブリ・ペロー干渉計の共振周波数を I_2 分子ビームスペクトルに固定した．なお，レーザー光と I_2 分子ビームとの交差角が直角からずれた場合のドプラーシフトを打ち消すためにレーザー光を分子ビーム中で往復させている．この周波数安定化レーザーシステムを2組作り，その間のビート周波数から周波数安定度を求めた．周波数変動を表わす Allan 分散の平方根 σ の値を **Fig. 7** に示す．

Fig. 7 によると積分時間 $\tau=10^3$s で $\sigma=7\times10^{-14}$ の安定度が得られている．さらに I_2 分子ビームを用いて色素レーザーの周波数安定化を行ない $\tau=25$ s で 6×10^{-13} の安定度を得ている[47]．いっぽう，Barger ら[52]は Ca 原子ビームの $^1S_0\rightarrow{}^3P_1$ 遷移スペクトルを用いて色素レーザーの周波数安定化を行なった．飽和吸収法を併用し，磁場による偏向によって高感度の測定を行なった．得られたスペクトル線の幅は 230 kHz (HWHM) で，これは予測値よりも大きいが磁気シールドなどを改善することで 10^{-15} の安定度を得ることも可能であると推定している[52]．以上の I_2, Ca ビームの例からもわかるように可視域では螢光測定，磁場による偏向の高感度検出法を用いているため原子分子ビームの流量は少なくてすみ，したがって指向性のよい，衝突数の少ない原子分子ビームが得られるのでレーザー周波数安定化のためのすぐれた周波数基準となっている．これに対し赤外域では検出感度と原子分子ビーム流量とのかねあいから，まだ十分に良質の原子分子ビームが得られておらず，レーザー周波数安定化への応用も遅れている．

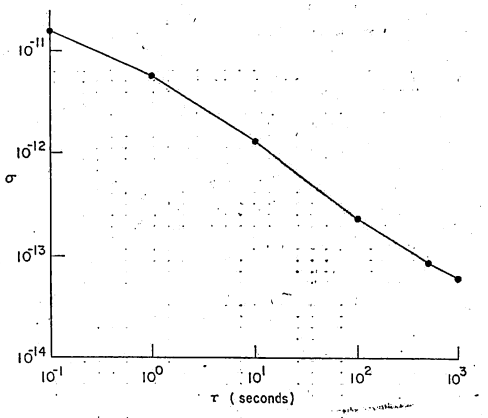

Fig. 7　Frequency fluctuation of Ar^+ laser oscillation stabilized by the I_2-beam (Hackel *et al.*[51]). : σ; square root of Allan variance, τ: integration time.

4.4　そ　の　他

前節までの他，原子分子ビームを用いた実験例を簡単に列挙する．Snyder ら[53]は Ne, H, (および Li^+) の原子ビームに色素レーザーの定在波を照射して第2次ドプラー効果を測定した．また，指向性の鋭さ，レーザー光束との直交性が必ずしも要求されない原子分子ビームが同位体分離の実験[54,55]で用いられている．さらに **2.4** の特徴を用いて量子ビートの測定[24,59]が行なわれている．また，Basov と Letokhov[57,58]は原子分子ビームをレーザー媒質として光ポンピングによりレーザー発振を起こさせることを提案した．このレーザー発振周波数の変動は少なく 10^{-11} 程度の周波数安定度が容易に得よれることが推定され[59]，周波数標準への応用も提案されている[60]．

5.　原子分子ビームの生成と特性

4. で引用した論文では一般に原子分子ビームの生成や基本特性についてほとんど述べられていないのでここで

はこれらについて簡単に述べる．

5.1 原子分子ビーム源

常温で固体である物質は高温に加熱し適当なスリットを通して真空容器中に噴出させることにより原子分子ビームが生成される．常温で気体または沸点の低いものについては容易であるが金属などの特に高温を要するものでは真空蒸着の場合と同様に電子ビーム加熱も利用される．高温加熱の必要な金属の場合，ハロゲン化物や有機金属化合物のような揮発性金属化合物を蒸発させてビームを作り，これを気相中で熱分解または他の物質と反応させて金属に還元し金属ビームを生成する手法がある．金属の有機化合物であるメタロセンを用いて U[61], Fe, Ni[62] の金属原子ビームを得た例が報告されている．

5.2 原子分子ビームの基本量

ここでは原子分子ビーム生成の際必要となる原子分子ビームの強度，指向性を表わす基本量を示す[15]．

(イ) 流量Nと排気速度S……ビーム源，スリットを通り単位時間内に噴出する原子分子の総数が流量 $N(s^{-1})$ であり噴出先の真空容器内圧力を P_1(Torr) に保つのに要する真空ポンプ（低温トラップによる吸着を含む）の排気速度 S は

$$S=kTN/P_1 \quad (l/s) \qquad (2)$$

で与えられる．kはボルツマン定数，Tは原子分子の熱運動の温度である．実際のSの値としては真空容器中の浮遊気体の排気も考慮して(2)式の約10倍（安全係数10）を確保すべきである．

(ロ) 指向性 $I(\theta)$ とその半値半幅 θ_h……スリットからの原子分子ビームの流量とスリット正面の法線方向からの角度 θ との関係が指向性 $I(\theta)$ $(s^{-1}\cdot cm^{-2})$ である．とくにその半値半幅 θ_h の値は原子分子ビームの性能を表わす重要な量である．

(ハ) 中心強度 I_o……$\theta=0$ における $I(\theta)$ の値が中心強度 I_o $(s^{-1}\cdot cm^{-2})$ であり原子分子ビーム分光の際に光と相互作用する原子分子の数が I_o に直接比例する．

(ニ) 密度 n_B……試料セル内の原子分子数密度と対応させるために原子分子ビーム内の原子分子数密度 n_B (cm^{-3}) を用いる．n_B と等しい密度をもつ試料セルの場合にくらべ原子分子ビーム中での衝突数は少ない．なお $\theta=0$ の方向の n_B の値は

$$n_B=I_o/\bar{v} \quad (cm^{-3}) \qquad (3)$$

と表わせる．ここで$\bar{v}$は原子分子ビームの平均速度である．

5.3 スリットの種類と特性

実用的な3種類のスリットから得られる原子分子ビームの I_o, θ_h の値，および3種類のスリットの比較について記す．

(イ) Thin orifice……薄板上に作ったピンホールであり $I(\theta)$ は $\cos\theta$ に比例し I_o は N に比例する．

(ロ) Multiparallel channel (以下 MPC と書く)……内径 d，長さ L の毛細管を平行に束ねたもので毛細管1本当りを通過する原子分子の流量によって流れのモードがかわることが Giordmaine と Wang[63] により示されている．すなわち毛細管内の原子分子の平均自由行程 $\lambda \gg L$ である低密度モード (transparent) では I_o は N に比例し θ_h は d, L できまる一定値になるが，毛細管出口付近で $\lambda \gg d/2$，入口付近で $\lambda < d/2$ である高密度モード (opaque) では I_o, θ_h は $\sqrt{N}$ に比例する．

(ハ) 超音速ノズル……ラバール管形のノズルによって超音速流を作り下流に設置したスキマーによって超音速流の殻部の乱流部分を除去して使用する原子分子ビームを得るものである．流れのマッハ数 $M>4$ のとき I_o は N に比例する[64]．θ_h は実験的にのみ求められる．

以上の3種類のスリットによる I_o の値を比較するために I_o と S との関係を **Fig. 8** に示す．**Fig. 8** は筆者らが 3.51 μm He-Xe レーザーを光源とした H_2CO 分子ビーム分光を行なう目的で計算したものである[65]．MPC としては市販のもの (Galileo Electro-Optics Corp.) を用いるとし $d=10, 5, 2\,\mu m$ のものについて示した．**Fig. 8** を参照して3種類のスリットを比較すると次のことがいえる．: Thin orifice では I_o の値が小さいのでこのスリットは螢光検出法などの高感度検出法が可能な

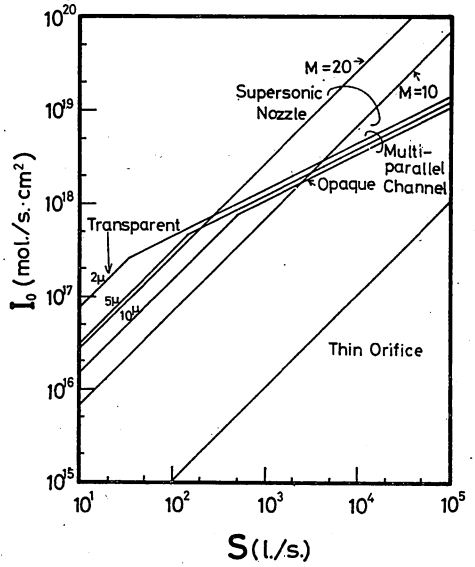

Fig. 8 Calculated relationship between pumping speed S and peak intensity I_0 of H_2CO molecular beam at 1cm downstream from slits[65]. The pressure P_1 in the chamber is kept at 10^{-6} Torr.

場合使用しうる．指向性は余弦則に従い鋭くないので通常は2枚以上の thin orifice を用いて改善する．MPC は thin orifice よりも指向性が鋭いので流量が節約できる．Transparent のモードで使うときは同じ S の値に対して超音速ノズルの場合よりも I_0 がかせげ θ_h の値も小さいので有利である．超音速ノズルは高流量の原子分子ビーム用であり M の値に比例して速度のそろった原子分子ビームが得られる．したがって吸収率測定のような感度の低い検出法には MPC が適し，さらに高密度原子分子ビームが必要であれば超音速ノズルが適している．複数の MPC を並列に並べて用い原子分子ビーム中のレーザー光路長を増すことは超音速ノズルの場合より技術的に容易であり，これを用いて H_2CO 分子ビームの吸収分光用の分子ビーム生成装置の設計が本節の内容をもとに行なわれた[65]．

5.4 原子分子ビームのスペクトルの形

励起用レーザー光に対する原子分子ビームの線形周波数応答特性すなわち線形スペクトルの形が原子分子ビームの指向性，レーザー光束との交差角の値によってどのような影響を受けるかについて記す．$\theta_h=0$ でレーザー光束との交差角が $\pi/2+\beta$ (rad) の場合はスペクトル線中心周波数は $ku\sin\beta$ だけドプラーシフトすることが容易に導かれる．ここで k は光の波数，u は原子分子の熱運動速度の平均値である．とくに $ku\sin\beta$ の値が均一幅 γ より大きくなるとスペクトルの形は非対称になる．この効果を避けるには光軸調整に注意して $\beta=0$ とする必要があるが，その調整精度にも限界があるので **4.3** の Ezekiel ら[51]の例のように原子分子ビーム中でレーザー光を往復させればよい．ただしこのとき $ku\sin\beta$ のドプラーひろがり (HWHM) が残るのでこれをも消去するにはたとえば飽和吸収法を併用する必要がある．次に $\theta_h\neq0$ である一般的な場合については数値計算によってスペクトルの特性が予測されるが Minkowski と Bruck[66] によるとスペクトル中心付近ではガウス形より鋭く，すそ付近ではゆるやかな形が得られている．しかし従来はスペクトルはドプラー幅 $\sqrt{\ln 2}\,ku\sin\theta_h$ のガウス形スペクトルと均一幅 γ のローレンツ形スペクトルとの畳み込み積分で得られる形をもつとして各種の特性の考察に用いている．

6. おわりに

本稿では高分解能レーザー分光の一方法である原子分子ビーム分光法について記した．現在までのところ原子分子ビーム分光法は可視域の例が大部分を占め赤外域での研究は遅れている．この原因としては信号の強度を上げることと良質の原子分子ビームを生成することとが両立しないことがあげられる．つまり原子分子ビームの流量の増加とともに信号号強度は増加するが原子分子ビームの指向性は劣化する．可視域の例では螢光法などの高感度検出法によって指向性の劣化は避けられているが赤外域では今のところ十分な指向性が得られていない．しかし赤外域の振動回転遷移の寿命は長くその均一幅の値は小さいのでそれが原子分子ビーム法で観測可能になれば高分解能分光のみにとどまらず新しい周波数標準などへの応用が可能になる．さらに原子分子ビーム分光法は **4.** で挙げた例によって有望な分光法であることが示されており，今後技術的困難さを克服することによりこの方法が発展することが期待される．本稿がその際の一助となれば幸いである．

文　献

1) L. Dunoyer : Comptes Rendus, **152** (1911) 594.
2) O. Stern and W. Gerlach : Ann. Physik, **74** (1924) 673.
3) I. I. Rabi, J. R. Zacharias, S. Millman and P. Kusch : Phys. Rev., **53** (1938) 318.
4) J. P. Gordon, H. J. Zeiger and C. H. Townes : Phys. Rev., **95** (1954) 282.
5) H. M. Goldenberg, D. Kleppner and N. F. Ramsey : Phys. Rev. Letters, **5** (1960) 361.
6) D. Marcuse : Proc. IRE, **49** (1961) 743.
7) F. C. DeLucia and W. Gordy : Phys. Rev., **187** (1969) 58.
8) A. F. Krupnov and V. A. Skvortsov : Izv. VUZ. Radiofiz., **5** (1962) 820.
9) D. A. Jackson and H. Kuhn : Proc. Roy. Soc., **A 167** (1938) 205.
10) K. W. Meissner and V. Kaufman : J. Opt. Soc. Amer., **49** (1959) 432, 942.
11) R. L. Barger and K. G. Kessler : J. Opt. Soc. Amer., **50** (1960) 7.
12) 中検報告，**7** (1959) 11月号，計量研ニュース，**10** (1962) 11月号．
13) P. Jacquinot : *High Resolution Laser Spectroscopy* (ed. by K. Shimoda, Springer, Berlin, Heidelberg, New York, 1976) p. 52.
14) N. F. : Ramsey : *Molecular Beams* (Oxford Univ. Press, London 1956).
15) 楠　勲 : 真空，**14** (1971) 1.
16) H. Schlossberg and A. Javan : Phys. Rev., **150** (1966) 267.
17) A. Ashkin : Phys. Rev. Letters, **25** (1970) 1321.
18) J. L. Picqué and J. L. Vialle : Optics Commun., **5** (1972) 402.
19) R. Schieder, H. Walther and L. Wöste : Optics Commun., **5** (1972) 337.
20) I. Nebenzahl and A. Szöke : Appl. Phys. Letters, **25** (1974) 327.
21) H. T. Duong, P. Jacquinot, S. Liberman, J. L. Picqué, J. Pinard and J. L. Vialle : Optics

Commun., **7** (1973) 371.
22) H. Bucka : Z. Phys., **191** (1966) 199.
23) H. T. Duong and J. L. Vialle : Optics Commun., **12** (1974) 71.
24) A. van Wynaarden, E. Coh, G. W. F. Drake and P. S. Farago : J. Phys. B, **9** (1976) 2017.
25) J. U. White : J. Opt. Soc. Amer., **32** (1942) 285.
26) 霜田光一：分光研究，**25** (1976) 3.
27) S. A. Tuccio, J. W. Dubin, O. G. Peterson and B. B. Snavely : IEEE J. Quant. Elect., **QE-10** (1974) 790.
28) U. Brinkmann, W. Hartig, H. Telle and H. Walther : Appl. Phys., **5** (1974) 109.
29) W. Lange, J. Luther, B. Nottbeck and H. W. Schröder : Optics Commun., **8** (1973) 157.
30) W. Hartig and H. Walther : Appl. Phys., **1** (1973) 171.
31) F. Schuda, M. Hercher and C. R. Stroud, Jr. : Appl. Phys. Letters, **22** (1973) 360.
32) F. Y. Wu, R. E. Grove and S. Ezekiel : Phys. Rev. Letters, **35** (1975) 1426.
R. E. Grove, F. Y. Wu and S. Ezekiel : Phys. Rev. A, **15** (1977) 227.
33) P. Jacquinot, S. Liberman, J. L. Picqué and J. Pinard : Optics Commun., **8** (1973) 163.
34) J. A. R. Griffith, G. R. Isaak, R. New, M. P. Ralls and C. P. van Zyl : J. Phys. B, **10** (1977) L 91.
35) F. Träger, R. Neumann, J. Kowalski and G. zu Putlitz : Appl. Phys., **12** (1977) 19.
36) J. C. Bergquist, S. A. Lee and J. L. Hall : Phys. Rev. Letters, **38** (1977) 159.
37) N. F. Ramsey : Phys. Rev., **78** (1950) 695.
38) Ye. V. Baklanov, B. Ya. Dubetsky and V. P. Chebotayev : Appl. Phys., **9** (1976) 171.
39) F. Y. Wu, S. Ezekiel, M. Ducloy and B. R. Mollow : Phys. Rev. Letters, **38** (1977) 1077.
40) B. Senitzky, G. Gould and S. Cutler : Phys. Rev., **130** (1963) 1460.
41) A. M. Bonch-Bruevich, V. A. Khodovoi and N. A. Chigir : Soviet Physics-JETP, **40** (1975) 1027.
42) R. E. Grove, F. Y. Wu and S. Ezekiel : Phys. Rev. A, **15** (1977) 227.
43) S. Ezekiel : *Laser Spectroscopy* (ed. by R. G. Brewer and A. Mooradian, Plenum, New York, 1974) p. 361.
44) D. G. Youmans, L. A. Hackel and S. Ezekiel : J. appl. Phys., **44** (1973) 2319.
45) D. J. Ruben, S. G. Kukolich, L. A. Hackel, D. G. Youmans and S. Ezekiel : Chem. Phys. Letters, **22** (1973) 326.
46) S. Ezekiel and R. Weiss : Phys. Rev. Letters, **20** (1968) 91.
47) F. Y. Wu, R. E. Grove and S. Ezekiel : Appl. Phys. Letters, **25** (1974) 73.
48) F. Y. Chu and T. Oka : J. appl. Phys., **46** (1975) 1204.
49) T. E. Gough, R. E. Miller and G. Scoles : Appl. Phys. Letters, **30** (1977) 338.
50) T. J. Ryan, D. G. Youmans, L. A. Hackel and S. Ezekiel : Appl. Phys. Letters, **21** (1972) 320.
51) L. A. Hackel, R. P. Hackel and S. Ezekiel : *Proc. of the 2nd Frequency Standards and Metrology Symposium*, (Copper Mt., USA, 1976) p. 107.
52) R. L. Barger, J. B. West and T. C. English : *Proc. of the 2nd Frequency Standards and Metrology Symposium*, (Copper Mt., USA, 1976) p. 83.
53) J. J. Snyder, J. L. Hall and M. S. Sorem : IEEE J. Quant. Elect., **QE-10** (1974) 692.
54) U. Brinkmann, W. Hartig, H. Telle and H. Walther : Appl. Phys., **5** (1974) 109.
55) M. J. Coggiola, P. A. Schulz, Y. T. Lee and Y. R. Shen : Phys. Rev. Letters, **38** (1977) 17.
56) Q. H. F. : Vrehen, M. J. Hikspoors and H. M. Gibbs : Phys. Rev. Letters, **38** (1977) 764.
57) N. G. Basov and V. S. Letokhov : JETP Letters, **2** (1965) 3.
58) V. S. Letokhov and B. D. Pavlik : Soviet Physics-JETP, **26** (1968) 656.
59) V. S. Letokhov and B. D. Pavlik : Soviet Physics-Tech. Phys., **15** (1971) 1275.
60) N. G. Basov and V. S. Letokhov : Soviet Physics-Uspekhi, **11** (1969) 855.
61) H. U. Lee and R. N. Zare : J. Chem. Phys., **64** (1976) 431.
62) 大山俊之，渡辺綱夫，中根良平：電気学会，レーザー工学研究会資料（1978年2月）LEG-78-1.
63) J. A. Giordmaine and T. C. Wang : J. appl. Phys., **31** (1960) 463.
64) J. B. Anderson, R. P. Andres and J. B. Fenn : *Advances in Atoms and Molecular Physics*, (ed. by D. R. Bates and I. Esterman, Academic Press, New York) **1** (1965) 345.
65) 大津元一，田幸敏治：応物学会発表，講演予稿集（1977年秋）13a A1, 13a A2.
66) R. Minkowski and H. Bruck : Z. Phys., **95** (1935) 274.

JAPANESE JOURNAL OF APPLIED PHYSICS
VOL. 21, NO. 6, JUNE, 1982 pp. 813–816

High Resolution Stark Spectroscopy of H_2CO at 3.51 μm by Saturated Absorption

Itiro SIIO, Motoichi OHTSU and Toshiharu TAKO

Research Laboratory of Precision Machinery and Electronics, Tokyo Institute of Technology, 4259 Nagatsuta-cho, Midori-ku, Yokohama, Kanagawa 227

(Received December 14, 1981; accepted for publication March 20, 1982)

Precise measurements were carried out on the Stark effect of the vibration-rotation transition $5_{1,5}(v=0)-6_{0,6}(v_5=1)$ in H_2CO using a low-noise, stable He–Xe laser at 3.51 μm. The intracavity saturated absorption technique was employed to improve the resolution.

Eight of the allowed transitions were resolved and the small Stark coefficients were determined with high accuracy under a maximum applied field strength of 4.39 kV/cm. Furthermore, the first observation of six cross resonance lines in this transition is reported.

§1. Introduction

Stark spectroscopy in the optical as well as the microwave region has been widely used as a potential tool for the study of molecular structure.[1-9] As an example, the Stark effects of the vibration-rotation transitions of H_2CO have been studied in the wavelength region between 3 and 10 μm.[10-16] The transition at 3.51 μm ($5_{1,5}(v=0)$–$6_{0,6}(v_5=1)$) in H_2CO has been studied using a Zeeman-tuned He–Xe laser.[10] However, the Stark coefficient of this transition has not yet been determined because it is too small to be measured by the conventional linear absorption technique. Recently, the saturated absorption signal of this transition has been studied, and the frequency of the Zeeman-tuned He–Xe laser has been stabilized using this line as a frequency reference.[17,18] Furthermore, a highly-stabilized frequency offset locked He–Xe laser system has been constructed for ultrahigh resolution laser spectroscopy.[19] As a result of this progress, it became possible to measure the Stark spectrum of this transition with higher resolution using the saturated absorption technique.

In this experiment, the Stark effect of this transition was studied with high resolution to assign the lines and to measure the Stark coefficient with higher accuracy using the intracavity saturated absorption technique.

§2. Experimental Apparatus

The experimental apparatus is shown in Fig. 1. The low-noise He–Xe laser tube used in this study is of the same type as in the previous work.[19] It has a discharge section of 5.8 mm inner diameter and 750 mm length, and is excited by a d.c. discharge current of 3.8 mA. Since the frequency of the transition $5_{1,5}(v=0)$–$6_{0,6}(v_5=1)$ is about 180 MHz higher than the center of the gain curve of the He–Xe laser, an axial magnetic field of 124G was applied to the laser tube to compensate for this frequency gap. Between two oppositely circularly-polarized Zeeman components oscillated simultaneously,[20] a higher-frequency component (the σ_+ mode) was used for the experiment. Its intensity was measured after being separated from the lower-frequency component (the σ_- mode) by a quater-wave plate and a polarizer.

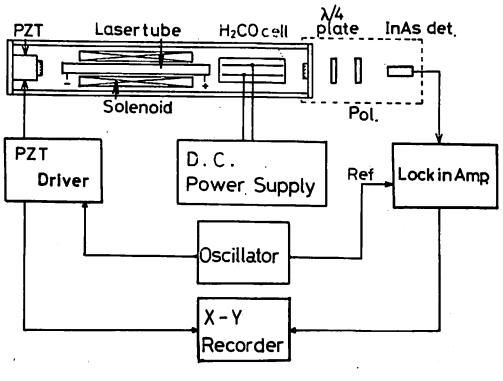

Fig. 1. Experimental apparatus.

The laser cavity was 155 cm long, corresponding to a longitudinal mode separation of 96.6 MHz. One of the cavity mirrors was mounted on a piezoelectric transducer (PZT) for frequency tuning and modulation. An a.c. voltage of 500 Hz was applied to the PZT for frequency modulation, and the maximum frequency deviation was 190 kHz. The first derivatives of the saturated absorption signal were measured by phase-sensitive detection and were displayed on an X-Y recorder. The value of the tuned frequency was estimated from the d.c. voltage applied to the PZT and the longitudinal mode separation.

The intracavity H_2CO absorption cell contained a pair of Stark electrodes made of aluminum plates, which were 330 mm long and faced each other with a separation of 6.38 mm. Since the flatness of the electrodes was better than 20 μm, the inaccuracy of the Stark field strength was estimated to be less than 0.3%. The maximum d.c. voltage applied in this experiment was 2.8 kV, corresponding to an electric field strength of 4.39 kV/cm.

§3. Experimental Results and Assignment

Figure 2 shows the derivative signals of the saturated absorption lines observed under a Stark field of 4.39 kV/cm. The H_2CO pressure was 10 mTorr. The signal obtained using a single scan of the laser frequency had a very high signal-to-noise ratio. As seen from Fig. 2, sixteen separate lines (Nos. 0–15) were clearly observed. Number 0 was assigned to the strongest line, which exhibits the lowest Stark shift. The width of each line was about 500 kHz. Figure 3 shows the relation between the fre-

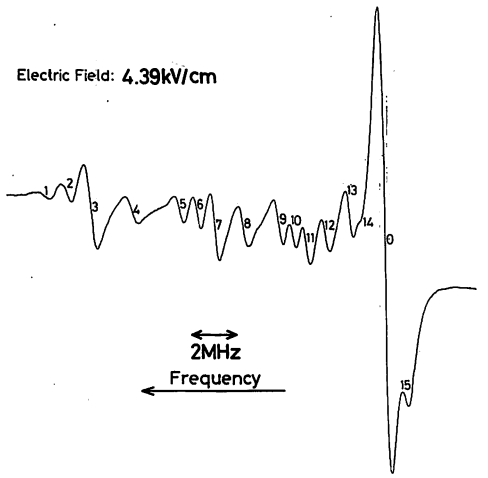

Fig. 2. Derivative of saturated absorption lines observed under Stark field of 4.39 kV/cm. H_2CO pressure was 10 m Torr. Sixteen lines (Nos. 0–15) were observed with high sensitivity in this measurement.

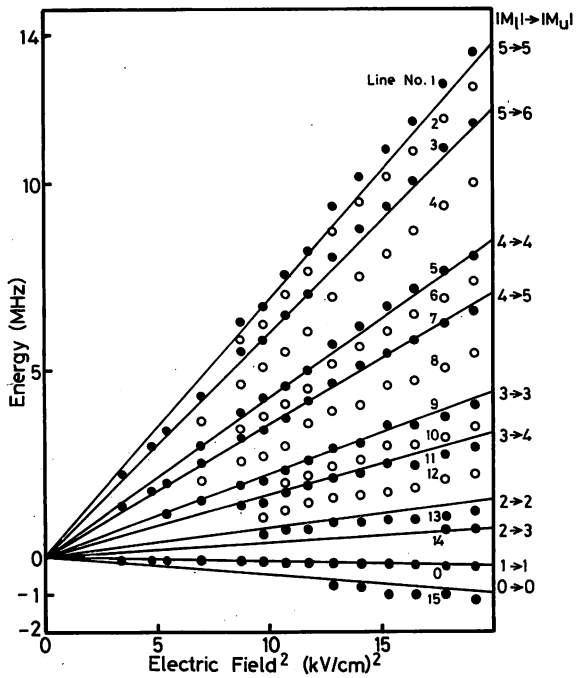

Fig. 3. Relation between frequency shifts of sixteen observed lines and square of Stark field strength. Circles and solid lines represent experimental and calculated results, respectively. Solid circles correspond to allowed transitions, and open circles to six cross-resonance lines. Solid lines are calculated results, where M_l and M_u represent magnetic quantum numbers of lower and upper levels of transitions, respectively.

quency shifts of the sixteen lines and the square of the Stark field strength. The solid and open circles in this figure show the experimental results. The solid lines represent the results of the assignment described below, for which a rigid asymmetric rotator model was employed.

The second-order perturbation due to the Stark effect for the nondegenerated rigid asymmetric rotator is expressed as[21]

$$\mathscr{H}(J\tau M)=W^0_{J\tau}+E^2\sum_{J',\tau',g}\frac{\mu_g^2[(\Phi_{Zg})_{J\tau M;J'\tau'M'}]^2}{W^0_{J\tau}-W^0_{J'\tau'}}, \quad (1)$$

where J is the total angular momentum, M is the magnetic quantum number, τ is the identification number for sublevels of the asymmetric rotator belonging to the same J, E is the applied electric field, μ is the electric dipole moment and Φ_{Zg} is the direction cosine between the space-fixed Z and molecular-fixed g axes.[22] Since only one component of μ_g has a value in H_2CO, summation over g can be eliminated. By using the formula in Table I of ref. 22, eq. (1) can be transformed as follows:

$$\mathscr{H}(J\tau M)=W^0_{J\tau}+\mu_A^2E^2[A_{J,\tau}+M^2B_{J,\tau}]. \quad (2)$$

In this equation, the value of the coefficients $A_{J,\tau}$ and $B_{J,\tau}$ for the lower and upper levels of the transition i.e., $5_{1,5}(v=0)$ and $6_{0,6}(v_5=1)$ can be obtained from the values in Table I, which are expressed as follows:

$$A_{5,-4}=2.7645\times10^{-8} \quad \text{and}$$
$$B_{5,-4}=-6.7914\times10^{-9} \quad \text{for } 5_{1,5}(v=0), \quad (3)$$
$$A_{6,-6}=2.0943\times10^{-8} \quad \text{and}$$
$$B_{6,-6}=-1.5142\times10^{-9} \quad \text{for } 6_{0,6}(v_5=1). \quad (4)$$

The Stark shifts of the sublevels in levels $5_{1,5}(v=0)$ and $6_{0,6}(v_5=1)$ can be derived from eqs. (2), (3) and (4). Figure 4 shows the results. Since the H_2CO molecules interact with the circularly-polarized laser beam (the σ_+ mode), the selection rules of the transition are $\Delta M=\pm1$ and 0. Following these rules, seventeen lines should appear. The third column of Table II shows the calculated

Table I. Molecular constants of H_2CO used for calculations.

	Ground state	Exited state ($v_5=1$)[c]
A (cm^{-1})	9.406 171(105)[a]	9.227 87(34)
B (cm^{-1})	1.295 430 4[a]	1.293 49(49)
C (cm^{-1})	1.134 192 7[a]	1.130 61(56)
μ_A (D)	2.331 5(5)[b]	2.284 4(47)

[a]References 24, 15.
[b]Reference 25.
[c]Reference 16.

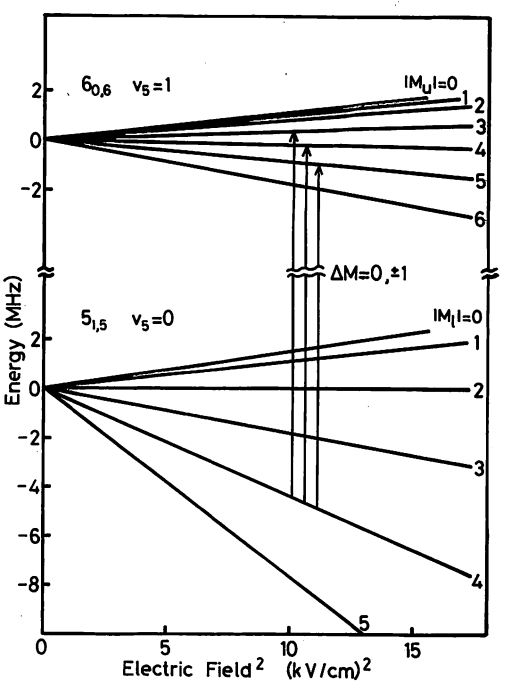

Fig. 4. Stark shifts of sublevels in $5_{1,5}(v=0)$ and $6_{0,6}(v_5=1)$ estimated using a rigid asymmetric rotator model.

Table II. Observed and calculated frequencies of H_2CO Stark spectrum.

Line number	Assignment $\lvert M_l\rvert$–$\lvert M_u\rvert$	Stark coef. (kHz/(kV/cm)^2) Calc.[c]	Obs.
0	1–1	−12.0	−12.
	1–0 etc.[a]	− 4.1	
15	0–0	−41.0	−59.
	0–1	−48.9	
	1–2 etc.[a]	−35.7	
14	2–3	35.6	45.
13	2–2	75.1	57.
12	2–3 and 3–3[b]	128.	108.
11	3–4	165.	145.
10	3–3 and 3–4[b]	193.	175.
9	3–3	220.	207.
8	4–4 and 3–4[b]	294.	283.
7	4–5	352.	341.
6	4–4 and 4–5[b]	388.	385.
5	4–4	423.	421.
4	5–5 and 4–5[b]	518.	528.
3	5–6	597.	615.
2	5–5 and 5–6[b]	641.	667.
1	5–5	684.	717.

[a]Overlapped lines.
[b]Cross resonance components.
[c]Calculated from the molecular constants shown in Table I.

Stark coefficients for some of these lines. The solid lines in Fig. 3 were drawn using these results, where M_l and M_u represent the magnetic quantum numbers of the lower and upper levels of the transitions, respectively.

Because no frequency reference was used in this experiment, only the separations between lines were measured, i.e., the absolute values of the Stark shifts were not determined. Therefore, the position of frequency origin had to be found by least-squares fitting so that the experimental results of all the Stark coefficients consistently agreed with that of the calculated ones.* As a result of the fitting, it can be seen from the third and fourth columns in Table II that the experimental results agree well with the calculated ones without any contradiction in the assignment. It became clear from the results of assignment that the solid circles of Nos. 1, 3, 5, 7, 9, 11, 13 and 14 in Fig. 3 correspond to eight of the allowed transitions. The transitions between the levels of $|M_l|<2$ were not clearly resolved because their Stark shifts were too small, i.e., their estimated values were less than 10% of the value of the line width. Lines Nos. 0 and 15 correspond to this case, being composed of several unresolved lines as shown in Table II. In the resolved case of $|M_l|\geq 2$, on the other hand, the lines of the transition $\Delta|M|=-1$ were not observed because their intensities I_M, estimated from the following formula,[1] were lower than 10% of those of $\Delta|M|=0$ and $+1$.

$$I_M=I_0\{(J+1)^2-M^2\} \quad \text{for } M\to M \text{ and}$$

$$I_M=\frac{1}{4}I_0\{(J\pm M+1)(J\pm M+2)\} \quad \text{for } M\to M\pm 1. \quad (5)$$

The lines shown by open circles in this figure correspond to cross-resonances[23] which are specific to saturated absorption spectroscopy. These resonances occur when two transitions inside the Doppler width share a common level. The cross-resonance appears at a frequency halfway between the two usual transitions and has an intensity proportional to the geometric mean of the two parent lines. As shown in Table II and Fig. 3, lines Nos. 2, 6, 10, 4, 8 and 12 appeared because of cross-resonance between the pairs of levels Nos. 1–3, 5–7, 9–11, 1–7, 5–11 and 9–14, respectively. These pairs share the common levels $|M_l|=5$, 4, 3, and $|M_u|=5$, 4, 3, respectively. This is, to the authors' knowledge, the first observation of cross-resonance in the transition $5_{1,5}(v=0)$–$6_{0,6}(v_5=1)$ in H_2CO.

Higher resolution can be expected by decreasing the H_2CO pressure, expanding the beam width, improving the flatness of the Stark electrodes, and so on.

Furthermore, precise direct frequency readout will be possible if a highly-stabilized frequency offset locked He–Xe laser system[19] is used. Further experiments are now in progress to improve the resolution and to determine the molecular constants with higher accuracy.

*The fitting was done considering also the cross-resonance lines mentioned later.

§4. Conclusions

Precise measurements were carried out on the Stark spectrum of the vibration-rotation transition $5_{1,5}(v=0)$–$6_{0,6}(v_5=1)$ in H_2CO using the intracavity saturated absorption technique. Eight of the allowed transitions were resolved and their small Stark coefficients were determined with high accuracy, the results agreeing well with the estimated values. Furthermore, the first observation of six cross-resonance lines in this transition and the result of their assignment are reported.

Acknowledgements

The authors wish to thank Professors E. Hirota and S. Saito of the Institute of Molecular Science for their valuable discussions on the computation of Stark parameters. This work was partially supported by a Grant-in-Aid for Scientific Research from the Ministry of Education, Science and Culture.

References

1) C. H. Towns and A. L. Shawlow: *Microwave Spectroscopy* (McGraw-Hill, New York, 1955).
2) T. Shimizu, K. Shimoda and A. Minoh: J. Phys. Soc. Jpn. **24** (1968) 1185.
3) G. Duxbury and R. G. Jones: Chem. Phys. Lett. **8** (1971) 439.
4) G. Duxbury and R. G. Jones: Mol. Phys. **20** (1971) 721.
5) G. Duxbury and R. G. Jones: Phys. Lett. **30A** (1969) 498.
6) F. Shimizu: J. Chem. Phys. **51** (1969) 2754.
7) F. Shimizu: J. Chem. Phys. **52** (1970) 3572.
8) F. Shimizu: J. Chem. Phys. **53** (1970) 1149.
9) A. C. Luntz and R. G. Brewer: J. Chem. Phys. **54** (1971) 3641.
10) K. Sakurai, K. Uehara, M. Takami and K. Shimoda: J. Phys. Soc. Jpn. **23** (1967) 103.
11) J. W. C. Johns and A. R. W. McKellar: J. Mol. Spectrosc. **48** (1973) 354.
12) J. W. C. Johns and A. R. W. McKellar: J. Chem. Phys. **63** (1975) 1682.
13) D. Coffey, Jr., C. Yamada and E. Hirota: J. Mol. Spectrosc. **64** (1977) 98.
14) J. W. C. Johns and A. R. W. McKellar: J. Mol. Spectrosc.

64 (1977) 327.
15) M. Allegrini, J. W. C. Johns and A. R. W. McKellar: J. Mol. Spectrosc. **66** (1977) 69.
16) M. Allegrini, J. W. C. Johns and A. R. W. McKellar: J. Mol. Spectrosc. **67** (1977) 476.
17) M. Ohtsu and T. Tako: J. Appl. Phys. **50** (1979) 599.
18) M. Ohtsu and T. Tako: Jpn. J. Appl. Phys. **17** (1978) 2169.
19) M. Ohtsu, S. Katsuragi and T. Tako: IEEE J. Quantum Electron. **QE-17** (1981) 1100.
20) M. Ohtsu and T. Tako: Jpn. J. Appl. Phys. **17** (1978) 177.
21) S. Golden and E. B. Wilson, Jr.: J. Chem. Phys. **16** (1948) 669.
22) P. C. Cross, R. M. Hainer and G. W. King: J. Chem. Phys. **12** (1944) 210.
23) H. R. Schlossberg and A. Javan: Phys. Rev. **150** (1966) 267.
24) F. Y. Chu, S. M. Freund, J. W. C. Johns and T. Oka: J. Mol. Spectrosc. **48** (1973) 328.
25) B. Fabricant, D. Krieger and J. S. Muenter: J. Chem. Phys. **67** (1977) 1576.

JAPANESE JOURNAL OF APPLIED PHYSICS
VOL. 21, NO. 5, MAY, 1982 pp. 722–724

Frequency Stabilization of a He–^{22}Ne Laser by Intracavity Polarization Spectroscopy of CH_4. II

Motoichi OHTSU* and Toshiharu TAKO

Research Laboratory of Precision Machinery and Electronics,
Tokyo Institute of Technology,
4259 Nagatsuta-cho, Midori-ku, Yokohama, Kanagawa 227

(Received January 14, 1982; accepted for publication February 20, 1982)

This paper reports the improvements in frequency stability of a saturated dispersion locked He–^{22}Ne laser at 3.39 μm. The intracavity polarization spectroscopy technique was employed to measure the saturated dispersion spectrum in CH_4 (the E component of the P (7) line in the ν_3 band), which was used as a frequency reference. To improve the frequency stability, the method using a Fabraday rotator was employed, which differs from that of the previous work. After stabilizing the temperature of the Faraday rotator crystal and the laser intensity, frequency stabilization was carried out. The highest frequency stability obtained was 3.0×10^{-13} at the integration time of 500s.

§1. Introduction

In the previous paper,[1] the authors proposed the intracavity polarization spectroscopy of CH_4 as a potential method for high resolution laser spectroscopy, and its application to frequency stabilization of a He–^{22}Ne laser at 3.39 μm was demonstrated using a saturated dispersion spectrum in CH_4 (the E component of the P(7) line in the ν_3 band). With this method, an optically induced circular birefringence in CH_4 was detected by measuring the direction of principal axis of the polarization ellipse of the laser beam. This method has an advantage in that a completely Doppler free spectrum can be obtained with high sensitivity and high resolution. Furthermore, it can be readily used for frequency stabilization without any need for frequency modulation.

Two ways of measuring the direction of the principal axis were proposed.[1] They are:

I. Method using a Wollaston prism and two detectors.

II. Method using a Faraday rotator, polarizer and a detector.

In the previous paper,[1] the frequency stabilization was carried out by employing method I only, and it was pointed out that the following three quantities should be reduced to suppress deformations of spectral shape of CH_4 and to improve frequency stability.[2]

1. Difference in detector sensitivities Δs.
2. Misalignment angle of the Wollaston prism ϕ.
3. Laser intensity fluctuations $\delta I/I$.

The most troublesome of these quantities is Δs. For example, from the estimation in the previous paper (eq. (34) in ref. 2), it can be seen that Δs has to be lower than 10^{-3}–10^{-4} to get a frequency stability higher than 10^{-12}, which is almost impossible even if one uses a high-performance detector array. The other two quantities can be reduced without any special practical trouble. Therefore, it seems preferable to employ method II to improve the frequency stability because only one detector is required, which means that it is free from the effect of Δs. Following this prospect, experiments were carried out by method II, and the results of improvements in frequency stability are reported in the following chapters.

§2. Experimental Apparatus

Figure 1 shows experimental apparatus. The laser used here is the same as for the previous work.[1,2] A YIG ($Y_3Fe_5O_{12}$) crystal 7 mm in length was used as a Faraday rotator in an a.c. axial magnetic field. The direction of the principal axis of the polarization ellipse of the laser beam was measured by a polarizer and an InAs photodetector behind the YIG crystal employing the phase sensitive detection method. An audio oscillator and a 100 W power amplifier were used to supply an a.c. current to a solenoid for the YIG crystal. The a.c. magnetic field strength was 420 G (peak-to-peak value) which corresponded to the Faraday rotation angle of 90 degrees. Its frequency was 2 kHz. A careful electromagnetic shield was supplied around the solenoid to reduce the inductive noise.

The misalignment angle ϕ mentioned as the second requirement in §1 corresponds to the angle between the optical axes of the Faraday rotator and the polarizer in the present experimental set-up. This angle ϕ can be accurately adjusted to zero by applying a small d.c. magnetic field to the YIG crystal. However, even after this adjustment, the misalignment will slowly be induced

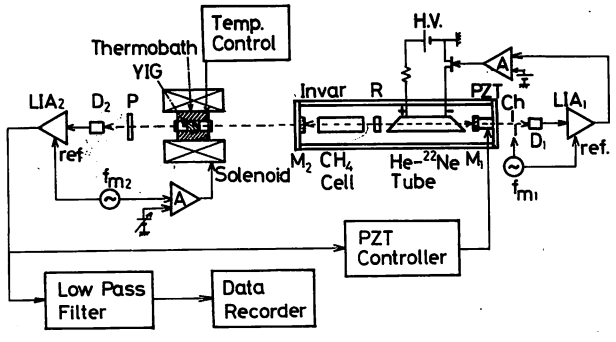

Fig. 1. Experimental apparatus. Ch: mechanical chopper. P: polarizer. R: phase plate. An InAs photodetector D_1 and lock-in amplifier 1 (LIA_1) were used for laser intensity stabilization. D_2 and LIA_2 were used for frequency stabilization.

*Present address: International Cooperation Center for Science and Technology, Tokyo Institute of Technology, 2-12-1 O-okayama, Meguro-ku, Tokyo 152.

again if the Faraday rotation angle is drifted by the temperature change of the crystal in the solenoid. To avoid this drift, the crystal was installed in a thermobath made of a Teflon block, and its temperature was controlled using a thermistor as a sensor.

Following the third requirement in §1, the laser intensity fluctuations $\delta I/I$ were reduced by conveniently controlling the discharge current of the laser tube, which is also schematically shown in Fig. 1. Laser intensity stability was measured using the error signals from the lock-in amplifier 1.

After these arrangements, the laser frequency was locked at the center of the saturated dispersion spectrum in CH_4 using a PZT controller, and the frequency stability was evaluated by the error signals from the lock-in amplifier 2 in Fig. 1.

§3. Experimental Results and Discussion

Figure 2 shows the observed saturated dispersion spectrum. It can be seen that it has a higher signal-to-noise ratio than that of the previous work (see Fig. 5 of ref. 1), and this ratio can be high enough to be used as a frequency discriminator for frequency stabilization.

Figure 3 shows the temperature fluctuations of the YIG crystal. These fluctuations were reduced as low as 0.01°C around 60.4°C. The amount of such fluctuations corresponds to the following value of the fluctuations of the

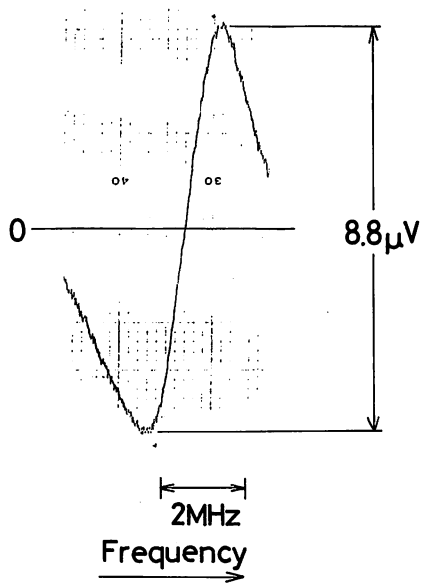

Fig. 2. The saturated dispersion spectrum in CH_4.

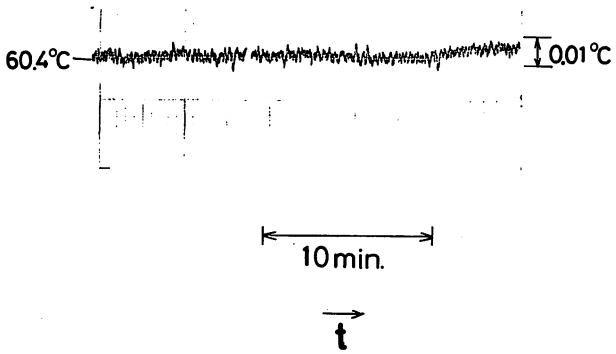

Fig. 3. Temperature fluctuations of the YIG crystal measured using a thermistor as a sensor.

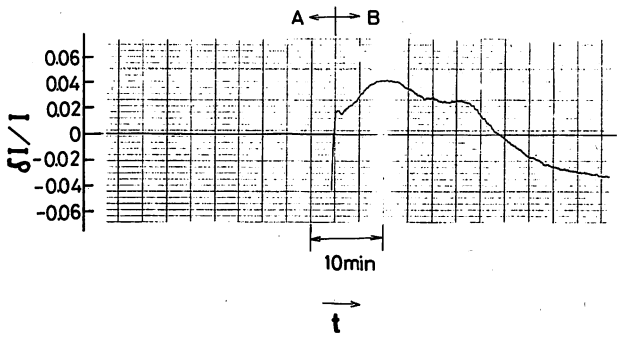

Fig. 4. Laser intensity fluctuations $\delta I/I$. The output signal from the lock-in amplifier 1 was recorded on a chart recorder. For this measurement, the laser frequency was locked at the center of the conventional saturated absorption spectrum in CH_4. A: Stabilized by controlling the discharge current. B: Free running.

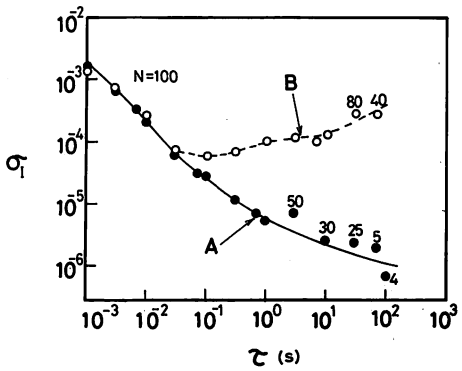

Fig. 5. Square root of the Allan variance σ_I^2 for laser intensity fluctuations. τ and N represent the integration time and number of data, respectively. The curves A and B correspond to parts A and B in Fig. 4, respectively.

Faraday rotation angle.*

$$|\phi| \leqq 0.14°. \tag{1}$$

Figure 4 shows the laser intensity fluctuations. In this measurement, the laser frequency was locked at the center of the conventional saturated absorption spectrum in CH_4. Part A represents the fluctuations when the intensity was stabilized by controlling the discharge current. In part B, the intensity was not stabilized. Figure 5 shows the square root of the Allan variance[3] σ_I^2 of these fluctuations. Curves A and B correspond to the results of parts A and B in Fig. 4, respectively. The stability of curve A can be approximately expressed as

$$\sigma_I = 1.0 \times 10^{-5} \cdot \tau^{-1/2} \quad \text{for } 1\text{ ms} \leqq \tau \leqq 100\text{ s}. \tag{2}$$

Here, τ represents the integration time of the stability measurements. By substituting eqs. (1) and (2) into eq. (37) of the ref. 2, expected frequency stability can be estimated and is expressed as

$$\sigma_f = 1.4 \times 10^{-13} \cdot \tau^{-1/2} \quad \text{for } 1\text{ ms} \leqq \tau \leqq 100\text{ s}. \tag{3}$$

Figure 6 shows the results of frequency stability measurements using the saturated dispersion spectrum in CH_4.

*This value was obtained using the following value of the temperature coefficient of the Faraday rotation angle for the YIG crystal employed.

$$d\phi/dT = 14\text{ deg/K for } 22°C \leqq T \leqq 72°C,$$

which was obtained in the preliminary measurements using a He–^{22}Ne laser at 3.39 μm.

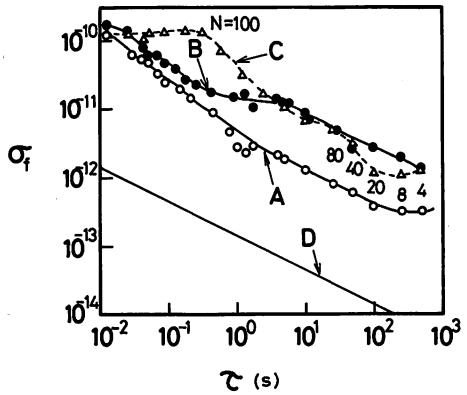

Fig. 6. Square root of the Allan variance σ_f^2 for frequency fluctuations. A: Result obtained when the laser intensity was simultaneously stabilized by controlling the discharge current. B: Laser intensity was not stabilized. C: Result of the previous work (curve A of Fig. 10 in ref. 1). D: Estimated frequency stability.

For curve A, the laser intensity was simultaneously stabilized, but not for curve B. Curves C and D represent the results of the previous work[1] and the estimated value (eq. (4)), respectively. It may be said that the stability of curve B is slightly higher than that of the curve C, i.e., a little improvement can be seen for 10 ms$\leqq\tau\leqq$10 s. However, curve A shows distinct improvements for the full range of τ in this figure. The frequency stability on this curve can be approximately expressed as

$$\sigma_f=4.0\times10^{-12}\cdot\tau^{-1/2} \quad \text{for } 10\text{ ms}\leqq\tau\leqq500\text{ s}, \tag{4}$$

and the highest stability obtained is

$$\sigma_f=3.0\times10^{-13} \quad \text{at } \tau=500\text{ s}. \tag{5}$$

It must be said that the stability on this curve is still lower than the estimated value of curve D. One of the causes is that the discharge current control was employed for the intensity stabilization. That is, changes in the discharge current apparently vary, *e.g.*, the electron density in the laser tube, and consequently introduce new sources of refractive index changes and frequency fluctuations. This effect was quantitatively measured and is shown in Fig. 7. This figure shows the frequency stability of the He–^{22}Ne laser which was stabilized by the conventional method of saturated absorption of CH_4. Because the frequency stability σ_f of the laser thus stabilized is known to be free of the intensity stability σ_I if $\sigma_f>10^{-13}$ and $\sigma_I<10^{-3}$,[4] it can be used to learn the effect of the current control on the frequency stability in this study. Curve A in this figure represents the result when the intensity was stabilized. For curve B, the intensity was not stabilized. Comparison between these curves shows that the discharge current control really sacrifices the frequency stability, and the stability lost by the current control is seen to be as much as 3 dB for 10 ms$\leqq\tau\leqq$10 s. For curve A in Fig. 6, it can be estimated that almost the same amount of stability must have been already lost by the current control. If a more sophisticated method of intensity stabilization is employed which does not disturb the frequency, higher stability can be obtained. Further improvements can be expected using the YIG crystal with lower temperature coefficient, improving the signal-to-noise ratio of the saturated dispersion spectrum in CH_4 and frequency servo controlling electronic circuit.

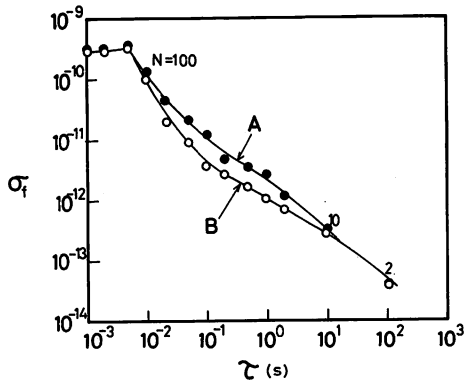

Fig. 7. Stability of the laser frequency locked at the center of the conventional saturated absorption spectrum in CH_4. A: Result obtained when the laser intensity was simultaneously stabilized by controlling the discharge current. B: Laser intensity was not stabilized.

Several experiments are now in progress to improve the stability and to measure it more accurately using the beat signal between the two equally stabilized lasers.

§4. Conclusion

Several experiments were carried out to improve the frequency stability of a He–^{22}Ne laser by the saturated dispersion spectrum in CH_4. For this purpose, a Faraday rotator was employed for spectral measurement. Temperature fluctuations of the YIG crystal for the Faraday rotator were reduced as low as 0.01°C, and the laser intensity was stabilized by controlling the discharge current. The intensity stability obtained was

$$\sigma_I=1.0\times10^{-5}\cdot\tau^{-1/2} \quad \text{for } 1\text{ ms}\leqq\tau\leqq100\text{ s}.$$

After these arrangements, the laser frequency was stabilized. The frequency stability obtained can be approximately expressed as

$$\sigma_f=4.0\times10^{-12}\cdot\tau^{-1/2} \quad \text{for } 10\text{ ms}\leqq\tau\leqq500\text{ s}.$$

The highest stability was

$$\sigma_f=3.0\times10^{-13} \quad \text{at } \tau=500\text{ s}.$$

References

1) M. Ohtsu, S. Ohta and T. Tako: Jpn. J. Appl. Phys. **20** (1981) 1701.
2) M. Ohtsu and T. Tako: Jpn. J. Appl. Phys. **20** (1981) 2133.
3) D. W. Allan: Proc. IEEE **54** (1966) 2.
4) K. Shimoda and T. Tako: *Proc. 2nd Frequency Standards & Metrology Symposium, Copper Mt., USA 1976* (National Bureau of Standards, Colorado, 1976) p. 187.

Improvements in the Short-Term Frequency Stability of AlGaAs DH Laser

Hidemi TSUCHIDA, Motoichi OHTSU *and*
Toshiharu TAKO, *Regular Members*

UDC 621.375.826.038.825.5 : 546.681'62'19

SUMMARY The frequency of an AlGaAs DH laser has been stabilized with respect to a Fabry-Perot interferometer by controlling the injection current. The frequency stability of 2.1×10^{-12} was obtained at $\tau =$ 90 ms, which was better than the free-running stability by three orders of magnitude.

Recently, spectral purities of semiconductor lasers have been improved. The spectral widths of AlGaAs double heterostructure (DH) lasers have been measured to be narrower than 1 MHz by interferometric measurements[1]. The frequency stability as well as the spectral width is a very important factor for many applications, such as heterodyne-type optical communication, high resolution spectroscopy, precise metrology and so on.

There have been several reports on the frequency stabilization of semiconductor lasers by using a Fabry-Perot interferometer as a frequency reference[2]–[7]. In a previous work[7], the frequencies of AlGaAs DH lasers were stabilized at the resonant frequency of an interferometer by controlling the injection current. In that case, the long-term stability was considerably improved because the interferometer was controlled by a Lamb dip stabilized He-Ne laser at 633 nm. However, short-term stability should be improved for such an application as heterodyne-type optical communication, in which a high-speed laser operation is required.

In this paper, the authors report the improvements in the short-term frequency stability of an AlGaAs DH laser.

Figure 1 shows the experimental apparatus for frequency stabilization. The experiment is carried out in an underground tunnel for long-distance interferometry with a constant temperature of ±0.1°C/day. A single mode AlGaAs DH laser[8] ($\lambda = 823$ nm) is driven by a dc current source. A Fabry-Perot interferometer is made of a cylindrical rod of fused silica with multilayer coatings on both end faces. The interferometer has a free spectral range of 3.4 GHz with a finesse of about 30. The linear part of the transmission spectrum of this interferometer is used as a frequency discriminator. Although the long-term stability is limited mainly by the thermal expansion of the optical pass length, this rigid interferometer has high short-term frequency stability. The laser beam is split into two beams by a beam splitter. One beam is directly detected by a photodiode A, whereas the other beam passes through the interferometer and is detected by a photodiode B. The output signal from the photodiode B is divided by that from the photodiode A to eliminate fluctuations in the laser output power. The output signal from the divider is compared with a reference voltage, and, then fed to the current source for the laser. The servo-controller for the laser consists of an integrator, a low pass filter (−7 dB/decade), a proportional amplifier and a differentiator ($I+P+D$ in Fig. 1) . In the present experiment, the cut-off frequency f_c of the proportional amplifier is varied between 72.3 Hz and 72.3 kHz (f_c = 72.3 Hz in the previous work[7]). The dependence of the laser frequency on the injection current is measured to be −2.75 GHz/mA. Error signals from the differential amplifier are proportional to frequency fluctuations and are recorded by a data recorder. The Allan variance σ^2, which is a measure of frequency stability commonly used, is calculated from these signals after analog-to-digital conversion.

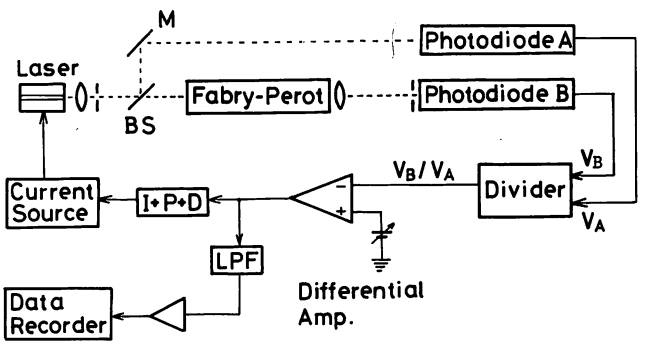

Fig. 1 The experimental apparatus for frequency stabilization.

Figure 2 shows short-term fluctuations of the laser frequency. The upper trace represents the frequency fluctuations of the free-running laser. It can be seen that the laser frequency fluctuates about 20 MHz. It can be thought that the observed periodic fluctuations with frequencies of 50 Hz and 3 Hz on this trace are from the power supply for the injection current and from the microvibration of the ground[9], respectively. The lower trace represents the frequency fluctuations of the stabilized laser. The short-term fluctuations of the laser frequency are reduced to 10 kHz, which are lower than those of the free-running laser by three orders of magnitude.

Figure 3 shows the square root of the Allan variance σ^2, where τ and N represent the integration time and the number of data, respectively. Measurements are carried out for 1 ms $\leqq \tau \leqq$ 100 ms in this work. The curve A represents the frequency stability of the free-running laser (the upper trace of Fig. 2). The frequency stability is better than 1.3×10^{-8} and the minimum value of σ on this curve is

Manuscript received June 19, 1981.
Manuscript revised September 2, 1981.

The authors are with Research Laboratory of Precision Machinery and Electronics, Tokyo Institute of Technology, Yokohama, 227 Japan.

57−12 [L−4]

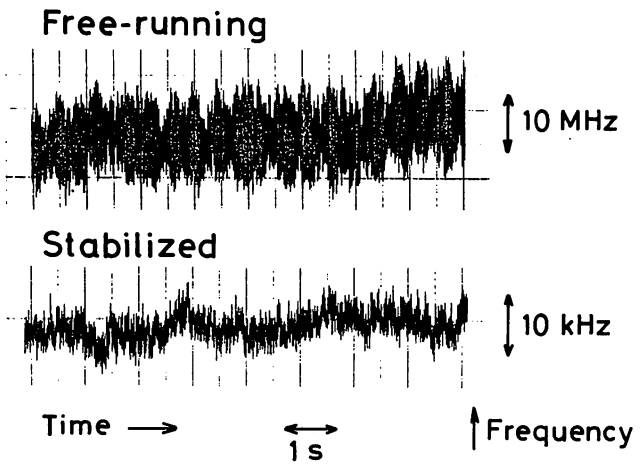

Fig. 2 Short-term fluctuations of the laser frequency (playback signals from the data recorder). The upper and the lower traces correspond to the free-running and the stabilized lasers, respectively.

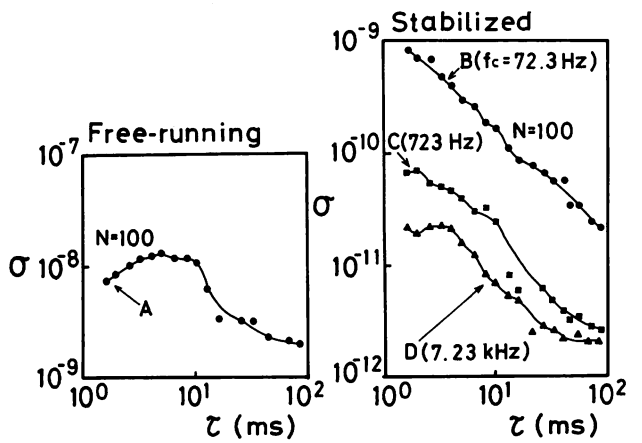

Fig. 3 The square root of the Allan variance σ^2, where τ and N represent the integration time and the number of data, respectively. The curve A represents the frequency stability of the free-running laser. The curves B, C, and D represents the frequency stabilities of the stabilized laser, where f_c represents the cut-off frequency of the proportional amplifier.

$$\sigma = 2.0 \times 10^{-9} \quad \text{at} \quad \tau = 90\,\text{ms}. \tag{1}$$

The curves B, C and D represent the frequency stabilities of the stabilized laser. In the present experiment, the frequency stability remarkably depends on the cutt-off frequency f_c of the proportional amplifier in the servo-controller. The curves B, C and D are the results for different value of f_c. The value of σ on the curves B, C and D are nearly proportional to τ^{-1}. The highest stability is obtained at 7.23 kHz $\leqq f_c \leqq$72.3 kHz. The curve D represents the result for f_c= 7.23 kHz (the lower trace of Fig. 2). The frequency stability is better than 2.2×10^{-11} and the minimum value of σ on the curve D is

$$\sigma = 2.1 \times 10^{-12} \quad \text{at} \quad \tau = 90\,\text{ms}. \tag{2}$$

It can be seen that the values of σ on the curve D are smaller than those on the curve A by three orders of magnitude. The results for $f_c > 7.23$ kHz are almost the same as that for $f_c = 7.23$ kHz.

In conclusion, the short-term frequency stability of an AlGaAs DH laser has been considerably improved by locking its frequency to a rigid Fabry-Perot interferometer. The frequency stability of 2.1×10^{-12} was obtained at $\tau = 90$ ms when the cut-off frequency of the proportional amplifier was set to 7.23 kHz. Both the short-term and the long-term frequency stabilities can be simultaneously improved by combining the method presented here with the method in the previous work [7].

Acknowledgements

The authors would like to express their thanks to Drs. M. Nakamura and K. Aiki of Hitachi, Ltd. for support to the experiment and to Associate Prof. K. Iga of Tokyo Institute of Technology for discussion.

This work was partially supported by a Grant-in-Aid for Scientific Research from the Ministry of Education, Science and Culture.

References

(1) Takakura, T., Iga, K. and Tako, T.: "Linewidth measurement of a single longitudinal mode AlGaAs laser with a Fabry-Perot interferometer", Jpn. J. Appl. Phys., 19, 12, pp. L725—L727 (1980).

(2) Bykovskii, Yu. A., Velichanskii, V.L., Goncharov, I.G. and Masrov, V.A.: "Use of a Fabry-Perot resonator for the stabilization of the frequency of an injection laser", Sov. Phys.-Semicond., 4, 4, pp. 580—583 (1970).

(3) Picque, J.L. and Roizen, S.: "Frequency-controlled cw tunable GaAs laser", Appl. Phys. Lett., 27, 6, pp. 340—342 (1975).

(4) Okoshi, T. and Kikuchi, K.: "Frequency stabilization of semiconductor lasers for heterodyne-type optical communication systems", Electron. Lett., 16, 5, pp. 179—181 (1980).

(5) Favre, F. and Le Guen, D.: "High frequency stability of laser diode for heterodyne communication systems", Electron. Lett., 16, 18, pp. 709—710 (1980).

(6) Tsuchida, H., Sanpei, S., Ohtsu, M. and Tako, T.: "Frequency stability measurement of feedback stabilized AlGaAs DH laser", Jpn. J. Appl. Phys., 19, 12, pp. L721—L724 (1980).

(7) Tsuchida, H., Ohtsu, M. and Tako, T.: "Frequency stabilization of AlGaAs DH lasers", Jpn. J. Appl. Phys., 20, 6, pp. L403—L406 (1981).

(8) Aiki, K., Nakamura, M., Kuroda, T., Umeda, J., Ito, R., Chinone, N. and Maeda, M.: "Transverse mode stabilized $Al_xGa_{1-x}As$ injection lasers with channeled-substrate-planar structure", IEEE J. Quantum Electron., QE-14, 2, pp. 89—94 (1978).

(9) Tako, T. and Asakawa, K.: "Frequency analysis of microvibration of earth surface by using a 50 m interferometer", Proceedings of ICO-11 Conference, Madrid, Spain, pp. 679—682 (1978).

JAPANESE JOURNAL OF APPLIED PHYSICS
VOL. 21, No. 1, JANUARY, 1982 pp. L1–L3

Frequency Stabilization of AlGaAs Semiconductor Laser to the Absorption Line of Water Vapor

Hidemi TSUCHIDA, Motoichi OHTSU and Toshiharu TAKO

Research Laboratory of Precision Machinery and Electronics, Tokyo Institute of Technology, 4259 Nagatsuta-cho, Midori-ku, Yokohama, Kanagawa 227

(Received November 12, 1981; accepted for publication December 19, 1981)

The absorption spectrum of water vapor in the (2, 1, 1) vibration-rotation band has been observed by using an AlGaAs semiconductor laser around 0.82 μm. The laser frequency was stabilized to one of the absorption lines by controlling the injection current. A frequency stability of $1.9\times10^{-9}\geqq\sigma\geqq1.1\times10^{-11}$ was obtained for $10\ \text{ms}\leqq\tau\leqq500\ \text{s}$.

§1. Introduction

Recently, the spectral properties of semiconductor lasers have been improved. AlGaAs semiconductor lasers operate in a single longitudinal and transverse mode, and the spectral widths of these lasers have been estimated, by interferometric measurements,[1] to be narrower than 1 MHz. The frequency stability, as well as the spectral width, is a very important factor for many applications, such as heterodyne-type optical communication, high resolution spectroscopy, precise metrology and so on.

There have been several reports on the frequency stabilization of semiconductor lasers using a Fabry-Perot interferometer as a frequency reference.[2-8] In a previous work,[7] the frequency of AlGaAs lasers was stabilized at the resonant frequency of an interferometer which was controlled by a Lamb dip stabilized He–Ne laser at 633 nm. By controlling the injection current, a frequency stability of $2.1\times10^{-9}\geqq\sigma\geqq2.0\times10^{-11}$ was obtained for $10\ \text{ms}\leqq\tau\leqq500\ \text{s}$, where σ and τ represent the square root of the Allan variance and the integration time, respectively.

Frequency stabilization of semiconductor lasers, based on atomic or molecular transition lines, is desirable especially for the use of frequency standards, which require higher frequency stability and reproducibility. Ohi[9] reproted the frequency stabilization of a PbSnTe laser to the methane absorption line in the ν_4 band at 7.7 μm, in which the laser operated at a low temperature and a stable cryostat had to be used. Yabuzaki *et al.*[10] reported the frequency stabilization of an AlGaAs laser to the Cs-D_2 line at 8521 Å. In this experiment, it was difficult to find a laser whose wavelength had a good coincidence with that of the Cs-D_2 line. If this coincidence is poor, it is impossible to stabilize the frequency of the laser.

This paper describes the experimental results for the frequency stabilization of an AlGaAs semiconductor laser based on the absorption line of water vapor. First, the absorption spectra in the (2, 1, 1) vibration-rotation band were observed by using the laser around 0.82 μm. This is described in §2. Then, the frequency stabilization was carried out as described in §3. Since water vapor has a great number of absorption lines in the near infrared at 0.81–0.84 μm, at least one of the lines must be observed by each AlGaAs laser at room temperature. Therefore, the frequency of every laser can be easily stabilized if these lines are used as a frequency reference, and from this point of view it can be said that this method is superior to previous methods.

§2. Observation of the Absorption Spectra

A water vapor molecule has an asymmetric top structure and has three normal modes of vibration ν_1, ν_2 and ν_3. The vibration-rotation band (0, 0, 0)–(2, 1, 1) lies in the near infrared at 0.81–0.84 μm. Baumann and Mecke[11] observed and assigned this band as atmospheric absorption lines in the solar spectrum. Figure 1 shows the assignment and the relative intensities of the main lines in this band.[11]

The authors observed the absorption spectra of water vapor using a CSP-type AlGaAs laser[12] around 0.82 μm. The threshold current of the laser was about 80 mA. The temperature of the laser was fixed at certain values between 17°C and 23°C using a thermoelectric cooler. The wavelength of the laser could be tuned between 8225 Å and 8245 Å if the temperature was varied within this range.* Fine tuning of the laser frequency was

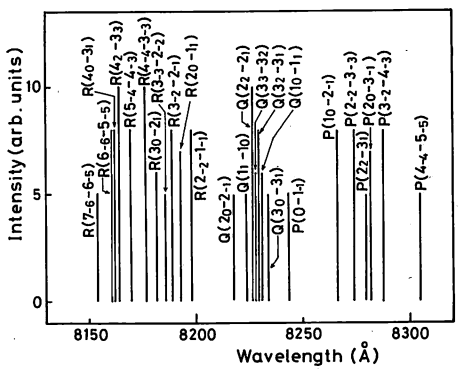

Fig. 1. The assignment and the relative intensities of the main lines in the (2, 1, 1) band observed by Baumann and Mecke.[11]

*There are several gaps in this wavelength range due to mode hopping.

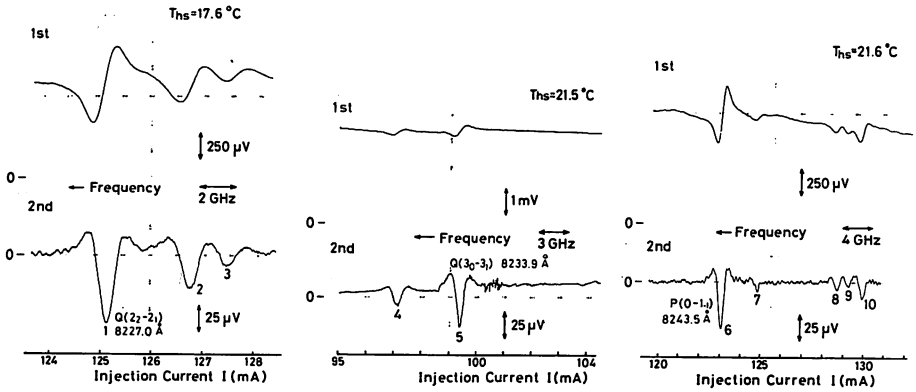

Fig. 2. The absorption spectra of water vapor obtained by sweeping the injection current, where T_{hs} represents the temperature of the heat sink to which the laser is attached. The upper and the lower traces correspond to the first and the second derivative signals, respectively. The lines 1, 5 and 6 correspond to $Q(2_2-2_1)$ at 8227.0 Å, $Q(3_0-3_1)$ at 8233.9 Å and $P(0-1_{-1})$ at 8243.5 Å, respectively. The remaining seven lines have not yet been identified.

achieved by adjusting the injection current. The laser frequency change with injection current was measured as -2.75 GHz/mA by using a Fabry-Perot interferometer.

An absorption cell of 10 cm length containing pure water was used at room temperature ($\cong$21°C). The corresponding vapor pressure was about 20 Torr. The laser beam was focused on an APD after passing through the cell. The laser frequency was modulated by applying an a.c. injection current to the laser. The output signals from the APD were synchronously detected with a lock-in amplifier to obtain the derivative signals of the spectra.

Ten absorption lines were observed in this work. Figure 2 shows the absorption spectra obtained by sweeping the injection current. The upper and the lower traces correspond to the first and second derivative signals, respectively. It can be seen from this figure that the center of the line is not a zero-crossing point due to the background of the light-current characteristics of the laser. Three lines in Fig. 2 can be identified using the results of Baumann and Mecke.[11] The lines 1, 5 and 6 correspond to $Q(2_2-2_1)$, $Q(3_0-3_1)$ and $P(0-1_{-1})$, respectively. The remaining seven lines have not yet been identified and were observed first by the authors.

Further experiments are now in progress to measure more accurately the wavelengths of the lines by using a wavelength stabilized He–Ne laser as a wavelength reference.

§3. Frequency Stabilization of the AlGaAs Laser

The frequency of the AlGaAs laser was stabilized to one of the absorption lines observed in §2 by controlling the injection current. As an example, the line $P(0-1_{-1})$ at 8243.5 Å was used as a frequency reference.

An a.c. injection current of 0.5 mA_{p-p} at a frequency of 5 kHz was applied to the laser to modulate the laser frequency. The third derivative signal of the absorption spectrum was used as a frequency discriminator, which is shown in Fig. 3. The peak-to-peak width of the curve is 740 MHz. It can be seen that the background

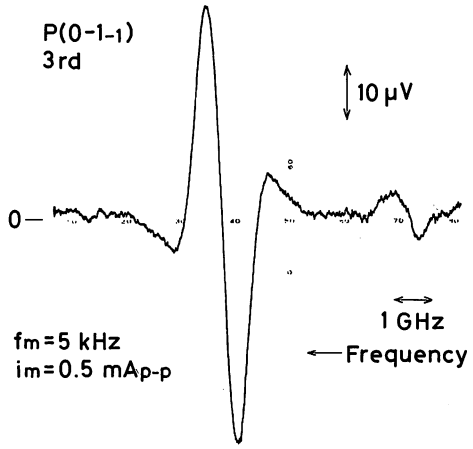

Fig. 3. The third derivative signals of the line $P(0-1_{-1})$ used for the frequency stabilization.

of the light-current characteristics of the laser discussed in §2 was eliminated. The output signals from the lock-in amplifier were fed to the current source for the laser. The servo-controller for the laser consists of an integrator, a low pass filter (-7 dB/decade), a proportional amplifier and a differentiator.[7]

Figure 4 shows the square root of the Allan variance σ^2 of the frequency fluctuations. In this figure, τ and N represent the integration time and the number of data, respectively. The curve A represents the frequency stability of the stabilized laser estimated by using the error signals for the frequency stabilization. The value of σ on the curve A is nearly proportional to $\tau^{-1/2}$. The minimum value on this curve is

$$\sigma = 1.1 \times 10^{-11} \quad \text{at} \quad \tau = 100\ \text{s}, \tag{1}$$

and the stability is better than 1.9×10^{-9} for $10\ \text{ms} \leqq \tau \leqq 500$ s. The curve B represents the results from the previous work (the curve D in Fig. 5 of ref. 7). The value of σ on the curve A is slightly smaller than that on the curve B. The curve C in Fig. 4 represents the frequency stability of the free-running laser.[6] The value of σ on the curve C increases with increasing τ for $\tau > 0.3$ s. This is mainly due

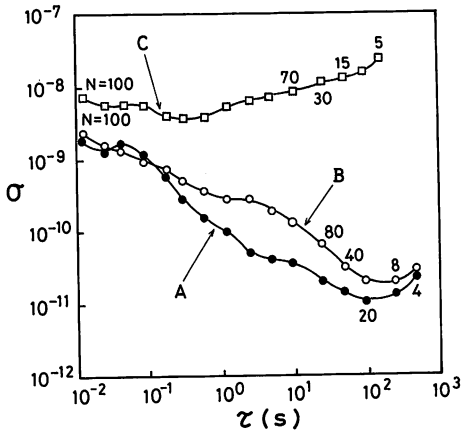

Fig. 4. The square root of the Allan variance σ^2 of the frequency fluctuations, where τ and N represent the integration time and the number of data, respectively. A(●): The frequency stability of the stabilized laser. B(○): The result in the previous work (The curve D in Fig. 5 of ref. 7). C(□): The frequency stability of the free-running laser.[6]

to the temperature change in the active region. Comparing the curves A and C, it can be seen that long-term frequency stability is improved considerably, which demonstrates the effectiveness of this simple method of stabilization. Similar stability can be expected if the frequencies of AlGaAs lasers are stabilized by using the other lines in Fig. 1 as a frequency reference.

§4. Conclusion

In the present work, the absorption spectra of water vapor in the (2, 1, 1) vibration-rotation band were observed using an AlGaAs semiconductor laser around 0.82 μm. Then, the laser frequency was stabilized to one of the absorption lines by controlling the injection current. The following frequency stability was obtained for 10 ms$\leqq\tau\leqq$500 s:

$$1.9\times10^{-9}\geqq\sigma\geqq1.1\times10^{-11}. \quad (2)$$

Acknowledgement

The authors would like to express their thanks to Drs. M. Nakamura and K. Aiki of Hitachi, Ltd. for support to the experiment.

This work was partially supported by a Grant-in-Aid for Scientific Research from Ministry of Education, Science and Culture.

References

1) T. Takakura, K. Iga and T. Tako: Jpn. J. Appl. Phys. **19** (1980) L725.
2) Yu. A. Bykovskii, V. L. Velichanskii, I. G. Goncharov and V. A. Masrov: Sov. Phys.-Semicond. **4** (1970) 580.
3) J. L. Picque and S. Roizen: Appl. Phys. Lett. **27** (1975) 340.
4) T. Okoshi and K. Kikuchi: Electron. Lett. **16** (1980) 179.
5) F. Favre and D. Le Guen: Electron. Lett. **16** (1980) 709.
6) H. Tsuchida, S. Sanpei, M. Ohtsu and T. Tako: Jpn. J. Appl. Phys. **19** (1980) L721.
7) H. Tsuchida, M. Ohtsu and T. Tako: Jpn. J. Appl. Phys. **20** (1980) L403.
8) H. Tsuchida, M. Ohtsu and T. Tako: Trans. Inst. Electron. & Commun. Eng. Jpn. **6** (1982) No. 1.
9) M. Ohi: Jpn. J. Appl. Phys. **19** (1980) L541.
10) T. Yabuzaki, T. Ibaragi, H. Hori, M. Kitano and T. Ogawa: Jpn. J. Appl. Phys. **20** (1981) L451.
11) W. Baumann and R. Mecke: Z. Phys. **81** (1933) 445.
12) K. Aki, M. Nakamura, T. Kuroda, J. Umeda, R. Ito, N. Chinone and M. Maeda: IEEE J. Quantum. Electron. **QE-14** (1978) 89.

JAPANESE JOURNAL OF APPLIED PHYSICS
VOL. 20, NO. 11, NOVEMBER, 1981 pp. 2133–2143

Saturated Dispersion Spectral Shape in CH_4 for Frequency Stabilization

Motoichi OHTSU and Toshiharu TAKO

Research Laboratory of Precision Machinery and Electronics, Tokyo Institute of Technology, 4259 Nagatsuta-cho, Midori-ku, Yokohama, Kanagawa 227

(Received July 10, 1981; acceted for publication August 22, 1981)

Several results of numerical calculations are presented to estimate the characteristics of a saturated dispersion spectrum in CH_4 for the frequency stabilization of a He–^{22}Ne laser at 3.39 μm. As a result of the calculations, the maximum of the signal intensity was estimated to be 0.465% of the probe beam intensity. The signal profile was deformed by the difference between the sensitivities of the two detectors Δs and by the misalignment of the Wollaston prism ϕ used for the measurement. These results were compared with experimental results, and close agreements were obtained. Furthermore, the relations between the laser frequency stability and several parameters (Δs, ϕ, and the intensity fluctuation of the laser beam $\delta I/I$) were estimated to design a laser apparatus with improved frequency stability.

§1. Introduction

Several works on laser frequency stabilization have been performed to develop new wavelength standards.[1-4] In these examples, derivative signals of the saturated absorption spectra in atoms or molecules have been used as frequency discriminators. The laser frequencies were modulated to obtain these derivative signals. As another possibility, the authors have developed a new method for frequency stabilization, in which a saturated dispersion spectrum was used as the frequency discriminator.[5] In this way, the laser frequency can be locked to the center of the saturated dispersion spectrum without any need for frequency modulation. In the previous paper,[5] the method of intracavity polarization spectroscopy was proposed to obtain a Doppler-free saturated dispersion spectrum in CH_4 (the E component of the P(7) line in the ν_3 band), and the results of frequency stabilization of a He–^{22}Ne laser at 3.39 μm were reported.

In this paper, several results of numerical calculations are presented to estimate the characteristics of the saturated dispersion spectrum for laser frequency stabilization.

In §2, basic treatments for calculation and several results are shown. These results are compared with the experimental results[5] in §3. In §4, the relations between frequency stability and several parameters are discussed to design a frequency stabilized laser apparatus.

§2. Numerical Calculations

2.1 *Basic treatments*

The experimental apparatus[5] is shown in Fig. 1(a). One of the cavity mirrors, M_1, is mounted on a piezoelectric transducer (PZT) for frequency tuning. R represents a phase plate made of a mica sheet. Two polarized beams from a Wollaston prism (WP) are detected by two InAs detectors, and the difference between the signals from these detectors is measured by a lock-in amplifier (LIA). Further details of the apparatus are shown in ref. 5. The saturated dispersion spectrum can be measured by this apparatus, and the principle of the measurement is shown in the following.

One of the two counterpropagating beams in the cavity, i.e., the one from M_1 to M_2, corresponds to a probe beam of the polarization spectroscopy in the present work. The other one works as a pump beam. As the laser tube has Brewster windows, these beams are linearly polarized at point A in this figure. At point B, they are elliptically polarized because of the phase plate R. These polarizations are illustrated in Fig. 1(b). If the intensity of the pump beam is high enough, anisotropic absorption, i.e., circular dichroism, will be induced in CH_4. That is, the absorption coefficients for the right (+) and left (−) handed circularly polarized components, in which the elliptically polarized probe beam can be decomposed, are expressed as[6]

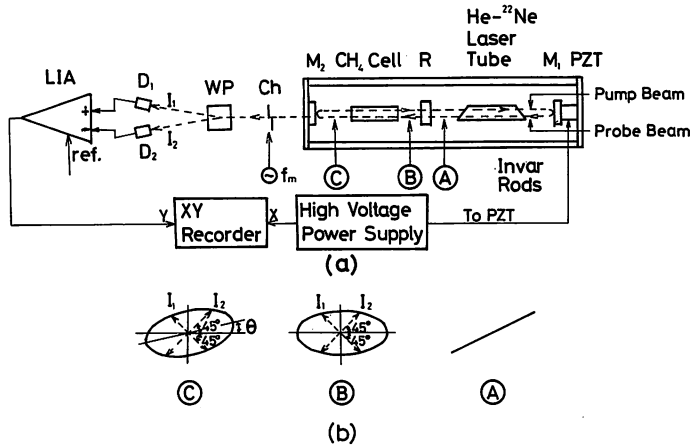

Fig. 1. (a) Experimental apparatus. R: A phase plate, WP: A Wollaston prism, D_1, D_2: InAs detectors, Ch: A chopper, LIA: A lock-in amplifier.
(b) The polarization ellipses for the electric vectors of the probe beam at points A, B, and C in Fig. 1(a). Due to the circular birefringence induced by the pump beam, the difference θ appears between the directions of the longer axes of the ellipses at points B and C. The difference I_D between the intensities I_1 and I_2 is measured using the Wollaston prism and two detectors to determine the value of θ.

$$\alpha_{\pm}=\alpha_0\left[1-\frac{1}{2I_S}(I_{\pm}+2dI_{\mp})\times\left\{1+\frac{\gamma^2}{(\omega-\omega_0)^2+\gamma^2}\right\}\right]. \quad (1)$$

At the same time, circular birefringence is also induced and the difference between the refractive indices for the two circularly polarized components of the probe beam is expressed as[6]

$$n_+-n_-=\frac{\alpha_0\lambda_0}{8\pi I_S}(I_+-I_-)(1-2d)\frac{(\omega-\omega_0)\gamma}{(\omega-\omega_0)^2+\gamma^2}, \quad (2)$$

where

α_0; the linear absorption coefficient of CH_4,
$I_{\pm}$; the intensities of the two circularly polarized components,
I_S; the saturation parameter of CH_4,
γ; the dipole relaxation constant of CH_4,
ω_0, λ_0; the transition frequency and wavelength of CH_4, and
ω; the laser frequency.

The parameter d is given by

$$d=\frac{2J^2+3}{2(6J^2-1)} \quad (J\leftrightarrow J-1), \quad (3)$$

where J represents the rotational quantum number of one of the resonant level in CH_4. It can be seen that eqs. (1) and (2) represent the saturated absorption and dispersion spectra, respectively. The circular birefringence induces phase difference δ between the oppositely circularly polarized components of the probe beam, and the polarization ellipse of the probe beam rotates. If this angle of rotation θ is measured, the saturated dispersion spectrum can be obtained. For this purpose, a Wollaston prism and two detectors are employed. As shown in Fig. 1(b), the directions of the two optical axes of the Wollaston prism are adjusted so that the directions of the linear polarizations of the two transmitted beams are symmetric with respect to the longer axis of the ellipse at point B. Then, the difference I_D between the intensities I_1 and I_2 of these two beams is measured. The expression for I_D is derived as follows:

The electric vector of the elliptically polarized probe beam at point B can be expressed as

$$E_B=a(x\cos\tau_B+y\sin\tau_B)+b(x\cos\tau_B-y\sin\tau_B), \quad (4)$$

where τ_B represents the phase factor at point B. The unit vectors x and y are along the x and y axes which are parallel to the longer and shorter axes of the polarization ellipse at this point, respectively. The first and second terms of eq. (4) correspond to the right and left handed circularly polarized components, and a and b are proportional to $\sqrt{I_+}$ and $\sqrt{I_-}$, respectively.

The electric vector at point C is expressed as

$$E_C = a(x\cos\tau_C + y\sin\tau_C) + b\{x\cos(\tau_C+\delta) - y\sin(\tau_C+\delta)\} \quad (5)$$

where τ_C represents the phase factor at this point. The phase difference δ is expressed as

$$\delta = \frac{2\pi}{\lambda_0}(n_+ - n_-)l, \quad (6)$$

where l represents the length of the CH_4 absorption cell. Then, the angle θ is derived by using a fundamental formula of classical optics[7] and is expressed as

$$\theta = \delta/2. \quad (7)$$

In this paper, the directions of the two optical axes of the Wollaston prism are expressed by the angles $\psi+\phi$ and $-\psi+\phi$ with respect to the x axis, where $\psi=45°$ and ϕ represents the misalignment of the prism on the xy plane. The transmittances of the prism for the laser beams are expressed as[7]

$$\kappa_{\pm\psi+\phi} = \frac{1}{2}\{1+\cos 2\beta\cdot\cos 2(\theta\mp\psi-\phi)\}. \quad (8)$$

In this equation,

$$\beta = \tan^{-1} b_\xi/b_\eta, \quad (9)$$

where b_ξ and b_η represent the lengths of the longer and shorter axes of the ellipse. By using eq. (8), the intensities I_1 and I_2 of the two beams from the prism are expressed as

$$I_1 = (b_\xi^2+b_\eta^2)\kappa_{\psi+\phi},$$
$$I_2 = (b_\xi^2+b_\eta^2)\kappa_{-\psi+\phi}. \quad (10)$$

Here, following approximations hold because $\delta \ll 1$[7]:

$$b_\xi^2+b_\eta^2 \cong 2(a^2+b^2) \propto 2(I_+ + I_-),$$
$$\cos 2\beta \cong \frac{2ab}{a^2+b^2} = \frac{2\sqrt{I_+I_-}}{I_++I_-}. \quad (11)$$

By eqs. (8), (9), (10), and (11), the difference I_D between I_1 and I_2 is given by

$$I_D = 2(I_++I_-)(s_1\kappa_{\psi+\phi} - s_2\kappa_{-\psi+\phi})$$
$$= (s_1-s_2)(I_++I_-) + 2\sqrt{I_+I_-}\{s_1\cos 2(\theta-\psi-\phi) - s_2\cos 2(\theta+\psi-\phi)\}, \quad (12)$$

where s_1 and s_2 represent the sensitivities of the two detectors.

Equation (12) represents the signal intensity obtained by the apparatus in Fig. 1(a). In the following sections, the explicit expressions for I_D are derived for several cases by using eq. (12).

2.2 *The ideal case* ($s_1=s_2$, $\phi=0$)

In this section, the ideal case is discussed, in which the two detectors have equal sensitivities ($s_1=s_2\equiv s$) and the Wollaston prism is perfectly aligned ($\phi=0$). In this case, I_D of eq. (12) is reduced to

$$I_D = s\alpha_0 l(1-2d)\frac{1}{I_S}\sqrt{I_+I_-}(I_+-I_-) \times \frac{(\omega-\omega_0)\gamma}{(\omega-\omega_0)^2+\gamma^2} \times \frac{(\omega-\omega_0)^2+\gamma}{(\omega-\omega_0)\gamma^2}, \quad (13)$$

by using eqs. (2), (6), (7), and (12). The intensities I_+ and I_- are given by

$$I_+ = \frac{1}{1+z}I, \quad I_- = \frac{z}{1+z}I, \quad (14)$$

where I represents the intensity of the probe beam and z is defined by

$$z \equiv I_-/I_+ \quad (0\leqq z\leqq 1). \quad (15)$$

This quantity z is related to the ratio y between b_ξ and b_η, which is given by

$$y \equiv b_\xi/b_\eta = \frac{1-\sqrt{z}}{1+\sqrt{z}} \quad (0\leqq y\leqq 1). \quad (16)$$

Since the value of y is easily measured in the experiments, the value of z can be also derived by eq. (16).

By using eq. (14), I_D of eq. (13) is transformed as

$$I_D = I_{Dp}\frac{(\omega-\omega_0)\gamma}{(\omega-\omega_0)^2+\gamma^2}, \quad (17)$$

where I_{Dp} corresponds to the peak-to-peak intensity of the signal and is expressed as

$$I_{Dp} = s\alpha_0 l(1-2d)I\frac{I}{I_S}\frac{\sqrt{z}(1-z)}{(1+z)^2}. \quad (18)$$

I_{Dp} takes the maximum I_{Dpm} if $z=0.172$ ($y=0.414$), which is given by

$$I_{Dpm} = \frac{1}{4}s\alpha_0 l(1-2d)I\frac{I}{I_S}. \quad (19)$$

Here, the following typical values[8] are substituted into eq. (19) to estimate the value of I_{Dpm}.

$\alpha_0=0.283\ \mathrm{m}^{-1}$, $l=20$ cm,

$d=0.171$ ($J=8$ for the P(7) line),

$I/I_S=0.5$. (20)

For these values,

$$I_{Dpm}=4.65\times10^{-3}\,sI, \tag{21}$$

i.e., the expected intensity is about 0.465% of the probe beam intensity. This is less than a half of the saturated absorption intensity. However, it must be large enough to be measured by the conventional phase sensitive detection. The broken curve in Fig. 2(a) represents the signal profile numerically calculated by eqs. (17), (19) and (20), and that in Fig. 2(b) represents its derivative. The value of the abscissa x in these figures is defined by

$$x\equiv(\omega-\omega_0)/\gamma. \tag{22}$$

The effect of the saturated absorption, i.e., the circular dichroism, should be considered here because it is induced simultaneously by the pump beam. In this case, $I_\pm$ in eq. (13) have to be replaced by $I_\pm+\mathrm{d}I_\pm$, where $\mathrm{d}I_\pm=-\alpha_\pm lI_\pm$. Therefore, the following term $\mathrm{d}I_D$ has to be added to I_D in eq. (13).

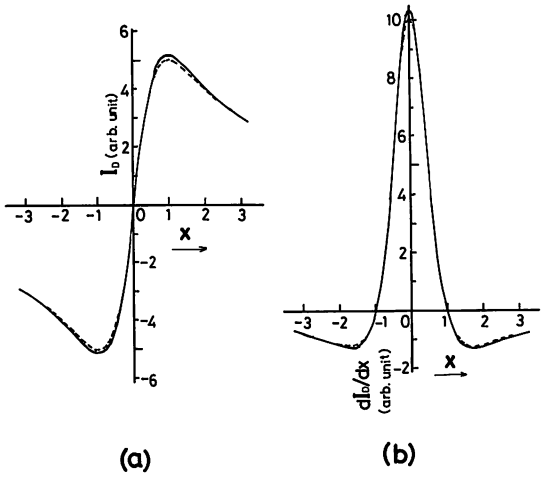

(a) (b)

Fig. 2. (a) The singnal profiles of the saturated dispersion spectrum numerically calculated.
(b) The derivatives of the signals in (a).
In both figures, the solid curves represent the results obtained by taking the effect of saturated absorption into account. The broken curves represent the results in which the effect of the saturated absorption is neglected.

$$\mathrm{d}I_D=\frac{\partial I_D}{\partial I_+}\mathrm{d}I_+ + \frac{\partial I_D}{\partial I_-}\mathrm{d}I_-, \tag{23}$$

where $\partial I_D/\partial I_\pm$ are obtained by eq. (13) and are expressed as

$$\frac{\partial I_D}{\partial I_\pm}=\pm\frac{1}{2}s\alpha_0 l(1-2d)\frac{1}{I_S}\sqrt{\frac{I_\mp}{I_\pm}}(3I_\pm-I_\mp). \tag{24}$$

By substituting these equations into eq. (23) and by using eq. (1), the signal intensity $I_D+\mathrm{d}I_D$ can be derived, in which the effect of the saturated absorption is considered. This intensity $I_D+\mathrm{d}I_D$, using here the previous notation I_D again, is expressed as

$$I_D=s\alpha_0 l(1-2d)\frac{1}{I_S}\sqrt{I_+I_-}(I_+-I_-)\frac{(\omega-\omega_0)\gamma}{(\omega-\omega_0)^2+\gamma^2}\left[1+\alpha_0 l\frac{3+2d}{4I_S}(I_++I_-)\left\{1+\frac{\gamma^2}{(\omega-\omega_0)^2+\gamma^2}\right\}\right]. \tag{25}$$

The second term in the square bracket corresponds to the contribution from the saturated absorption. The solid curve in Fig. 2(a) represents the profile obtained by eqs. (20) and (25), and that in Fig. 2(b) represents its derivative. Comparison between the solid and broken curves in each figure shows that the signal is almost free from the influence of the saturated absorption, i.e., the correction required is less than 3% of the signal intensity.

2.3 *The case in which two detectors have different sensitivities* ($s_1\neq s_2$)

When two independent detectors are employed, it should be expected that their sensitivities are generally different from each other. In this section, several calculations are carried out for the case in which two detectors have different sensitivities ($s_1\neq s_2$) and the Wollaston prism is perfectly aligned ($\phi=0$).

By using eqs. (2), (6), (7), and (12), the following equation is derived.

$$I_D=(s_1-s_2)(I_++I_-)+\frac{s_1+s_2}{2}\alpha_0 l(1-2d)\frac{\sqrt{I_+I_-}}{I_S}(I_+-I_-)\frac{(\omega-\omega_0)\gamma}{(\omega-\omega_0)^2+\gamma^2}. \tag{26}$$

The second term in this equation is just the same as eq. (13) if $s=(s_1+s_2)/2$. Now, the contribution from the saturated absorption is considered. Equation (26) is transformed as follows by using eqs. (1) and (23).

$$I_D=(s_1-s_2)\Bigg[\underbrace{(1-\alpha_0 l)(I_++I_-)}_{(A)\ (B)}+\underbrace{\frac{\alpha_0 l}{2I_S}(I_+^2+I_-^2+4dI_+I_-)\left\{1+\frac{\gamma^2}{(\omega-\omega_0)^2+\gamma^2}\right\}}_{(C)}\Bigg]$$
$$+\underbrace{\frac{s_1+s_2}{2}\alpha_0 l(1-2d)\frac{\sqrt{I_+I_-}}{I_S}(I_+-I_-)\frac{(\omega-\omega_0)\gamma}{(\omega-\omega_0)^2+\gamma^2}}_{(D)}$$
$$\times\left[1+\alpha_0 l\frac{3+2d}{4I_S}(I_++I_-)\left\{1+\frac{\gamma^2}{(\omega-\omega_0)^2+\gamma^2}\right\}\right]. \tag{27}$$

Comparison between eqs. (26) and (27) shows that three terms (A, B, and C) appeared in eq. (27) for the first time because of the difference in the detector sensitivities. The first term A represents the intensity of the light incident on the CH_4 cell. The second and third terms (B and C) represent linear and saturated absorption, respectively. The fourth term D represents the saturated dispersion signal, which corresponds to the signal obtained in §2.2. As these three terms are superposed on the term D, the signal profile will be deformed. Figure 3 shows signal profiles for several values of the difference in the detector sensitivities Δs, which are derived from eqs. (20) and (27). Here, Δs is defined by

$$\Delta s=2(s_1-s_2)/(s_1+s_2). \tag{28}$$

Figure 4 shows the derivatives of the signals in Fig. 3.

2.4 *The case in which the Wollaston prism is misaligned* ($\phi\neq 0$)

In this section, several calculations are carried out for the case in which two detectors have equal

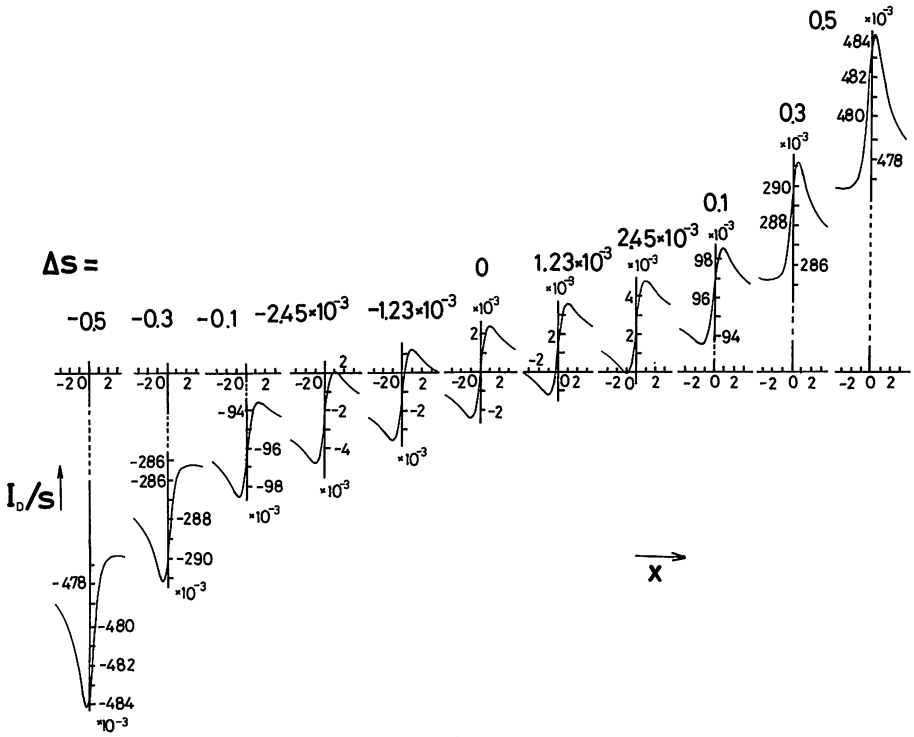

Fig. 3. The signal profiles numerically calculated for several values of the difference Δs in the detector sensitivities.

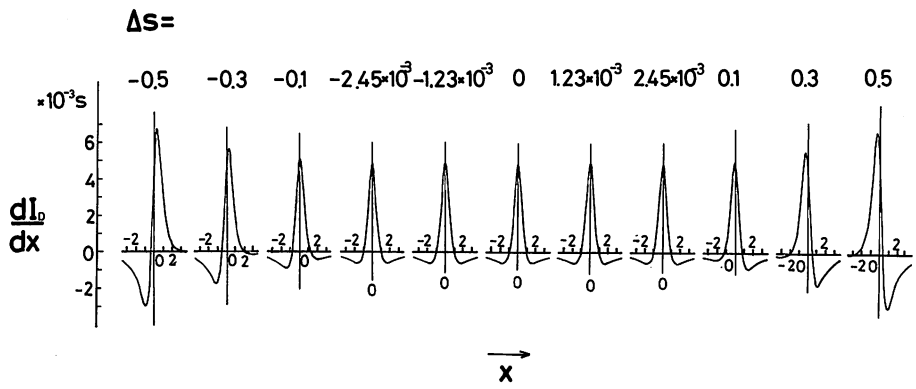

Fig. 4. The derivatives of the signals in Fig. 3.

sensitivities ($s_1=s_2\equiv s$) and the Wollaston prism is misaligned ($\phi\neq 0$). By using eqs. (2), (6), (7), and (12), the following equation is derived for I_D.

$$I_D=-4s\sqrt{I_+I_-}\sin 2\phi+s\alpha_0 l(1-2d)\frac{1}{I_S}\sqrt{I_+I_-}(I_+-I_-)\frac{(\omega-\omega_0)\gamma}{(\omega-\omega_0)^2+\gamma^2}\cos 2\phi. \tag{29}$$

The second term in this equation corresponds to the signal of eq. (13). When the contribution from the saturated absorption is also introduced, eq. (29) is transformed as follows by eqs. (1) and (23).

$$I_D=-4s\sqrt{I_+I_-}\underbrace{\left[\underbrace{(1-\alpha_0 l)}_{(A')}+\underbrace{\frac{\alpha_0 l(1+2d)}{4I_S}(I_++I_-)\left\{1+\frac{\gamma^2}{(\omega-\omega_0)^2+\gamma^2}\right\}}_{(C')}\right]}_{(B')}\sin 2\phi$$
$$+\underbrace{s\alpha_0 l(1-2d)\frac{1}{I_S}\sqrt{I_+I_-}(I_+-I_-)\frac{(\omega-\omega_0)\gamma}{(\omega-\omega_0)^2+\gamma^2}}_{(D')}$$
$$\times\left[1+\alpha_0 l\frac{3+2d}{4I_S}(I_++I_-)\left\{1+\frac{\gamma^2}{(\omega-\omega_0)^2+\gamma^2}\right\}\right]\cos 2\phi. \tag{30}$$

Three terms (A′, B′ and C′) in this equation correspond to the incident light intensity, linear, and saturated absorption, respectively. The fourth term (D′) represents the saturated dispersion. The first three terms appeared because of the misalignment of the prism. It can be seen from this equation that the conventional saturated absorption signal is obtained when $\phi=\pm\pi/4$. Figures 5 and 6 show signal profiles and their derivatives for several values of ϕ which are derived from eqs. (20) and (30).

§3. Comparisons with Experimental Results

Figure 7(a) shows the signal profile measured by the apparatus in Fig. 1.[5] The CH_4 pressure and the value of y in eq. (16) were 18 mTorr and 0.29, respectively. Figure 7(b) shows its derivative signal obtained by modulating the laser frequency. For this modulation, a small a.c. voltage was applied to the PZT. Close agreements can be seen between the curves in Fig. 2 and those in Fig. 7. The peak-to-peak intensity in Fig. 7(a) is 6.5 μV, which is about 0.65% of the probe beam intensity because it was measured to be about 1 mV. This value is consistent with the approximately estimated value of eq. (21) in §2.

Figure 8 shows the relation between the peak-to-peak intensity of the signal I_{Dp}, the parameters z, and y. The white circles represent the experimental results.[5] The CH_4 pressure employed in this experiment was 15 mTorr. The solid curve was drawn by using eq. (18). Here, the least-square fitting was employed because the values of s and I in eq. (18) cannot be accurately determined from the experiment. Again, close agreement can be seen between this curve and the experimental results in this figure.

Figure 9 shows the derivative signal profiles

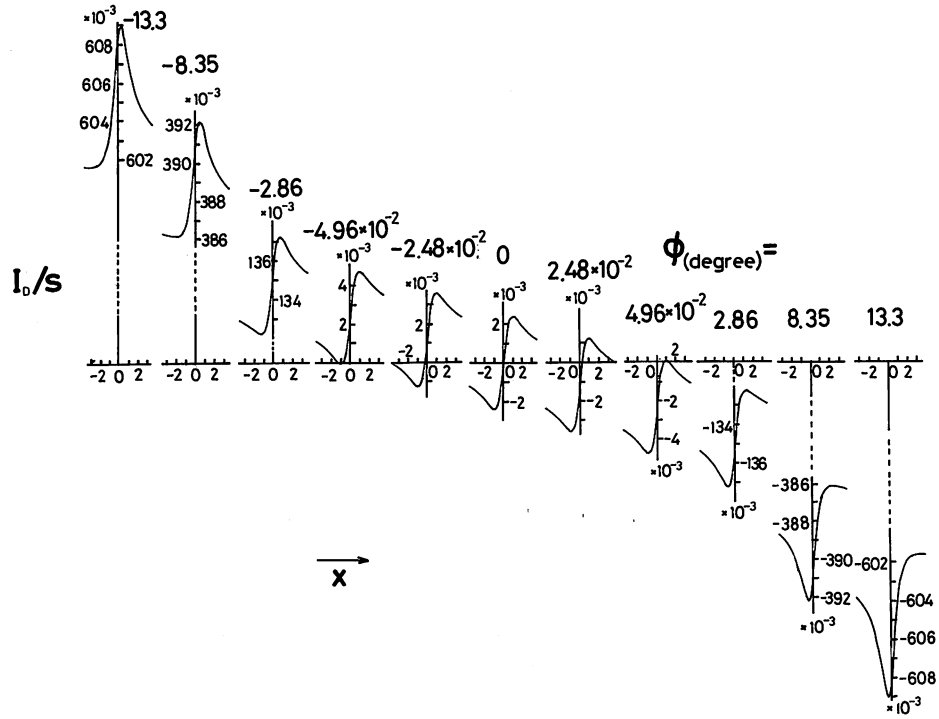

Fig. 5. The signal profiles numerically calculated for several values of the misaligned angle of the Wollaston prism ϕ.

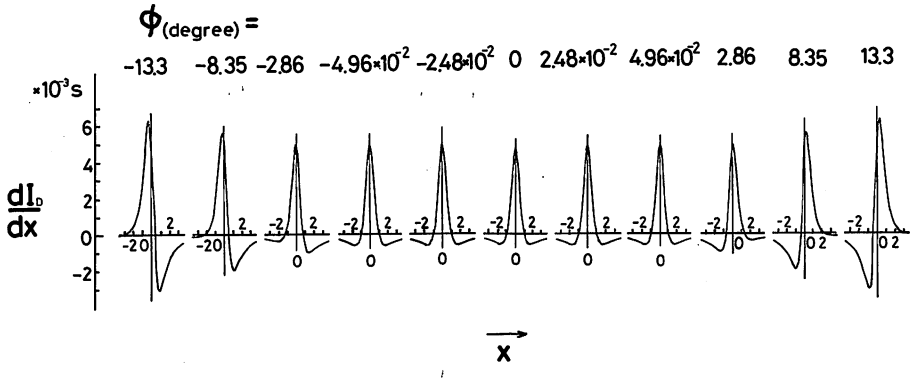

Fig. 6. The derivatives of the signals in Fig. 5.

experimentally obtained for several values of Δs. For this measurement, the sensitivity of one detector was varied by an attenuator which was connected between the detector and the lock-in amplifier as shown in Fig. 1. The deformation characteristics of these derivative signal profiles are similar to those of the numerically estimated results in Fig. 4.

As a result of the comparisons shown in this chapter, the calculated results agree well with the experimental results and are useful to estimate signal characteristics of the saturated dispersion spectrum.

§4. Discussion

In this chapter, necessary conditions for laser frequency stabilization are discussed, and expected frequency stability as well as resettability are estimated by using the results of the previous chapters.

According to Fig. 3, the signal profile is deformed with increasing $|\Delta s|$, and the zero-crossing point of the profile x_0 is shifted. The signal crosses the abscissa if

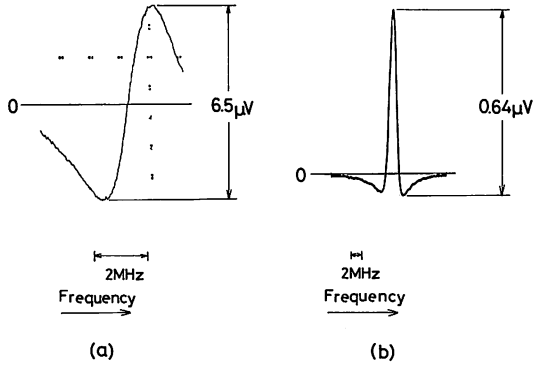

Fig. 7. (a) The saturated dispersion spectrum experimentally obtained using the apparatus shown in Fig. 1(a).[5] The CH_4 pressure and the value of y in eq. (16) were 18 mTorr and 0.29, respectively.

(b) The derivative of the spectrum in (a). The modulation frequency and the maximum frequency deviation used for the laser were 500 Hz and 570 kHz, respectively.

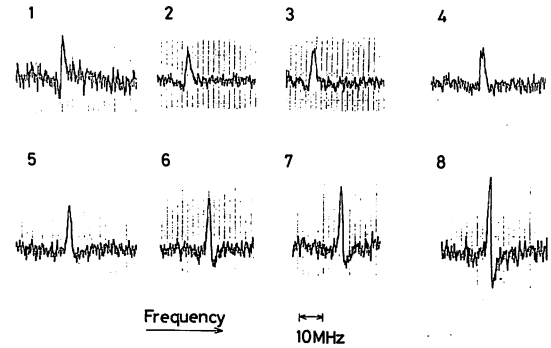

Fig. 9. The derivatives of the saturated dispersion spectra experimentally obtained for several values of Δs. The value of Δs was varied using an attenuator connected between one of the detectors and a lock-in amplifier. Each curve is given a number in the order of increasing value of Δs. Though its value cannot be accurately determined, $\Delta s<0$ for curves 1–4, $\Delta s>0$ for curve 5, and $\Delta s>0$ for curves 6–8.

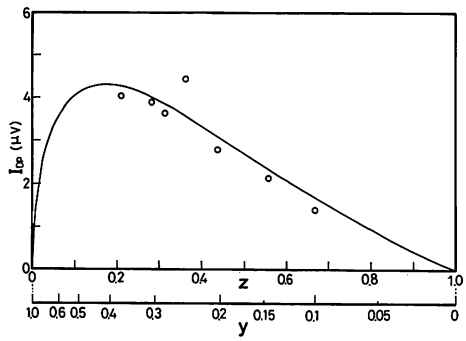

Fig. 8. The relation between the peak-to-peak intensity of the saturated dispersion spectrum I_{Dp}, the parameter z, and y. White circles represent the experimental results,[5] where the CH_4 pressure used was 15 mTorr. The solid curve was drawn by eq. (18).

$$|\Delta s| \leqq 2.45 \times 10^{-3}. \tag{31}$$

Figure 10 shows the relation between x_0 and Δs calculated from eqs. (29) and (27). In this figure, the following equation approximately holds for a small value of $|\Delta s|$:

$$x_0 = -2.08 \times 10^2 \Delta s. \tag{32}$$

When this signal is used as a frequency discriminator for the laser frequency stabilization, the laser frequency is locked at x_0. Therefore, the value of Δs has to be adjusted so that it satisfies the relation of eq. (31). Under this condition, Fig. 10 and eq. (32) show the effect of Δs on the stabilized laser frequency. That is, the frequency stability is reduced if Δs fluctuates

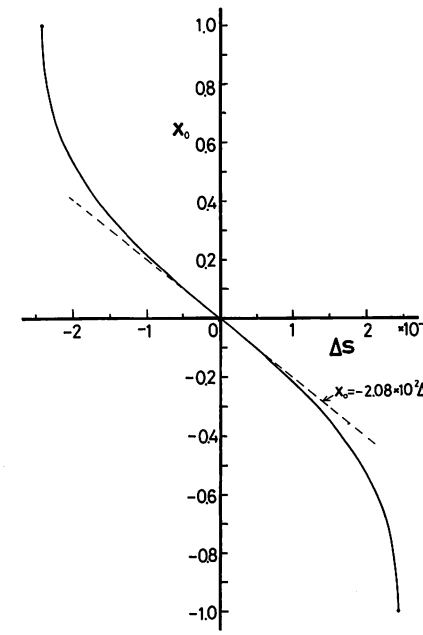

Fig. 10. The relation between Δs and the zero-crossing point of the saturated dispersion spectrum x_0, which was derived from eqs. (20) and (27).

during the period of stability measurment. Even if Δs does not fluctuate, the frequency resettability is reduced if another pair of detectors are used because each pair has a different value of Δs.

Figure 11 shows the relations between x_0 and relative laser intensity fluctuation $\delta I/I$ for several values of Δs, which were derived from eqs. (20) and (27). It can be seen from this

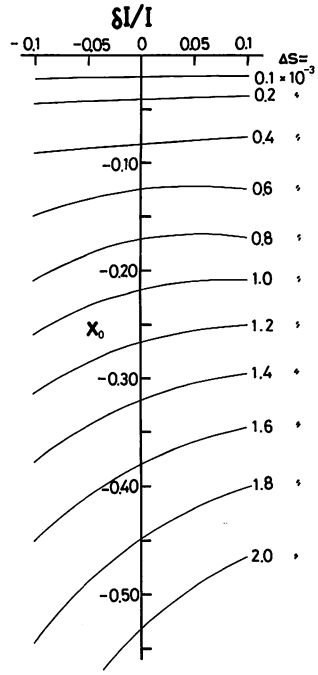

Fig. 11. The relations between x_0 and the relative laser intensity fluctuation $\delta I/I$ for several values of Δs. These were derived from eqs. (20) and (27).

figure that the frequency stability also depends on the intensity fluctuation $\delta I/I$ if $\Delta s \neq 0$, and this dependence becomes more significant with increasing $|\Delta s|$. Figure 12 shows the relations between $\delta I/I$ and Δs for several values of $\delta x_0(\Delta s)$, which were derived from the results in Fig. 11. In this figure, $\delta x_0(\Delta s)$ represents the shift of the zero-crossing point x_0 due to the intensity fluctuation, which is defined by

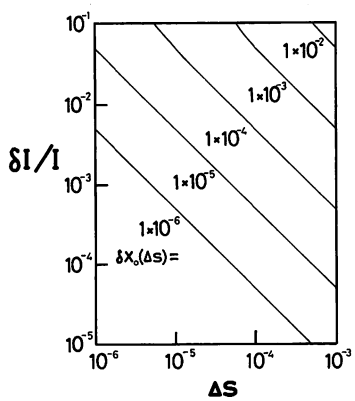

Fig. 12. The relations between $\delta I/I$ and Δs for several values of the shifts $\delta x_0(\Delta s)$ of the zero-crossing points. The definition of $\delta x_0(\Delta s)$ is given by eq. (33). These relations were derived from the results in Fig. 11.

$$\delta x_0(\Delta s) \equiv x_0(\delta I/I) - x_0(\delta I/I = 0). \quad (33)$$

The curves were drawn for $|\delta I/I| \leqq 1 \times 10^{-1}$ and $|\Delta s| \leqq 1 \times 10^{-3}$. The following approximation holds in this range:

$$\delta I/I = 4.92 \times 10^{-3} \frac{\delta x_0(\Delta s)}{\Delta s}. \quad (34)$$

The error in this approximation is less than 5% if $|\delta I/I| \leqq 1 \times 10^{-1}$ and $|\Delta s| \leqq 2.45 \times 10^{-3}$. According to Fig. 12 and eq. (34), the intensity fluctuation $|\delta I/I|$ has to be lower than 4.92×10^{-4}, for example, to get $\delta x_0(\Delta s) \leqq 1 \times 10^{-4}$ if $\Delta s = 1 \times 10^{-3}$. Since the half width of the saturated dispersion spectrum in Fig. 7(a) is about 1 MHz, the relation $\delta x_0(\Delta s) \leqq 1 \times 10^{-4}$ means that the frequency fluctuation is less than 100 Hz, which corresponds to a frequency stability higher than 1×10^{-12} for the He–^{22}Ne laser at 3.39 μm.

It can be seen from Fig. 5 that the signal profile is also deformed with increasing $|\phi|$, as was the case in Fig. 4. The signal crosses the abscissa if

$$|\phi| \leqq 4.96 \times 10^{-2} \quad \text{(degree)}. \quad (35)$$

For the frequency stabilization, The value of ϕ has to be adjusted so that it satisfies the relation of eq. (35). Figure 13 shows the relation between

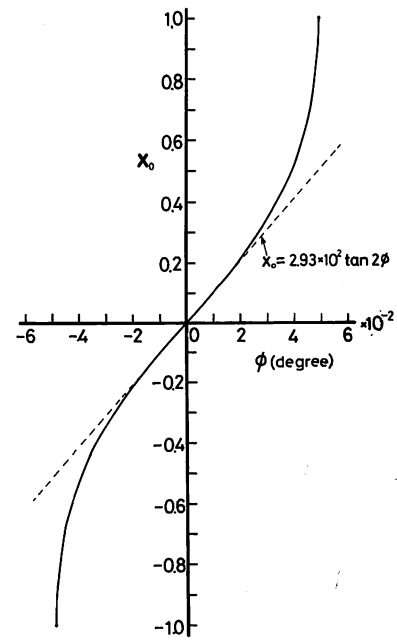

Fig. 13. The relation between ϕ and x_0 which was derived from eqs. (20) and (30).

x_0 and ϕ, which was derived from eqs. (20) and (30). In this figure, the following relation approximately holds for small values of $|\phi|$:

$$x_0 = 2.93 \times 10^2 \tan 2\phi. \qquad (36)$$

Figure 13 and eq. (36) show that the frequency stability and resettability also depend on ϕ. Figure 14 shows the relations between $\delta I/I$ and x_0 for several values of ϕ, which were derived from eqs. (20) and (30). By using this figure, the relation between $\delta I/I$ and ϕ can be obtained and is illustrated in Fig. 15 for several values of $\delta x_0(\phi)$, where $\delta x_0(\phi)$ follows the same definition as $\delta x_0(\Delta s)$ of eq. (33). Here, the curves were drawn for $|\delta I/I| \leqq 1 \times 10^{-1}$ and $|\phi| \leqq 1 \times 10^{-1}$ degree. In this range, the following approximation holds within an error of 5%:

$$\delta I/I = -3.48 \times 10^{-3} \frac{\delta x_0(\phi)}{\tan 2\phi}. \qquad (37)$$

From this equation the value of $|\delta I/I|$ has to be less than 1×10^{-4} to get $\delta x_0(\phi) \leqq 1 \times 10^{-4}$ (a frequency stability higher than 1×10^{-12}) if $\phi = 1 \times 10^{-2}$ degree.

In this chapter, the effects of Δs, ϕ, and $\delta I/I$ on the frequency stability were discussed. For more a general case in which $\Delta s \neq 0$ and $\phi \neq 0$, the effects of Δs and ϕ on the frequency stability can be a simple arithmetic sum of both effects, i.e., $\delta x_0(\Delta s) + \delta x_0(\phi)$, because $|\Delta s| \ll 1$ and $|\phi| \ll 1$ as shown by eqs. (31) and (35). Improved laser design and a frequency stability higher than those in the previous work[5] are expected by using these results as a guiding principle. If the values of Δs, ϕ, and $\delta I/I$ are sufficiently reduced, the attainable frequency stability will be limited by other factors such as the noise in the spectrum, the pressure shift, and so on.[9]

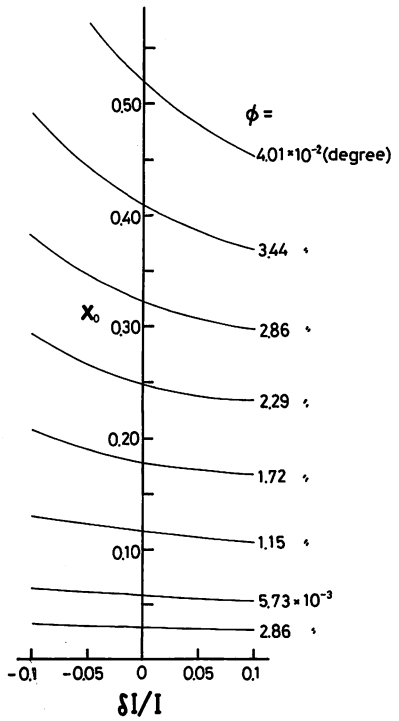

Fig. 14. The relations between x_0 and $\delta I/I$ for several values of ϕ, which were derived from eqs. (20) and (30).

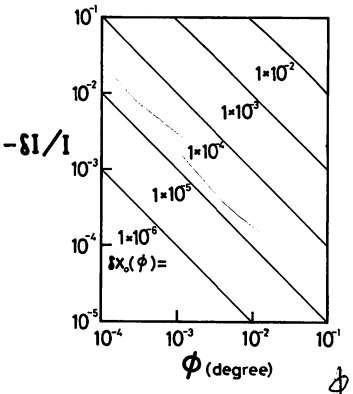

Fig. 15. The relations between $\delta I/I$ and Δs for several values of the shifts δx_0 (ϕ), which were derived from the results in Fig. 14. The definition of δx_0 (ϕ) is the same as that of δx_0 (Δs).

§5. Summary

The theoretical background was presented to estimate the characteristics of a saturated dispersion spectrum in CH_4. Furthermore, the effects of several parameters on the laser frequency stability were estimated to apply this spectrum for the frequency stabilization of a He–^{22}Ne laser. The results obtained are summarized in the following.

(1) The signal intensity takes the maximum if $y = 0.414$, where y represents the ratio between the lengths of the longer and shorter axes of the polarization ellipse of the probe beam. The maximum value is 0.465% of the probe beam intensity.

(2) The signal profile is deformed by the difference between the sensitivities of the two detectors Δs.

The signal crosses the abscissa if

$$|\Delta s| \leqq 2.45 \times 10^{-3}. \qquad (38)$$

When this deformed signal is used for the frequency stabilization, the following relation holds:

$$\delta I/I = 4.92 \times 10^{-3} \frac{\delta x_0(\Delta s)}{\Delta s}, \qquad (39)$$

where $\delta x_0(\Delta s)$ and $\delta I/I$ represent the laser frequency shift normalized to the half width of the saturated dispersion spectrum and the relative fluctuation of the laser intensity, respectively.

(3) The signal profile is also deformed by the misalignment of the Wollaston prism ϕ, and crosses the abscissa if

$$|\phi| \leqq 4.96 \times 10^{-2} \quad \text{(degree)}. \qquad (40)$$

When this signal is used for frequency stabilization, the following relation holds:

$$\delta I/I = -3.48 \times 10^{-3} \frac{\delta x_0(\phi)}{\tan 2\phi}, \qquad (41)$$

where $\delta x_0(\phi)$ follows the same definition as that of $\delta x_0(\Delta s)$.

Close agreements were obtained between the results of (1) and the experimental results. The results of (2) and (3) can be used to design a laser apparatus to improve the frequency stability.

References

1) R. L. Barger and J. L. Hall: Phys. Rev. Lett. **22** (1969) 4.
2) G. R. Hanes and K. H. Baird: Metrologia **5** (1969) 32.
3) C. Freed and A. Javan: Appl. Phys. Lett. **17** (1970) 53.
4) M. Ohtsu, S. Katsuragi and T. Tako: IEEE J. Quantum Electron. **QE-17** (1981) 1100.
5) M. Ohtsu, S. Ohta and T. Tako: Jpn. J. Appl. Phys. **20** (1981) 1701.
6) W. Radloff and H. H. Ritze: Appl. Phys. **20** (1979) 247.
7) M. Born and E. Wolf: *Principles of Optics* (Pergamon Press, London, 1970) 4th ed., Chap. 1.
8) T. Tako, M. Ohi, Y. Akimoto, T. Akahane and T. Hara: Kogaku, **4** (1974) 255 [in Japanese].
9) K. Shimoda and T. Tako: *Proc. 2nd Frequency Standards & Metrology Symposium, Copper Mt. USA, 1976* (National Bureau of Standards Colorado, 1976) p. 187.

BULL. P.M.E. (T.I.T.), *No. 48, September 1981* 621.375.826

The Real-time Measurement System for Stability of Laser Frequency*

By

Itiro Siio**, Motoichi Ohtsu*** and Toshiharu Tako****

(Received May 26, 1981)

The authors have made an Allan variance real-time processing system (ARPS) to measure the laser frequency stability, where the Allan variance is a measure of frequency stability, i.e., the average of standard deviations of samples of two successive averaged frequencies. The ARPS has two frequency counters of 24 bit length and an Allan variance processor using a micro processor LSI 6802. The frequency counters are also controlled by the micro processor, and have zero dead time of the gate. The ARPS unables us to compute the Allan variance in wide range of integration time τ, that is, $1\,\text{ms} \leq \tau < 2^{32} \times f^{-1}$ where f is the frequency of the input signal measured in Hz. From this system we can obtain Allan variances on two different signals independently.

1. Introduction

There have been considerable works on the stabilization of laser frequency,[1-5] and the stability has been improved up to 10^{-13}, which is enough to be utilized as a frequency standard. Some of the authors (M. O. and T. T.) have developed the frequency-offset-locked He-Xe laser system at 3.51μm.[5-7] The frequency stability of all three lasers in this system have to be simultaneously measured at real time when this system operates. For measuring the laser frequency stability, a frequency counter with an off-line mini computer or a real-time computing counter (HP5390A) is conventionally used. These are not necessarily suitable for measuring the frequency stability of many lasers simultaneously, since they are designed as universal measurement systems and moreover complex and expensive.

The square root of the Allan variance σ_y[2,8-10] is used as a typical measure of frequency stability, which is the average of standard deviations of samples of two successive averaged frequencies. Since only a simple arithmetical operation is required for the computation, it is suitable to apply a micro processor to a single purpose system for calculating the Allan variance.

For the purpose of computing and characterizing the frequency stability of a group of lasers the authors have developed a real-time system for measuring the stability of laser frequency, which we call an Allan variance real-time processing system, ARPS, for short.

2. The Measurement of Laser Frequency Stability

The Allan variance is defined as

$$\sigma_y^2(\tau) = \frac{1}{n-1} \sum_{k=1}^{n-1} \frac{(\bar{y}_{k+1} - \bar{y}_k)^2}{2}, \qquad (1)$$

* Originally published in Trans. IECE Vol. J64-C No. 3 (1981)

** Graduate student.
*** Associate, Dr. Eng.
**** Professor, Dr. Sci.

Published by Research Laboratory of Precision Machinery and Electronics, Tokyo Institute of Technology, Nagatsuta, Midori-ku, Yokohama 227, Japan

where we define,

$$\bar{y}_k = \bar{f}_k / \bar{f},$$

$\bar{f}_k$: the k-th averaged signal frequency measured within the integration time τ.
$\bar{f}$: the nominal frequency of the signal,
τ : an integration time, and
n : the number of the data $\bar{f}_k$'s.

In Eq. (1), $\bar{f}_k$ and $\bar{f}_{k+1}$ are successively measured with zero dead time of the gate. This situation is schematically explained in Fig. 1.

Figure 2 shows the block diagram for the measurement of laser frequency stability using the beat signal between two lasers.[7] The frequency stability of each laser is estimated by calculating the Allan variance using counts of the beat frequency.

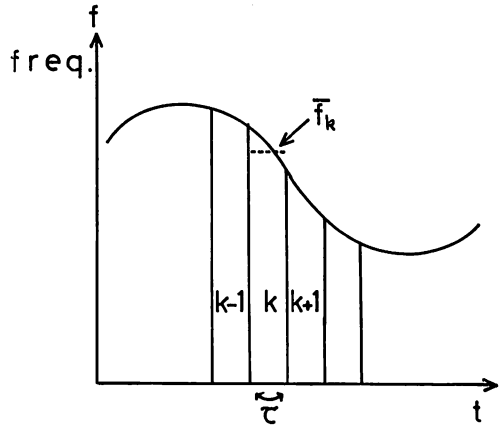

Fig. 1. Frequency change of the signal source.

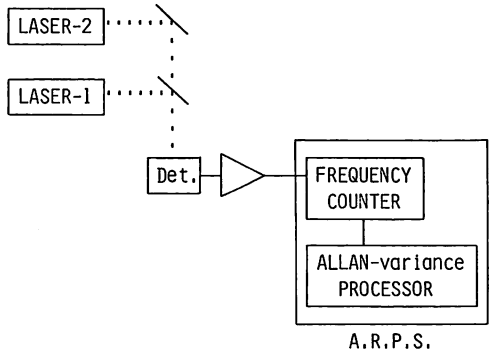

Fig. 2. The measurement system of the laser frequency stability.

3. The Hardware of the ARPS

Figure 3 shows the block diagram of the ARPS. An 8 bit micro processing unit (MPU) LSI 6802 is used.[11] All the programs including floating-point operations routines are fixed on a read only memory (ROM), and the frequency data are stored in a read write memory (RWM) of 3 k byte. Each peripheral interface adapter (PIA) is an LSI processing two group of 8 bit and four 1 bit input and output ports.[11] They are available for data transfer and control of interrupt-request. One of the two PIA's is used for data transfer from keyboard switches and transfer to silent thermal printer as shown in Fig. 3. Another PIA controls interrupt-requests from counters which indicate that the gate time for count is over. The result of count are directly transferred to the data bus lines of the system using tri-state gates.

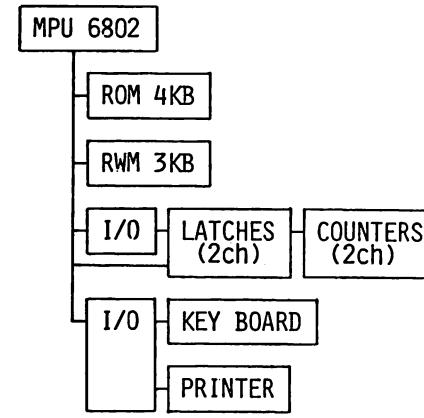

Fig. 3. The block diagram of the ARPS.

The frequency counters consist of two binary counters and latches (Fig. 4 (a)). As these counters work without reset at every gate time, they always overflow counts. The count is latched after the gate time. It takes several tens ns for counters to settle their counts after the rising edge of input signal. In order to prevent an ambiguity error, falling edge of the gate clock which decides a latch timing is delayed untill the

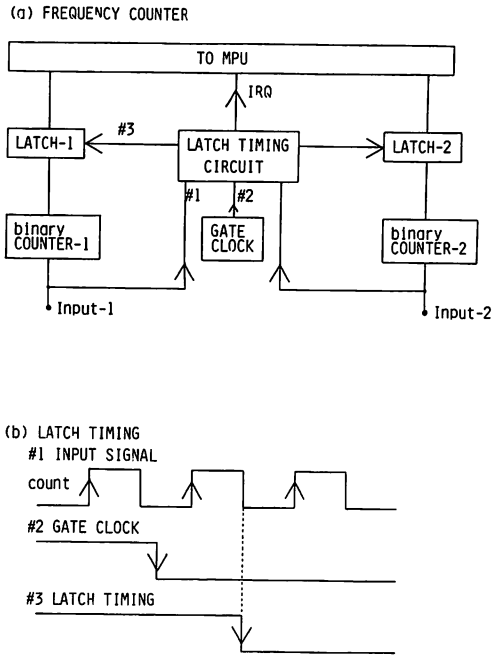

Fig. 4. The frequency counters.

falling edge of input signal. (Fig. 4 (b)) When the count is latched, the PIA switches the level of the interrupt-request (IRQ) bus line. Then the interrupt processing program runs where the acquisition of the data of count and calculation of the frequency are executed. As binary counters are 24 bit length, the accuracy of the frequency calculation is about 7 digit. Thus, the frequency is measured with zero dead time because counters are never reset.

4. The Software of the ARPS

Figure 5 shows the flowchart of the program. In the main routine, the parameters of the Allan variance are set initially by the operator. The n and τ are given to two measured values of counters, independently. The following instruction of the main routine makes a loop where a termination of acquisitions of appointed number of frequency data is checked. When the appointed number of frequency data n on one of the two input signals are acquired, data acquisitions on

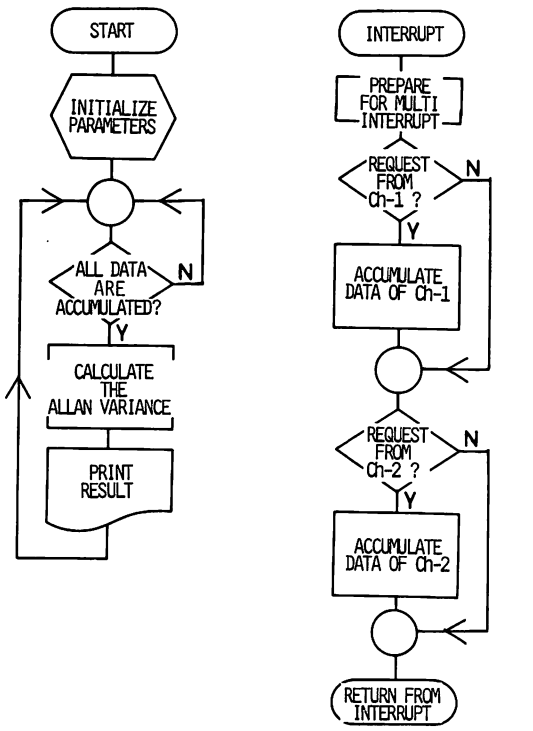

Fig. 5. The flowchart of the program.

the input signal is stopped and the Allan variance is calculated. It takes about 0.7 s to complete calculation the Allan variance if the number of the data is 100.

On the other hand, as an interrupt-request occurs in every period of the gate time, the interrupt is identified and the data of count are acquired. As the interrupt-request occurs every period of the gate time of two frequency counters independently, the interrupt-request can occur when the interrupt processing routine is being executed. Considering this case, the ARPS is designed to be able to execute multi-level interrupt processing. In the interrupt processing routine, difference between two successive data of count is calculated and the difference is accumulated for the integration time τ. As the interrupt processing routine is used only for acquisition and accumulation of the data of count, the ARPS needs memory of the data number n for storage. The interrupt processing

routine, however, terminates more rapidly than the case that the routine takes charge of whole calculation of the Allan variance. The Allan variance is calculated in the main routine using the accumulated values of the frequency. The interrupt processing routine is executed in every period of the gate time, and the main routine is proceeded for the time left. As it takes less than 400μs for the interrupt processing routine to terminate even though two frequency counters request interrupts simultaneously, more than 600μs is left for the main routine in the busiest case of the gate time of 1 ms. Thus, by using the two level structure of the main routine and the interrupt processing routine, the ARPS processes the Allan variances on the two signals simultaneously.

For the calculation of the Allan variance, floating-point operation routines have been developed. By the floating-point representation, the real number x is described as

$$x = \left(\frac{a_1}{N} + \frac{a_2}{N^2} + \ldots + \frac{a_m}{N^m}\right) \times N^{\alpha}, \qquad (2)$$

where $a_1, a_2, \ldots$ is a fixed point part, α is an exponent and N is a base. For the larger base N, the indicating range becomes wider, however the error increases due to the falling out of the fixed point part by some operations,[12] here 2 is adopted as N. The ARPS requires a high speed floating-point operation for real-time processing, and requires an accuracy of 3 byte length because subtractions between two frequency data of 3 byte length counters are executed in the calculation of the Allan variance. The data type of floating point data is shown in Fig. 6.[13] A floating-point number is expressed using 4 byte length which consists of a fixed point part of 3 byte, an exponent of 6 bit and signs of 1 bit

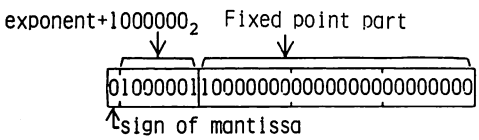

Fig. 6. The data type of floating-point data (the case of +1.).

for the fixed point part and the exponent, respectively. The range of the floating-point number x using this notation is about $10^{-19} < |x| < 10^{+19}$, and the accuracy is about seven digits. The floating-point operation routines of the Allan variance are attempt to be first in their execution for the real-time processing even though the program itself becomes tedious. Their execution speeds are less than 2.6 ms for a multiplication, about 350μs for an addition and less than 16.6 ms for a square root. Thus real-time processing is available as the ARPS calculate the Allan variance of data number of 100 within 1 s.

5. Operation Test

The normal operation of the ARPS is confirmed by two experiments – the simulation using frequency modulated signal and the comparison with the conventional measurement system.

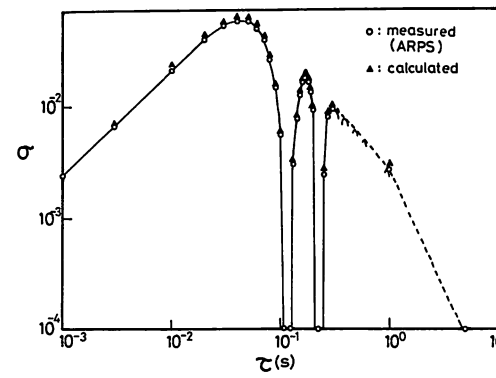

Fig. 7. The result of the operation test of the ARPS.

Figure 7 shows the result of simulation using frequency modulated signal, of which center frequency, the modulation frequency, and the maximum frequency deviation are 500 kHz, 8.6 Hz and 92 kHz, respectively. The Allan variance of the signal is calculated according to the Eq. (1), then

$$\sigma_y(\tau) = \frac{92}{500} \times \frac{\sin^2(\omega\tau/2)}{\omega\tau}, \qquad (3)$$

where $\omega = 2\pi \times 8.6$ rad/s. The measured Allan variance of the modulated signal does not converge with increase of number of the data n when $\omega\tau = m\pi$ ($m = 1, 2, 3, \ldots$), but is determined only by the starting time of the measurement. In this case the Eq. (3) indicates the average of the result of measurements. As the result of the measurements by the ARPS agree with that of the calculation by Eq. (3), it has been confirmed that the ARPS functions correctly.

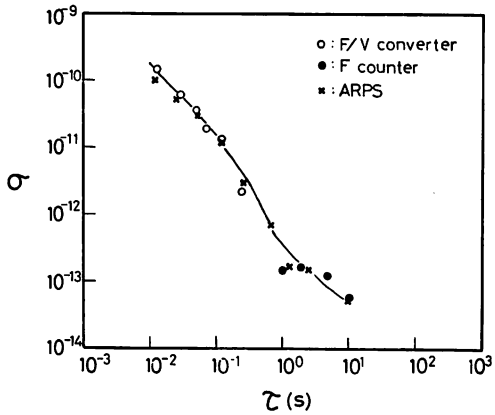

Fig. 8. The result of the frequency stability of He-Xe lasers at 3.51 μm.

Figure 8 shows the result of the measurement of the frequency stability of the laser by using the ARPS and using the conventional measurement system simultaneously. The experimental set up is shown in Fig. 2, and the two lasers are stabilized frequency-offset-locked 3.51 μm He-Xe lasers.[7] The beat frequency was locked to be 2 MHz, and the Allan variance was measured by the ARPS and by the conventional system. To measure the beat frequency for this purpose, authors conventionally used a commercial frequency counter and frequency to voltage (F/V) converter, because the commercial frequency counter yields some errors at the short term shorter than 1 s which comes from the dead time of counting for reset and display.† The F/V converter, however, is less precise for the purpose of measuring the long term stability of authors' lasers.†† Then no reliable Allan variance has been measured in the region between $0.1\text{ s} < \tau < 1\text{ s}$. The acquired data of the frequency have been recorded on paper tape and analogue data recorder, respectively, and processed to calculate the Allan variance by an off-line minicomputer (LSI-11). On the other hand, the Allan variance can be measured by the ARPS in wide range of τ, that is, $1\text{ ms} \leq \tau < 2^{32} \times f^{-1}\text{ s}$ where f is the frequency of the input signal measured in Hz. The maximum value of the τ depends on accumulation of the counter data using 4 byte length. As the result of the measurement by the ARPS agree with that of the conventional system, it has been confirmed that the ARPS can be used for the real-time measurement of the stability of the laser frequency.

6. Summary

Performances of the ARPS are summarized as follows:

i) The ARPS can be used for real-time measurement.
ii) Real Allan variance is computed without dead time of the gate.
iii) Allan variances of two independent signal sources are available.
iv) The Allan variance in wide range of $1\text{ ms} \leq \tau < 2^{32} \times f^{-1}\text{ s}$ is available.
v) More accurate Allan variance is achievable compared with conventional F/V converters, because the ARPS adopts 24 bit frequency counters and accumulate counts on memory of 32 bit length.
vi) The present system is easily handled and with low cost as it is designed for a single purpose system.

†: The dead time is longer than 50 ms in commercially available frequency counters.
††: σ_y is about 10^{-11} at $\tau = 10^{-1}$ s, in the case of the 3.51 μm He-Xe laser of the authors' group.

As the input stage of the ARPS is composed of simple TTL frequency counters, the ARPS would give us wide variety of application such as the stability measurement of quartz oscillators, and signal frequencies in general. Furthermore, if a V/F converter is used with the ARPS, it can be also used to measure the amplitude stability of any analog signals.

Acknowledgements

The authors are much indebted to E. Hatakoshi of their laboratory for his help to prepare some of electronic circuits in the ARPS. This work is partially supported by Grant-in-Aid for Scientific Research from Ministry of Education, Science and Culture.

References

1) R. L. Barger and J. L. Hall: Phys. Rev. Letters, 22, 4, (1969)
2) G. R. Hanes and K. M. Baird: Metrologia 5, 32, (1969)
3) H. Hellwig, H. E. Bell, P. Kartaschoff and J. C. Bargquist: J. Appl. Phys., 43, 450, (1972)
4) F..R. Peterson, D. C. McDonald, J. D. Cupp and B. L. Danielson: Phys. Rev. Lett. 31, 573, (1973)
5) M. Ohtsu and T. Tako: Jpn. J. Appl. Phys., 17, 2169, (1978)
6) M. Ohtsu, R. Koyama, A. Kusunowo and T. Tako: Jpn. J. Appl. Phys., 18, 1619, (1979)
7) M. Ohtsu, S. Katsuragi and T. Tako: IEEE J. Quantum Electron. QE-17 (1981), to be published.
8) D. W. Allan: Proc. IEEE 54, 221, (1966)
9) J. A. Barnes, A. R. Chi, L. S. Culter, D. J. Healey, D. B. Leeson, T. E. McGunigal, J. A. Mullen Jr., W. L. Smith, R. L. Sydnor, R. F. C. Vessot and G. M. R. Winkler: NBS Tech. Note, 394, (1970)
10) Technical Report of the Committee on Precision Frequency Measurement, IEEE of Japan: 41, 8, (1976)
11) Hitachi, Ltd. *Micro Computer System Device Data Book* (1978)
12) Y. Muda: *the Interface* 25, 33, (1979)
13) T. Inami: *the Interface* 25, 65, (1979)

JAPANESE JOURNAL OF APPLIED PHYSICS
VOL. 20, NO. 9, SEPTEMBER, 1981 pp. 1701–1707

Frequency Stabilization of a He–^{22}Ne Laser by Intracavity Polarization Spectroscopy of CH_4

Motoichi OHTSU, Satoru OHTA and Toshiharu TAKO

Research Laboratory of Precision Machinery and Electronics, Tokyo Institute of Technology, 4259 Nagatsuta-cho, Midori-ku, Yokohama, Kanagawa 227

(Received May 7, 1981; accepted for publication June 20, 1981)

The method of intracavity polarization spectroscopy was employed to measure the Doppler-free saturated dispersion spectrum in CH_4 (the E component of the P(7) line in the ν_3 band). A He–^{22}Ne laser at 3.39 μm was used as a light source. The experimental results agreed well with the results of numerical calculations. This spectrum was used to stabilize the laser frequency without frequency modulation, and a stability of 1.1×10^{-12} was obtained for an integration time of 200 s. The second derivative signal of the spectrum was also used for the stabilization by modulating the laser frequency. The stability obtained was 2.5×10^{-13} for an integration time of 300 s. Furthermore, an alternative method using a Faraday rotator is proposed to get higher frequency stability.

§1. Introduction

Frequencies of several lasers have been highly stabilized by using saturated absorption spectra in atoms or molecules to develop new wavelength standards.[1–4] In these examples, the derivative signals of the spectra were obtained by modulating the laser frequencies, and were used as frequency discriminators. However, the short-term stabilities of the laser frequencies were reduced by this modulation. If saturated dispersion spectra are used instead of the saturated absorption spectra, the laser frequencies can be stabilized without any need for modulation because these dispersive-shaped spectra immediately give error signals for the servo loop, as do the derivative signals of the saturated absorption spectra.

In this paper, the measurement of the saturated dispersion spectrum in CH_4 (the E component of the P(7) line in the ν_3 band) and its application to frequency stabilization of a He–^{22}Ne laser at 3.39 μm are reported.

The method of polarization spectroscopy is employed here to measure the saturated dispersion spectrum. In the conventional method of polarization spectroscopy,[5,6] an absorption cell is placed outside the laser cavity, and the directions of two counterpropagating waves, i.e., the pump and probe beams, are set slightly nonparallel to avoid feedback into the laser cavity. Due to this nonparallelism, Doppler broadening of the spectrum is not completely eliminated. To eliminate this residual Doppler broadening, the absorption cell was placed inside the laser cavity in the present study.

§2. Measurement Method

Figure 1(a) shows the He–^{22}Ne laser used. The laser tube has a discharge part of 3 mm in inner diameter and 470 mm in length. The total gas pressure was 2 Torr and the pressure ratio of He to ^{22}Ne was 9. The length of the CH_4 cell was 300 mm. Cavity mirrors, M_1 and M_2, had reflectances of 90%, and one of the mirrors, M_1, was mounted on a piezoelectric transducer (PZT) for frequency tuning and modulation. The cavity length was 1010 mm, and four Invar rods were used to reduce the thermal expansion of the cavity. R represents the phase plate made of a mica sheet.

The standing wave in the cavity is composed of two counterpropagating waves. One of them, i.e., the wave propagating from M_1 to M_2 in this figure, can be considered as a probe beam in polarization spectroscopy because this beam was monitored after transmission through M_2 (see Fig. 2). The other one can be considered as a pump beam.

Since the laser tube has Brewster windows, both beams are linearly polarized at point A in Fig. 1(a). At point B, they are elliptically polarized by the phase plate R. Figure 1(b) shows the vibrational ellipse for the electric vector of the

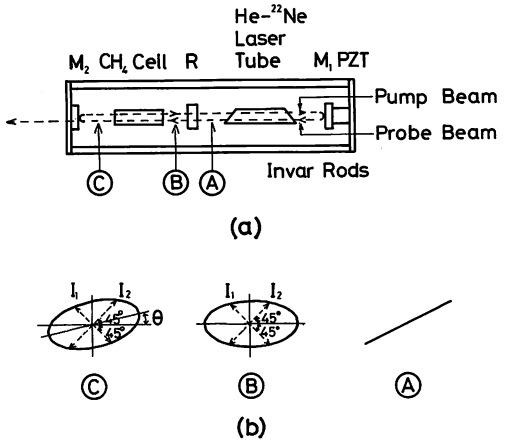

Fig. 1. (a) The He-^{22}Ne laser at 3.39 μm which was used in the experiments. R represents the phase plate made of mica sheet. One of the cavity mirrors, M_1, is mounted on a piezoelectric transducer (PZT) for frequency tuning and modulation. One of the counterpropagating waves in the cavity, the one from M_1 to M_2, is considered as a probe beam, and the other as a pump beam, respectively. (b) The vibrational ellipses for the electric vectors of the probe beam at points A, B, and C in Fig. 1(a). Due to the circular birefringence induced by the pump beam, the difference θ appears between the directions of the large axes of the ellipses at points B and C. By measuring the difference I_D between the intensities I_1 and I_2 of the directions shown in this figure, the value of θ can be obtained.

probe beam at each point in the cavity. If the intensity of the pump beam is high enough, the CH_4 transition is saturated, and this saturation induces circular dichroism and circular birefringence.[7] That is, the absorption coefficients α_+ and α_- for the right (+) and left (−) handed circularly polarized components, in which the elliptically polarized probe beam can be decomposed, are expressed as

$$\alpha_\pm = \alpha_0\left[1-\frac{1}{2I_S}(I_\pm+2dI_\mp)\times\left\{1+\frac{\gamma^2}{(\omega-\omega_0)^2+\gamma^2}\right\}\right]. \quad (1)$$

And the difference between the refractive indices, n_+ and n_-, for both components is expressed as

$$n_+-n_- = \frac{\alpha_0\lambda_0}{8\pi I_S}(I_+-I_-)(1-2d)\frac{(\omega-\omega_0)\gamma}{(\omega-\omega_0)^2+\gamma^2}, \quad (2)$$

where α_0 is the linear absorption coefficient of CH_4, $I_\pm$ are the intensities of the two circularly polarized components of the probe beam, I_S is the saturation parameter of CH_4, γ is the dipole relaxation constant of CH_4, ω_0, λ_0 are the transition frequency and wavelength of CH_4, and ω is the laser frequency.

The parameter d can be expressed as

$$d=\frac{2J^2+3}{2(6J^2-1)} \quad (J\leftrightarrow J-1), \quad (3)$$

where J represents the rotational quantum number of one of the resonant levels in CH_4. It can be easily seen that eqs. (1) and (2) correspond to the saturated absorption and dispersion spectra, respectively. The direction of the large axis of the polarization ellipse of the probe beam rotates because of the difference between n_+ and n_-. That is, this direction at point C in Fig. 1(a) is different from that at point B. This situation is shown in Fig. 1(b) where the θ is the angle between the two directions. The information about the saturated dispersion can be obtained if the angle θ is measured.

Figure 2 shows two ways of performing the measurement. Figure 2(a) shows a method using a Wollaston prism followed by two InAs detectors. The directions of the two optical axes of the Wollaston prism are adjusted so

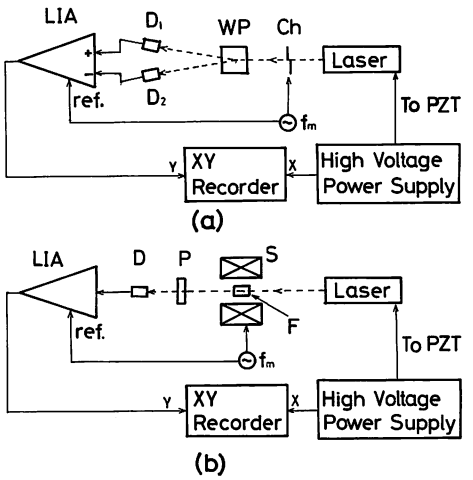

Fig. 2. Experimental apparatus used to measure the difference I_D between the intensities I_1 and I_2 in Fig. 1(b). (a) The method using a Wollaston prism and two detectors. WP: The Wollaston prism made of MgF_2. D_1, D_2: In As detectors. Ch: Mechanical chopper (1 kHz). LIA: Lock-in amplifier. (b) The method using a Faraday rotator and a detector. F: YIG crystal for the Faraday rotator. S: Solenoid for the a.c. axial magnetic field. P: Polarizer. D: An InAs detector.

that the directions of the linear polarizations of the transmitted light beams are symmetrical about the large axis of the ellipse at position B in Fig. 1(a). The signal, which is proportional to θ, can be obtained by measuring the difference between the intensities I_1 and I_2 of these light beams, as shown in Fig. 1(b). In this method, however, the difference between the sensitivities of the two detectors can produce signal waveform asymmetry. Furthermore, it is rather difficult to measure the signal at a high speed because a mechanical chopper is used for phase sensitive detection. The frequency of the chopper used was 1 kHz.

Another method is proposed to avoid these difficulties, in which a Faraday rotator is employed. This method is shown in Fig. 2(b), which is basically the same as that in Fig. 2(a). The direction of the large axis of the ellipse is oscillated by applying an axial a.c. magnetic field to a YIG($Y_3Fe_5O_{12}$) crystal. The difference between I_1 and I_2 can be measured by a polarizer and a detector behind the crystal when phase sensitive detection is employed. The output of the oscillator for the a.c. magnetic field is used as a reference input for the phase sensitive detection. This method is better than that in Fig. 2(a) because only one detector is required and the frequency of the magnetic field can be easily set higher than that of the mechanical chopper.

In §4, the results obtained by both methods will be given.

§3. Estimation of the Signal Intensity

Numerical calculation is carried out in this chapter to estimate the signal intensity. Only the case of Fig. 2(a) is discussed here because the method shown in Fig. 2(b) is basically the same as that of Fig. 2(a).

The circular birefringence (eq. (2)) induces the phase difference δ between the oppositely circularly polarized components of the probe beam This is expressed as

$$\delta=\frac{2\pi}{\lambda_0}(n_+-n_-)l, \tag{4}$$

where l represents the length of the CH_4 absorption cell. The rotation angle θ of the ellipse shown in Fig. 1(b) is given by

$$\theta=\delta/2. \tag{5}$$

Then, the difference I_D between the output intensities from the two detectors in Fig. 2(a) can be easily calculated by using eqs. (2), (4), (5) and several formulae from optics theory.[8] This is expressed as

$$I_D=s\alpha_0 l(1-2d)\frac{1}{I_S}\sqrt{I_+I_-}(I_+-I_-) \times\frac{(\omega-\omega_0)\gamma}{(\omega-\omega_0)^2+\gamma^2}, \tag{6}$$

where s represents the quantity which corresponds to the detector sensitivity. It can be seen from eq. (6) that I_D is proportional to the saturated dispersion signal. Actually, as the circular dichroism (eq. (1)) is simultaneously induced, I_+ and I_- in eq. (6) have to be replaced by $I_+(1-\alpha_+ l)$ and $I_-(1-\alpha_- l)$ to the approximation of the first order, respectively. These replacements lead to the following expression for I_D.

$$I_D=s\alpha_0 l(1-2d)\frac{1}{I_S}\sqrt{I_+I_-}(I_+-I_-) \times\frac{(\omega-\omega_0)\gamma}{(\omega-\omega_0)^2+\gamma^2}\left[1+\alpha_0 l\frac{3+2d}{4I_S}(I_++I_-) \times\left\{1+\frac{\gamma^2}{(\omega-\omega_0)^2+\gamma^2}\right\}\right], \tag{7}$$

The second term in the square brackets in eq. (7) represents this correction. However, eq. (6) will be used in the following discussion because this term is negligibly small, as is shown in Fig. 3.

Here, the intensity ratio z between two circularly polarized components is defined by

$$z\equiv I_-/I_+ \quad (0\leqq z\leqq 1). \tag{8}$$

Then, I_+ and I_- are expressed as

$$I_+=\frac{1}{1+z}I, \qquad I_-=\frac{z}{1+z}I, \tag{9}$$

where I represents the total intensity of the probe beam. Substituting eq. (9) into eq. (6), the following equation is obtained.

$$I_D=s\alpha_0 l(1-2d)I\frac{I}{I_S}\frac{\sqrt{z}(1-z)}{(1+z)^2}\frac{(\omega-\omega_0)\gamma}{(\omega-\omega_0)^2+\gamma^2} =I_{Dp}\frac{(\omega-\omega_0)\gamma}{(\omega-\omega_0)^2+\gamma^2}, \tag{11}$$

where I_{Dp} represents the peak-to-peak value of the signal in eq. (10), and is expressed as

$$I_{Dp}=s\alpha_0 l(1-2d)I\frac{I}{I_S}\frac{\sqrt{z}(1-z)}{(1+z)^2}. \quad (12)$$

This quantity I_{Dp} corresponds to the signal intensity. It can be easily seen that the parameter z in eq. (8) is related to the ratio between the lengths of the two axes of the ellipse, which is expressed as[8]

$$y=\frac{1-\sqrt{z}}{1+\sqrt{z}} \quad (0\leqq y\leqq 1). \quad (13)$$

If $z=0.172$, I_{Dp} in eq. (11) takes the maximum which is given by

$$I_{Dpm}=\frac{1}{4}s\alpha_0 l(1-2d)I\frac{I}{I_S}. \quad (14)$$

The value of y here is 0.414. The following values are substituted into eq. (14) to estimate the value of I_{Dpm}:

$$\begin{aligned}&\alpha_0=0.283\ \mathrm{m}^{-1},\\ &l=20\ \mathrm{cm},\\ &d=0.171 \quad (J=8 \text{ for the P(7) line}),\\ &I/I_S=0.5.\end{aligned} \quad (15)$$

The value of α_0 in this equation is for a CH_4 pressure of 18 mTorr.[9] The value of I/I_S was obtained with a discharge current of a few milliampere, and a conventional saturated absorption signal has been clearly observed at this value of I/I_S.[9] Substituting eq. (15) into eq. (14),

$$I_{Dpm}=4.65\times 10^{-3}sI. \quad (16)$$

This equation implies that the maximum signal intensity will be 0.465% of the total intensity of the probe beam, which is about a half of that of the conventional saturated absorption signal. However, it must be able to be detected without any special difficulties.

Figure 3(a) shows the signal waveforms numerically calculated from eq. (15). Figure 3(b) shows their derivative signals. In both figures the solid curves represent the results obtained by using eq. (7) i.e., the effect of the saturated absorption was considered. The broken curves are the results using eq. (6), in which the saturated absorption was neglected. Comparison between the solid and broken curves shows that the signal waveform is almost free from the effect of saturated absorption.

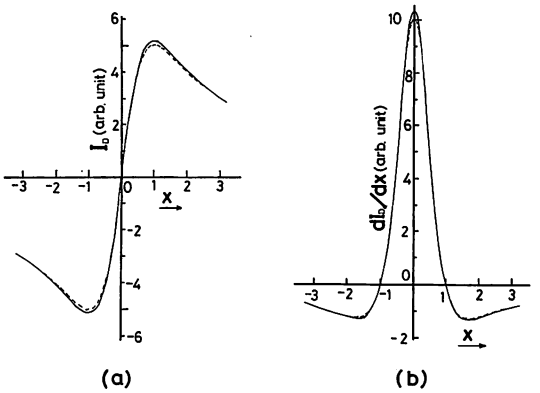

Fig. 3. (a) The saturated dispersion spectrum numerically calculated. (b) The derivative of the spectrum in (a).

$$x\equiv(\omega-\omega_0)/\gamma$$

In both figures, the solid curves represent the results obtained by considering the saturated absorption. The broken curves represent the results in which the saturated absorption is neglected.

§4. Experimental Results

Figure 4(a) shows the signal waveform measured using the apparatus shown in Fig. 2(a). The discharge current of the laser tube and CH_4 pressure were 10 mA and 18 mTorr, respectively. The value of y in eq. (13) was 0.29 (which corresponds to $z=0.55$). The value of y was easily measured by using a polarizer and a detector instead of the apparatus shown in Fig. 2(a). That is, y corresponds to the square root of the ratio between the maximum and

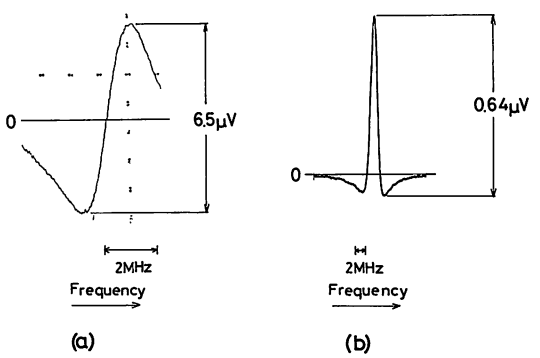

Fig. 4. (a) The saturated dispersion spectrum obtained by using the apparatus in Fig. 2(a). The discharge current of the laser and the CH_4 pressure were 10 mA and 18 mTorr, respectively. The value of z of eq. (8) and y of eq. (13) were 0.55 and 0.29, respectively. (b) The derivative of the spectrum in (a). The modulation frequency and the maximum frequency deviation used were 500 Hz and 570 kHz, respectivey.

minimum intensities of the transmitted light through the polarizer, which were measured by rotating the optical axis of the polarizer. The peak-to-peak value of the signal in Fig. 4(a) is 6.5 μV, which corresponds to about 0.6% of the total intensity of the probe beam because it was measured to be about 1 mV. This value of the signal intensity is almost the same as the roughly estimated value in eq. (16).

Figure 4(b) shows the derivative signal. Here, the laser frequency was modulated by applying an a.c. voltage of 2.6 V (peak-to-peak value, which corresponded to the maximum frequency deviation of 570 kHz) to the PZT. The modulation frequency, i.e., the frequency of the a.c. voltage, was 500 Hz. It can be seen that the curves in Figs. 4(a) and (b) are similar to those in Figs. 3(a) and (b).

Figure 5 shows the signal waveform measured using the apparatus shown in Fig. 2(b). The strength of the a.c. magnetic field was 420 G (peak-to-peak value), which corresponded to the Faraday rotation of 80 degree. Its frequency was 2 kHz. As this frequency is higher than that of the chopper in Fig. 2(a), faster measurements were able to be performed using this apparatus. However, the signal-to-noise ratio of the curve in Fig. 5 is unexpectedly lower than that in Fig. 4(a). The noise on the curve is thought to be from the current source for the a.c. magnetic field. A larger signal-to-noise ratio is possible and experiments are now in progress to achieve this by improving the current source. In the following experiment in the present work, the method of Fig. 2(a) was employed.

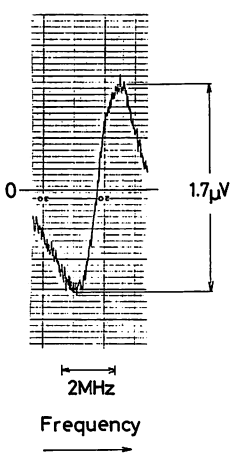

Fig. 5. The saturated dispersion spectrum obtained by using the apparatus in Fig. 2(b). The frequency of the a.c. magnetic field was 2 kHz. Its strength was 420 G (peak-to-peak value), which corresponded to a Faraday rotation of 80 degrees. The values of other parameters were the same as given in Fig. 4(a).

Figure 6 shows the relation between the peak-to-peak value I_{Dp} of the signal and the CH_4 pressure. It can be seen from this figure that the value of I_{Dp} is maximum at a CH_4 pressure of 18 mTorr.

Figure 7 shows the relation between I_{Dp}, z, and y. The value of the parameters z and y were varied by rotating the direction on the optical axis of the phase plate R. The solid curve in this figure was drawn by using eq. (12). Here, the least-square fitting was employed because the values of s and I in eq. (12) cannot be accurately determined. Close agreement can be seen between this curve and experimental results.

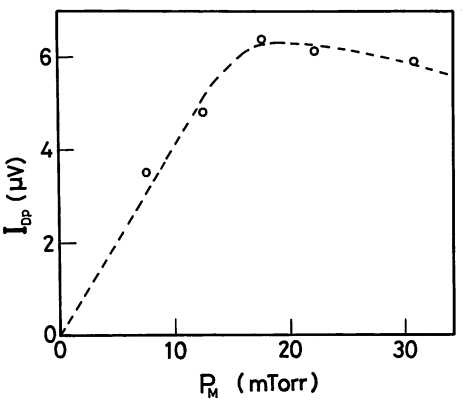

Fig. 6. Relation between the peak-to-peak value I_{Dp} of the saturated dispersion spectrum and the CH_4 pressure P_M. The value of y in eq. (13) was 0.25. The discharge current of the laser was 10 mA.

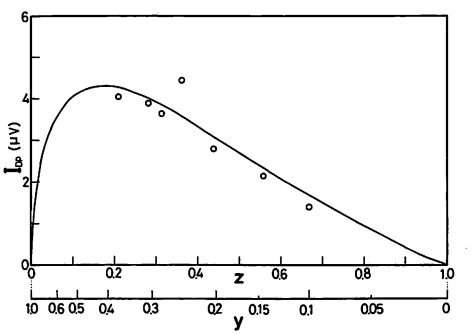

Fig. 7. Relation between the peak-to-peak value I_{Dp} of the saturated dispersion spectrum, the parameter z and y. The discharge current of the laser and the CH_4 pressure were 10 mA and 15 mTorr, respectively. The solid curve was drawn by using eq. (12).

§5. Application to Frequency Stabilization

The laser frequency can be stabilized without frequency modulation when the signal in Fig. 4(a) is used as a frequency discriminator. Figure 8(a) shows the apparatus used for the frequency stabilization. The laser frequency can be also stabilized by the second derivative of the saturated dispersion signal when the laser frequency is modulated. Figure 8(b) shows the apparatus used for this method of stabilization. Figures 9(a) and (b) show the second derivative signal used as a frequency discriminator. The modulation frequency and the maximum frequency deviation were 500 Hz and 660 kHz, respectively. For comparison with the methods of Figs. 8(a) and (b), Fig. 8(c) shows the apparatus for frequency stabilization by the derivative of the conventional saturated absorption signal shown in Fig. 9(c). The values of the modulation frequency and the maximum frequency deviation were the same as in Fig. 9(a). In all the cases of Fig. 8, error signals from the lock-in amplifier were recorded by a data recorder, and the frequency stability was estimated from these signals after analog-to-digital conversion.

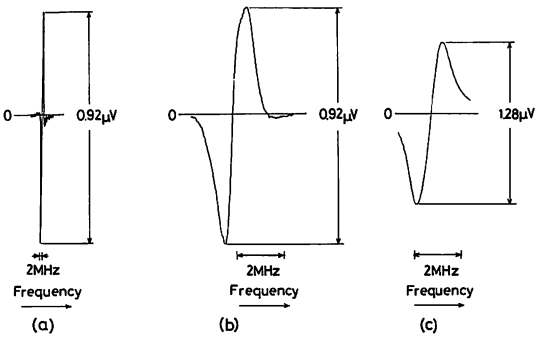

Fig. 9. (a), (b) The second derivative of the spectrum in Fig. 4(a). The central part of the spectrum in (a) is magnified and is shown in (b). The modulation frequency and the maximum frequency deviation of the laser were 500 Hz and 660 kHz, respectively. The values of other parameters were the same as in Fig. 4(a). (c) The derivative of the conventional saturated absorption spectrum. The output beam through the mirror M_1 was used for this measurement, which is shown in Fig. 8(c). The values of the parameters were the same as in (a).

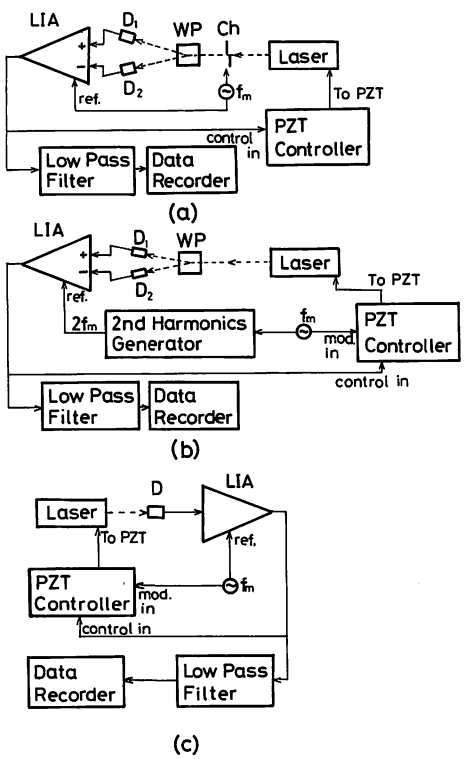

Fig. 8. (a) Apparatus for frequency stabilization without frequency modulation by the signal in Fig. 4(a). (b) Apparatus for frequency stabilization with frequency modulation by the signal in Fig. 9(a). (c) Apparatus for the conventional frequency stabilization with frequency modulation by the signal in Fig. 9(c).

Figure 10 shows the square root of the Allan variance σ^2 of the frequency fluctuations, which is a useful measure of the frequency stability.[10] In this figure, curves A, B and C represent the results when the apparatuses in Figs. 8(a), (b) and (c) were used, respectively.

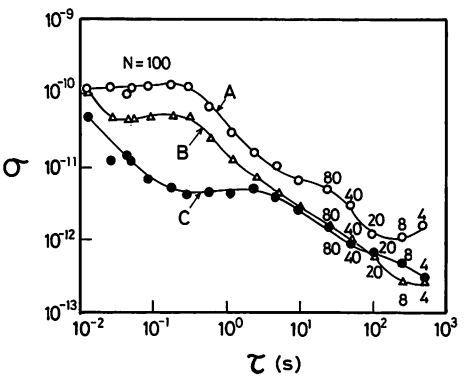

Fig. 10. The square root of the Allan variance σ^2 of the frequency fluctuations. τ and N represent integration time and the number of data, respectively. Curves A, B, and C represent the results obtained by using the apparatuses in Fig. 8(a), (b), and (c), respectively.

On the three curves in Fig. 10, the values of σ are approximately proportional to $\tau^{-1/2}$, where τ represents the integration time. In the range of $12\,\text{ms} \leqq \tau \leqq 500\,\text{s}$, the minimum values of σ on these curves are

$$\begin{aligned} &\text{curve A;} \quad \sigma = 1.1 \times 10^{-12} \quad \text{at } \tau = 200\,\text{s}, \\ &\text{curve B;} \quad \sigma = 2.5 \times 10^{-13} \quad \text{at } \tau = 300\,\text{s}, \\ &\text{curve C;} \quad \sigma = 2.7 \times 10^{-13} \quad \text{at } \tau = 500\,\text{s}. \end{aligned} \tag{17}$$

For $\tau \geqq 1\,\text{s}$, the value of σ on curve B is almost the same as that on curve C. However, the value on curve A is larger than both of them. One of the reasons may be the difference between the sensitivities of the two detectors in Fig. 8(a), which slowly fluctuated with time. It can be inferred that this fluctuation is due to the temperature changes of these detectors. This trouble can be avoided by using the method shown in Fig. 2(b). Higher stability can be expected if a signal with higher signal-to-noise ratio is obtained by the method shown in Fig. 2(b).

§6. Conclusion

The method of intracavity polarization spectroscopy was employed to measure the Doppler-free saturated dispersion spectrum in CH_4. A He–^{22}Ne laser at 3.39 μm was used as a light source. From the numerical calculations, the signal intensity was estimated to be as large as 0.465% of the total intensity of the probe beam. The experimental results agreed well with the results obtained from numerical calculations. This signal was used to stabilize the laser frequency without frequency modulation, and a stability of 1.1×10^{-12} was obtained for an integration time of 200 s. The second derivative signal of the spectrum was also used for the stabilization by modulating the laser frequency. The stability obtained was 2.5×10^{-13} for an integration time of 300 s. These stability values were comparable to those obtained by using the conventional saturated absorption spectrum in CH_4. Furthermore, an alternative method using a Faraday rotator was proposed to get higher frequency stability.

Acknowledgements

The authors wish to express their gratitude to Mr. E. Hatakoshi of their laboratory for his help with the experiments. This work was partially supported by a Grant-in-Aid for Scientific Research from the Ministry of Education, Science and Culture.

References

1) R. L. Barger and J. L. Hall: Phys. Rev. Lett. **22** (1969) 4.
2) G. R. Hanes and K. H. Baird: Metrologia **5** (1969) 32.
3) C. Freed and A. Javan: Appl. Phys. Lett. **17** (1970) 53.
4) M. Ohtsu, S. Katsuragi and T. Tako: to be published in IEEE J. Quantum Electron. **QE-17** (1981).
5) C. Wieman and T. W. Hänsch: Phys. Rev. Lett. **36** (1976) 1170.
6) J. C. Keller and C. Delsart: Opt. Commun. **20** (1977) 147.
7) W. Radloff and H. H. Ritze: Appl. Phys. **20** (1979) 247.
8) M. Born and E. Wolf: *Principles of Optics* (Pergamon Press, London, 1970) 4th ed., Chap. 1.
9) T. Tako, M. Ohi, Y. Akimoto, T. Akahane and T. Hara: Kogaku **4** (1974) 225 [in Japanese].
10) D. W. Allan: Proc. IEEE **54** (1966) 2.

JAPANESE JOURNAL OF APPLIED PHYSICS
VOL. 20, NO. 7, JULY, 1981 pp. L508–L510

Frequency Stabilization of a He–Xe Laser Using a Stark Spectrum in H_2CO

Itiro SIIO, Motoichi OHTSU and Toshiharu TAKO

Research Laboratory of Precision Machinery and Electronics, Tokyo Institute of Technology, 4259 Nagatsuta-cho, Midori-ku, Yokohama 227

(Received May 2, 1981; accepted for publication June 9, 1981)

The frequency of a 3.51 μm He–Xe laser has been stabilized without frequency modulation by means of the derivative signal of the Stark-modulated inverted Lamb dip in the ν_5 transition of H_2CO. We have obtained $\sigma=1.2\times10^{-14}$ as the square root of the Allan variance of the frequency fluctuation for an integration time of 25 s, showing comparable stability to that obtained using a conventional method.

Frequencies of several lasers have been stabilized by using saturated absorption spectra in atoms or molecules to develop new wavelength standards.[1–4] In these samples, the derivative signals of the saturated absorption spectra, i.e., the inverted Lamb dips, have been used as frequency discriminators. To obtain these signals, the laser frequencies have been modulated by applying a.c. voltage to piezoelectric transducers (PZTs).

In the present work, the frequency stabilization of a He–Xe laser at 3.51 μm is demonstrated by the Stark modulation technique. The derivative signal of the inverted Lamb dip in H_2CO ($5_{1,5}(v_5=0)$-$6_{0,6}(v_5=1)$) is obtained by applying an a.c. electric field (the Stark field) to H_2CO molecules. By using this signal, the laser frequency can be stabilized without any need for frequency modulation.

The experimental apparatus is shown in Fig. 1. A laser tube with a discharge part of 5.8 mm inner diameter and 750 cm length is used. The total pressure is 4.0 Torr and the pressure ratio of Xe to the total pressure is 0.025. The discharge current is 3.8 mA. Since the center frequency of the spectrum in H_2CO is about 200 MHz higher than the center frequency of the gain curve of a He–Xe laser, an axial d.c. magnetic field of 124 G is applied to the laser tube to compensate for this frequency gap. Under the axial magnetic field, the two oppositely circularly polarized Zeeman components (σ_+ and σ_-) oscillate.[5] The σ_+ mode is used in the present work because the center frequency of the gain curve of this mode coincides with the absorption line frequency of

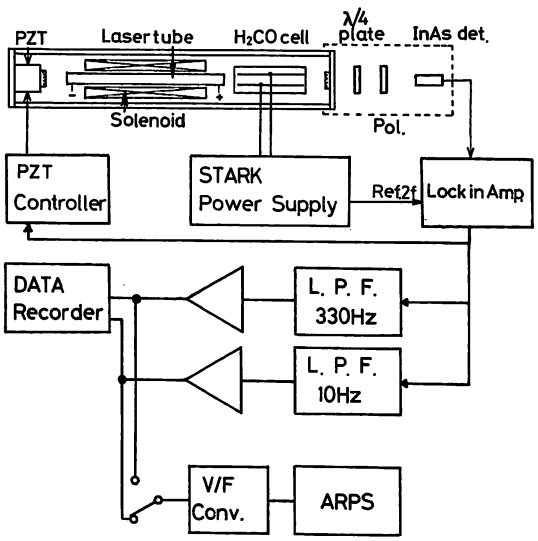

Fig. 1. Experimental apparatus: ARPS represents an Allan variance realtime processing system using a micro processor.[7]

H_2CO. A quarter-wave plate and polarizer are used to separate the σ_+ mode from the σ_- mode. One of the cavity mirrors is mounted on a PZT for frequency tuning. The absorption cell contains Stark electrodes of 10 mm separation and 26 cm length. The electrodes are made of 36 silver coated steel wires of 0.1 mm in diameter which are separated by 1 mm. An a.c voltage of up to 6 kV (peak-to-peak value) is applied to the electrodes for Stark modulation. The second harmonic signal of the applied electric field is used as the reference for the phase sensitive detection. This is because the absorption line shows the second order Stark effect, i.e., the frequency shift is proportional

to the square of the electric field.[6] Its Stark coefficient is $5.90_0 \times 10^2$ kHz/(kV/cm)^2.* The ARPS represents an Allan variance realtime processing system using a micro processor developed by the authors.[7]

The first derivative signals of the inverted Lamb dip are shown in Fig. 2. Figure 2(a) shows the signal obtained by using the conventional method of cavity modulation, i.e., by applying the a.c. voltage to the PZT. In this figure, the value of the maximum frequency deviation used is 770 kHz. Figure 2(b) shows the first derivative signal using the Stark modulation mentioned above. The a.c. electric field of 2.5 kVp-p/cm is applied and the modulation frequency is 3 kHz.

The linear part between the two peaks of this signal is used as a frequency discriminator to control the laser frequency. The control system consists of a lock-in amplifier and a PZT driver with an integrator, a proportional amplifier and a differentiator.[8] As the derivative signal using Stark modulation has a d.c. offset value, it is compensated by the lock-in amplifier.

Error signals from the lock-in amplifier are proportional to the fluctuations of the laser frequency, and are recorded and analyzed by means of the square root of the Allan variance[9] σ^2, which is the measure of frequency stability. The results are shown in Fig. 3, where τ and N represent the integration time and the number of data, respectively. The curves A and B show the results of stabilization using conventional cavity modulation and Stark modulation, respectively. It can be seen that the result obtained by using Stark modulation exhibits better stability than that obtained using cavity modulation for $\tau \geq 0.1$ s.

As mentioned above, it is necessary to compensate for the d.c. offset value for the stabilization required when the Stark modulation is employed. By using the sixth harmonic of the a.c. Stark field as the reference signal for the phase sensitive detection, the third derivative signal can be obtained for stabilization and the d.c. offset is eliminated. Curve C shows the result of laser stabilization using the third derivative signal. As the intensity of the third derivative signal is about one half that of the first derivative signal in the present work, the stability of the stabilized laser using the third derivative signal (curve C) is worse than that for the first derivative (curve B).

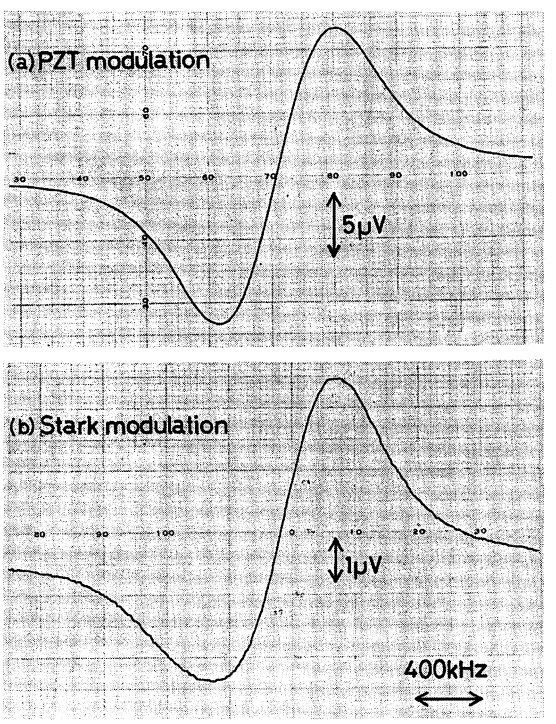

Fig. 2. The first derivative signal of the inverted Lamb dip in H_2CO, using PZT modulation (a), and Stark modulation (b).

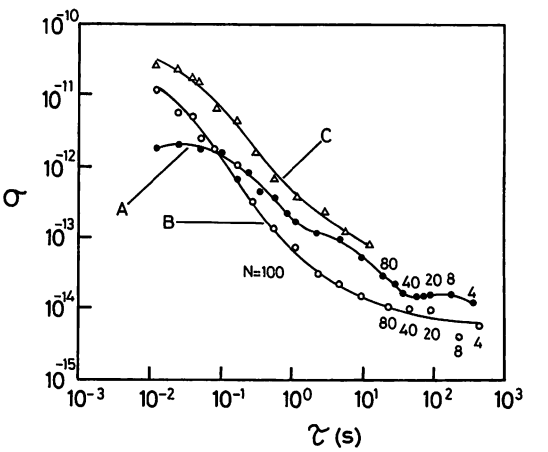

Fig. 3. The square root of the Allan variance σ^2 of the frequency fluctuations. N and τ represent the number of data and the integration time, respectively: Curves A, B and C represent results of stabilization using cavity modulation, Stark modulation (first derivative signal) and Stark modulation (third derivative signal), respectively.

*K. Uehara: Dr. Thesis, Faculty of Science, University of Tokyo, Hongo, Tokyo, 1968.

On the three curves in this figure, the minimum values are,

curve A; $\sigma = 1.7 \times 10^{-14}$ at $\tau = 40$ s,

curve B; $\sigma = 1.2 \times 10^{-14}$ at $\tau = 25$ s,

curve C; $\sigma = 8.3 \times 10^{-14}$ at $\tau = 12$ s.

By comparing these results, it can be said that the frequency stability obtained by using Stark modulation is as high as that using conventional cavity modulation. This stabilized laser is considered to be almost free from frequency modulation, apart from some slight modulation owing to the dispersion effect in H_2CO. An evaluation of the dispersion effect can be obtained from a measurement of the beat frequency between two stabilized lasers.

This work is partially supported by a Grant-in-Aid for Scientific Research from the Ministry of Education, Science and Culture. The authors wish to thank Professor K. Uehara of Keio University for his valuable discussions.

References

1) R. L. Barger and J. L. Hall: Phys. Rev. Lett. **22** (1969) 4.
2) G. R. Hanes and K. M. Baird: Metrologia **5** (1969) 32.
3) F. R. Peterson, D. C. McDonald, J. D. Cupp and B. L. Danielson: Phys. Rev. Lett. **31** (1973) 573.
4) M. Ohtsu and T. Tako: Jpn. J. Appl. Phys. **17** (1978) 2169.
5) M. Ohtsu and T. Tako: Jpn. Appl. Phys. **17** (1978) 177.
6) K. Sakurai, K. Uehara, M. Takami and K. Shimoda: J. Phys. Soc. Jpn. **23** (1967) 103.
7) I. Shiio, M. Ohtsu and T. Tako: Trans. Inst. Electron. & Commun. Eng. (1981) 204 [in Japanese].
8) M. Ohtsu, S. Katsuragi and T. Tako: to be published in IEEE J. Quantum Electron. **QE-17** (1981).
9) D. W. Allan: Proc. IEEE **54** (1966) 2.

JAPANESE JOURNAL OF APPLIED PHYSICS
VOL. 20, NO. 6, JUNE, 1981 pp. L403–L406

Frequency Stabilization of AlGaAs DH Lasers

Hidemi TSUCHIDA, Motoichi OHTSU and Toshiharu TAKO

Research Laboratory of Precision Machinery and Electronics,
Tokyo Institute of Technology,
4259 Nagatsuta-cho, Midori-ku, Yokohama, Kanagawa 227

(Received March 28, 1981; accepted for publication May 12, 1981)

The frequency of AlGaAs DH lasers was stabilized at the resonant frequency of a Fabry-Perot interferometer by controlling the injection current. The interferometer was controlled by a Lamb dip stabilized He–Ne laser at 633 nm. The frequency stability obtained here was $2.0\times10^{-11}\leqq\sigma\leqq2.1\times10^{-9}$ for $10\text{ ms}\leqq\tau\leqq500\text{ s}$, where σ and τ represent the square root of the Allan variance and the integration time, respectively.

§1. Introduction

The frequency stabilization of semiconductor lasers is very important for a number of applications, such as heterodyne-type optical communication, high resolution spectroscopy, precise metrology and so on. Several results for the frequency stabilization of semiconductor lasers have been reported by using a Fabry-Perot interferometer as a frequency reference.[1–5] In this method, the resulting frequency stability depends not only on the frequency traceability of the laser to the interferometer but also on the stability of the interferometer. Therefore, it is necessary to improve both to obtain higher frequency stability.

In the previous work,[5] the long-term frequency stability ($\tau>10$ s) of AlGaAs double heterostructure (DH) lasers was improved by controlling the temperature. In this case, however, the frequency stability was limited mainly by the slow response of the feedback loop and by the stability of the interferometer.

In this paper, the authors report experimental results for improving the frequency stability of single mode AlGaAs DH lasers by using a Fabry-Perot interferometer. First, the injection current is controlled to improve the frequency traceability, which is shown in §2. Then the frequency stabilization is carried out and is described in §3. For this experiment, the interferometer is stabilized by using a Lamb dip stabilized He–Ne laser at 633 nm and the method shown in §2 is employed. This method was used for the frequency stabilization of dye lasers by Barger *et al.*[6]

§2. Improvement of the Frequency Traceability of DH Lasers

The frequency of single mode AlGaAs DH lasers[7] was locked at the resonant frequency of a Fabry-Perot interferometer. The experimental apparatus used was almost the same as in the previous work,[5] except that the injection current was controlled instead of the temperature. The laser frequency has a fast response to the injection current. The experiments were carried out in an underground tunnel for long-distance interferometry. As the temperature in the tunnel was constant within 0.1°C/day, no special methods were employed for controlling the temperature of the DH laser. The interferometer had two Al-coated flat mirrors with a reflectivity of 85% whose distance was kept at 12.3 cm by using an Invar tube and a piezoelectric transducer (PZT) as a spacer. The laser beam was focused on a photomultiplier after passing through the interferometer whose length was piezoelectrically modulated at a frequency of 1 kHz. The first derivative signal of the transmission spectrum of the interferometer was obtained by synchronously detecting the output signal of the photomultiplier with a lock-in amplifier and was used as a frequency discriminator. The output signal from the lock-in amplifier was fed to the current source for the DH laser. The dependence of the laser frequency on the injection current was measured by using the interferometer at -2.75 GHz/mA. The servo-controller for the DH laser is shown schematically in Fig. 1, which consists of an integrator, a low pass

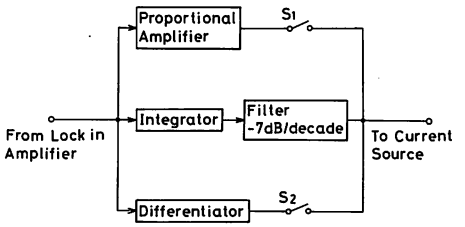

Fig. 1. Block diagram of the servo-controller for the DH laser.

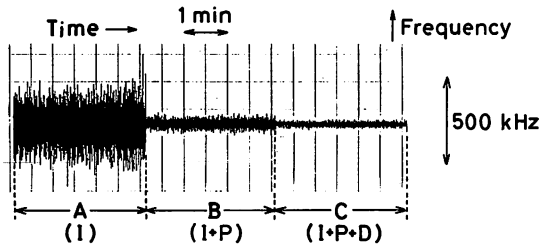

Fig. 2. Error signals from the lock-in amplifier.
A: The result obtained by using the integrator and the low pass filter in Fig. 1 (I).
B: The result obtained by turning on switch 1 in Fig. 1 (I+P).
C: The result obtained by turning on switches 1 and 2 in Fig. 1 (I+P+D).

filter (−7 dB/decade), a proportional amplifier and a differentiator.

Error signals from the lock-in amplifier are shown in Fig. 2. Part A represents the result obtained by using the integrator and the low pass fiiter in Fig. 1(I). It can be seen that the laser frequency follows the resonant frequency of the interferometer with residual fluctuations of 500 kHz. Part B represents the result obtained by turning on switch 1 in Fig. 1 (I+P). Part C represents the result obtained by turning on switches 1 and 2 in Fig. 1 (I+P+D). In part C, the residual fluctuations are reduced to 50 kHz, which are about a hundred times smaller than the results in the previous work.[5]

The square root of the Allan variance[8] σ^2, which represents the frequency traceability of the DH laser to the interferometer, is shown in Fig. 3. In this figure, τ and N represent the integration time and the number of data, respectively. Measurements were carried out for $10\ \text{ms} \leqq \tau \leqq 500\ \text{s}$ in this work. Curves A, B and C correspond to parts A, B and C in Fig. 2, respectively. On every curve, σ is nearly proportional to τ^{-1} for $10\ \text{ms} \leqq \tau \leqq 500\ \text{s}$ and the minimum value of σ on each curve is

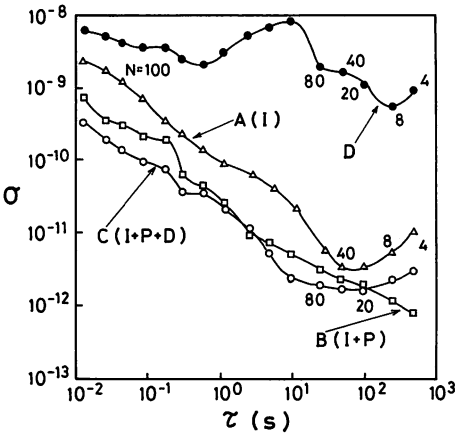

Fig. 3. The square root of the Allan variance σ^2 which represents the frequency traceability of the DH laser to the interferometer, where τ and N represent the integration time and the number of data, respectively. Curves A (△), B (□) and C (○) correspond to parts A, B and C in Fig. 2, respectively. Curve D (●) represents the result in the previous work (The curve D in Fig. 3 of ref. 5).

$$A:\ \sigma = 3.4 \times 10^{-12} \quad \text{at } \tau = 50\ \text{s}, \tag{1}$$

$$B:\ \sigma = 8.0 \times 10^{-13} \quad \text{at } \tau = 500\ \text{s}, \tag{2}$$

$$C:\ \sigma = 1.8 \times 10^{-12} \quad \text{at } \tau = 100\ \text{s}. \tag{3}$$

It can be seen from this figure that the value of σ on curve C is about ten times smaller than that on curve A. This fact shows that it is effective to use the proportional amplifier and the differentiator to improve the traceability for a wide range of τ. Curve D in Fig. 3 represents the result in the previous work (curve D in Fig. 3 of ref. 5). It can be seen that the value of σ on curve C is more than a hundred times smaller than that on curve D, which shows that it is better to control the injection current than the temperature. The results obtained in this chapter indicate the feasibility of stabilizing the frequency of DH lasers to the order of 10^{-12} by using a very stable frequency reference.

§3. Frequency Stabilization Using a Stabilized Interferometer

To make the Fabry-Perot interferometer a more stable frequency reference, the resonant frequency of this interferometer was stabilized by using a frequency stabilized He–Ne laser at 633 nm. The experimental apparatus is shown in Fig. 4. The frequency of the He–Ne laser was locked at the center of the Lamb dip in Ne.

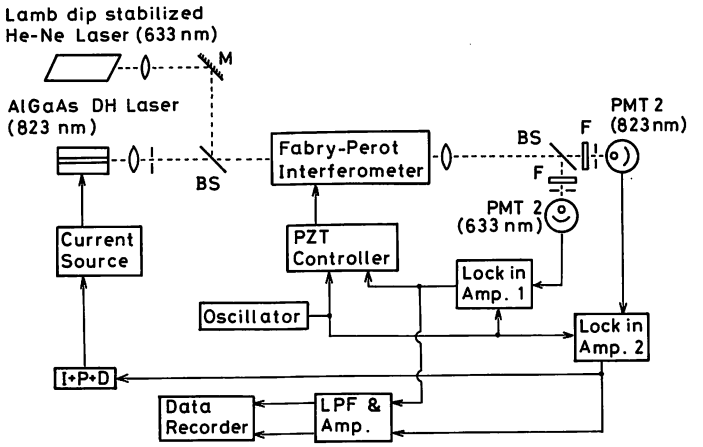

Fig. 4. The experimental apparatus for the frequency stabilization of DH lasers.

The servo-controller for the He–Ne laser consisted of an integrator and a low pass filter (−7 dB/decade). The interference fringe of the He–Ne laser was measured by adjusting the DC voltage applied to the PZT and the error signal from a lock-in amplifier 1 was fed to the PZT to control the length of the interferometer. The servo-controller for the interferometer consisted of an integrator. The interference fringe of the DH laser was measured by adjusting the injection current, then the frequency of the DH laser was stabilized to this stabilized interferometer by the same method as in §2.

The square root of the Allan variance σ^2 is shown in Fig. 5. Curve A represents the frequency stability of the He–Ne laser σ_{Ne} estimated by using the error signal for the frequency stabilization. Curves B and C in Fig. 5 represent the frequency traceability of the interferometer to the He–Ne laser σ_{FP} and the frequency traceability of the DH laser to the interferometer σ'_{DH}, respectively. The value of σ on curve C is about three times larger than that on curve C in Fig. 3. The reason for this can be considered as follows: In Fig. 4, the light intensity of the DH laser detected by the photomultiplier 2 was reduced to about 1/10 after passing through two beam splitters, which caused a reduction in the signal-to-noise ratio of the first derivative signal used for frequency stabilization. The frequency stability of the stabilized DH laser σ_{DH} can be estimated by using the following relation:[8]

$$\sigma_{DH} \cong (\sigma_{Ne}^2 + \sigma_{FP}^2 + \sigma_{DH}'^2)^{1/2}. \quad (4)$$

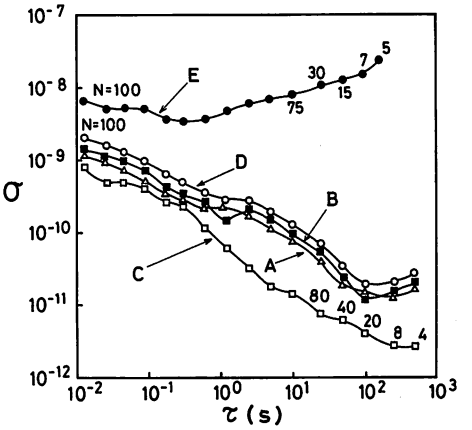

Fig. 5. The square root of the Allan variance σ^2, where τ and N represent the integration time and the number of data, respectively.
A(△): The frequency stability of the Lamb dip stabilized Ne–Ne laser at 633 nm.
B(■): The frequency traceability of the Fabry-Perot interferometer to the He–Ne laser.
C(□): The frequency traceability of the DH laser to the interferometer.
D(○): The frequency stability of the stabilized DH laser estimated by using eq. (4), curves A, B and C.
E(●): The frequency stability of the free-running DH laser.[5]

Curve D in Fig. 5 represents the frequency stability σ_{DH} estimated by using eq. (4), curves A, B and C. The value of σ on curve D is nearly proportional to $\tau^{-1/2}$. The minimum value on this curve is

$$\sigma = 2.0 \times 10^{-11} \quad \text{at} \quad \tau = 100\,\text{s}, \quad (5)$$

and the stability is better than 2.1×10^{-9}. Curve E in Fig. 6 represents the frequency

stability of the free-running DH laser obtained in the previous work.[5] The value of σ on curve E increases with increasing τ for $\tau > 0.3$ s, which is mainly due to the temperature change in the active region. Comparing curves D and E, it can be seen that the frequency stability of the DH laser was improved by about one order of magnitude for $\tau < 0.1$ s and more than two orders of magnitude for $\tau > 10$ s. It also can be seen from this figure that the method used in this chapter is effective for improving the frequency stability, especially the long-term stability, and that the frequency stability is limited mainly by the frequency stability of the He–Ne laser. Higher stability can be expected by using a stabilized laser by saturated absorption of molecules, such as CH_4-stabilized He–Ne laser at 3.39 μm.[6]

§4. Conclusion

In the present experiments, the frequency of AlGaAs DH lasers was stabilized at the resonant frequency of a Fabry-Perot interferometer which was controlled by a Lamb dip stabilized He–Ne laser at 633 nm. By controlling the injection current, the frequency traceability of the DH laser to the interferometer was improved considerably compared to results in the previous work.[5] The following stability was obtained for the DH laser frequency:

$$2.0 \times 10^{-11} \leqq \sigma \leqq 2.1 \times 10^{-9} \quad \text{for } 10\ \text{ms} \leqq \tau \leqq 500\ \text{s}. \tag{6}$$

Acknowledgements

The authors would like to express their thanks to Drs. M. Nakamura and K. Aiki of Hitachi, Ltd. for their support in the experiments and to Associate Prof. K. Iga of the Tokyo Institute of Technology for his valuable discussions.

This work was partially supported by a Grant-in-Aid for Scientific Research from the Ministry of Education, Science and Culture.

References

1) Yu. A. Bykovskii, V. L. Velichanskii, I. G. Goncharov and V. A. Masrov: Sov. Phys.-Semicond. **4** (1970) 580.
2) J. L. Picque and S. Roizen: Appl. Phys. Lett. **27** (1975) 340.
3) T. Okoshi and K. Kikuchi: Electron. Lett. **16** (1980) 179.
4) F. Favre and D. Le Guen: Electron. Lett. **16** (1980) 709.
5) H. Tsuchida, S. Sanpei, M. Ohtsu and T. Tako: Jpn. J. Appl. Phys. **19** (1980) L721.
6) R. L. Barger, J. B. West and T. C. English: Appl. Phys. Lett. **27** (1975) 31.
7) K. Aiki, M. Nakamura, T. Kuroda, J. Umeda, R. Ito, N. Chinone and M. Maeda: IEEE J. Quantum Electron. **QE-14** (1978) 89.
8) D. W. Allan: Proc. IEEE **54** (1966) 221.

Performances of a Frequency Offset Locked He–Xe Laser System at 3.51 μm

MOTOICHI OHTSU, SEIICHI KATSURAGI, AND TOSHIHARU TAKO

Abstract—A highly stabilized frequency offset locked He–Xe laser system was constructed for high resolution laser spectroscopy of H_2CO $[5_{1,5}(v=0) \rightarrow 6_{0,6}(v_5=1)]$ at 3.51 μm. It is composed of three He–Xe lasers. The first laser is H_2CO-stabilized and is used as a frequency reference in the system. The second laser is frequency offset locked to the first laser by using the beat frequency between these lasers, and is used as a local oscillator. The third laser is frequency offset locked to the second laser, and is used to observe the H_2CO spectrum by slowly varying the beat frequency between these lasers. The frequency stability of the first laser, measured against a similarly stabilized and synchronously modulated laser, was 1.0×10^{-14} at $\tau = 100$ s, where τ represents the integration time. The frequency traceability of the second laser to the first laser was expressed as $8.0 \times 10^{-13} \cdot \tau^{-1}$ for 10 ms $\leqq \tau \leqq$ 100 s. It was found that this value of the traceability was independent of the frequency modulation of the first and second lasers. The frequency traceability of the third laser to the second laser was nearly equal to that of the second laser described previously. The variable range of the frequency of the third laser was 19 MHz. In this range, the frequency traceability of the third laser to the second laser was independent of the beat frequency between these two lasers. From these results, it was concluded that this system can be used for the observation of the H_2CO spectrum.

Manuscript received June 16, 1980; revised December 1, 1980. This work was supported in part by a Grant-in-Aid for Scientific Research from the Ministry of Education, Science, and Culture, Japan.

M. Ohtsu and T. Tako are with the Research Laboratory of Precision Machinery and Electronics, Tokyo Institute of Technology, 4259 Nagatsuta-cho, Midori-ku, Yokohama 227, Japan.

S. Katsuragi was with the Research Laboratory of Precision Machinery and Electronics, Tokyo Institute of Technology, 4259 Nagatsuta-cho, Midori-ku, Yokohama 227, Japan. He is now with the Toshiba Corporation, Kanagawa, Japan.

I. INTRODUCTION

SEVERAL experimental methods in high resolution laser spectroscopy have recently been developed. For some experiments, it is necessary that the laser frequency must be varied while a high frequency stability is maintained. As an example of such a method, a frequency offset locked He–Ne laser system at 3.39 μm has been constructed using a CH_4-stabilized He–Ne laser. The system was used for ultrahigh resolution laser spectroscopy of CH_4 with a resolution of about 1×10^{-10} [1]. It can be seen from this example that frequency offset locking is an effective technique for constructing a light source for high resolution laser spectroscopy.

0018-9197/81/0600-1100$00.75

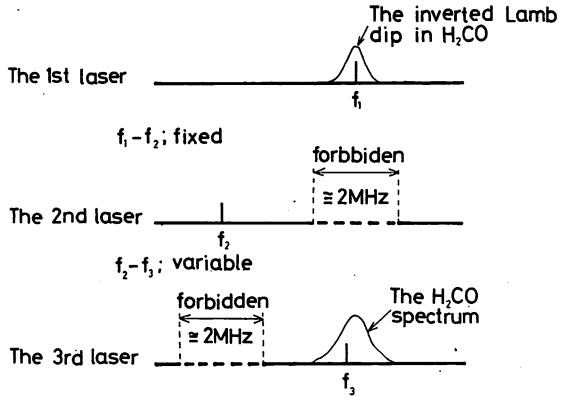

Fig. 1. Relation between frequencies of the three lasers of the frequency offset locked He-Xe laser system. The frequency f_1 of the first laser is locked at the center frequency of the inverted Lamb dip in H_2CO. The frequency f_2 of the second laser is frequency offset locked to f_1. The beat frequency $f_1 - f_2$ is fixed at a constant value. The frequency f_3 of the third laser is frequency offset locked to f_2 in the same way as for f_2. The beat frequency $f_2 - f_3$ is swept and the H_2CO spectrum is measured by the third laser. To reduce disturbance of the stable oscillation caused by the injection from one laser to the other, $|f_1 - f_2|$ and $|f_2 - f_3|$ should be kept larger than about 1 MHz.

The authors have carried out some experiments on frequency stabilization of an He-Xe laser at 3.51 μm by using the inverted Lamb dip in H_2CO $[5_{1,5}(v=0) \rightarrow 6_{0,6}(v_5=1)]$ [2], [3]. Furthermore, a frequency offset locked He-Xe laser system has been prepared using an H_2CO-stabilized He-Xe laser as a reference for high resolution laser spectroscopy of H_2CO $[5_{1,5}(v=0) \rightarrow 6_{0,6}(v_5=1)]$ [4].

In this paper, the performance of this system is reported.

II. Experimental Apparatus

The frequency offset locked He-Xe laser system is composed of three lasers, i.e., an H_2CO-stabilized He-Xe laser and two frequency offset locked lasers. Fig. 1 shows the relation between the frequencies of these lasers. The first laser is H_2CO-stabilized and its frequency f_1 is locked at the center frequency of the inverted Lamp dip in H_2CO. This laser is used as a frequency reference in the system. The second laser is used as a local oscillator whose frequency f_2 is controlled so that the beat frequency $f_1 - f_2$ is maintained constant at a few megahertz. This technique is called frequency offset locking. The third laser is used to observe the Doppler-free spectrum (saturated absorption, molecular beam absorption, etc.) in H_2CO whose width is less than a few megahertz. This laser is frequency offset locked to the second laser by the same method as used for the second laser. In this case, however, the beat frequency $f_2 - f_3$ is slowly varied while the high frequency stability of $f_2 - f_3$ is maintained. Since f_3 can be stably varied over more than about 10 MHz around the center frequency of the H_2CO spectrum by this method, the spectral profile of H_2CO can be measured with high resolution.

The frequency f_2 of the second laser can also be varied while it is frequency offset locked to f_1. However, $|f_1 - f_2|$ must be higher than about 1 MHz. If not, the frequency of one laser will be disturbed by the other by such phenomena as the injection locking which occurs because of the reflection of the laser

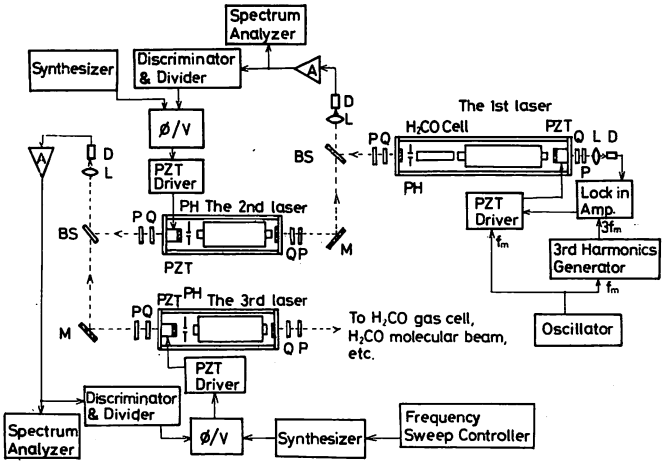

Fig. 2. Experimental apparatus. ϕ/V: phase-to-voltage converter. *A*: wide-band amplifier. *BS*: beam splitter. *D*: InAs detector. *L*: lens. *M*: mirror. *P*: polarizer. *PH*: pinhole. *Q*: quarter-wave plate.

beams on the plane, such as the detector window. Since this condition must be satisfied, the frequency f_2 cannot be varied through the center frequency of the H_2CO spectrum which is equal to f_1. Therefore, the second laser cannot be used to observe the H_2CO spectrum even though f_2 can be varied. For this reason, the third laser is required. Although the value of $|f_2 - f_3|$ must also satisfy the same condition as above, f_3 can be varied through the center frequency of the H_2CO spectrum, as shown in Fig. 1, if the value of $|f_1 - f_2|$ satisfies the previously mentioned condition.

Fig. 2 shows the experimental apparatus of the frequency offset locked laser system, which is composed of three lasers. These lasers and optical elements were placed on an optical bench with air dampers. Each laser was placed in an aluminum case with glass wool to reduce the acoustic vibration.

It has been rather difficult to get a stable oscillation in the He-Xe laser for the following two reasons. The first is the separation between the He and Xe gases when they are excited by a dc discharge. The second is that the Xe pressure decreases with time by the clean-up effect and, as a result, the discharge current decreases when a regulated voltage power supply is used for the discharge. To avoid these phenomena, a radio frequency discharge and an Xe gas reservoir have been used [5], [6]. In the present work, on the other hand, a solenoidal return path was used to avoid the separation of the gases, and the discharge current was stabilized by using a Ti-cold cathode [7]. Fig. 3 shows the laser tube used.

Since the absorption line frequency of H_2CO is about 200 MHz higher than the center frequency of the gain curve of the He-Xe laser, an axial dc magnetic field of 129.8 G was applied to the laser tube to compensate for this frequency gap. In this case, two opposite circularly polarized Zeeman components (the σ_+ and σ_- modes) oscillated because the laser windows were fixed perpendicular to the optical axis. As the center frequency of the gain curve of the σ_+ mode coincided with the absorption line frequency of H_2CO, this mode was used for the present work. The center frequency of the gain curve of the σ_- mode was about 400 MHz lower than that of the σ_+ mode. A quarter-wave plate and a polarizer were used to separate the σ_+ mode from the σ_- mode. One of the cavity

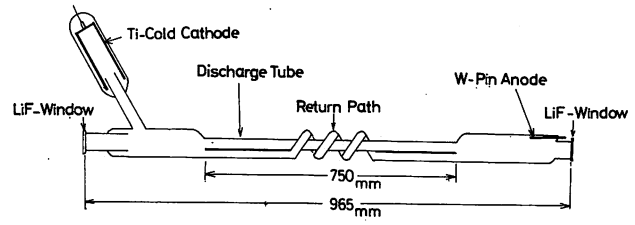

Fig. 3. The laser tube used for the first laser. The inner diameters of discharge tube and the return path are 5.8 mm. The length of those tubes are 750 and 852 mm, respectively. The lengths and inner diameters of the discharge tubes used for the second and third lasers are 505 and 5.8 mm, respectively. Those of the return paths are 607 and 5.8 mm, respectively.

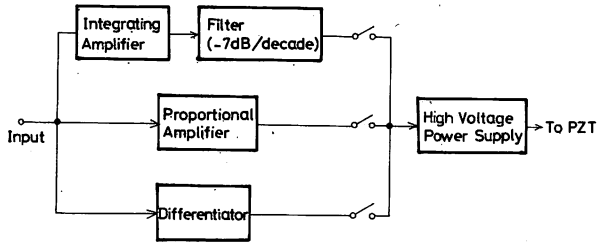

Fig. 4. Block diagram of the PZT driver used for the three lasers.

mirrors of each laser was mounted on a piezoelectric transducer (PZT, Burleigh PZ-80) for frequency tuning and modulation.

The control system for the frequency of the first laser was composed of an InAs detector, a lock-in amplifier, and a PZT driver. The block diagram of the PZT driver is shown in Fig. 4. A proportional amplifier, a differentiator, an integrating amplifier, and a filter (-7 dB/decade) were connected in parallel in the PZT driver. The filter was used to improve long-term frequency stability[1] because the voltage gain of the PZT driver in the low frequency range increased when this filter was connected in series with the integrating amplifier [3].

The control system for the frequency offset locking of the second laser was composed of an InAs detector, a wide-band amplifier, a discriminator and divider, a phase-to-voltage (ϕ/V) converter, a digital frequency synthesizer, and a PZT driver. The PZT driver used here was the same as that for the first laser. The beat signal between the first and second lasers detected by the InAs detector was converted into a TTL compatible signal by the discriminator after amplification by the wide-band amplifier. The phase of the beat signal was then compared with that of the signal from the digital frequency synthesizer by the ϕ/V converter after the beat frequency was divided by the divider ($\frac{1}{10}$ or $\frac{1}{20}$). The output of the ϕ/V converter was applied to the PZT driver, and the frequency f_2 of the second laser was controlled so that the frequency $f_1 - f_2$ was locked at the frequency of the digital frequency synthesizer. In this way, the frequency f_2 of the second laser was frequency offset locked to the frequency f_1 of the first laser. The control system for the frequency offset locking of the third laser was the same as that for the second laser.

Since the output frequencies of the digital frequency synthesizers for the second and third lasers were programmable, the frequencies of these lasers could be slowly swept while they were frequency offset locked. However, the synthesizer frequency for the second laser is fixed at a constant value as shown in Fig. 1 when this system is used for high resolution laser spectroscopy of H_2CO. The synthesizer frequency for the third laser is, on the other hand, automatically swept by using a frequency sweep controller.

[1]In the present paper, this term is used to represent frequency stability for $\tau \geqq 1$ s, where τ represents the integration time.

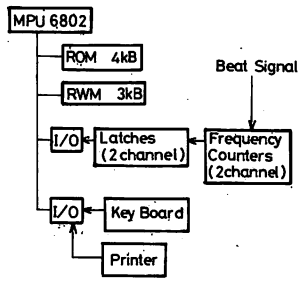

Fig. 5. Block diagram of the Allan variance real-time processor (ARP).

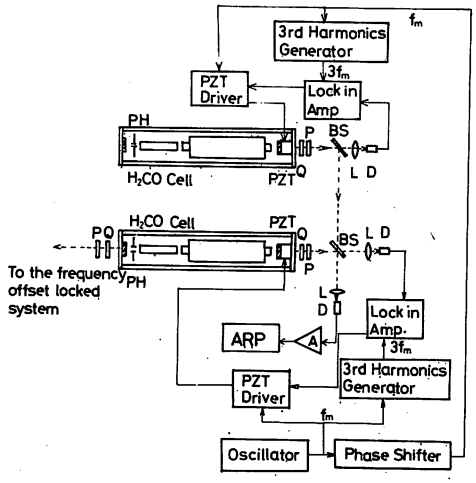

Fig. 6. Experimental apparatus used to measure the frequency stability of the first laser.

The frequency stabilities of the three lasers are represented by the square root of the Allan variance σ^2 [8]. The value of σ for the three lasers were measured by the Allan variance real-time processors (the ARP) developed by the authors [9]. The block diagram of the ARP is shown in Fig. 5. Since the frequency stability is estimated from the beat frequency between the two lasers [10], the first stage of the ARP is composed of a frequency counter. The value of the counted frequency is processed by a microprocessor 6802, and the calculated value of σ is recorded on a printer. As we have developed the frequency counter with zero dead time at the gate, we are able to measure the value of σ over a wide range of the integration time τ (1 ms $\leqq \tau \leqq 3 \times 10^3$ s).

To measure the frequency stability of the first laser, a conventional method was used, as was employed by Hellwig *et al.* [10]. That is, another similar H_2CO-stabilized He-Xe laser was constructed and frequency fluctuations of the best signal between these two lasers were measured by the ARP. The experimental apparatus is shown in Fig. 6. The beat frequency was fixed at 5.0 MHz by placing a small dc bias at the input of

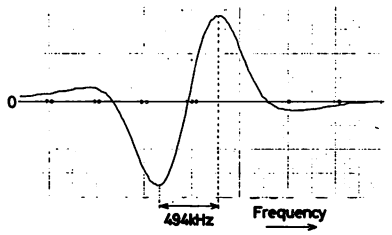

Fig. 7. The third derivative signal of the inverted Lamb dip in H_2CO.

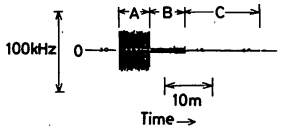

Fig. 8. Time dependence of the frequency fluctuations of the first laser. Curve *A*: the result obtained by using the integrating amplifier and the filter in the PZT driver in Fig. 4. Curve *B*: the result obtained by using the proportional amplifier, the integrating amplifier, and the filter. Curve *C*: the result obtained by using the differentiator, the proportional amplifier, the integrating amplifier, and the filter.

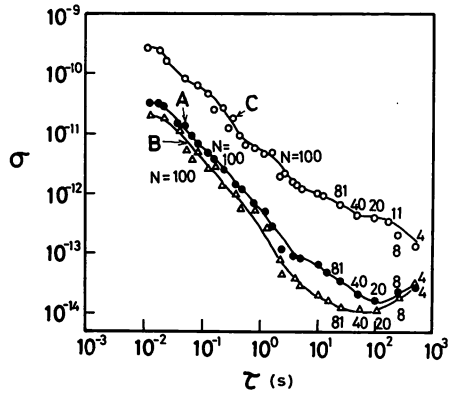

Fig. 9. Square root of the Allan variance σ^2 of the frequency fluctuations of the first laser, measured against a similarly stabilized and synchronously modulated laser. τ and N represent the integration time and the number of data, respectively. Curve *A*: the result obtained by using the proportional amplifier with the integrating amplifier and the filter in the PZT driver. Curve *B*: the result obtained by using the differentiator with the proportional amplifier, the integrating amplifier, and the filter. Curve *C*: the result from a previous work [3].

the integrating amplifier of the PZT driver. In this figure, the InAs detector and wide-band amplifier are the same kinds as those in Fig. 2, with bandwidths of about 30 MHz. Using a phase shifter, the frequency of one laser was modulated synchronously with that of the other so that the beat frequency was not modulated. By this synchronous modulation, the fluctuations due to the frequency modulation, i.e., artificially forced fluctuations for stabilization, were removed from the stability measurement.

The square root of the Allan variance of the frequency fluctuations between the first and second lasers was measured by the ARP. It can be interpreted as representing the frequency traceability of the second laser to the first laser. At the same time, the frequency traceability of the third laser to the second laser was also measured by using the beat signal between these lasers. In the next section, these results are shown, and the frequency stabilities of the second and third lasers are approximately estimated by using the results of the frequency traceabilities.

III. Experimental Results and Discussions

A. Frequency Stabilization of the First Laser

Fig. 7 shows the third derivative signal of the inverted Lamb dip in H_2CO used for the frequency stabilization. The laser frequency was modulated by applying the ac voltage of 3 V (peak-to-peak value, which corresponds to the maximum frequency deviation of 1.15 MHz) to the PZT to obtain this derivative signal. The modulation frequency f_m, i.e., the frequency of the ac voltage, was 500 Hz. The signal-to-noise ratio of this signal was larger than that of the first derivative signal used in the previous work [3, Fig. 2]. The improvement was attained by carefully choosing the values of the total gas pressure P_T and the discharge current i_d of the laser tube to get a stable discharge. The values of P_T, k, and i_d used in the present work were 4.0 torr, 0.025, and 3.5 mA, respectively, where k represents the pressure ratio of Xe to P_T. Fig. 8 shows the time dependence of the frequency fluctuations of the first laser when its frequency was locked at the center frequency of the derivative signal of Fig. 7. Part *A* in this figure represents the result obtained by using the PZT driver with the integrating amplifier and the filter of Fig. 4. Part *B* represents the result when the proportional amplifier was used with the integrating amplifier and the filter in the PZT driver. Part *C* represents the result when the differentiator was used with them. It can be seen that the frequency fluctuation of part *B* is lower than that of part *A*, and that of part *C* is still lower than that of part *B*. This is because the bandwidth of the voltage gain of the PZT driver was expanded. The bandwidth was about 100 Hz when the proportional amplifier was used with the integrating amplifier and the filter. When the differentiator was also used with them, it was about 1 kHz. Fig. 9 shows the frequency stability of the first laser measured by the ARP using the setup of Fig. 6. Curve *A* in this figure represents the result obtained by using the proportional amplifier with the integrating amplifier and the filter in the PZT driver. Curve *B* was obtained when the differentiator was also used with them. Curve *C* represents the result in the previous work [3]. It can be seen from this figure that a higher stability was obtained when the differentiator was also used, as was seen in Fig. 8. The minimum values of σ on these curves are as follows:

$$\begin{aligned} &\text{curve } A: \quad \sigma = 1.6 \times 10^{-14} \quad \text{at} \quad \tau = 100\ \text{s} \\ &\text{curve } B: \quad \sigma = 1.0 \times 10^{-14} \quad \text{at} \quad \tau = 100\ \text{s}. \end{aligned} \tag{1}$$

Fig. 10 represents the power spectral densities S of the frequency fluctuations. The results represented by curves *A* and *B* correspond to those by curves *A* and *B* in Fig. 9, respectively. The value of S on curve *B* is smaller than that on curve *A* except around $f = 50$ Hz, which is the frequency of the power supply. From this figure, it can be also said that a higher stability was obtained on curve *B* than on curve *A*. Therefore, the method of frequency control used to obtain curve *B* in Figs. 9 and 10 was used for the first laser in the following

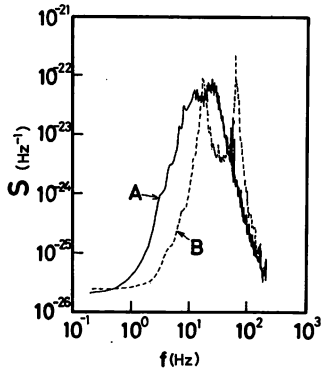

Fig. 10. Power spectral density S of the frequency fluctuations of the first laser. Curves A and B represent results corresponding to those of curves A and B in Fig. 9, respectively.

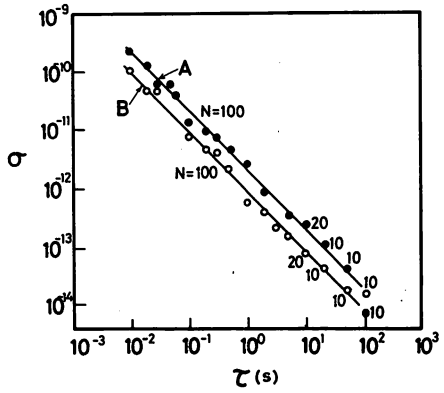

Fig. 11. Frequency traceability of the second laser in terms of the square root of the Allan variance σ^2 of the frequency fluctuations of the beat signal between the first and second lasers. The second laser was frequency offset locked to the first laser. The value of σ is normalized to the He-Xe laser frequency at 3.51 μm. Curve A: the result obtained by using the proportional amplifier with the integrating amplifier and the filter in the PZT driver. Curve B: the result obtained by using the differentiator with the proportional amplifier, the integrating amplifier, and the filter.

experiments. It was seen from a comparison between curves A or B and curve C in Fig. 9 that long-term stability was improved. Improvements in short-term stability will also be expected by expanding the bandwidth of the voltage gain of the PZT driver and by using a fast PZT.

B. Frequency Traceability of the Second Laser

Fig. 11 shows the experimental results of the frequency fluctuations of the beat signal between the first and second lasers measured by the ARP when the second laser was frequency offset locked and the frequency of the first laser was stabilized. Here, the beat frequency $f_1 - f_2$ was locked at 4.0 MHz. In this figure, the value of σ represents the fluctuations of the beat frequency normalized to the frequency of the He-Xe laser at 3.51 μm. These results can be interpreted as representing the traceability of the frequency of the second laser to that of the first laser. Therefore, the frequency stability of the second laser can be approximately expressed as the square root of the sum of σ^2 on the curves of Figs. 9 and 11 at each value of τ. Curve A represents the result when the proportional amplifier was used with the integrating amplifier and the filter in the PZT driver. Curve B represents the results when the differentiator was also used with them. It can be seen that a higher stability was obtained on curve B than on

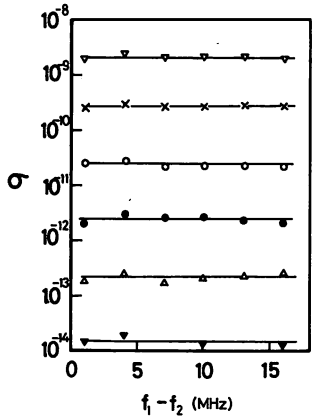

Fig. 12. Relation between the value of σ and the value of the beat frequency $f_1 - f_2$ between the first and second laser, where σ represents the same quantity as that shown in Fig. 11. The same PZT driver was used as for curve B in Fig. 11. ▽: $\tau = 1$ ms, $N = 100$; ×: $\tau = 10$ ms, $N = 100$; ○: $\tau = 100$ ms, $N = 100$; ●: $\tau = 1$ s, $N = 100$; △: $\tau = 10$ s, $N = 20$; ▼: $\tau = 100$ s, $N = 10$.

curve A, as in Figs. 9 and 10. The values of σ on both curves are proportional to τ^{-1} and are expressed as

$$\text{curve } A: \quad \sigma = 2.0 \times 10^{-12} \cdot \tau^{-1} \quad (10\text{ ms} \leqq \tau \leqq 100\text{ s})$$
$$\text{curve } B: \quad \sigma = 8.0 \times 10^{-13} \cdot \tau^{-1} \quad (10\text{ ms} \leqq \tau \leqq 100\text{ s}). \qquad (2)$$

It can be said that the frequency stability of the second laser is $\sigma < 1.0 \times 10^{-13}$ at $\tau = 100$ s, which was roughly estimated by the square root of the sum of σ^2 on curves B in Figs. 9 and 11. In the following experiments, the differentiator was used with the proportional amplifier, the integrating amplifier, and the filter in the PZT driver for the second laser.

Fig. 12 shows the relation between the value of σ of the beat frequency $f_1 - f_2$ and the value of $f_1 - f_2$. It can be seen from this figure that the value of σ was independent of the value of $f_1 - f_2$ for 1 MHz $\leqq f_1 - f_2 \leqq$ 16 MHz. Furthermore, it became clear from subsequent experiments that this independence held for 1 MHz $\leqq f_1 - f_2 \leqq$ 20 MHz. Therefore, the results in Fig. 11 hold within this range of $f_1 - f_2$.

In the experiments with the results shown in Figs. 11 and 12, the frequency of the first laser was modulated but that of the second laser was not. Consequently, the beat frequency $f_1 - f_2$ was modulated. Fig. 13 shows the experimental results of the effect of frequency modulation on the stability of the beat frequency $f_1 - f_2$. White circles in this figure represent the result in which only the frequency of the first laser was modulated. This is the result of the same experiment shown by curve B in Fig. 11. Black circles, on the other hand, represent the result in which the frequency of the second laser was modulated synchronously with that of the first laser. Therefore, the beat frequency was not modulated because of this synchronous modulation. It can be said that the stability of the beat frequency is independent of the frequency modulation for 1 ms $\leqq \tau \leqq$ 100 s because no difference is clearly seen between the two experimental results in this figure.

C. Frequency Traceability and Tunability of the Third Laser

In these experiments, the frequency of the first laser was stabilized and the second laser was frequency offset locked

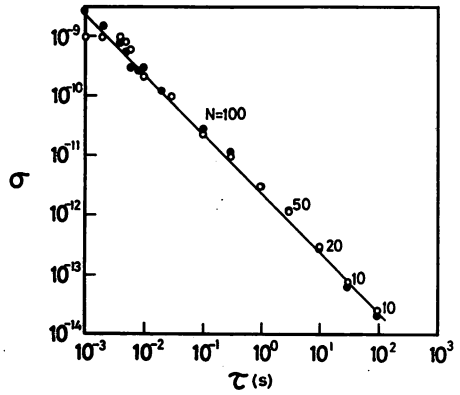

Fig. 13. Frequency traceability of the second laser in terms of the square root of the Allan variance σ^2 of the frequency fluctuations of the beat signal between the first and second lasers. The second laser is frequency offset locked to the first laser. The value of σ is normalized to the He-Xe laser frequency at 3.51 μm. The same PZT driver was used as for curve B in Fig. 11. ○: the frequency of the first laser only was modulated. Therefore, the beat frequency was modulated. ●: the frequency of the second laser was modulated synchronously with that of the first laser. Therefore, the beat frequency was not modulated.

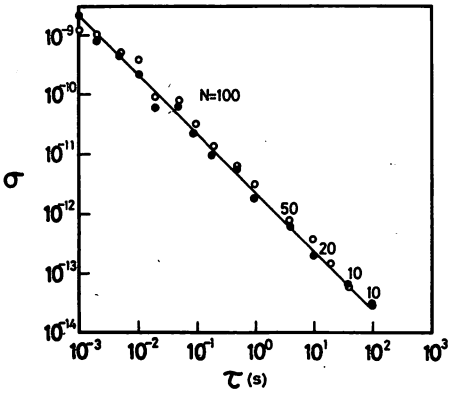

Fig. 14. Frequency traceability of the third laser in terms of the square root of the Allan variance σ^2 of the frequency fluctuations of the beat signal between the second and third lasers. The third laser was frequency offset locked to the second laser. The value of σ is normalized by the He-Xe laser frequency at 3.51 μm. The differentiator was used with the proportional amplifier, the integrating amplifier, and the filter in the PZT driver for the third laser. ○: the beat frequency was modulated. ●: the beat frequency was not modulated.

to the first laser. Fig. 14 shows the normalized frequency fluctuations of the beat signal between the second and third lasers. In these experiments, the differentiator was used with the proportional amplifier, the integrating amplifier, and the filter in the PZT driver for the third laser. The white circles represent the result in which the beat frequency $f_2 - f_3$ was modulated and the black circles are for the experiment in which $f_2 - f_3$ was not modulated, as shown in Fig. 2. Since no difference was clearly seen between the two results, it can also be said that the stability of the beat frequency $f_2 - f_3$ was independent of the frequency modulation. The value of σ in Fig. 14 is nearly equal to that in Fig. 13. Furthermore, it was found that other characteristics of the stability of the beat frequency $f_2 - f_3$ were almost the same as those of $f_1 - f_2$ which are shown in Figs. 11 and 12. Since the value of σ in Fig. 14 can be interpreted as representing the traceability of the frequency of the third laser to that of the second laser, the frequency stability of the third laser can be approximately expressed by the square root of the sum of σ^2 on curves B in

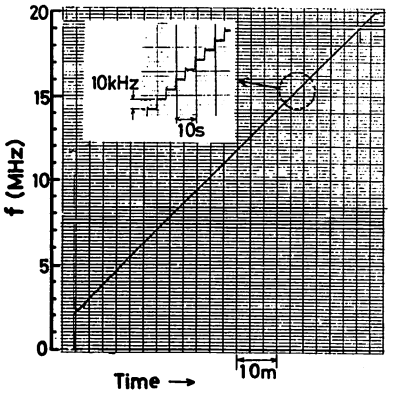

Fig. 15. Experimental result in which the beat frequency $f_2 - f_3$ between the second and third lasers was automatically swept at a 10 kHz interval when the third laser was frequency offset locked to the second laser. Therefore, the frequency of the third laser was swept at a 10 kHz interval in this figure.

Figs. 9 and 11 and that on the curve in Fig. 14. Its stability at $\tau = 100$ s can be estimated to be about 1.0×10^{-13} from these figures.

Next, the frequency tunability of the third laser is reported. Fig. 15 shows the experimental result in which the frequency of the third laser was automatically swept at a 10 kHz interval while the third laser is frequency offset locked to the second laser. In this experiment, the frequency of the first laser was stabilized and the second laser was frequency offset locked to the first laser so that the value of the beat frequency $f_1 - f_2$ was fixed at 8 MHz. It is seen from this figure that the variable range in which the beat frequency $f_2 - f_3$ was locked was 18 MHz, i.e., 2 MHz $\leqq f_2 - f_3 \leqq$ 20 MHz. From subsequent experiments, it was found that this range was 19 MHz, i.e., the lowest value of $f_2 - f_3$ was 1 MHz. When $f_2 - f_3$ was lower than 1 MHz, the frequency stabilities of the second and third lasers were decreased because the oscillation of one laser was disturbed by the injection from the other laser, as described in Section II. When $f_2 - f_3$ was higher than 20 MHz, on the other hand, the amplitude of the beat signal was too low to convert it into a TTL compatible signal by the discriminator in Fig. 2. The variable range of the beat frequency will be increased by improving the bandwidth of the InAs detector. However, since a variable range higher than 10 MHz was obtained and the frequency stability was found to be high in the present work, it is said that this frequency offset locked laser system can be used for high resolution laser spectroscopy of H_2CO whose spectral width is narrower than a few megahertz.

IV. Conclusion

A frequency offset locked He-Xe laser system was constructed for high resolution laser spectroscopy of H_2CO at 3.51 μm. The frequencies of the three lasers were controlled by the PZT drivers with the bandwidth of about 1 kHz, and the following results were obtained.

1) The frequency stability of the first laser, the H_2CO-stabilized He-Xe laser used as the frequency reference, was

$$\sigma = 1.0 \times 10^{-14} \quad \text{at} \quad \tau = 100 \text{ s} \tag{3}$$

which is the minimum value of σ in the present experiment for the first laser.

2) The frequency traceability of the second laser, the frequency offset locked laser used as a local oscillator, to the first laser was

$$\sigma = 8.0 \times 10^{-13} \cdot \tau^{-1} \quad \text{for} \quad 10\ \text{ms} \leqq \tau \leqq 100\ \text{s}. \tag{4}$$

It was found that the value of the traceability was independent of the frequency modulation of the first and second lasers.

3) The frequency traceability of the third laser, the frequency offset locked laser used to observe the H_2CO spectrum, to the second laser was nearly equal to that of (4).

4) The variable range of the beat frequency $f_2 - f_3$ was

$$1\ \text{MHz} \leqq f_2 - f_3 \leqq 20\ \text{MHz}. \tag{5}$$

Therefore, the variable range of the frequency of the third laser was 19 MHz. In this range, the frequency traceability of the third laser to the second laser was independent of the value of $f_2 - f_3$. This independence also held for the frequency traceability of the second laser to the first laser.

References

[1] J. L. Hall and C. J. Bordé, "Measurement of methane hyperfine structure using laser saturated absorption," *Phys. Rev. Lett.*, vol. 30, pp. 1101-1104, 1973.

[2] M. Ohtsu and T. Tako, "Frequency stability of an H_2CO-stabilized He-Xe laser in an axial magnetic field," *Japan. J. Appl. Phys.*, vol. 17, pp. 2169-2170, 1978.

[3] M. Ohtsu, R. Koyama, and T. Tako, "Improvements in the long-term frequency stability of the He-Xe laser at 3.51 μm," *Japan. J. Appl. Phys.*, vol. 18, pp. 1621-1622, 1979.

[4] M. Ohtsu, R. Koyama, A. Kusnowo, and T. Tako, "Development of a frequency-offset-locked He-Xe laser at 3.51 μm," *Japan. J. Appl. Phys.*, vol. 18, pp. 1619-1620, 1979.

[5] Y. Ohwada and T. Tako, "Output power characteristics of Xe 5d-6p laser lines" (in Japanese), *Kogaku*, vol. 5, pp. 93-98, 1976.

[6] G. J. Linford, "High-gain natural laser lines in pulsed noble-gas discharges," *IEEE J. Quantum Electron.*, vol. QE-8, pp. 477-482, June 1972.

[7] M. Ohtsu, I. Mitamura, and T. Tako, "Oscillating characteristics of He-Xe lasers at 3.51 μm—a Fabry-Perot resonator-type and waveguide-type" (in Japanese), *J. Spectrosc. Soc. Japan*, vol. 28, pp. 327-336, 1979.

[8] D. W. Allan, "Statistics of atomic frequency standards," *Proc. IEEE*, vol. 54, pp. 221-230, Feb. 1966.

[9] I. Siio, M. Ohtsu, S. Katsuragi, and T. Tako, "Development of the Allan variance real-time processor" (in Japanese), *Trans. IECE Japan*, to be published.

[10] H. Hellwig, H. E. Bell, P. Kartaschoff, and J. C. Bargquist, "Frequency stability of methane-stabilized He-Ne lasers," *J. Appl. Phys.*, vol. 43, pp. 450-452, 1972.

Motoichi Ohtsu was born in Kanagawa, Japan, on October 5, 1950. He received the B.S., M.S., and Ph.D. degrees in electronics engineering from Tokyo Institute of Technology, Tokyo, Japan, in 1973, 1975, and 1978, respectively.

Since joining the Research Laboratory of Precision Machinery and Electronics, Tokyo Institute of Technology, Yokohama, Japan, in 1978, he has been engaged in research of frequency stabilization of gas lasers and high resolution laser spectroscopy.

Dr. Ohtsu is a member of the Institute of Electronics and Communication Engineers of Japan and the Japan Society of Applied Physics.

Seiichi Katsuragi was born in Kumamoto, Japan, on February 8, 1954. He received the B.S. and M.S. degrees in applied physics from the Tokyo Institute of Technology, Tokyo, Japan, in 1977 and 1980, respectively.

In 1980 he joined Toshiba Corporation, Kanagawa, Japan.

Mr. Katsuragi is a member of the Japan Society of Applied Physics.

Toshiharu Tako was born in Inuyama, Aichi, Japan, on July 1, 1923. He received the B.S. and D.Sci. degrees in physics from the University of Tokyo, Tokyo, Japan, in 1947 and 1961, respectively.

From 1955 to 1971 he was a Research Officer and later a Division Chief at the National Research Laboratory of Metrology. From 1967 to 1968 he was a Visiting Senior Research Associate at the Department of Electrical Engineering, University of Rochester, Rochester, NY. In 1971 he was appointed Professor at the Research Laboratory of Precision Machinery and Electronics, Tokyo Institute of Technology, Yokohama, Japan. His present research interests include frequency stabilization of gas and semiconductor lasers and laser applications to metrology.

Dr. Tako is a fellow of the Optical Society of America and a member of the Institute of Electronics and Communication Engineers of Japan and the Japan Society of Applied Physics.